

Doctoral Dissertation  
博士論文

**Full Commissioning of Liquid Xenon  
Scintillation Detector to Search for  $\mu^+ \rightarrow e^+\gamma$   
with the Highest Sensitivity in MEG II  
Experiment**

(MEG II 実験における最高感度での  $\mu^+ \rightarrow e^+\gamma$  探索のための  
液体キセノンシンチレーション検出器のコミッショニング)

A Dissertation Submitted for the Degree of Doctor of Philosophy

December 2022

令和4年12月博士(理学)申請

Department of Physics, Graduate School of Science,  
The University of Tokyo

東京大学大学院理学系研究科  
物理学専攻

**Satoru Kobayashi**  
小林 暁



# Abstract

A charged lepton flavor violating decay of a muon,  $\mu^+ \rightarrow e^+\gamma$ , is a promising probe in the search for physics beyond the Standard Model. The MEG experiment set an upper limit of the branching ratio of  $\mu^+ \rightarrow e^+\gamma$  of  $4.2 \times 10^{-13}$  (90% confidence level). An upgrade experiment of MEG called MEG II is designed to improve the sensitivity by one order of magnitude using detectors with improved performance. This upgrade is motivated by the fact that the resolutions of the detectors are essential to discriminate the  $\mu^+ \rightarrow e^+\gamma$  signal from the accidental background. To improve the resolutions of the liquid xenon scintillation detector for the gamma-ray measurement, a new photosensor VUV-MPPC was installed. This thesis describes the commissioning of the upgraded liquid xenon detector for the  $\mu^+ \rightarrow e^+\gamma$  search with the highest sensitivity in the MEG II experiment. Precise calibration measurements for the new VUV-MPPC are developed to achieve uniform and stable gamma-ray measurements. The systematic uncertainty of the gamma-ray measurement is suppressed to 0.4% and 0.6 mm for energy and position, respectively, by several calibration measurements. The resolutions for the signal gamma ray are estimated based on measurements with 17.6 MeV and 54.9 MeV gamma rays. The best resolutions of 1.7%, 2.5 mm, and 61 ps are achieved for energy, position, and time, respectively. Improvements in the energy and position resolutions for gamma-ray hits close to the entrance face are achieved compared to the MEG liquid xenon detector. By utilizing the pileup analysis algorithm, a reduction of the rate of accidental background events in the analysis region by 25% is achieved. The MEG II experiment started a pilot physics data taking in 2021, followed by the first long-term data acquisition in 2022. The experimental sensitivity is estimated based on the measured resolutions and counting rate in 2021. It is  $(8.1 \pm 0.4) \times 10^{-13}$  with the 2021 dataset, and it evolves down to  $(2.1 \pm 0.1) \times 10^{-13}$  by adding the 2022 dataset. Another three years of data acquisition will improve the sensitivity down to  $(8.1 \pm 0.4) \times 10^{-14}$ , which is six times better than the sensitivity of  $5.3 \times 10^{-13}$  in the MEG experiment. The upgraded liquid xenon detector has been fully commissioned and is ready to search for the  $\mu^+ \rightarrow e^+\gamma$  with the highest sensitivity.

# Contents

Chapter 1	Introduction	1
1.1	Physics motivation of $\mu^+ \rightarrow e^+\gamma$ search . . . . .	3
1.2	$\mu^+ \rightarrow e^+\gamma$ search in MEG experiment . . . . .	6
Chapter 2	MEG II Experiment	14
2.1	Beam & Target . . . . .	14
2.2	Positron Spectrometer . . . . .	17
2.3	Liquid Xenon gamma-ray detector . . . . .	23
2.4	Radiative Decay Counter . . . . .	43
2.5	$\pi^0$ measurement setup . . . . .	43
2.6	17.6 MeV CW-Li gamma-ray . . . . .	49
2.7	Data acquisition system . . . . .	50
2.8	Trigger . . . . .	53
2.9	Detector simulation . . . . .	56
Chapter 3	Run 2021	60
3.1	Overview . . . . .	60
3.2	Preparation for physics run . . . . .	61
3.3	Physics run . . . . .	62
3.4	$\pi^0$ run . . . . .	66
Chapter 4	Calibration and Monitoring of the Liquid Xenon Detector	69
4.1	Overview . . . . .	69
4.2	Noise reduction . . . . .	71
4.3	MPPC gain and ECF calibration . . . . .	75
4.4	PMT gain calibration . . . . .	78
4.5	PDE and QE calibration . . . . .	82
4.6	Light yield and energy scale . . . . .	89
4.7	Alignment of MPPC . . . . .	93
Chapter 5	Radiation Damage to VUV-MPPC	103
5.1	Radiation environment for MPPC . . . . .	103
5.2	Decrease in MPPC PDE . . . . .	104

---

5.3	Thermal annealing . . . . .	109
5.4	Impact on the experimental sensitivity . . . . .	115
Chapter 6	Position Resolution	118
6.1	Position Reconstruction . . . . .	118
6.2	Resolution Measurement . . . . .	121
Chapter 7	Energy Resolution	130
7.1	Reconstruction Algorithm . . . . .	130
7.2	Uniformity . . . . .	131
7.3	Resolution . . . . .	135
7.4	Energy scale . . . . .	140
7.5	Summary . . . . .	141
Chapter 8	Time Resolution	142
8.1	Time Reconstruction . . . . .	142
8.2	Resolution Measurement . . . . .	143
Chapter 9	Efficiency	149
9.1	Efficiency for signal gamma-ray in MC simulation . . . . .	149
9.2	Efficiency measurement . . . . .	150
9.3	Conclusion . . . . .	152
Chapter 10	Background	154
10.1	Pileup analysis . . . . .	154
10.2	Cosmic-ray rejection . . . . .	161
10.3	Background rate . . . . .	163
Chapter 11	Sensitivity	165
11.1	Maximum Likelihood Analysis . . . . .	165
11.2	2021 dataset . . . . .	166
11.3	PDF . . . . .	167
11.4	Normalization and single event sensitivity with 2021 dataset . . . . .	173
11.5	Estimated number of background events with 2021 dataset . . . . .	174
11.6	Sensitivity with 2021 dataset . . . . .	175
11.7	Sensitivities with 2022 run dataset and further . . . . .	176
11.8	Discussion . . . . .	178
Chapter 12	Conclusion	181
Appendix A	Summary of commissioning runs	182
A.1	Commissioning run 2017 . . . . .	182
A.2	Commissioning run 2018 . . . . .	182

---

A.3	Commissioning run 2019 . . . . .	182
A.4	Commissioning run 2020 . . . . .	183
Appendix B	Optimization of weights for uniform online $E_\gamma$ reconstruction	185

# Chapter 1

## Introduction

The Standard Model (SM) is a fundamental model that describes physics below the electroweak energy scale precisely. However, it faces many problems, such as the hierarchy problem and dark matter, and is considered to be a low-energy approximation of a more general theory. In building such a theory, it is important to discover phenomena that are suppressed or prohibited in the SM, such as neutrino oscillations. In this context, charged lepton flavor violation (cLFV), flavor mixing for charged leptons, has attracted much attention. This is because the cLFV is prohibited in the SM while it is predicted to be detectable based on many promising new theories. Therefore the discovery of the cLFV would be clear evidence of the physics beyond the SM.

The current upper limit on the branching ratio of the  $\mu^+ \rightarrow e^+\gamma$  of  $4.2 \times 10^{-13}$  (90% C.L.) was set by the MEG experiment [1]. The sensitivity of MEG was limited by the rate of accidental backgrounds, and it motivated an upgraded experiment MEG II with detectors with improved resolutions to achieve a higher sensitivity by one order of magnitude,  $\mathcal{O}(10^{-14})$ . In particular, the upgrade of the gamma-ray detector is important because the number of accidental backgrounds greatly depends on the gamma-ray energy resolution. The MEG II liquid xenon (LXe) gamma-ray detector uses a new small photosensor VUV-MPPC to improve the position and energy resolutions with the granular readout on the entrance face.

The detector performance studies with datasets collected in 2017–2020 with a limited readout region are summarized in Ref. [2]. The energy resolution is estimated from the continuous spectrum under a high-intensity muon beam, and the time resolution is estimated based on the intrinsic time difference between the time reconstructed by using a different set of photosensors. The observations of unexpected radiation damage of the VUV-MPPC under a high-intensity muon beam environment are described, and its impact on the detector performance is evaluated with simulations. The analysis of the background gamma rays implies that the fraction of the events with two coincident background gamma rays is twice larger than expected from the simulation, and it could lead to a worse sensitivity of the  $\mu^+ \rightarrow e^+\gamma$  search.

Ref. [3] describes the suppression of accidental background with the LXe detector and a tagging detector called RDC. A new analysis algorithm is developed to reduce the accidental background using the waveforms and the light distribution of the LXe detector. It implies that the measured time resolution might be considerably worse than expected, possibly due to the systematic error

in the estimation. A measurement to suppress the systematic error to measure the resolution accurately is proposed.

This thesis describes the full commissioning of the upgraded LXe detector, which can be categorized into a few works as follows.

- Calibration measurements of the detector with the new VUV-MPPC.
- Performance evaluation of the gamma-ray measurement.
- Study of the rate and distributions of background events.

Calibration measurements for the VUV-MPPC are newly developed to monitor the performance of the VUV-MPPCs and to have stable, uniform, and precise gamma-ray reconstruction. A novel measurement method of the MPPC positions was developed to measure the positions with good accuracy and to suppress the systematic uncertainty of the gamma-ray position measurement.

The detector performance for the signal gamma ray with the full scintillation readout is understood by this work. Dedicated performance measurement was performed to collect 55 MeV gamma rays from  $\pi^0 \rightarrow \gamma\gamma$  decay. The energy and time resolutions and detection efficiency for the signal gamma ray are estimated by the measured performance for 55 MeV gamma rays. The position resolution of the detector is estimated based on a measurement with 17.6 MeV gamma rays.

The qualitative analysis of background events is essential to estimate the sensitivity of the experiment. The pileup analysis algorithm is applied to the real dataset to identify pileup gamma rays and reduce the rate of accidental backgrounds. The measured rate and distributions of the background are studied, and they agree well with the rate and distributions of background events in MC simulation.

At the end of this thesis, the experimental sensitivity with the achieved performance and the measured background rate in 2021 is estimated. It is proved that the search for the  $\mu^+ \rightarrow e^+\gamma$  decay with the highest sensitivity is achievable with the measured detector performance.

This thesis is organized as follows. In this chapter, the physics motivation of the  $\mu^+ \rightarrow e^+\gamma$  and the previous  $\mu^+ \rightarrow e^+\gamma$  search in the MEG experiment are discussed. The experimental setup of MEG II is introduced in Chap. 2. The situation of the 2021 run is summarized in Chap. 3. The calibration measurements for the stable and precise gamma-ray reconstruction are described in Chap. 4. The observation of the unexpected radiation damage of the VUV-MPPC and our countermeasure, thermal annealing, are summarized in Chap. 5. The position, energy, and time resolution measurements are described in Chap. 6, Chap. 7, and Chap. 8, respectively. The evaluation of the detection efficiency for the signal gamma-ray is explained in Chap. 9. The analysis of the rate and distribution of background events is presented in Chap. 10. The projected sensitivity of the MEG II experiment based on current estimates of the detector performance will be discussed in Chap. 11. Finally, the conclusion of this thesis is given in Chap. 12.

## 1.1 Physics motivation of $\mu^+ \rightarrow e^+ \gamma$ search

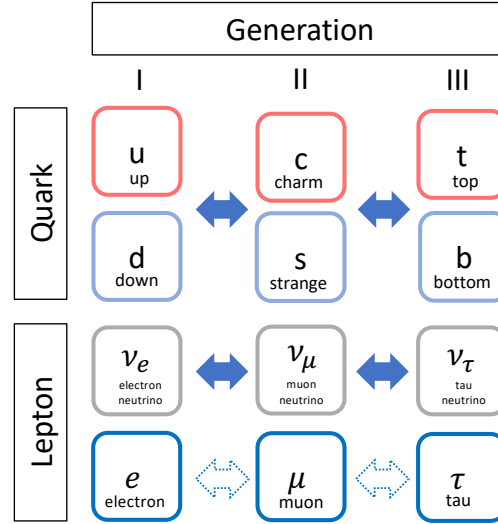


Figure 1.1: Fermions and their mixing in the Standard Model (SM). There are 12 fermions in three flavors (generations). While the mixing between flavors is observed for quarks and neutrinos, the mixing in the charged lepton sector has never been observed to date.

The Standard Model (SM) is a field theory based on the fundamental fermions and the gauge theory. The electromagnetic and the weak interactions are unified into a single  $SU(2) \times U(1)$  electroweak interaction and the strong interaction is described by quantum chromodynamics (QCD,  $SU(3)$ ) in this model. The SM has been verified by a wide variety of experiments so far, and it successfully describes the physics of an energy range from  $\mathcal{O}(1)$  eV to  $\mathcal{O}(100)$  GeV. However, the SM is considered to be only a low-energy approximation of a higher scale theory beyond the Standard Model (BSM) because it faces both theoretical and experimental problems.

One of the theoretical problems of the SM is the hierarchy problem [4]. The hierarchy problem is related to the huge difference between the weak scale ( $\mathcal{O}(100)$  GeV) and the reduced Planck scale ( $\mathcal{O}(10^{18})$  GeV). Since the SM Higgs mass parameter  $m$  is affected by the presence of fermion and boson particles with squared masses  $m_i^2 + \lambda_i^2 \phi^2/2$ , where  $m_i$  and  $\lambda_i$  are the mass and the Higgs quartic coupling of the particle  $i$ , respectively, the running of the mass parameter from the scale  $\mu$  to the scale  $Q$  is calculated as [5]

$$m^2(Q) = m^2(\mu) + \delta m^2, \quad (1.1)$$

$$\delta m^2 = \sum_i g_i (-1)^{2S_i} \frac{\lambda_i^2 m_i^2}{32\pi^2} \log\left(\frac{Q^2}{\mu^2}\right), \quad (1.2)$$

where the sum is over all particles and  $g_i$  and  $S_i$  correspond to the number of degrees of freedom and the spin of the particle  $i$ . Particles that couple to the Higgs and have a large squared mass parameter  $m_i^2$  would induce very large corrections to the Higgs mass parameter. This

nature requires a large fine-tuning to keep  $m^2$  small. Hence, the mass of the Higgs boson is not protected in the presence of heavy states at higher energy scales such as grand-unification or Planck scales. The SM also has several other theoretical issues, such as that the electro-weak force and the strong force are not unified and that the SM does not account for the existence of the three generations of quarks and leptons shown in Fig. 1.1.

The SM is not complete also from the experiment point of view. The discovery of neutrino oscillation [6, 7] and the existence of dark matter [8] are clear evidence of the incompleteness of the SM.

In order to construct the theory that describes physics at the high energy scale beyond the SM, it is important to search for phenomena prohibited in the SM and predicted by BSM theories. One promising probe is charged lepton flavor violation (cLFV) process, flavor mixing between charged leptons. As shown in Fig. 1.1, the flavor mixing in the quark sector and in the neutrino sector has already been observed, whereas the cLFV has never been observed. The discovery of neutrino oscillation indicates that the lepton flavor is not strictly conserved and implies that the flavor mixing process may occur in the charged lepton sector as well. In the following sections, the small branching ratio of the  $\mu^+ \rightarrow e^+\gamma$  in the extension of the SM with neutrino oscillation is explained in Sec. 1.1.1 and the detectable branching ratio in the BSM models is discussed in Sec. 1.1.2.

### 1.1.1 $\mu^+ \rightarrow e^+\gamma$ decay through neutrino oscillation

The neutrino oscillation, transition in flight between the different flavor neutrinos  $\nu_e, \nu_\mu, \nu_\tau$ , is evidence of the nonzero neutrino masses and the mixing. The unitary transformation between flavor eigenstates and mass eigenstates of the neutrino can be written as,

$$\nu_\alpha = \sum_i U_{\alpha i} \nu_i \quad (i = 1, 2, 3) \quad (1.3)$$

$$\nu_i = \sum_\alpha U_{\alpha i}^* \nu_\alpha \quad (\alpha = e, \mu, \tau) \quad (1.4)$$

where  $\nu_\alpha = \nu_e, \nu_\mu, \nu_\tau$  are flavor eigenstates and  $\nu_i = \nu_1, \nu_2, \nu_3$  are mass eigenstates with mass eigenvalues  $m_1, m_2, m_3$ .  $U$  is a unitary matrix known as Pontecorvo-Maki-Nakagawa-Sakata (PMNS) matrix. The time evolution of the mass eigenstate of  $i$  after a time interval  $t$  can be given by

$$|\nu_i(t)\rangle = e^{-iE_i t} |\nu_i(0)\rangle, \quad (1.5)$$

where  $E_i$  is the energy of the mass eigenstate  $i$ . Thus the time evolution of flavor eigenstate of  $\alpha$  is given by Eq. 1.3 and Eq. 1.5 as

$$|\nu_\alpha(t)\rangle = \sum_i U_{\alpha i} e^{-iE_i t} |\nu_i(0)\rangle. \quad (1.6)$$

The probability of finding flavor  $\nu_\beta$  in  $\nu_\alpha$  beam at a distance  $x$  from the source is given by

$$P_{\nu_\alpha \rightarrow \nu_\beta} = \sum_i |U_{\alpha i}|^2 |U_{\beta i}|^2 + \sum_{i \neq j} U_{\alpha i} U_{\beta i}^* U_{\alpha j}^* U_{\beta j} \cos\left(\frac{2\pi x}{L_{ij}}\right) \quad (1.7)$$

where  $L_{ij} = 2\pi/(E_i - E_j) \simeq 4\pi p/|m_i^2 - m_j^2|$  is the oscillation length.

While the cLFV is strictly forbidden in the SM, flavor mixing in the neutrino sector is the source of the cLFV in a simple extension of the SM with neutrino oscillations. The  $\mu^+ \rightarrow e^+\gamma$  decay occurs in a process through neutrino oscillation as shown in Fig. 1.2. The branching ratio of this process can be calculated as [9]

$$\mathcal{B}(\mu \rightarrow e\gamma) = \frac{3\alpha}{32\pi} \left| \sum_{i=2,3} U_{\mu i}^* U_{ei} \frac{\Delta m_{i1}^2}{M_W^2} \right|^2 \simeq 10^{-54}, \quad (1.8)$$

where  $\alpha$  is the fine-structure constant,  $M_W$  is the mass of the W boson,  $\Delta m_{i1}^2$  is the mass difference of neutrinos. The branching ratio is very small and far from the experimental reach because the neutrino mass difference is very small compared to the mass of the W boson. Since the cLFV processes are free from the SM and the neutrino oscillation background, the discovery of the cLFV processes would be clear evidence of BSM.

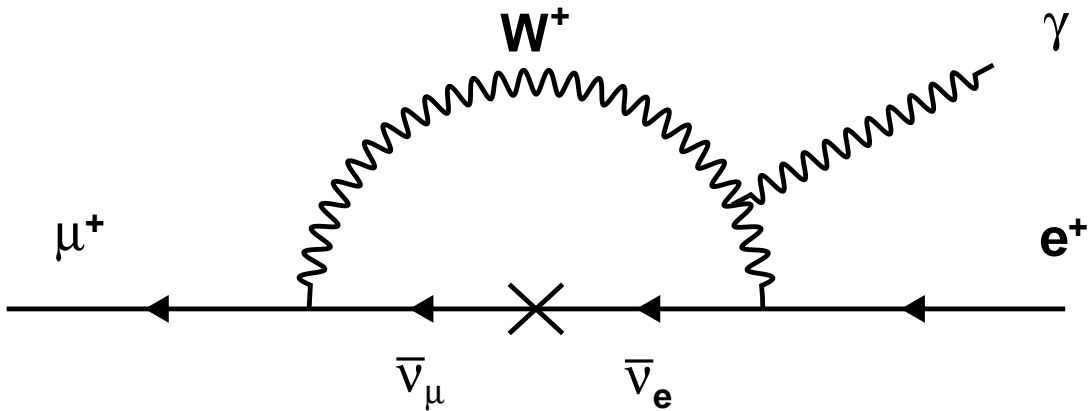


Figure 1.2: Feynmann diagram of the  $\mu^+ \rightarrow e^+\gamma$  through neutrino oscillation.

### 1.1.2 $\mu^+ \rightarrow e^+\gamma$ in BSM models

The supersymmetric (SUSY) model is one of promising BSM models. The SUSY transformation is such that fermions are converted to bosons and bosons to fermions, and all particles have supersymmetric partners. If such partners exist, the quantum corrections to the mass of the Higgs boson are canceled between the corrections due to fermions and the corrections due to bosons, and the mass of the Higgs boson is protected without fine-tuning. A SUSY partner is introduced to each SM particle in the minimal extension of the SM with SUSY called MSSM. In the context of the SUSY, the SM particles and their superpartners have the same mass when the SUSY is not broken. However, the superpartners with the same masses have not been found, and thus the symmetry is broken. In the SUSY models, the source of the

cLFV is off-diagonal elements in the slepton mass matrix that comes from the misalignment between particle and superparticle mass eigenstates. Here we present the off-diagonal elements expected in two representative SUSY scenarios, SUSY-seesaw and SUSY-GUT, and then discuss the expected branching ratio in a model incorporating both of them [10].

The seesaw model can naturally explain the extremely light neutrino masses with respect to other fermions by introducing heavy right-handed neutrinos. The SUSY-seesaw model introduces the seesaw mechanism to the SUSY model [11, 12]. In this model, Majorana right-handed heavy neutrinos are introduced. The Yukawa coupling constant for the neutrinos becomes a large source of the LFV. In this model, the LFV off-diagonal components are

$$(m_{iL}^2)_{ij} \simeq -\frac{1}{8\pi^2}(3m_0^2 + A_0^2)(Y_\nu)_{ik}(Y_\nu^\dagger)_{jk} \ln\left(\frac{M_X}{M_{Rk}}\right), \quad (1.9)$$

where  $M_X$  is the scale of the SUSY breaking,  $m_0$  is the universal scalar mass,  $A_0$  is the trilinear coupling,  $M_{Rk}$  is the mass of the right-handed Majorana neutrino,  $Y_\nu$  is the Yukawa coupling of the neutrinos.

Another example is the SUSY-GUT model [13, 14]. A Grand Unified Theory (GUT) is a model to unify the electroweak and strong interactions into a single force at the GUT scale. In the SUSY-GUT model, the interactions are integrated with the help of the SUSY particles. While the model with SU(5) symmetry, which is the simplest Lie group that contains the SM, is already excluded by the longer lifetime of the proton than the prediction [15], many other models, including an extended version of SU(5) with SUSY, predict a longer lifetime and are therefore not excluded. The off-diagonal terms of the right-handed slepton mass matrix are

$$(m_{iR}^2)_{i \neq j} = -3\frac{3m_0^2 + A_0^2}{8\pi^2}V_{ti}V_{tk} \ln\left(\frac{M_X}{M_{\text{GUT}}}\right), \quad (1.10)$$

where  $V$  is the CKM matrix,  $M_{\text{GUT}}$  is the mass scale of the GUT.

Ref. [10] calculates the branching ratio of the  $\mu^+ \rightarrow e^+\gamma$  in a SUSY model incorporating both grand unification and see-saw mechanism, by paying attention to Casas–Ibarra parameters that affect the mixing structure of the neutrino Yukawa matrix. Fig. 1.3 shows the expected branching ratio of the  $\mu^+ \rightarrow e^+\gamma$  on  $(m_0, \tan\beta)$  plane [10]. It indicates that the current limit of the  $\mu^+ \rightarrow e^+\gamma$  by MEG already excluded a part of the expected regions, and the extensive search for the  $\mu^+ \rightarrow e^+\gamma$  will explore the parameter space with higher  $m_0$  and lower  $\tan\beta$ .

## 1.2 $\mu^+ \rightarrow e^+\gamma$ search in MEG experiment

Fig. 1.4 shows the progress of cLFV searches of three muonic channels,  $\mu \rightarrow e\gamma$ ,  $\mu N \rightarrow eN$ , and  $\mu \rightarrow eee$ . The sensitivity of the muon cLFV search has been continuously improved with the evolution of experimental techniques. The current upper limit on the branching ratio of  $\mu^+ \rightarrow e^+\gamma$  of  $4.2 \times 10^{-13}$  (90% C.L.) was set by the MEG experiment [1]. In this section, the principle, experimental setup, and limitations of the MEG experiment are described. They will help us to understand the approaches to realize the search for  $\mu^+ \rightarrow e^+\gamma$  with the highest sensitivity of  $\mathcal{O}(10^{-14})$  in the upgraded experiment MEG II.

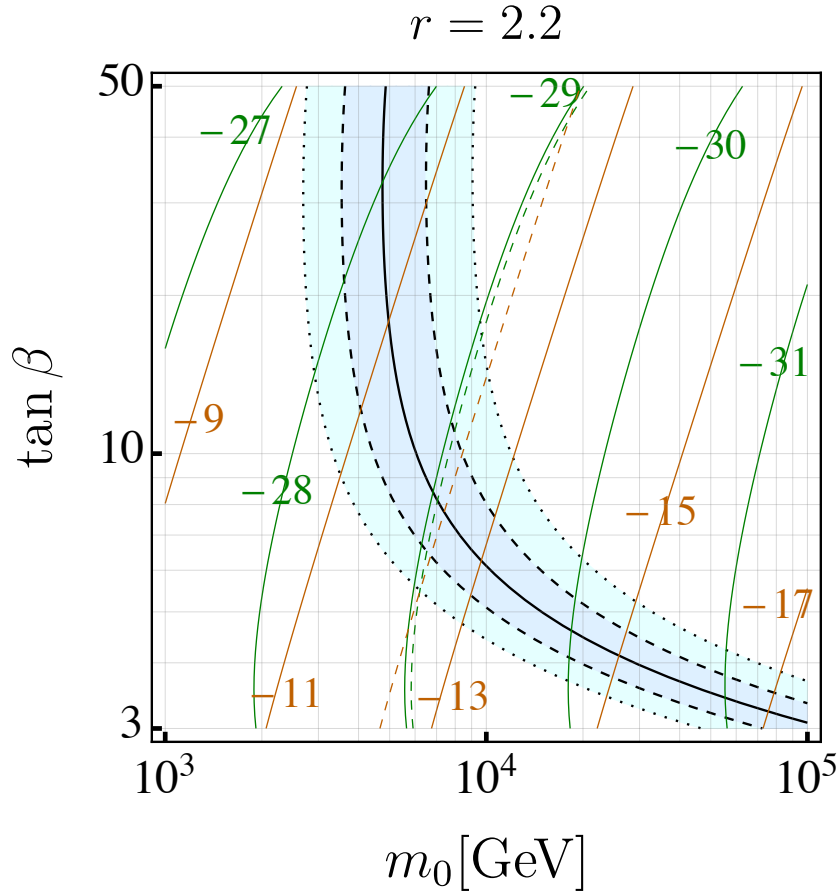


Figure 1.3: Expected  $\mu \rightarrow e\gamma$  branching ratio (orange) and electron electric dipole moment (green) on  $(m_0, \tan\beta)$  plane [10]. The parameters are chosen as follows: the universal right-handed neutrino mass  $M_{N_R} = 10^{13}$  GeV, Casas–Ibarra parameters  $(r, \theta, \phi) = (2.2, \frac{\pi}{2}, 0)$ . Black lines show the Higgs mass  $M_H = 123, 124, 125, 126, 127$  GeV from left to right. Orange and green dashed lines show the present limit of the  $\mu^+ \rightarrow e^+\gamma$  branching ratio and electron electric dipole moment.

### 1.2.1 Principle of $\mu^+ \rightarrow e^+\gamma$ search

The MEG experiment used positive muons to avoid the formation of muonic atoms and to take full advantage of a high-intensity polarized muon beam. Since the  $\mu^+ \rightarrow e^+\gamma$  is a two-body decay, a positron and a gamma ray are produced in opposite directions and at the same time. The energies of the positron and gamma ray are well approximated to be half of the muon mass ( $m_\mu c^2/2 = 52.8$  MeV). Thus, the signal of  $\mu^+ \rightarrow e^+\gamma$  can be searched for by measuring the following variables and discriminating from backgrounds.

- $E_{e^+}$ : energy of positron
- $E_\gamma$ : energy of gamma-ray
- $t_{e^+\gamma}$ : time difference between the positron and gamma-ray

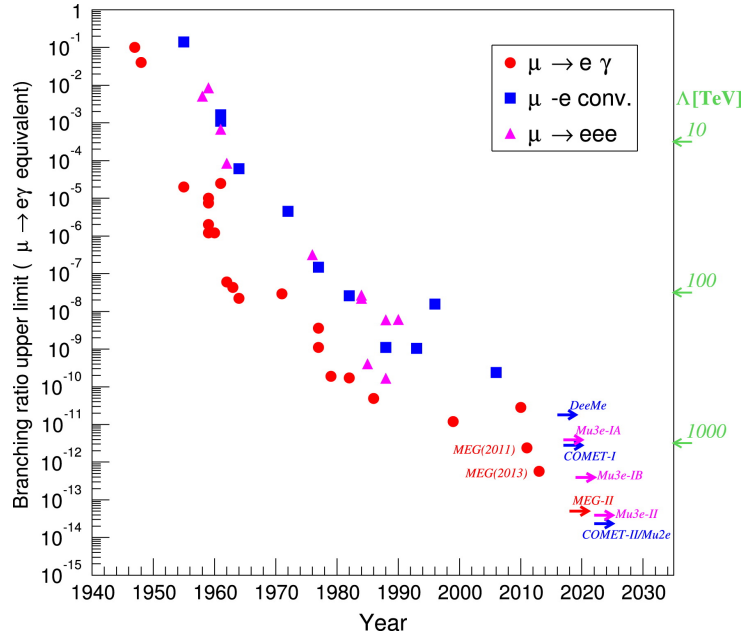


Figure 1.4: Experimental upper limits (90% C.L.) on cLFV muon processes as a function of the year where the  $\mu \rightarrow eee$  and  $\mu \rightarrow e$  conversion bounds are converted into equivalent  $\mu \rightarrow e\gamma$  bounds [16].

- $\Theta_{e+\gamma}$ : opening angle between the positron and gamma-ray

The relative angle between the positron and gamma ray is also defined by the relative azimuthal angle  $\theta_{e+\gamma}$  and polar angle  $\phi_{e+\gamma}$ .

To search for the rare  $\mu^+ \rightarrow e^+\gamma$  decay with the highest sensitivity, a large number of muon decays are necessary. The most intense DC muon beam at Paul Scherrer Institute (PSI) was used. Since the accidental background is dominant in the search, a DC beam is better than a pulsed beam for collecting a large number of muon decays without increasing instantaneous intensity. The MEG experiment employed a positron spectrometer and a liquid xenon (LXe) scintillation detector to detect a positron and a gamma ray from a  $\mu^+ \rightarrow e^+\gamma$  decay at the target in the center of the detectors, as shown in Fig. 1.5.

Tracks of positrons were measured by 16 drift chamber modules [17], and the time of the positrons was measured by timing counter arrays that consist of two layers of different plastic scintillators along the beam axis [18, 19, 20]. Both detectors were placed in a thin-wall superconducting solenoid magnet called “COBRA” (Constant Bending RADIUS).

The gradient magnetic field generated by COBRA (1.27 T at the center and 0.49 T at both ends) was designed such that the bending radius of the positron trajectory depends on the momentum but almost not on the emission polar angle [21]. Only high-momentum positrons, including the signal positrons, can reach the drift chamber and the timing counter.

The position, energy, and time of the gamma rays were measured by the LXe gamma-ray detector outside of the COBRA [22].

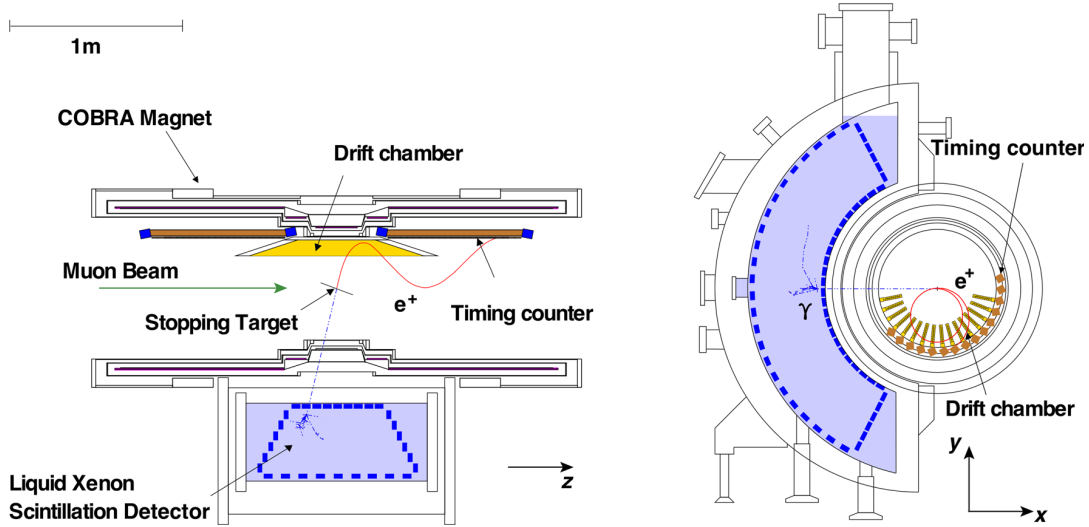


Figure 1.5: Schematic view of the MEG experiment [23]. The top view (left) and view from downstream (right) are shown. The track and time of positrons (red) are measured by the drift chamber and timing counter, respectively. Gamma rays (blue) are measured by the liquid xenon scintillation detector.

## 1.2.2 Backgrounds

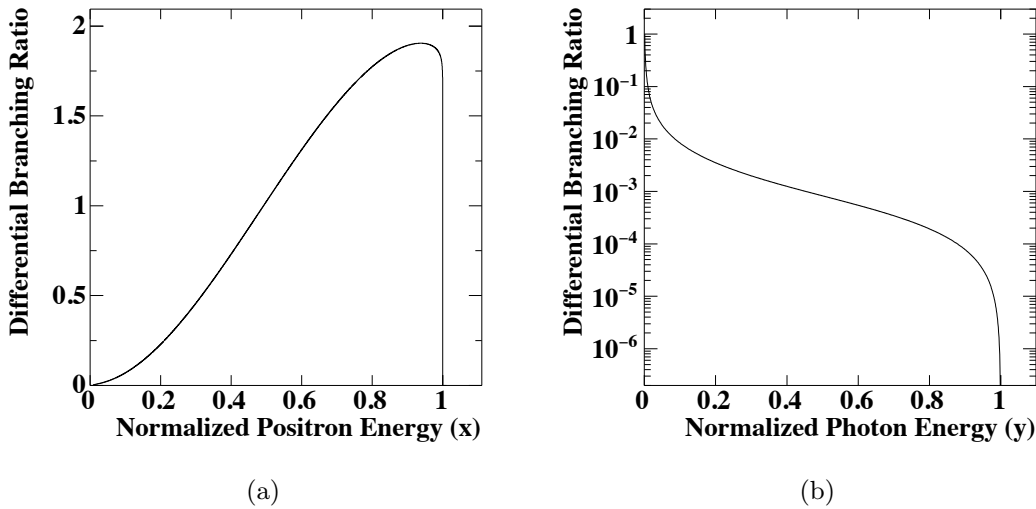


Figure 1.6: (a) Simulated energy spectrum of the Michel positron [24]. (b) Simulated energy spectrum of the RMD gamma ray. Energies on the  $x$ -axis are normalized to the half of the muon mass (52.8 MeV).

There are two kinds of backgrounds that have a similar event signature to the signal. One is physics background from the radiative muon decay (RMD,  $\mu^+ \rightarrow e^+ \nu_e \bar{\nu}_\mu \gamma$ ), and the other is accidental background.

### 1.2.2.1 Physics background

When the two neutrinos from the RMD have little energy, a pair of a gamma ray and a positron is simultaneously emitted nearly in the opposite direction and with signal-like energies. Thus it imitates the  $\mu^+ \rightarrow e^+ \gamma$  signal. The differential branching ratio of this physics background was calculated within the framework of V–A interactions described in Ref. [25]

$$d\mathcal{B}_{\text{RMD}}(\mu^+ \rightarrow e^+ \nu_e \bar{\nu}_\mu \gamma) = \frac{\alpha}{64\pi^3} \beta dx \frac{dy}{y} d\Omega_e d\Omega_\gamma [F(x, y, d) \quad (1.11)$$

$$- \beta \vec{P}_\mu \cdot \hat{p}_e G(x, y, d) \quad (1.12)$$

$$- \vec{P}_\mu \cdot \hat{p}_\gamma H(x, y, d) \quad (1.13)$$

where  $\vec{P}_\mu$  is the muon polarization vector,  $\hat{p}_e$  and  $\hat{p}_\gamma$  are the unit vectors of momenta of the positron and gamma ray, respectively,  $\beta$  is defined as  $\beta \equiv |\vec{p}_e|/E_{e^+}$ ,  $d$  is given by  $d \equiv 1 - \beta \hat{p}_e \cdot \hat{p}_\gamma$ , and  $x$  and  $y$  are normalized positron and gamma energies,  $x = 2E_{e^+}/m_\mu$  and  $y = 2E_\gamma/m_\mu$ . The formulas of  $F(x, y, d)$ ,  $G(x, y, d)$ , and  $H(x, y, d)$  in the SM are given in Appendix A of Ref. [26]. In addition, we define here  $z$  as  $z \equiv \pi - \Theta_{e\gamma}$ . In this notation, an RMD event with  $x \approx 1$ ,  $y \approx 1$ , and  $z \approx 0$  becomes a physics background event. Let us take  $\delta x$ ,  $\delta y$ , and  $\delta z$  to be the kinematic range of the signal region for positron energy ( $1 - \delta x \leq x \leq 1$ ), gamma-ray energy ( $1 - \delta y \leq y \leq 1$ ), and the opening angle ( $0 \leq z \leq \delta z$ ), respectively. Then, the partial branching ratio is given as

$$d\mathcal{B}(\mu^+ \rightarrow e^+ \nu_e \bar{\nu}_\mu \gamma) = \frac{\alpha}{16\pi} [J_1 (1 - P_{\mu^+} \cos \theta_{e^+}) + J_2 (1 + P_{\mu^+} \cos \theta_{e^+})] d(\cos \theta_{e^+}), \quad (1.14)$$

when the angular resolution is better than the kinematic constraint  $\delta z < 2\sqrt{\delta x \delta y}$ .  $J_1$  and  $J_2$  are given by

$$J_1 = \frac{8}{3} (\delta x)^3 (\delta y) \left(\frac{\delta z}{2}\right)^2 - 2(\delta x)^2 \left(\frac{\delta z}{2}\right)^4 + \frac{1}{3} \frac{1}{(\delta y)^2} \left(\frac{\delta z}{2}\right)^8, \quad (1.15)$$

$$J_2 = 8(\delta x)^2 (\delta y)^2 \left(\frac{\delta z}{2}\right)^2 - 8(\delta x)(\delta y) \left(\frac{\delta z}{2}\right)^4 + \frac{8}{3} \left(\frac{\delta z}{2}\right)^6. \quad (1.16)$$

When we use the detector resolutions ( $\delta x \sim 0.07$ ,  $\delta y \sim 0.02$ ,  $\delta z \sim 17$  mrad) and muon polarization ( $-0.86$ ) in the MEG experiment [1], the effective branching ratio of the physics background is the order of  $\mathcal{O}(10^{-15})$ . Thus, the physics background is not a problem to achieve a sensitivity of  $\mathcal{O}(10^{-14})$ .

### 1.2.2.2 Accidental background

An uncorrelated pair of a positron and a gamma ray can mimic the signal by an accidental coincidence when they are emitted nearly in the opposite direction and have signal-like energies at a close time. The effective branching ratio of the accidental background can be estimated as

$$\mathcal{B}_{\text{acc}} = R_\mu \cdot f_{e^+}^0 \cdot f_\gamma^0 \cdot \left(\frac{\delta\omega_{e^+\gamma}}{4\pi}\right) \cdot (2\delta t_{e^+\gamma}), \quad (1.17)$$

where  $R_\mu$  is an instant muon intensity,  $\delta t_{e+\gamma}$  is half width of the signal region for time coincidence,  $\delta\omega_{e+\gamma}$  is that for back-to-back constraint. The terms  $f_{e^+}^0$  and  $f_\gamma^0$  are the fractions of the spectrum within the signal box of positron and gamma ray, respectively. The source of background positrons is Michel decay,  $\mu^+ \rightarrow e^+ \nu_e \bar{\nu}_\mu$ . Michel decay provides high energy positrons abundantly, as shown in Fig. 1.6a. Since the spectrum is almost flat at  $x \approx 1$ ,  $f_{e^+}^0$  can be estimated as  $f_{e^+}^0 \approx 2\delta x$ .

The background gamma rays can come from RMD, annihilation in flight (AIF) of positrons, and bremsstrahlung of positrons. The differential branching ratio of the gamma ray from the RMD is given by Ref. [25]

$$\frac{dB(\mu^+ \rightarrow e^+ \nu_e \bar{\nu}_\mu \gamma)}{dy d \cos \theta_\gamma} = \frac{1}{y} [J_+(y) (1 + P_\mu \cos \theta_\gamma) + J_-(y) (1 - P_\mu \cos \theta_\gamma)], \quad (1.18)$$

where  $\theta_\gamma$  is the angle between muon polarization and  $\gamma$  momentum. Terms suppressed by  $m_e/m_\mu$  are neglected.  $J_+(y)$  and  $J_-(y)$  are defined by Ref. [25] as

$$\begin{aligned} J_+(y) = & \frac{\alpha}{6\pi} (1-y) \left[ \left( 3 \ln \frac{1-y}{r} - \frac{17}{2} \right) \right. \\ & + \left( -3 \ln \frac{1-y}{r} + 7 \right) (1-y) \\ & \left. + \left( 2 \ln \frac{1-y}{r} - \frac{13}{3} \right) (1-y)^2 \right] \end{aligned} \quad (1.19)$$

$$\begin{aligned} J_-(y) = & \frac{\alpha}{6\pi} (1-y)^2 \left[ \left( 3 \ln \frac{1-y}{r} - \frac{93}{12} \right) \right. \\ & + \left( -4 \ln \frac{1-y}{r} + \frac{29}{3} \right) (1-y) \\ & \left. + \left( 2 \ln \frac{1-y}{r} - \frac{55}{12} \right) (1-y)^2 \right] \end{aligned} \quad (1.20)$$

where  $r = (m_e/m_\mu)^2$ . Fig. 1.6b shows the theoretical energy spectrum of the RMD gamma-ray. In contrast to the Michel spectrum, the spectrum rapidly decreases with the energy. By integrating the differential branching ratio by neglecting the higher order terms of  $(1-y)$ ,  $f_\gamma^0$  purely from RMD gamma ray can be calculated as

$$f_\gamma^0 \approx \frac{\alpha}{2\pi} (\delta y)^2 [\ln(\delta y) + 7.33]. \quad (1.21)$$

The source of the AIF gamma ray is the interaction of Michel positrons with the material of the apparatus, such as the drift chamber and target. The contribution of the AIF gamma ray to the sensitivity depends on the design of the experiment. In the MEG experiment, contributions from the two processes (RMD and AIF) were comparable.

The effective branching ratio of accidental background (a Michel positron and an RMD gamma ray) can be approximately calculated by the discussions above as

$$\mathcal{B}_{acc} = R_\mu \cdot 2\delta x \cdot \frac{\alpha}{2\pi} (\delta y)^2 [\ln(\delta y) + 7.33] \cdot \left( \frac{(\delta z)^2}{4} \right) \cdot (2\delta t_{e+\gamma}). \quad (1.22)$$

With the parameters in MEG, the effective branching ratio is  $\mathcal{O}(10^{-13})$ . This calculation indicates that the accidental background must be reduced by an order of magnitude to achieve the search for  $\mu^+ \rightarrow e^+\gamma$  with a sensitivity of  $\mathcal{O}(10^{-14})$ .

### 1.2.3 Sensitivity

The expected number of signal events in an experiment  $N_{\text{sig}}$  can be formulated as

$$N_{\text{sig}} = \mathcal{B} \times R_{\mu} \times T \times \Omega \times \epsilon_{e^+} \times \epsilon_{\gamma} \times \epsilon_{\text{sel}} \quad (1.23)$$

$$= \mathcal{B} \times k, \quad (1.24)$$

where  $T$  is the livetime of the measurement,  $\Omega$  is the solid angle subtended by the acceptance of the detector,  $\mathcal{B}$  is the branching ratio of  $\mu^+ \rightarrow e^+\gamma$ ,  $\epsilon_{e^+}$  and  $\epsilon_{\gamma}$  are the detection efficiency of positron and gamma-ray, respectively.  $\epsilon_{\text{sel}}$  is the efficiency of event selection.  $k$  is the inverse of the single event sensitivity (SES).

The MEG experiment collected physics data from 2008 to 2013. The sensitivity was updated in steps as shown in Fig. 1.7 [27]. The improvement of the sensitivity slowed down as the statistics were accumulated because the effective branching ratio of the accidental background was dominant over the SES. As discussed in Sec. 1.2.2, the number of accidental backgrounds heavily depends on the detector resolutions. Though a high-rate muon beam up to  $1 \times 10^8$  /s can be provided to the experimental setup [28], the beam rate in MEG was limited to  $3.3 \times 10^7$  /s to mitigate the rate of the accidental background that increases with the worse detector performance at a higher intensity. To search for the  $\mu^+ \rightarrow e^+\gamma$  with the higher sensitivity of  $\mathcal{O}(10^{-14})$ , the resolutions for both positron and gamma-ray measurement must be improved to reduce accidental background.

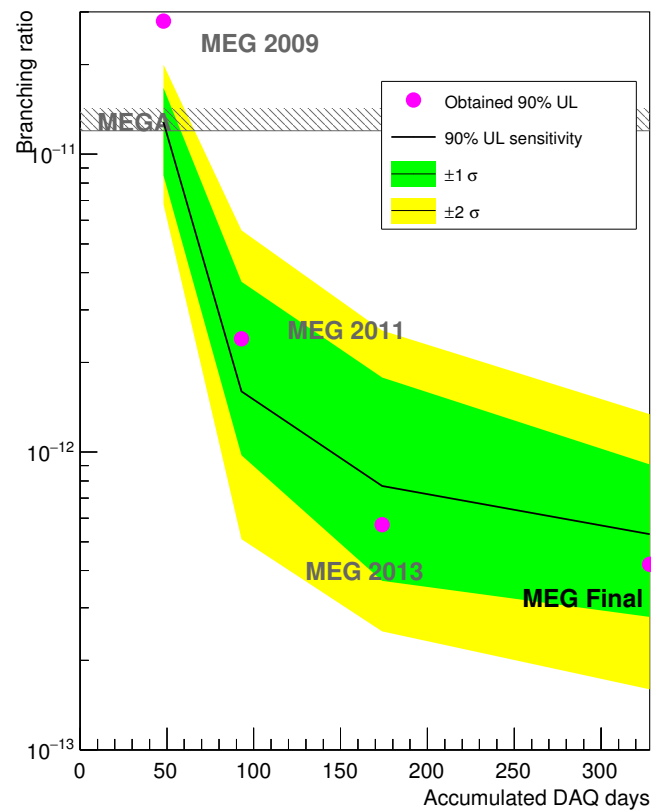


Figure 1.7: Observed 90% upper limit (pink circle) of the  $\mu^+ \rightarrow e^+\gamma$  in the MEG experiment as a function of the accumulated livetime of the experiment [27]. The black solid line shows the 90% upper limit sensitivity, and  $1\sigma$  and  $2\sigma$  bands are shown in green and yellow, respectively.

## Chapter 2

# MEG II Experiment

In this chapter, the experimental apparatus of the MEG II experiment is explained. The detectors are shown in Fig. 2.1. The main upgrades from the MEG experiment are listed as follows:

- Improvement of the detector resolutions.
- Improvement of the positron detection efficiency.
- Installation of a radiative decay counter (RDC) to tag RMD gamma rays.

The global coordinate is defined as follows. The  $z$ -axis is parallel with the beam axis, the  $y$ -axis is perpendicular to the ground, the  $x$ -axis bisects both  $y$  and  $z$  axes at right angles. The origin of the coordinate is the center of the COBRA magnet.

## 2.1 Beam & Target

### 2.1.1 Beamline

The MEG II experiment is being carried out at the  $\pi E5$  beamline at PSI, where the world's most intense continuous muon beam is available.

The ring cyclotron at PSI can supply a 590 MeV proton beam of 2.2 mA. The current of the proton beam was limited to 1.9 mA in the 2021 run because of the limitation of the beam dump. In the 2022 run, the proton beam current was even lower at 1.76 mA because one of the three cavities for the beam injection was broken. The proton beam is injected into a pion production target (target E) made of 4 cm-thick graphite, and positive pions are produced through a reaction such as  $p + p \rightarrow p + n + \pi^+$ .

The muons from pion decays ( $\pi^+ \rightarrow \mu^+ + \nu_\mu$ ) around the surface of the target within a few  $\mu\text{m}$  is called surface muons. A surface muon has a low energy loss and a trivial depolarization during a short path length in a target and has an upper edge of its momenta of 29.8 MeV. The low momentum of the surface muons (28 MeV) with a good momentum byte of about 7% (FWHM) enables us to stop the muons by a thin target.

A Wien-filter (often called Separator) is installed in the  $\pi E5$  beam line to separate positron contamination in the muon beam, which comes from the Michel decay of the muon and the  $\pi^0$

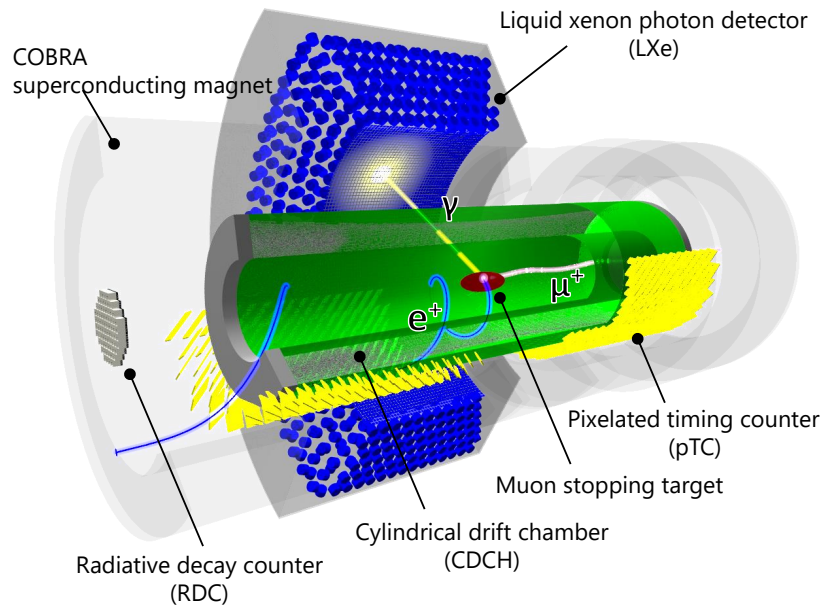


Figure 2.1: Schematic view of the MEG II experiment [29]. A high-intensity  $\mu^+$  beam is stopped at the muon stopping target (red) at the center. The track and time of positrons (blue line) are measured by the cylindrical drift chamber (CDCH) and pixelated timing counter (pTC), respectively. The energy, position, and time of gamma rays are measured by the liquid xenon photon detector. The radiative decay counter (RDC) for tagging background is installed in the downstream.

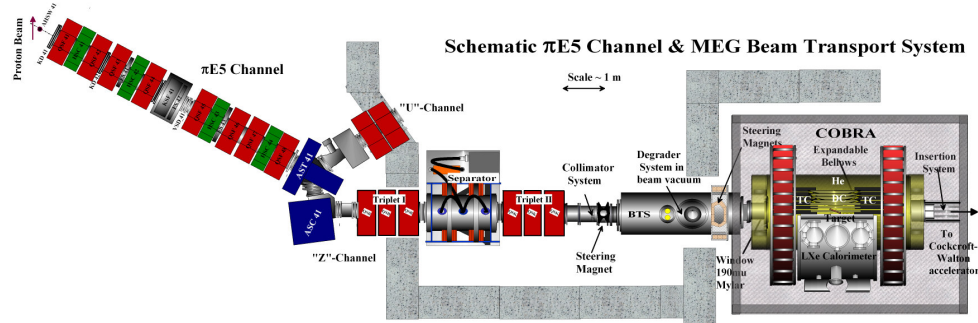


Figure 2.2: Schematic view of the  $\pi E5$  beam line and the MEG (II) experimental area [29]. The production target E and the  $\pi E5$  area are connected by the  $\pi E5$  channel shown on the left. The MEG beam line is composed of a Wien filter, two sets of quadrupole triplet magnets, and a collimator system to eliminate beam contamination. The final momentum adjustment and focusing are performed by the BTS, before the muons are stopped in an ultra-thin target placed at the center of the COBRA positron spectrometer.

decay in the target.

A superconducting Beam Transport Solenoid (BTS) is installed to deliver the muon beam to the MEG II detectors. It applies a magnetic field to focus the beam. A degrader made of 300  $\mu\text{m}$  thick Mylar is placed at the center of the BTS to adjust the muon momentum.

Three systems are used to measure the beam profile and rate. One system is a quasi-non-invasive detector based on scintillation fibers (SciFi) coupled to Silicon Photomultipliers (SiPM), the second system is a non-destructive system based on a thin CsI(Tl) scintillation foil (lumiphore) and a CCD camera, and the third one is a  $9 \times 9$  matrix of small scintillation counters called “MatriX” detector.

The maximum muon beam rate is  $(1.11 \pm 0.01) \times 10^8$  /s when the proton current is 2.2 mA. The stopping rate was adjusted to be  $2\text{--}5 \times 10^7$  /s during the physics data-taking in the 2021 run. The lowest beam rate in the 2021 run was  $1 \times 10^6$  /s, which was used to investigate the muon decay events with a low pileup condition. The beam profiles were  $\sigma_x \sim 12$  mm and  $\sigma_y \sim 12$  mm at the muon stopping target.

The beam rate in the physics run is optimized to achieve the best sensitivity based on the detector performance. The following items must be taken into account.

- Radiation damage of the VUV-MPPC of the LXe detector.
- Performance of positron and gamma-ray measurement.

As later discussed in Chap. 5, the radiation damage of the VUV-MPPC was observed through a series of commissioning runs. Since the detector resolutions for the signal gamma ray deteriorates with a degraded PDE ( $<0.04$ ), the beam rate must be adjusted so that the MPPC PDE stays higher than 0.04. While this constraint was taken into account in the 2021 run, our experiment is not limited by this constraint from the 2022 run because the annealing procedure for all VUV-MPPCs was established at the beginning of 2022, and most MPPCs have a high PDE through the beam time by annual annealing. Another point is the performance of positron and gamma-ray measurements. Though the detectors are designed to measure positrons and gamma rays with good resolutions under a high-intensity muon beam environment, the actual resolutions and efficiencies, particularly for positrons, are worse at higher beam rates. In particular, the analysis efficiency of positrons gets worse at higher beam rates. In this thesis, it is supposed that the physics data will be collected at the beam rate of  $5 \times 10^7$  /s in the future data acquisition. This is because a higher beam rate than  $5 \times 10^7$  /s would not be beneficial in terms of sensitivity. While the rate of accidental backgrounds increases as the beam rate increases, the rate of the effective number of muons for the  $\mu^+ \rightarrow e^+ \gamma$  search does not increase because of the beam rate dependence of the positron analysis efficiency.

### 2.1.2 Muon stopping target

The muon-stopping target is placed at the center of the COBRA magnet. There are two trade-off requirements for the target. One is to maximize the muon-stopping efficiency, and the other

is a small material budget to avoid multiple scattering, annihilation, and bremsstrahlung of the emitted positrons. A  $174\ \mu\text{m}$  thick plastic scintillating film in Fig. 2.3 is used, and it is tilted at an angle of  $15^\circ$  with respect to the beam axis. This configuration realizes a longer effective thickness for the muon beam and a shorter thickness for positrons. In the MEG experiment, a distortion of the target during the data-taking was a dominant systematic uncertainty in the reconstructed positron direction. To suppress the systematic uncertainty, the ellipse plastic film is supported by a rigid carbon-fiber frame of  $200\ \mu\text{m}$  thick and a system to monitor the distortion is implemented. Optical markings are printed on the target and are monitored by CCD cameras [30][31].



Figure 2.3: Muon stopping target for the MEG II experiment [29]. An ellipse plastic film of  $174\ \mu\text{m}$  thick with holes is supported by a rigid carbon-fiber frame of  $200\ \mu\text{m}$  thick.

## 2.2 Positron Spectrometer

The MEG II positron spectrometer is composed of the COBRA magnet, cylindrical drift chamber (CDCH), and pixelated timing counter (pTC).

### 2.2.1 COBRA magnet

The MEG II experiment reuses the COBRA magnet used in MEG. The magnetic field in the COBRA magnet ranges from  $1.27\ \text{T}$  at the center to  $0.49\ \text{T}$  at the edge ( $z \sim 120\ \text{cm}$ ). The concept of the magnetic field is shown in Fig. 2.4. Thanks to the gradient magnetic field along the beam axis shown in Fig. 2.5, the positrons with the same momentum have almost constant bending radii independently of their emission angles. This leads to a high detection efficiency of high-energy positrons, while uninteresting low-energy positrons are quickly swept out of the detector system.

Fig. 2.6 shows the design of the COBRA magnet. A superconducting solenoidal magnet with a step structure of different radii forms the gradient magnetic field [21]. A high-strength superconducting cable of the COBRA magnet consists of a NbTi multi-filament embedded in a copper matrix and aluminum stabilizer. The operating temperature of the coil is about  $5\ \text{K}$ .

At both ends of the COBRA, a pair of two large resistive coils cancel the stray field around the photomultiplier tubes (PMTs) of the LXe detector less than 50 Gauss as shown in Fig. 2.7. The thickness of the magnet is limited to  $0.197 X_0$  within the acceptance of the LXe detector so that the gamma rays from the target can traverse, thanks to the small material budget of the support structure.

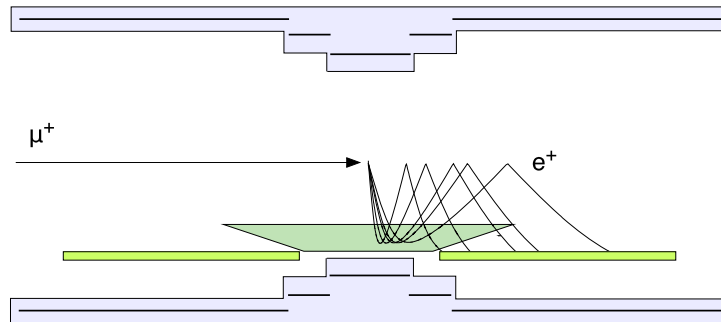


Figure 2.4: Positron trajectory in COBRA B-field [32]. The MEG detectors are drawn.

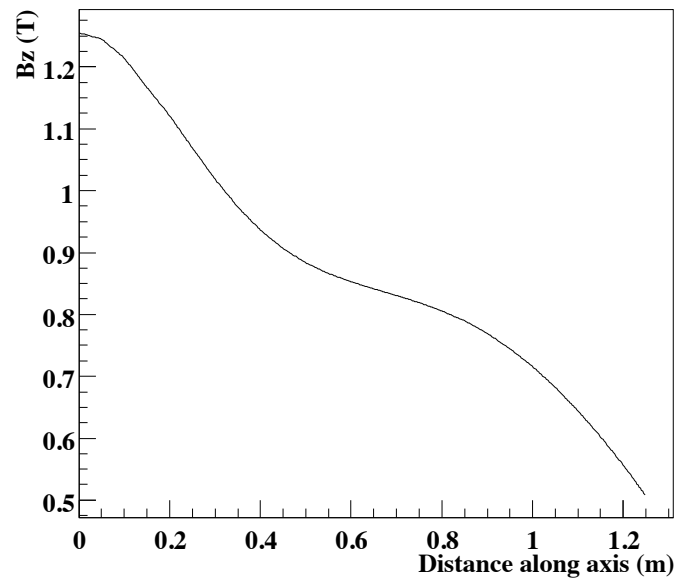


Figure 2.5: Magnetic field of the COBRA along the beam axis [21]. The magnetic field strength is 1.25 T at the center of the magnet ( $z=0$ ) and 0.5 T at the end of the magnet ( $z=1.2$  m).

## 2.2.2 Pixelated Timing Counter (pTC)

The pixelated timing counter (pTC) is designed to measure the time of positrons with a number of pixel counters, each of which consists of a fast scintillator and SiPMs. The pixel counters are arranged so that a single positron track crosses many counters, and a good resolution can be achieved by combining time measurements at each counter. Another important role of the pTC is to generate the trigger signal because the CDCH cannot provide a fast enough signal due to

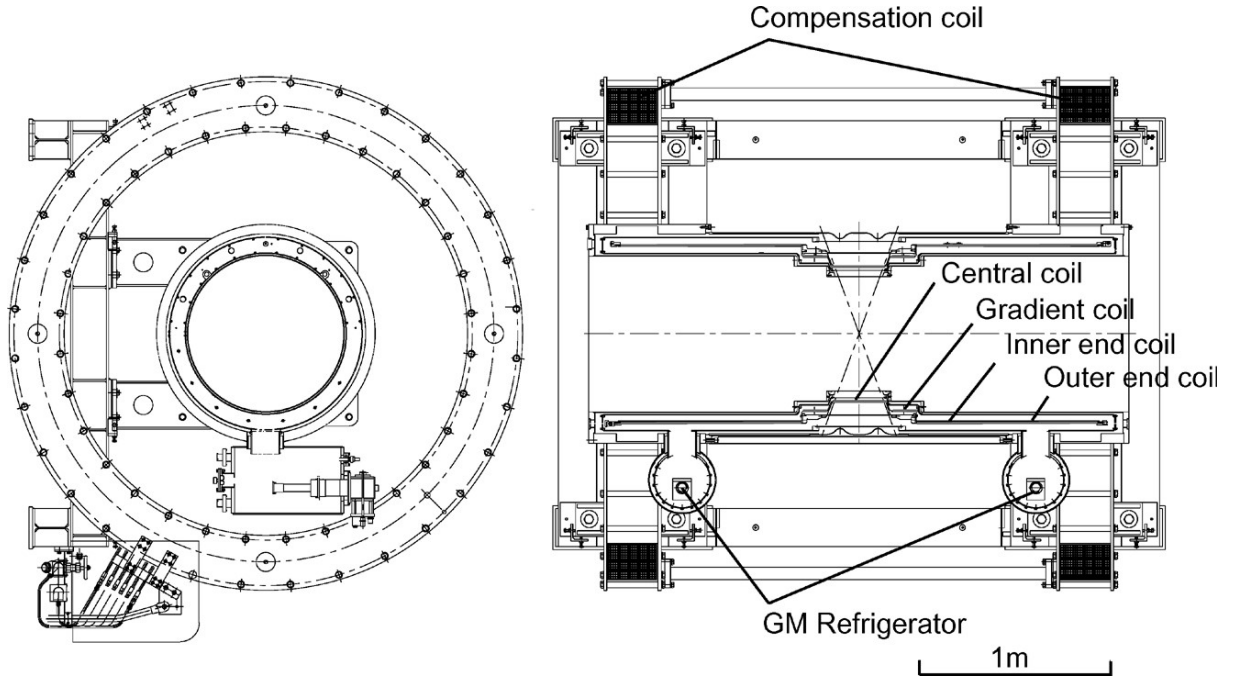


Figure 2.6: The design of the COBRA magnet in side view (left) and top view (right) [21]. The superconducting solenoid magnet has a step structure of different radii. There are two compensation coils at both ends to cancel the residual magnetic field that affects the PMTs of the LXe detector.

the latency introduced by the drift time.

The pTC has two modules consisting of 256 pixel counters, one each for upstream and downstream. The pixel counters are tilted by  $45^\circ$  to the beam axis so that they are nearly perpendicular to the positron tracks, and are cylindrically arranged in 16 lines as shown in Fig. 2.8.

Fig. 2.9 shows a single pixel counter. Each pixel counter is  $120 \times 40/50 \times 5 \text{ mm}^3$  fast plastic scintillator (BC422, Saint-Gobain) coupled to six SiPMs from AdvanSiD (ASD-NUV3S-P High-Gain (MEG)) at both sides. The SiPMs at each side are connected in series to realize a fast response which is essential to achieve a good time resolution.

The overall time resolution is  $\sigma_t^{\text{single}} / \sqrt{N_{\text{hit}}}$ , where  $\sigma_t^{\text{single}}$  is the time resolution of a counter ( $< 100 \text{ ps}$ ).  $N_{\text{hit}}$  is the number of hit counters, which is nine on average for signal positrons. The time resolution of the pTC was measured with Michel positrons in 2017. A resolution of better than 40 ps was achieved for events with more than 6 hits. The overall resolution for signal positrons is estimated to be 40 ps, by weighting the number of  $N_{\text{hit}}$  distribution obtained by MC [33].

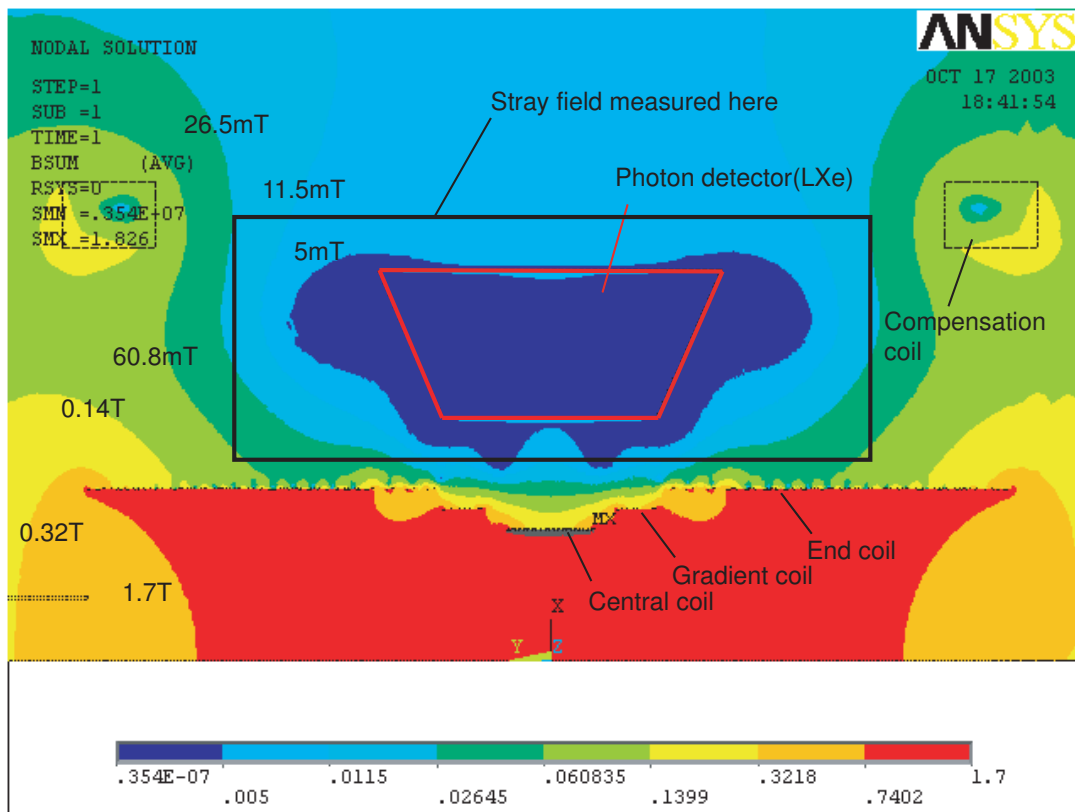


Figure 2.7: Magnetic field in- and outside of the COBRA magnet [21]. The magnetic field at the LXe detector is cancelled by the compensation coils at both ends of the COBRA magnet.

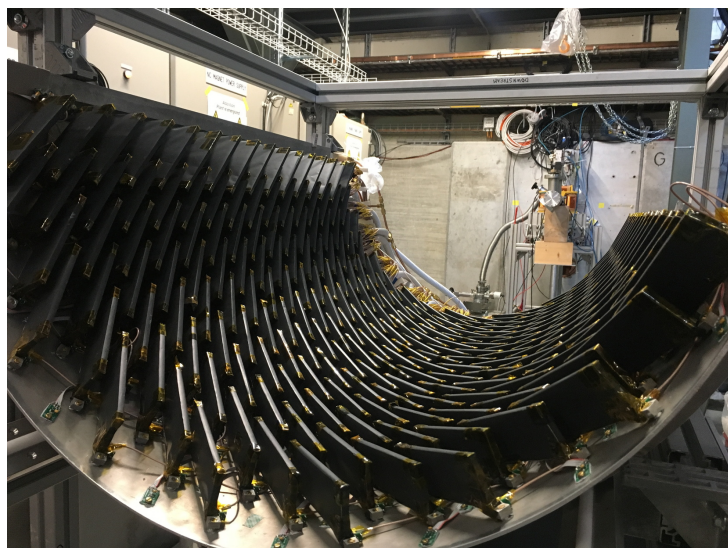


Figure 2.8: Timing counter module assembled with 256 pixel counters. The pixel counters are shielded by black sheets.

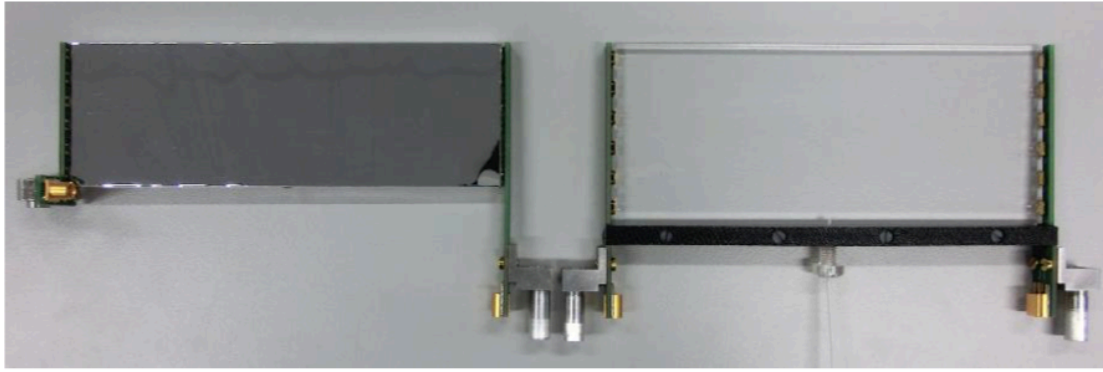


Figure 2.9: A scintillator tile used for pTC. (left) 40 mm height tile with reflector wrapping, (right) 50 mm height tile before wrapping. An optical fiber for the calibration using laser is inserted into the tile [29].

### 2.2.3 Cylindrical Drift Chamber (CDCH)



Figure 2.10: Drift chamber with all wires [29].

The drift chamber of the MEG II experiment is a single volume detector with cylindrical symmetry along the  $\mu^+$  beam axis [34],[35]. It is designed to achieve a good tracking performance by dense stereo wires while positron scattering is suppressed thanks to the low material budget. Fig. 2.10 shows the drift chamber before the installation. The length is 1.91 m, and the radial width ranges from 17 to 29 cm.

Fig. 2.11 shows the drift cell configuration of the CDCH. The readout has nine layers of 192 drift cells, with four times as many hits as MEG per signal-positron track on average. In each drift cell, one sense wire is surrounded by field wires. The size of the drift cell is 5.8–8.7 mm, and it increases linearly in the radial direction and varies in  $z$ . The ratio of the number of field wires to sense wires is five, and there are  $\sim 12,000$  wires in total. Sense (field) wires is gold-plated tungsten (silver-plated aluminum) and their diameter is 20 (40 or 50)  $\mu\text{m}$ . The sense wire is read out from both ends, which makes it possible to reconstruct the hit position along the wire by both charge division and the time difference between the two readouts.

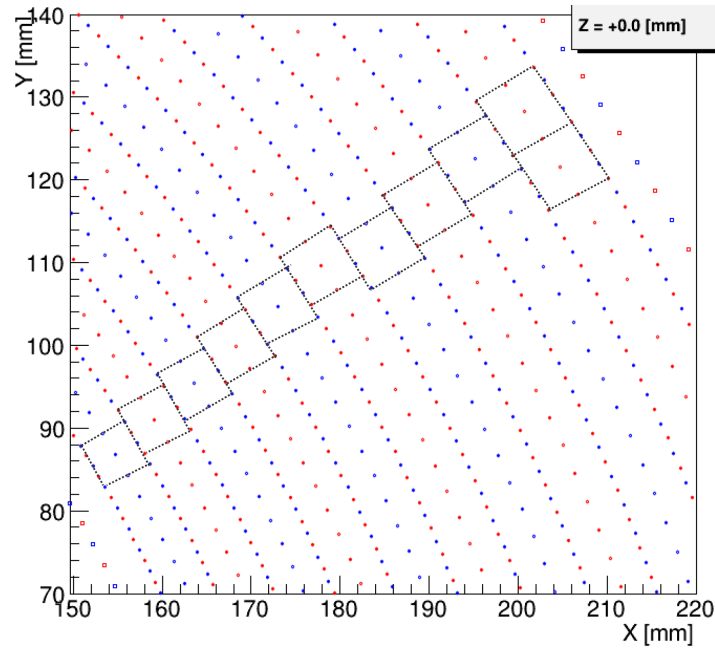


Figure 2.11: Drift cell configuration at the center of the CDCH [29]. Red wires and blue wires are with different stereo angles. The field wires between the layers form a mesh structure.  $40\ \mu\text{m}$  wire is adopted for the field wire. The actual CDCH has nine layers instead of ten.

The sensitive volume is filled with a low-mass gas mixture. The gas mixture in the 2021 run was  $\text{He}/i\text{C}_4\text{H}_{10}/\text{O}_2/2\text{-propanol}$  (88.5%/9.8%/0.5%/1.2%). Isobutane plays an important role in preventing self-sustained discharge. Small amounts of oxygen and 2-propanol were added to improve operational stability. The material budget per positron turn is  $1.5 \times 10^{-3} X_0$ , while it was  $2.0 \times 10^{-3} X_0$  in the MEG drift chamber.

## 2.3 Liquid Xenon gamma-ray detector

### 2.3.1 Overview

The MEG II LXe gamma-ray detector uses 900 ℓ of LXe together with 4,092 VUV-MPPCs and 668 PMTs to achieve good resolutions for the gamma-ray position, energy, and timing with high efficiency.

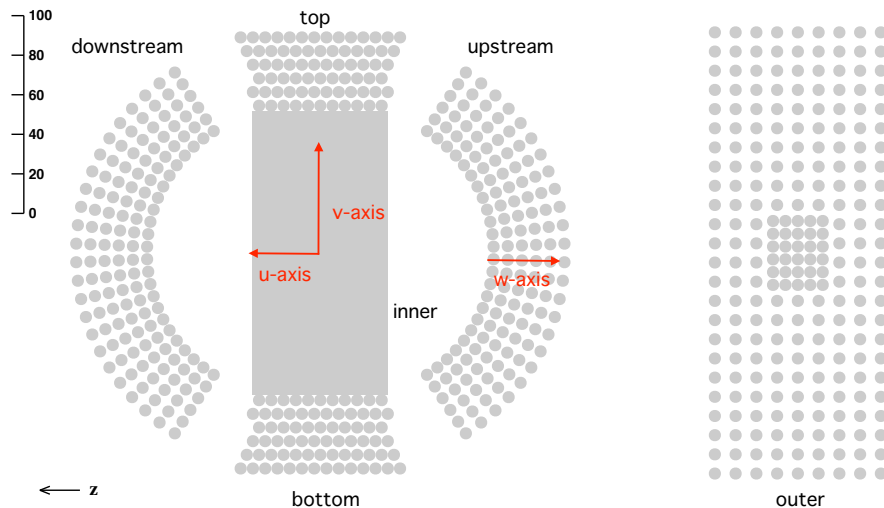


Figure 2.12: Development view of the MEG II LXe detector [3]. The directions of the axes of the local coordinates are shown in red. The inner surface of the detector is covered by six faces called inner, outer, upstream, downstream, bottom, and top faces, respectively.

Fig. 2.12 illustrates the layout of MPPCs and PMTs in the detector. The six faces are called inner, outer, upstream, downstream, bottom, and top faces, respectively. The local coordinate system of the detector ( $u, v, w$ ) is defined as Eq. 2.1–2.3 and illustrated in Fig. 2.12.  $R_{\text{in}}$  is the radial distance from the beam axis to the surface of the photosensors on the inner face, which is 64.84 cm.

$$u = z \quad (2.1)$$

$$v = \arctan(-y/x) \times R_{\text{in}} \quad (2.2)$$

$$w = \sqrt{x^2 + y^2} - R_{\text{in}} \quad (2.3)$$

The acceptance of the detector is defined as

$$|u| < 23.9 \text{ cm} \quad (2.4)$$

$$|v| < 67.9 \text{ cm} \quad (2.5)$$

$$0 \text{ cm} < w < 38.5 \text{ cm} \quad (2.6)$$

The fiducial volume is 800 ℓ, subtending 11% of the solid angle viewed from the center of the stopping target.

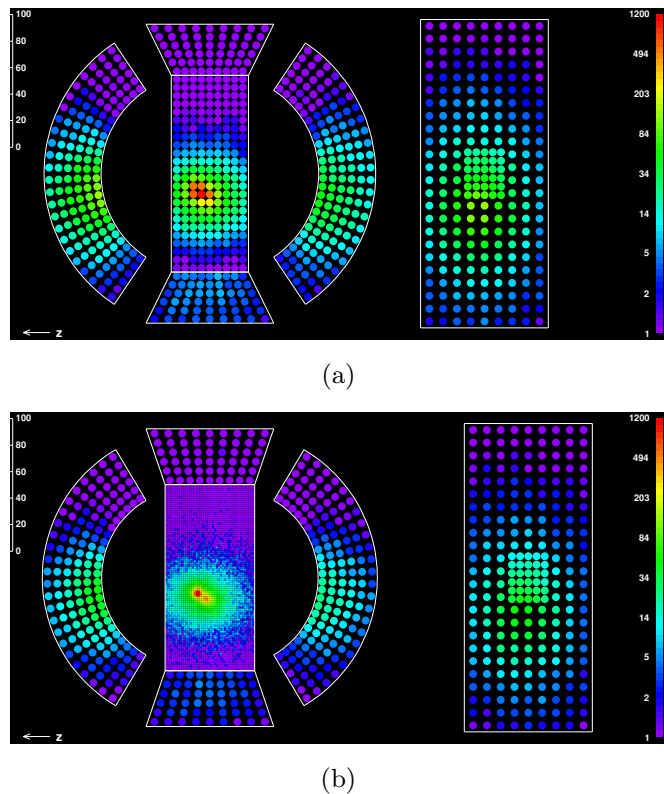


Figure 2.13: Light distribution for the same gamma-ray event in development view in (a) MEG and (b) MEG II in MC simulation [29].

Compared to the MEG LXe detector that used 216 PMTs for the scintillation readout of the inner face, the MEG II LXe detector has a granular and uniform scintillation readout of the inner face by 4,092 VUV-MPPCs. Fig. 2.13 shows the light distribution of the MEG (II) LXe detector for the same gamma ray in MC simulation. It indicates that the imaging power of the scintillation is greatly improved with smaller photosensors. This upgrade improved the position and energy resolutions for gamma-ray hits close to the inner face, as later presented in Chap. 6 and Chap. 7.

### 2.3.2 Liquid xenon

Table 2.1 summarizes the properties of LXe. LXe has several advantages in detecting the 52.8 MeV signal gamma rays. Thanks to the high density, short radiation length, and small Moliere radius, gamma rays are stopped efficiently and the electromagnetic shower is largely contained in a reasonable size of the LXe volume.

When ionizing radiation is injected into xenon, excited atoms ( $\text{Xe}^*$ ) or ions ( $\text{Xe}^+$ ) are generated. Correspondingly, there are two types of scintillation processes with different W-values and time constants. In the fast scintillation process with time constants of 4.2 ns and 22 ns, excited

Table 2.1: Properties of liquid xenon

Atomic number	54
Atomic weight	131.293 [36]
Density [g/cm <sup>3</sup> ]	2.95 [37]
Radiation length[cm]	2.77 [36]
Critical energy [MeV]	14.5 [38]
Morielle radius [cm]	4.2 [38]
W-value for electron [eV]	21.6 [39]
W-value for $\alpha$ -particle [eV]	19.6 [39]
Scintillation Wavelength (mean) [nm]	174.8 $\pm$ 0.1(stat.) $\pm$ 0.1(syst.) [40]
Scintillation Wavelength (FWHM) [nm]	10.2 $\pm$ 0.2(stat.) $\pm$ 0.2(syst.) [40]
Rayleigh scattering length [cm]	45 [41]
Refractive indices	1.69 [42]

atoms form excited xenon molecules immediately, and scintillation photons are emitted.



The scintillation from the recombination process with the electron and ions has a longer time constant of 45 ns [43].



In both processes, a scintillation photon is emitted from the excited state of the Xe molecule via  $\text{Xe}_2^* \rightarrow 2\text{Xe} + h\nu$ . Fig. 2.14 shows scintillation signals by different ionization particles [43]. While scintillation processes with a short time constant dominate for alpha particles, rather slower processes with 45 ns time constants dominate for electrons. One can perform particle discrimination by scintillation signal waveform. As shown in Fig. 2.15a, pair creation is the dominant process around the energy of the signal gamma ray.

The number of scintillation photons is sufficient to achieve a good energy resolution thanks to the small W-value of 21.6 eV and the absence of self-absorption. A good time resolution is achievable thanks to the fast response.

On the other hand, it also has a few difficulties as follows.

- Xenon must be stably cooled down to a low-temperature (165 K) to stay liquid.
- The light yield of LXe is sensitive to impurities.
- The Rayleigh scattering length of LXe is short and inconsistent with the theoretical value.

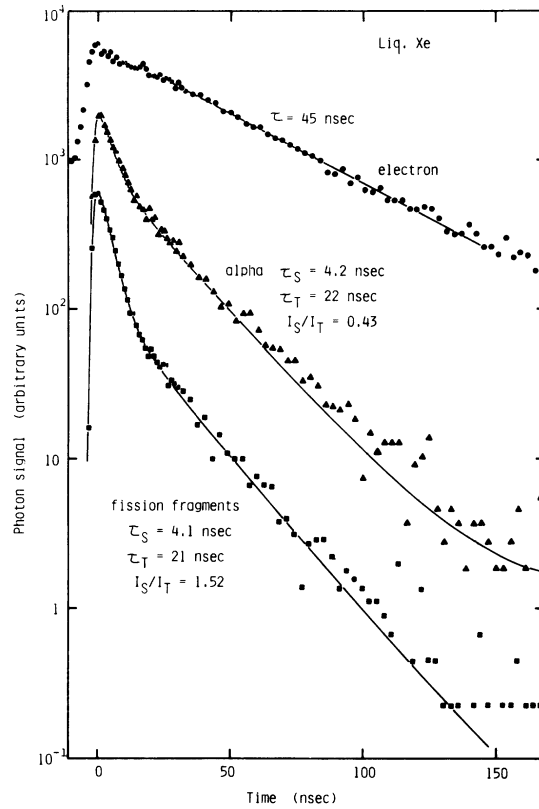
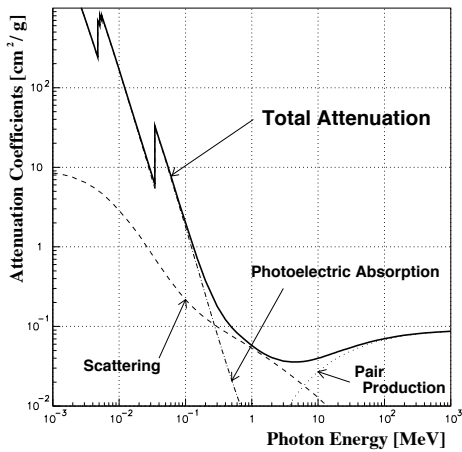
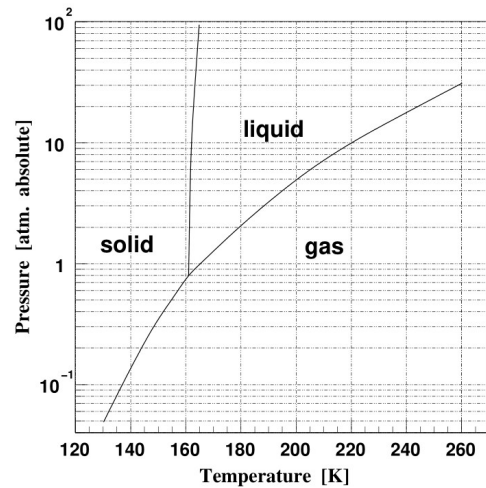


Figure 2.14: LXe scintillation signals by electrons (circle), alpha rays (triangle), fission fragments (square) [43]. The solid lines show the double exponential curves fitted to signals.



(a)



(b)

Figure 2.15: (a) Photon cross section of xenon as a function of photon energy [44]. The cross-section of the pair production (dotted line) is dominant over the photoelectric absorption (dashed-dotted line) and Compton scattering (dashed line) at the energy of the signal gamma ray (52.8 MeV). (b) Phase diagram of xenon [45]. At the nominal detector pressure (1.2 atm), xenon is liquid at 161–169 K.

- The scintillation light is in the VUV range.

Fig. 2.15b shows the three-phase diagram of xenon. Since the detector is operated at 1.2 atm, the temperature of xenon must be controlled between 161 K and 169 K. Contaminations such as oxygen, nitrogen, and water decrease the light yield of scintillation light. Therefore, a xenon control system that keeps xenon at a low temperature and keeps purifying xenon is necessary. Furthermore, light yield monitoring is required for stable gamma-ray measurement.

It is known that there is a difference between experimental and theoretical Rayleigh scattering lengths [42]. This discrepancy is one reason why it is difficult to reproduce the actual scintillation light propagation by MC simulations accurately.

The wavelength of the scintillation light is in the vacuum ultraviolet (VUV) region, which is outside the sensitive region of common photosensors. The MEG II LXe detector has two types of VUV-sensitive photosensors, PMT and MPPC, and both of them were developed for the MEG/MEG II experiments.

### 2.3.3 PMT

The PMT for the LXe detector has to detect the VUV light in a demanding environment, at a low temperature (165 K), under 50 Gauss magnetic field. Furthermore, a low current operation is required to suppress the heat inflow. A new VUV-sensitive PMT was developed in collaboration with Hamamatsu Photonics K.K. Bialkali (K-Cs-Sb) is used as a VUV-sensitive photo-cathode. The basic properties of the PMT are shown in Table 2.2. The PMT window is made of synthetic quartz glass and is transparent to light with wavelengths from 160 nm to several thousand nm, with a transmittance of about 80% at 178 nm. The bleeder circuit of the PMT is shown in Fig. 2.17. The last two stages of the 12-stage dynode are equipped with Zener diodes to ensure stable operation even under a high-intensity environment.

A few instabilities are known for our PMTs. One is the degradation of the gain. Under a high-intensity environment, the gain of a PMT decreases by the large photoelectric current induced by scintillation photons. The decrease is about 2% in one month of the muon beam run. The gain is adjusted to  $8 \times 10^5$  by changing the bias voltage. The measured radiation damage and gain adjustment are later described in Sec. 4.4.

Another instability is called “gain shift”. The gain of the PMT decreases or increases by 10% at maximum when the beam is turned on or off. The time variation of the gain due to the gain shift can be expressed with a few time constants. While the dominant fast time constant is  $\mathcal{O}(10)$  s, the slow time constant is  $\mathcal{O}(100 - 1000)$  s. In the 2021 run, since the data collection started a few minutes after the beam blocker operation, the impact of the gain shift was moderate, and it was not corrected, as discussed in Sec. 4.4.

Furthermore, the variation of the quantum efficiency (QE) is  $\mathcal{O}(1)\%$ . Because of these instabilities and variations of the sensor performance, the monitoring and correction of gain and QE are important to reconstruct the number of collected photons at each PMT accurately.



Figure 2.16: VUV-sensitive PMT for MEG (II) (R9869).

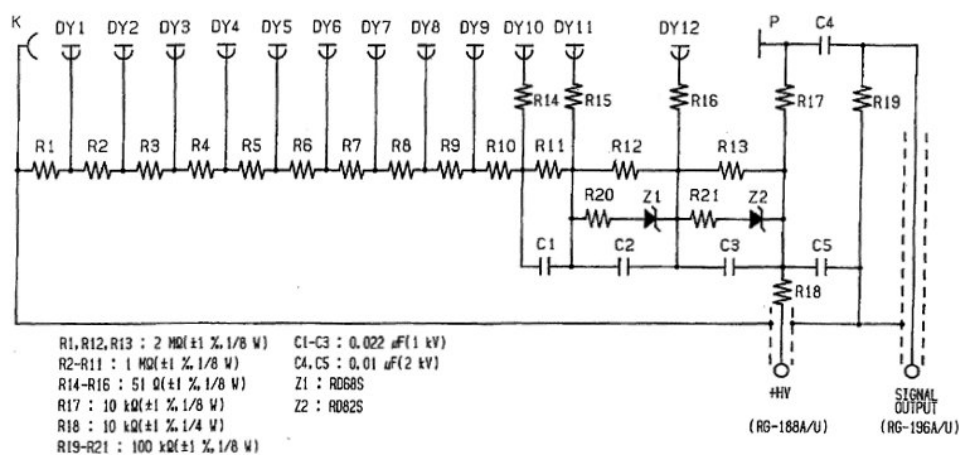


Figure 2.17: Bleeder circuit of the PMT for the MEG (II) LXe detector [46]. The circuit has a 12-stage dynode. Two Zener diodes are installed in the last two dynode stages to ensure stable operation under a high-intensity environment.

Table 2.2: PMT of the MEG (II) LXe detector

Specification	PMT
Number	R9869
Total size	57 mm $\phi$
Size of sensitive region	45 mm $\phi$
Length	32 mm
Material of cathode	K-Cs-Sb
Type of dynode	metal-channel
Number of dynodes	12
Typical operation voltage	900 V
Typical Gain	$8.0 \times 10^5$
Typical QE	0.16

### 2.3.4 VUV-MPPC

MPPC (Multi-Pixel Photon Counter) is a kind of semiconductor photo-sensor SiPM produced by Hamamatsu Photonics K.K. In general, an MPPC has several prominent advantages to a PMT, such as small size, low operation voltage, and insensitivity to the magnetic field. Since the commercially available MPPCs were not sensitive to vacuum ultraviolet (VUV) light, an MPPC sensitive to VUV light was developed for the MEG II experiment together with Hamamatsu Photonics K.K [47].

The detection mechanism of VUV light and the installation into the detector will be presented in Sec. 2.3.4.1. The drawbacks and their impacts on the detector performance will be discussed in Sec. 2.3.4.2–5.

#### 2.3.4.1 VUV-sensitive MPPC

Fig. 2.18a illustrates the detection mechanism of a typical MPPC pixel. As an ordinary semiconductor photosensor, it extracts signals from electron-hole pairs generated by photons incident on the depletion layer. The MPPC is characterized by the operation with a reverse bias voltage higher than the breakdown voltage, which is called Geiger mode. In the Geiger mode, the generated electron-hole pairs are accelerated by the electric field and collide with the silicon crystal lattice, generating electron-hole pairs one after another. It is called avalanche amplification.

The avalanche amplification is quenched once sufficient gain and adequate output signal amplitude have been attained so that the pixel is ready to detect a subsequent photoelectron signal. Each pixel is quenched by a quenching resistor connected in series, as shown in Fig. 2.18b. The magnitude of the amplified signal is determined by the quenching resistance, capacitance, and bias voltage. The electric field strength in the amplification region is proportional to the difference between the bias voltage and the breakdown voltage, which is called over-voltage. The number of incident photons on an MPPC is measured by arranging a large number of pixels and counting the number of fired pixels using the charge or the amplitude of the output signal waveform.

The standard MPPCs are not sensitive to vacuum ultraviolet (VUV) light because the VUV light is absorbed by the protective layer and does not produce electron-hole pairs in the Silicon layer.

A VUV-sensitive MPPC (VUV-MPPC) was developed (S10943-4372, also called VUV3) for the MEG II LXe detector. The VUV-MPPC is protected with a transparent quartz window instead of the protective layer. Fig. 2.19 shows the detection mechanism of VUV light by the VUV-MPPC. VUV light creates electron-hole pairs in the vicinity of the interface between Si and the passivation layer, and then the electrons are drifted and induce avalanche amplification. The VUV-MPPC is also sensitive to visible light. Visible light reaches a deeper region of the Si layer than VUV light does. The PDE for the LXe scintillation photon was measured to be

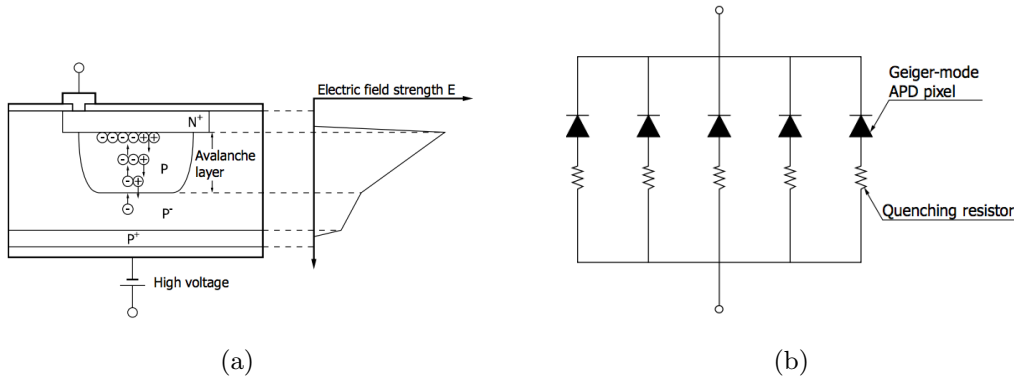


Figure 2.18: (a) Detection mechanism of a typical MPPC [48]. An electron produced in the  $P^-$  layer is drifted to the P layer and induces avalanche amplification because of the strong electric field. (b) Simplified circuit of an MPPC. MPPC pixels are connected with quench resistors in series [48].

0.18–0.20 at the overvoltage of 7 V [47].

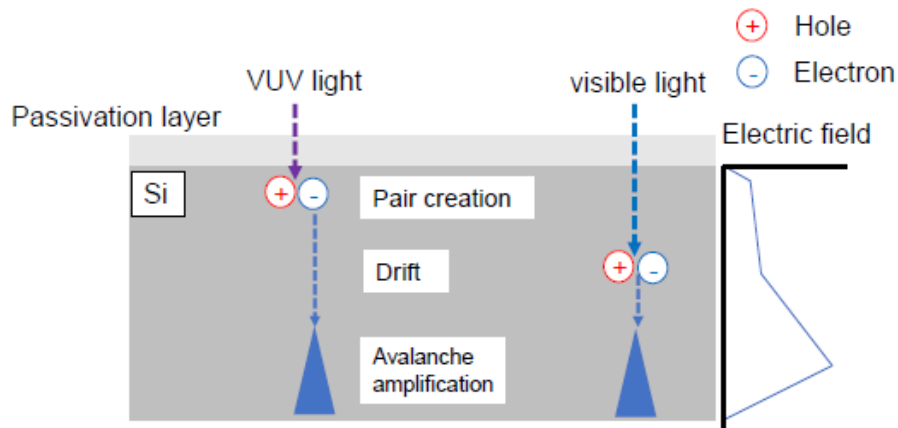


Figure 2.19: Detection mechanism of VUV light by the VUV-MPPC. The VUV light creates e-h pairs in the vicinity of the interface between the passivation layer and the Silicon layer. The electrons are drifted to the amplification region, and the signal is amplified by the avalanche amplification.

The area of a typical MPPC is at most 6 mm square. With this small size of an MPPC, more than 10,000 channels and readout electronics are necessary to cover the entire inner face of the LXe detector. This is not realistic, considering the cost and the heat inflow through the sensor cables. This problem was solved by connecting four MPPC chips together in what is called a “hybrid connection” to form a large  $12 \times 12 \text{ mm}^2$  MPPC. Fig. 2.20 shows the circuit of the connection. The hybrid connection is designed so that the same bias voltage is distributed to each chip, while the signal is read out in a series connection to keep the signal time constant short, as shown in Fig. 2.21. Fig. 2.22a and 2.22b show a picture of a single MPPC and its



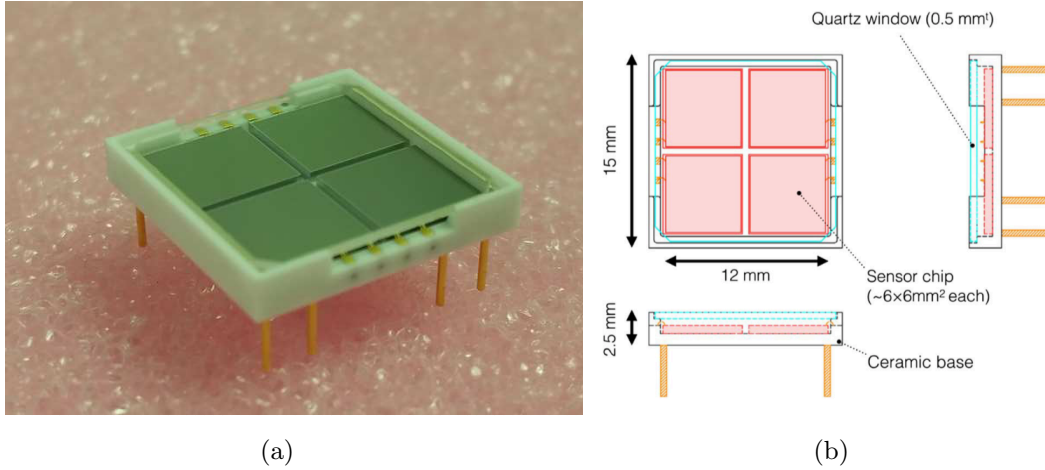


Figure 2.22: (a) Picture and (b) sketch of the VUV-MPPC developed for the MEG II [47]

Table 2.3: Specification of MPPC of MEG II LXe detector

Specification	MPPC
Number	S10943-4372, VUV3
Total Size	$15 \times 15 \text{ mm}^2$
Size of sensitive region	$12 \times 12 \text{ mm}^2$
Pixel pitch	$50 \mu\text{m}$
The number of pixels	57600
Typical breakdown voltage at room temperature	54 V
Temperature coefficient of breakdown voltage	56 mV/K [29]
Typical Gain at overvoltage 7 V	$1.5 \times 10^6$
PDE at overvoltage 7 V	0.18–0.20 [47]
Excess charge factor at overvoltage 7 V	1.3–2.5

of malfunctioning MPPC chips that have anomalous IV curves was 0.2%, and they were not installed in the LXe detector.

Fig. 2.23a shows how the MPPCs are fixed to the detector. Each MPPC is connected to a printed circuit board (PCB), and the PCBs are supported by carbon-fiber-reinforced polymers (CFRP). The gaps between PCB and MPPC, PCB, and CFRP are filled with spacers to prevent LXe from entering the gaps. Fig. 2.23b shows the material that makes up the entrance face of the detector. In reality, there is a  $\sim 1 \text{ mm}$  gap between the CFRP and cryostat because of the difference between the curvature of the CFRP and that of the inner surface of the cryostat and it is filled with LXe. The thickness of the LXe volume and its impact on the detection efficiency will be discussed in Sec. 4.7. Each PCB carries 22 MPPCs, and a row consists of two PCBs. One CFRP carries 23 or 24 PCB rows, and it is fixed to the cryostat with screws at its four corners. Four CFRPs are used to mount the entire MPPC array that has 93 rows lined up, with 4,092 MPPCs mounted overall. While there was no gap between the CFRPs in the  $\phi$  direction,

their  $z$  position can be different by  $\mathcal{O}(1)$  mm.

Fig. 2.24 shows the installation location of the MPPCs in different production lot. Most PCB carries the MPPCs from the same lot, and the PCBs are arranged so that PCBs from the same production lot are not next to each other as much as possible in order to obtain a uniform response as a whole as much as possible.

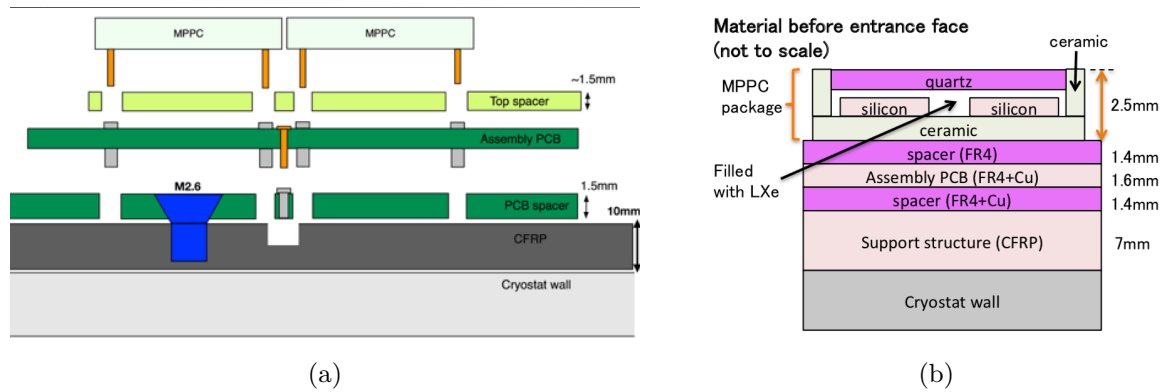


Figure 2.23: (a) Schematic view of the support structure of the MPPCs. The gap between the MPPCs and the PCB is filled with top spacers. The gap between the PCB and the CFRP is filled with PCB spacers. The PCB spacers are fixed to the CFRP by screws. (b) Material of the entrance face before the LXe volume [2].

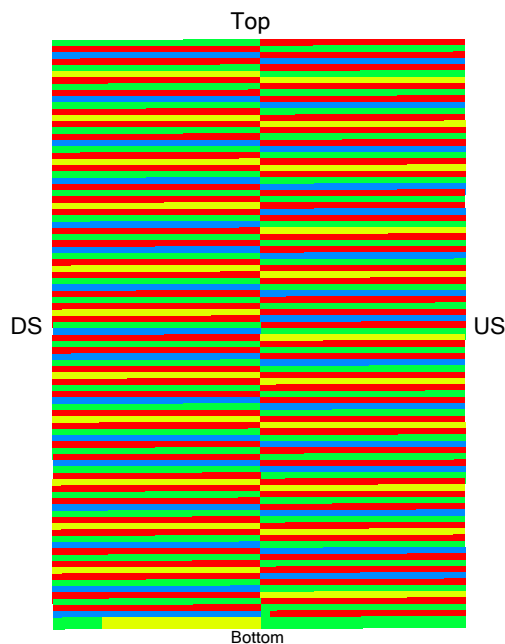


Figure 2.24: Distribution of the production lot of MPPCs. MPPCs of lot A are shown in blue, Lot B in green, Lot C in yellow, and Lot D in red.

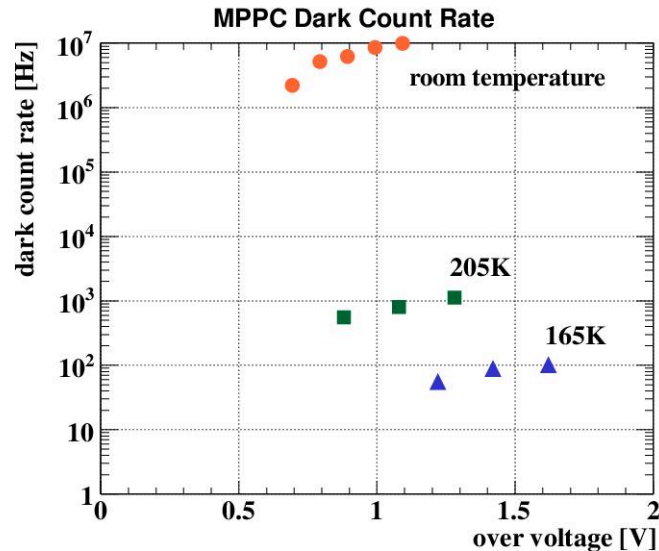


Figure 2.25: Dark count rate measured at room temperature (orange), 205 K (green), and 165 K (blue) [29] as a function of the over voltage.

#### 2.3.4.2 Dark current

The MPPC is known to have fake signals without external photons due to thermal excitation, called dark current. The dark current of the MPPC has a strong temperature dependence. The dark count rate at 165 K is lower by a factor of  $10^5$  than that at room temperature as shown in Fig. 2.25. Therefore, dark current is not a problem as long as the MPPC is used in LXe at 165 K.

#### 2.3.4.3 Correlated noise

A single photon may fire multiple pixels, and it is called correlated noise. Cross-talk and after-pulsing are known as main correlated noises. Cross-talk is a signal occurring at the same time as the primary signal because an infrared photon produced in the avalanche amplification by the primary photon generates electron-hole pairs in a neighboring pixel. After-pulsing occurs at a later time than the primary signal. An avalanching carrier trapped by an impurity energy level is released after a short delay and generates another avalanche. The magnitude of the correlated noises of an MPPC was evaluated using excess charge factor (ECF), which stands for the fake amplification of the signal by the correlated noises. The ECF of the VUV-MPPCs for the LXe detector was measured to be large up to 2.5 at the over-voltage of 7 V based on calibration measurements with  $\mathcal{O}(1)\%$  precision as described in Sec. 4.3.

A large excess noise factor due to the correlated noises does not deteriorate the energy resolution significantly since it is not limited by the photoelectron statistics, as discussed in Sec. 7.3.

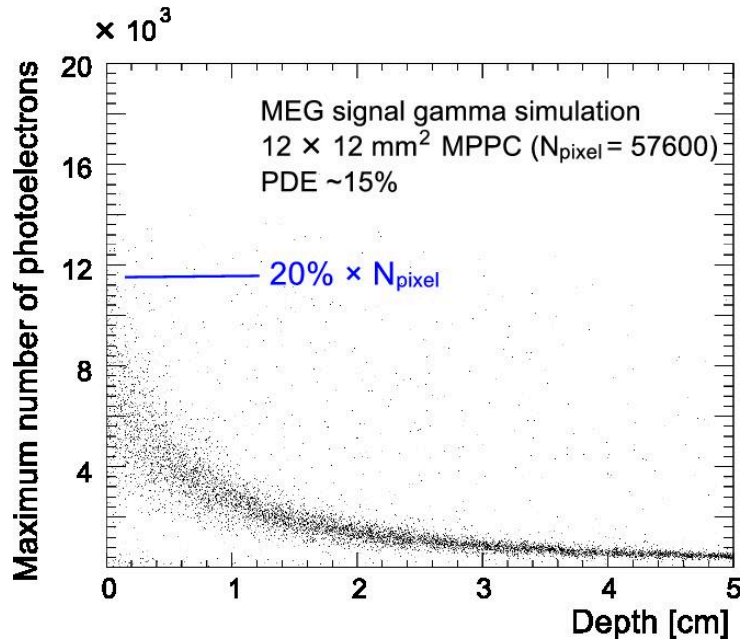


Figure 2.26: The maximum number of photoelectrons collected by MPPCs in a detector simulation for the signal gamma-ray [29]. Only 20% of the pixels are fired for a gamma-ray hit in the shallow region.

#### 2.3.4.4 Non-linearity and saturation

The MPPC is known to exhibit a nonlinear response when a number of photons comparable to the number of pixels enter the detector. Fig. 2.26 shows the depth dependence of the number of photoelectrons when a signal gamma-ray is injected into the detector in the simulation, and the number of photoelectrons at the shallowest part is only about 20 % of the number of pixels. Therefore, the nonlinearity of the MPPC response is not likely a severe issue in our case.

#### 2.3.4.5 Temperature dependence of breakdown voltage

The temperature coefficient of the breakdown voltage of the MPPC is 56 mV/K. The higher the temperature is, the higher the breakdown voltage is. Since the characteristics of the MPPC heavily depend on the overvoltage, the instability of the temperature leads to the instability of the performance. The LXe control system is designed to keep the temperature of LXe stable at  $\sim 169 \text{ K}$  with a precision of 0.1 K, as later described in Sec. 2.3.7.

In the middle of the 2021 run, there was nevertheless an instability in the temperature of the detector hut where the detectors and electronics are located. Fig. 2.27 shows the time variation of the temperature of the LXe detector and the detector hut. The hut temperature became unstable around the 5th of November because one pump responsible for the air-conditioning of the hut became inoperative due to technical issues. Since the increase in the heat inflow from the detector hut was too fast to keep the LXe temperature stable, the temperature of the LXe detector was also affected. The temperature rise of the LXe by  $1^\circ \text{C}$  increased the breakdown

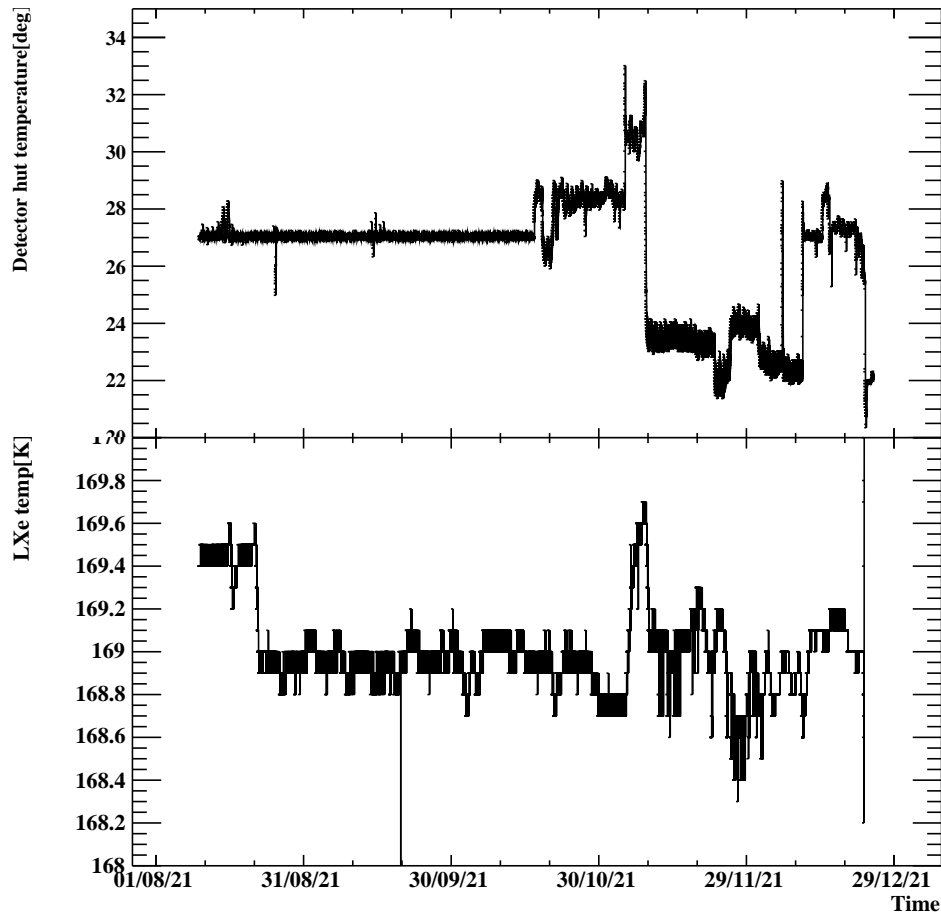


Figure 2.27: Temperature of the detector hut in celsius (top) and the detector in kelvin (bottom) as a function of time in the 2021 run. While the temperature of the detector hut had been under control until the 4th of November, it became unstable due to an operational issue.

voltage of MPPCs by 0.8% at overvoltage 7 V.

However, the instability of the MPPC response due to the temperature instability was monitored and corrected so that it did not cause a problem, as later discussed in Sec. 4.3.

### 2.3.5 Signal transmission and readout electronics

The sketch of the signal transmission of the detector is shown in Fig. 2.28. The signals from MPPCs are transmitted through the coaxial structure in the PCBs as shown in Fig. 2.29. The signals from the PCBs are transmitted by coaxial cables from the cable connectors on the edge to the feedthrough of the cryostat. On both sides of custom-made feed-throughs shown in Fig. 2.30, coaxial cables are directly soldered. The detector has 12 flanges as the feedthrough on the chimney of the detector, and each flange accommodates 432 readout channels.

A patch panel is mounted on the detector for selecting channels to read. After the patch panel, sixteen cables are bundled and connected to a DAQ module (WaveDREAM board, later described in Sec. 2.7). Fig. 2.31 shows the grouping scheme of the MPPCs to the modules.

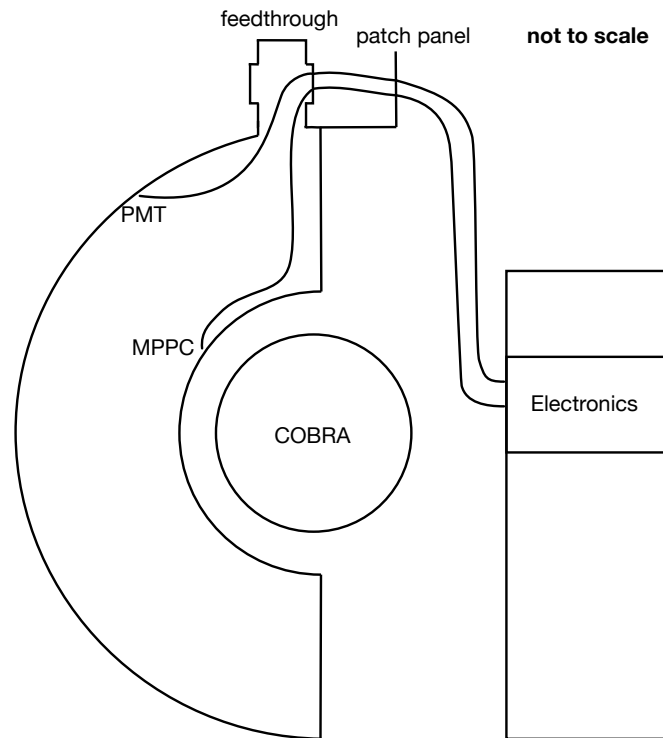


Figure 2.28: Concept of the signal transmission [2]. The signal cables of the photosensors are connected to the feedthrough at the top of the detector. The cables from the feedthrough are connected to the patch panel where they are connected to the cables to the readout electronics.

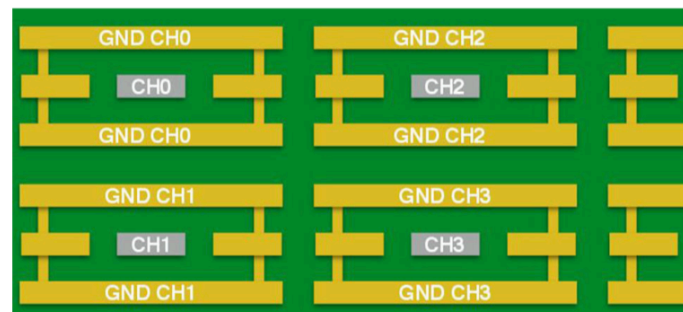


Figure 2.29: Cross sectional view of a PCB [29]. The signal lines from the MPPCs (grey) are transmitted in the ground lines (yellow).

A square group of  $4 \times 4$  MPPCs is read out by a module, and this unit is used for the online position reconstruction of gamma rays. For this purpose, channels read out by the same module are designed to have the same cable length.



### 2.3.6 Calibration sources

#### LED

Fig. 2.32 shows the positions of the LEDs installed in the detector. In addition to 36 LEDs used in the MEG experiment (Toyoda Gosei E1L493B1A02 [49]), 48 LEDs (Kingbright KA-3021QBS-D [50]) are installed on the outer face and lateral (upstream and downstream) faces for the calibration of the MPPC. These LEDs are dimmed by Teflon as shown in Fig. 2.33 for stable operation.

As described later in Sec. 4.3, a short pulse LED is desirable to measure the magnitude of after-pulsing for each MPPC. A function generator Agilent 81150A [51] is used to flash the LEDs. It can provide a short (10 ns width) pulse with an amplitude of 5 V, and it is sufficient to drive two LEDs simultaneously. A system to select a set of two LEDs, one in upstream and another in downstream, to send a pulse was developed to calibrate all MPPCs with the new LEDs. Fig. 2.34 shows the circuit to operate the 12 new LEDs on the outer face. A combination of 12 high-speed relays (G6K-2F-RF-S DC24, Omron [52]) and SCS3000 (Slow Control System module developed at PSI [53]) is used to distribute the driver signal to an arbitrary set of one upstream LED and one downstream LED. The high-speed relays are mounted on a board and connected to the LEDs. A synchronous signal is sent from the function generator to the trigger system to trigger the LED events. The operation condition of the function generator for the calibration in the 2021 run is summarized in Table 2.4.

Table 2.4: Configuration of the driver signal for LED calibration.

Offset [V]	1.67–1.69
Amplitude [V]	1.3
Frequency [Hz]	100
Pulse width [ns]	10

#### Am source

The detector is equipped with twenty-five spots of  $^{241}\text{Am}$   $\alpha$  sources for the PDE calibration of photosensors. Each spot source emits alpha rays at 5.485 MeV (84.5%) and 5.443 MeV (13.0%) at an activity of  $\sim 200$  Bq, which is low enough not to interfere with other measurements. Each source is surrounded by a thin gold foil and wound around a thin gold-plated tungsten wire with a diameter of  $100\ \mu\text{m}$  [54], as shown in Fig. 2.35.

Fig. 2.36 shows the position of the sources inside the detector. Five sources are mounted to each wire with the same spacing of 12 cm. The wires are stretched parallel between the upstream and downstream faces. Since an  $^{241}\text{Am}$  source produces scintillation light of fixed energy from a fixed position, it is very useful to measure the PDE of photosensors and optical properties of LXe, such as absorption length and light yield.

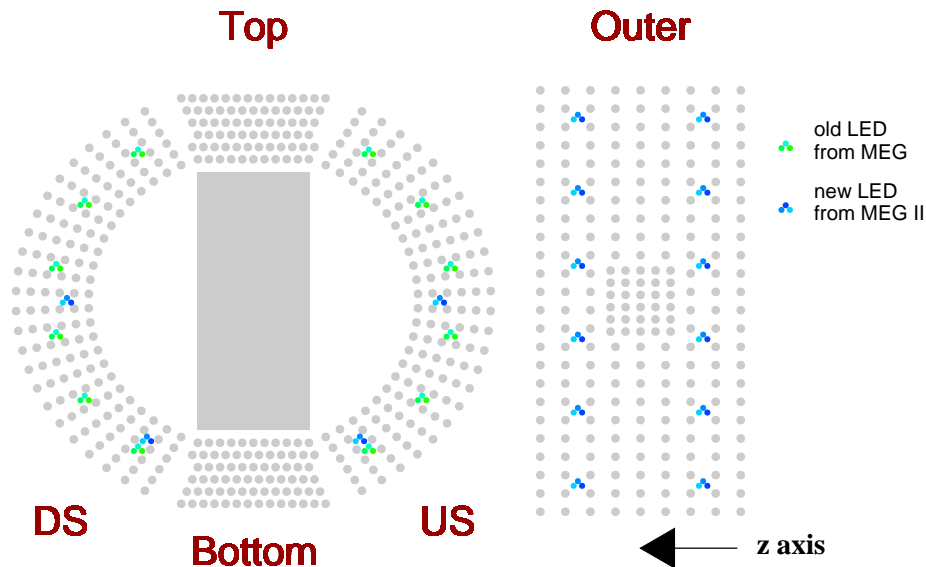


Figure 2.32: Location of the LEDs in the LXe detector. Green and blue points show the LEDs reused from MEG and ones installed for the MPPC calibration in the MEG II, respectively.



Figure 2.33: A unit of the LED system for MPPC calibration. Three LEDs are mounted to each PCB and dimmed by Teflon.

### 2.3.7 Xenon control system

The purposes for the xenon control system in the LXe detector are listed below.

- Keep the temperature of the detector at 165 K.
- Keep purifying xenon to have a good light yield and to suppress the absorption in LXe.
- Store xenon when it is not used for the experiment.

Fig. 2.37 shows the xenon control panel of the gaseous and liquid purification system. The whole system consists of the detector cryostat, refrigerators, storage tanks, and purifiers. The control system was developed for MEG [55], and the cooling capability was upgraded to compensate

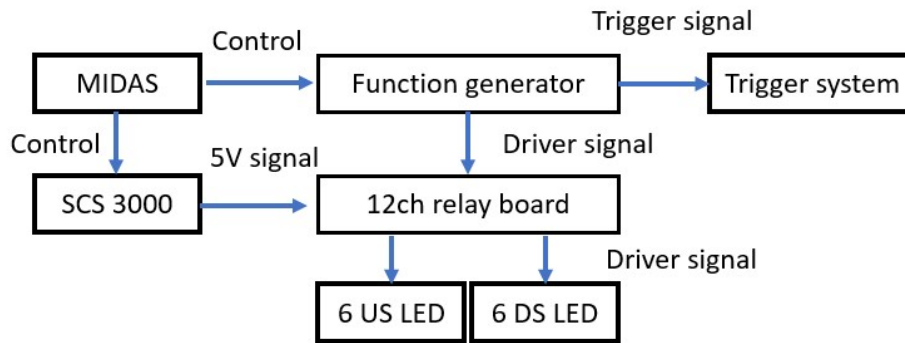


Figure 2.34: Diagram of the circuit to distribute the driver signal from the function generator to the LEDs for the MPPC calibration. The driver signal is transmitted to the 12-channel relay board, and then it is distributed to a pair of LEDs: one on the upstream side and the other on the downstream side of the detector. The function generator and the fast relays on the relay board are controlled by the MIDAS system and an SCS3000 module, respectively. The amplitude of the driver signal and the LEDs to flash can be changed through the control system.



Figure 2.35:  $^{241}\text{Am}$  source mounted on a gold-plated tungsten wire. The black crosses show the points where the wires are fixed to the upstream and downstream faces.

for the heat inflow from the increased number of cables. A 200 W pulse-tube refrigerator placed at the top of the detector is reused from MEG, and a new 400 W Gifford-McMahon (GM) refrigerator is introduced.

A 1000  $\ell$  Dewar with a pulse-tube refrigerator is used to safely store LXe when the detector is not operated. Since it is thermally insulated and is tolerable up to 6 bar, it can store the LXe for 100 hours even without cooling power.

The xenon control system is equipped with two purification systems in the gaseous phase and in the liquid phase. The gaseous phase purification is performed by a metal-heated getter. The circulation of gaseous xenon (gXe) for the gaseous phase purification is continued when the detector is operating. This is also useful to efficiently transfer the cooling power from the GM refrigerator to the detector. The liquid phase purification is performed by molecular sieves in the liquid purifier module at the back of the detector.

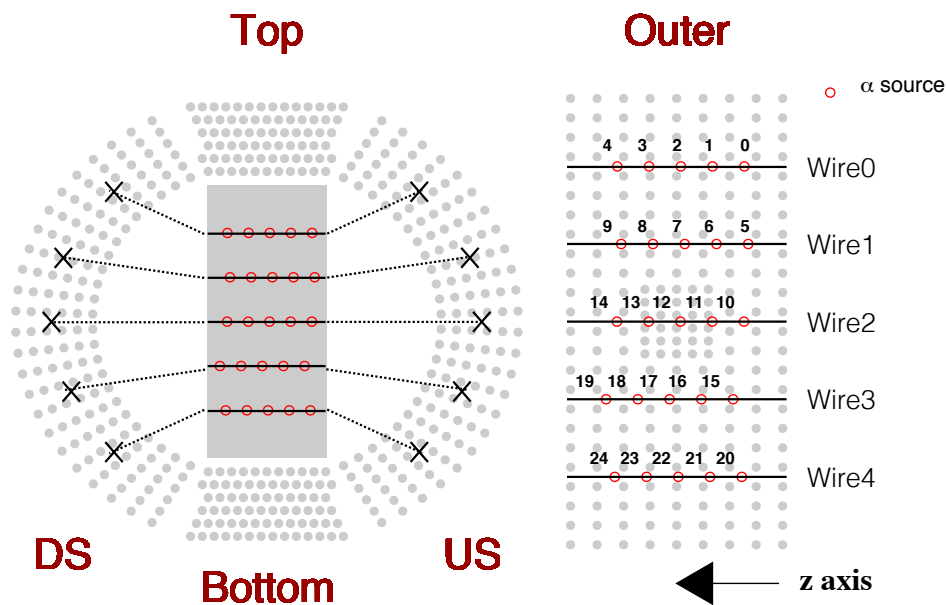


Figure 2.36: Location of 25  $^{241}\text{Am}$  source spots in the detector. Red circles on the inner and outer faces show the projected positions of the source spots.

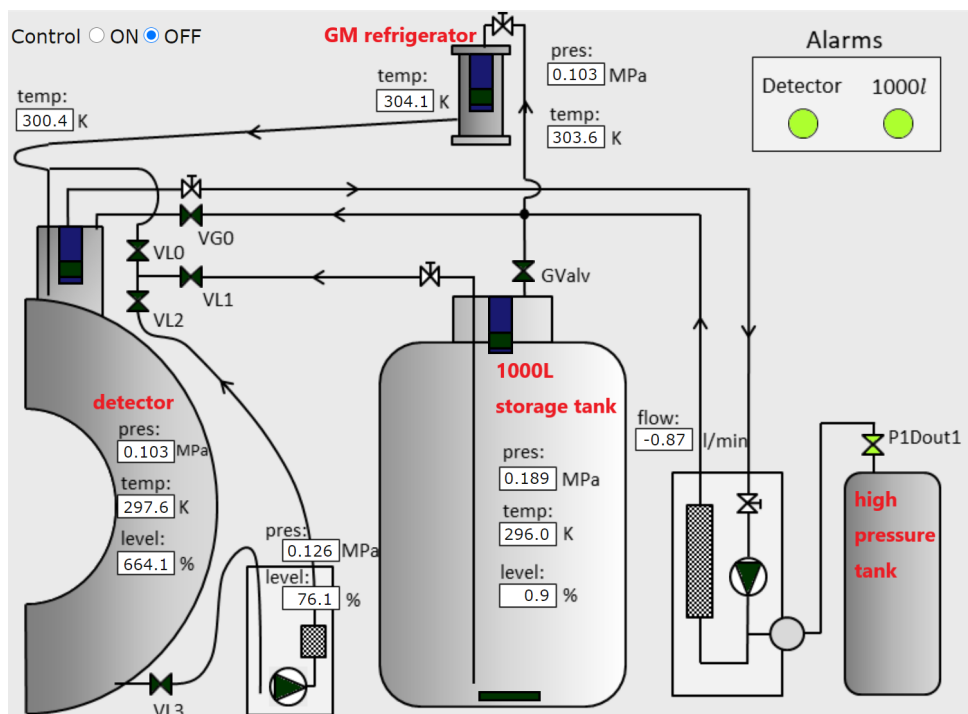


Figure 2.37: Xenon control panel in MEG II. The valves with the prefix “VL” are the valves in the liquid circulation line, and those with the prefix “VG” are in the gaseous circulation line. The detector (left), GM refrigerator (top), and 1000 l storage tank (middle) have a heater (blue and black box) at the top of each module to control the temperature.

The temperature of the MEG II LXe detector is kept stable by a PID control of the xenon pressure with a precision of 0.1 K unless the temperature of the detector hut is changed too rapidly.

## 2.4 Radiative Decay Counter

In the MEG II experiment, the Radiative Decay Counter (RDC) is newly introduced to identify the accidental RMD gamma ray. The typical energy of a positron from the RMD is about 3 MeV when a high-energy gamma ray is emitted. This low-energy positron is swept out with a small radius along the beam axis by the gradient magnetic field. The gamma ray from the RMD background can be identified by detecting this positron as shown in Fig. 2.38. The RDC consists of time- and energy-measurement parts, as shown in Fig. 2.39 and Fig. 2.40. The time measurement part is composed of 12 fast plastic scintillators (BC-418, Saint-Gobain) and 60 SiPMs (S13360-3050PE, Hamamatsu Photonics). Two or three SiPMs are attached to both sides of scintillators and connected in series. The energy measurement part is composed of 76 cubic LYSO crystals (Shanghai Institute of Ceramics) of  $2 \times 2 \times 2 \text{ cm}^3$ . Each crystal is read out with a single SiPM (S12572-25P, Hamamatsu Photonics).

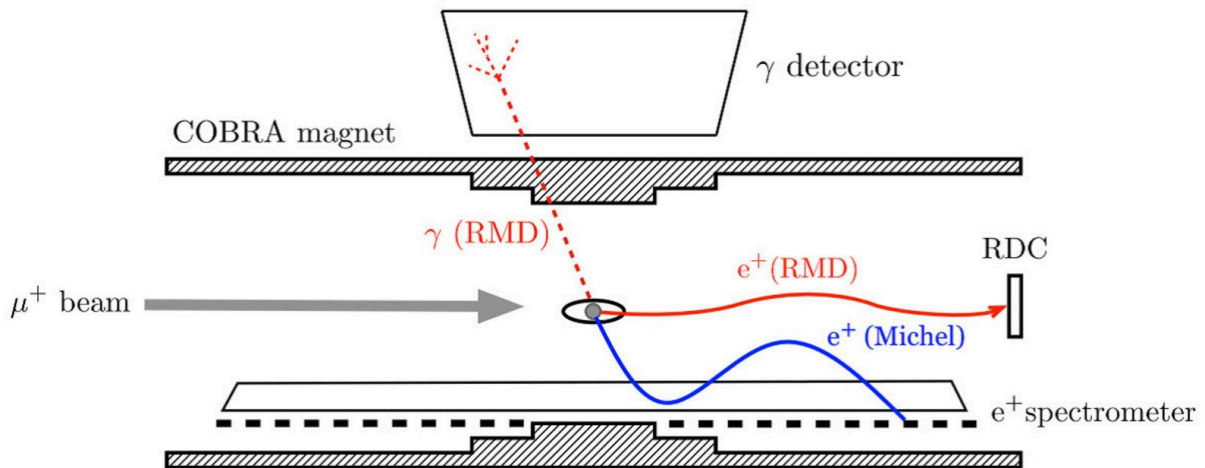


Figure 2.38: Principle of radiative muon decay (RMD) tagging with RDC. A low-energy positron from RMD (red) is swept with a small bending radius and detected by RDC downstream. On the other hand, a high-energy positron (blue) has a large bending radius and detected by the spectrometer.

## 2.5 $\pi^0$ measurement setup

Gamma rays from a  $\pi^0$  decay,  $\pi^0 \rightarrow \gamma\gamma$ , is the most promising calibration source to understand the response and performance of the LXe detector for a high-energy gamma ray. The MEG II collaboration has a dedicated setup for the calibration with the  $\pi^0$  decay. Fig. 2.41 shows the experimental setup of the  $\pi^0$  run. The negative pion beam supplied from the PSI accelerator

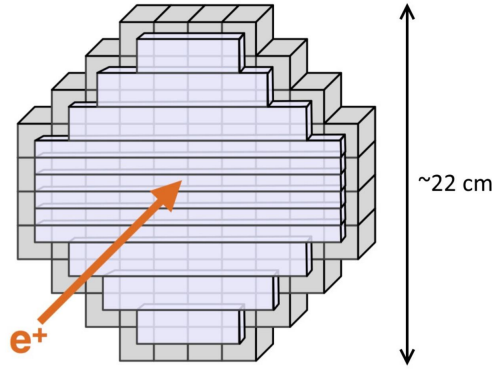


Figure 2.39: Structure of the RDC. The front side is the time measurement part composed of plastic scintillator bars, and the back side is the energy measurement part composed of LYSO crystals.

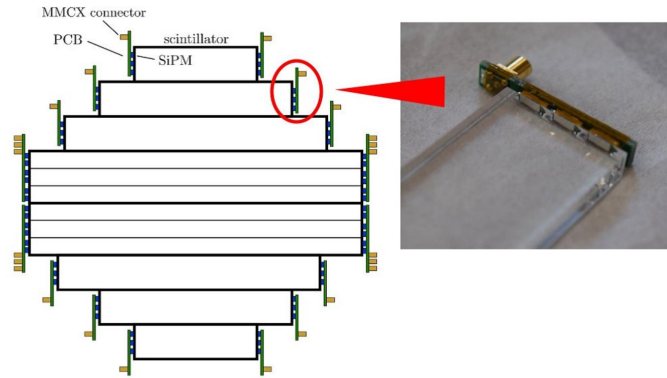


Figure 2.40: Structure of the time-measuring part of the RDC. The scintillation photons generated by an incoming positron in a plastic scintillator are read out by SiPMs connected in series.

is injected into a liquid hydrogen ( $\text{LH}_2$ ) target placed at the center of the experimental system instead of the normal target for the muon beam run. A dedicated detector system to measure the gamma ray from the  $\pi^0 \rightarrow \gamma\gamma$  decay is placed at the opposite side of the LXe detector. It consists of an energy measurement part, a BGO detector, and a time measurement part, a pre-shower counter.

When the  $\pi^-$  beam is introduced to the target, a part of negative pions are converted to  $\pi^0$  mesons by a charge-exchange reaction  $\pi^- + p \rightarrow \pi^0 + n$ . The energy of the  $\pi^0$  meson is

$$E_{\pi^0} = \frac{(m_{\pi^-} + m_p)^2 + m_{\pi^0}^2 - m_n^2}{2(m_{\pi^-} + m_p)} = 137.85 \text{ MeV} \quad (2.14)$$

where the mass of the particles is summarized in Table 2.5. The  $\pi^0$  meson has a short lifetime ( $8.5 \times 10^{-17} \text{ s}$  [36]), and it immediately decays to two gamma rays with a branching ratio of  $\text{Br}(\pi^0 \rightarrow \gamma\gamma) = 0.988$  [36].

The energies of the gamma rays are  $m_{\pi^0}/2$  in the center-of-momentum frame. In the laboratory

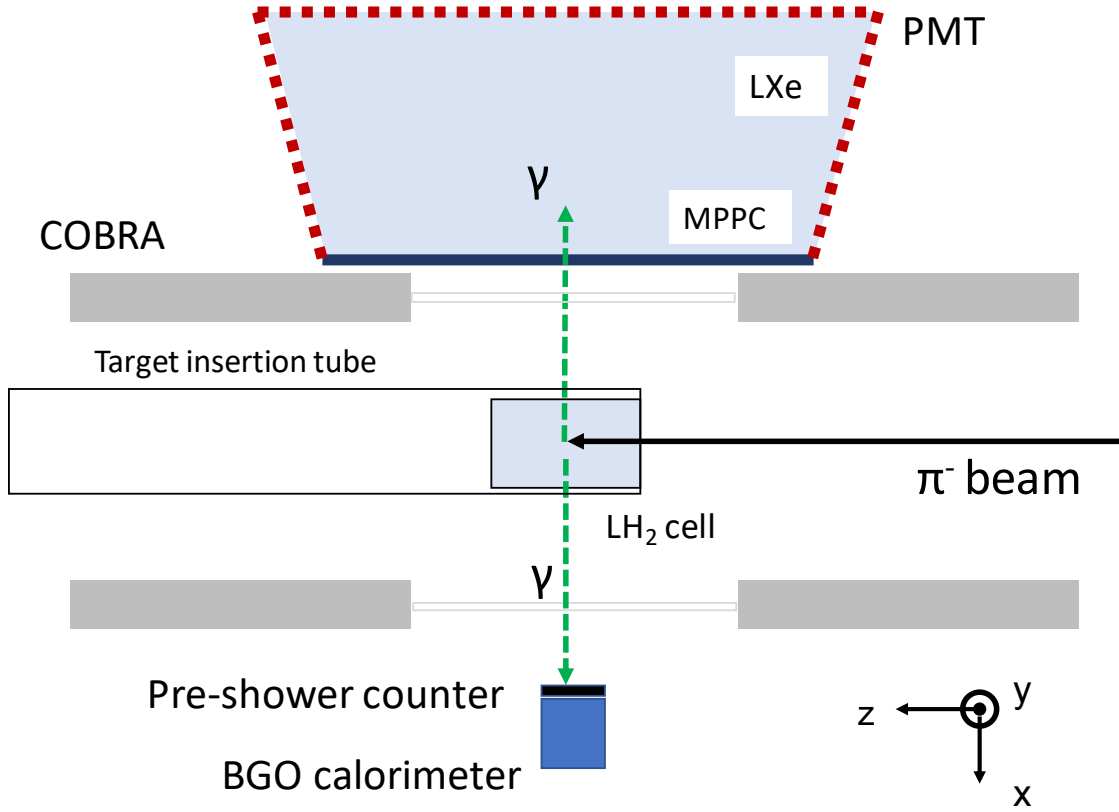


Figure 2.41: Schematic view of the experimental setup of the  $\pi^0$  run (top view). The negative pion beam is introduced to the  $\text{LH}_2$ -target cell and two gamma rays from a  $\pi^0 \rightarrow \gamma\gamma$  decay are emitted in nearly opposite directions. One gamma ray is detected by the LXe detector and the other gamma ray is detected by the BGO calorimeter and the pre-shower counter on the opposite side of the LXe detector.

Table 2.5: Mass of the particles

Particle	Mass [MeV]
$\pi^-$	139.57
$\pi^0$	134.97
$p$	938.27
$n$	939.57

frame, the energies of the two gamma rays are characterized by the opening angle  $\Theta_{\gamma\gamma}$  as

$$E_\gamma = \frac{E_{\pi^0}}{2} \pm \sqrt{\frac{E_{\pi^0}^2}{4} - \frac{m_{\pi^0}^2}{2(1 - \cos \Theta_{\gamma\gamma})}}. \quad (2.15)$$

In particular, the back-to-back gamma-ray pair has energies of 55 and 83 MeV. The kinematic topology of the  $\pi^0$  decay allows measuring the detector response for a high-energy gamma ray through the measurement of the other gamma ray by the pre-shower counter and BGO detector at the opposite side of the LXe detector.

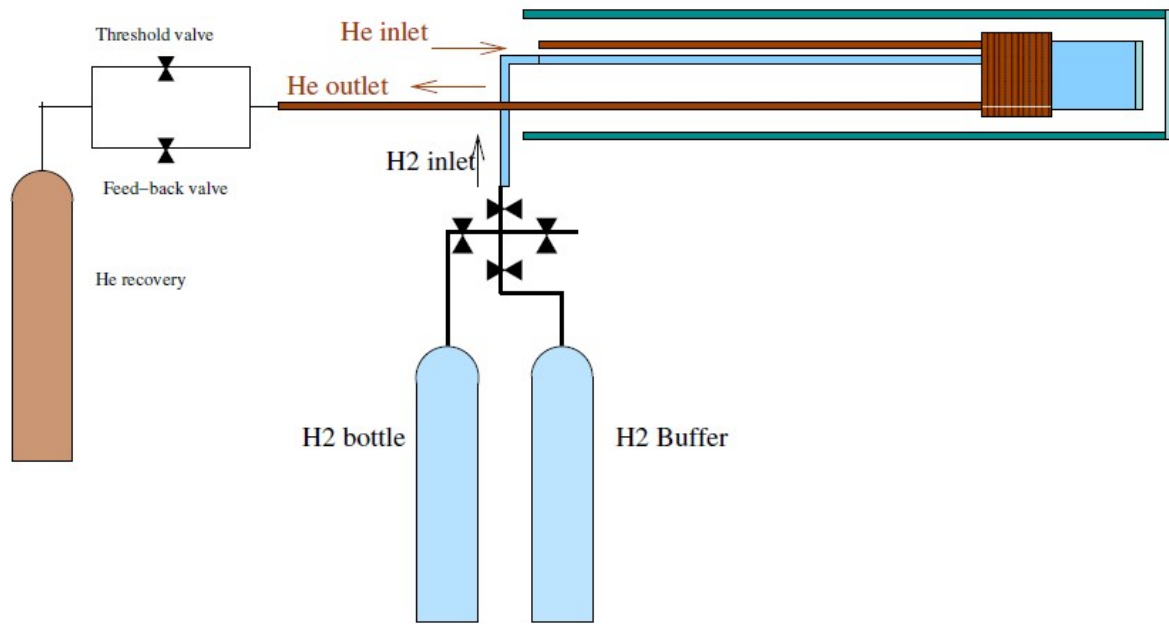


Figure 2.42: Scheme to hold liquid hydrogen in the LH<sub>2</sub>-target cell for the  $\pi^0$  run [27]. LH<sub>2</sub> is contained in a target cell cooled by the He circuit.



Figure 2.43: Cell of the LH<sub>2</sub> target used in the 2021  $\pi^0$  run.

In addition to the charge exchange reaction, a radiative capture reaction  $\pi^- p \rightarrow \gamma n$  also happens in the target. The ratio of the cross-section of the charge exchange reaction to that of the radiative capture is known as the Panofsky ratio,

$$P = \frac{\sigma(\pi^- p \rightarrow \pi^0 n)}{\sigma(\pi^- p \rightarrow \gamma n)}, \quad (2.16)$$

which was measured in the previous measurements to be 1.5 [57, 58]. The radiative capture emits a 129 MeV monochromatic gamma ray and a 9 MeV neutron in opposite directions. The monochromatic 129 MeV gamma ray is useful to understand the linearity of energy reconstruction and the energy dependence of the energy resolution.

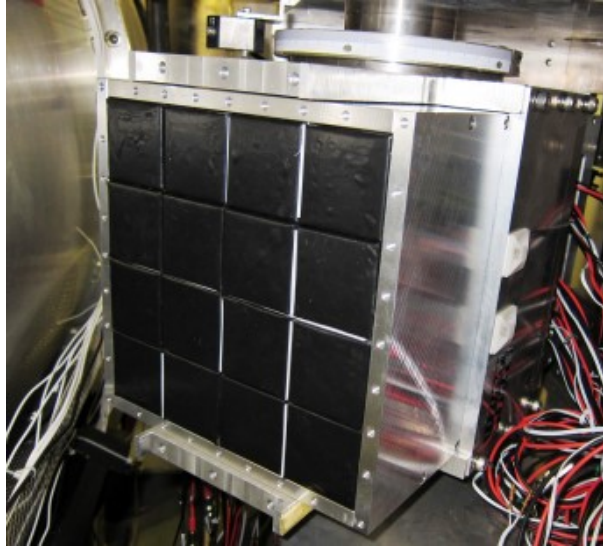


Figure 2.44:  $4 \times 4$  BGO crystals [27]. The scintillation photons of the BGO crystal are read out by 16 PMTs on the back.



Figure 2.45: Pre-shower counter module [56]. A fast plastic scintillator is wrapped with reflectors of aluminized mylar and then shielded by a black sheet. The scintillator is read out by 16 MPPCs at both ends.

## Pion beam

The negative pions used in the  $\pi^0$  run are produced by the reaction  $p + n \rightarrow p + p + \pi^-$  from the proton beam coming from the cyclotron, and their momentum is 70.5 MeV. It has the same time structure as the proton and has a bunch structure of 50 MHz. The beam intensity is adjusted by the slits upstream of the detector system to have a sufficient  $\pi^0 \rightarrow \gamma\gamma$  event rate to accumulate the statistics in the limited beam time. The pion beam rate in the 2021  $\pi^0$  run was  $9.5 \times 10^4/\text{s}$ .

## LH<sub>2</sub> target

A schematic of the LH<sub>2</sub> target is shown in Fig. 2.42. The LH<sub>2</sub> target consists of a cell in the center of the experimental coordinate, a cooling circuit that circulates liquid helium, and a vacuum tube that prevents heat dissipation from the LH<sub>2</sub> cell. The cell that contains LH<sub>2</sub>

is a stainless steel cylinder of 0.5 mm thick, 60 mm diameter, and 75 mm length, as shown in Fig. 2.43. The cooling circuit is connected to a  $\sim 60$  l liquid helium dewar. The vacuum level of the tube is kept to be  $\mathcal{O}(10^{-6})$  mbar. The LH<sub>2</sub> target was upgraded from the MEG experiment to reduce the heat dissipation and improve the stability by introducing a new cooling helium circuit. The material of the LH<sub>2</sub> target before and after the upgrade is summarized in Table 2.6.

Table 2.6: LH2 target material

Type	Cell diameter	Cell wall thickness	Tube wall thickness
MEG	50 mm	Stainless, 0.5 mm	Stainless, 1 mm
MEG II	60 mm	Stainless, 0.5 mm	Stainless, 3 mm

## BGO detector

The BGO detector is a scintillation detector that consists of 4×4 BGO crystals and 16 PMTs coupled to each crystal, as shown in Fig. 2.44. The fundamental specifications of the BGO detector are summarized in Table 2.7.

Table 2.7: Specifications of the BGO detector

Density [g/cm <sup>3</sup> ]	7.13
Radiation length [mm]	11.2
Scintillation wavelength [nm]	480
Size	46 × 46 × 200 mm <sup>3</sup>
Readout	PMT (Hamamatsu H8409-70)

## Pre-shower counter

The design of the pre-shower counter is based on that of the pTC. One module of the pre-shower counter consists of four MPPCs connected in series to a fast plastic scintillator on both sides. By stacking two of these modules orthogonally, the position and time of gamma rays can be measured more precisely. A set of two pre-shower counter modules and a lead converter with 4 mm thickness are placed in front of the BGO detector. About a quarter of incoming gamma-rays is converted to electrons and positrons by the lead converter, and detected by the two pre-shower counter plates.

The BGO detector and the pre-shower counter are moved by rails along the  $z$  and  $\phi$  directions to scan the whole LXe detector with back-to-back gamma-ray pairs.

## 2.6 17.6 MeV CW-Li gamma-ray

The MEG II collaboration has a Cockcroft–Walton (CW) accelerator in the downstream side of the  $\pi$ E5 area, as shown in Fig. 2.46. By irradiating the  $\text{Li}_2\text{B}_4\text{O}_7$  target with 440 keV protons obtained by this accelerator, 17.6 MeV gamma-rays are emitted from the  ${}^7_3\text{Li}(p, \gamma){}_4^8\text{Be}$  reaction. The monochromatic gamma rays provided by this system are quite useful for the light yield monitoring and the uniformity study over the detector volume. The beamline switching between CW and muon beam can be done relatively quickly ( $\sim 10$  minutes) by pulling down the MEG II target upstream and installing the CW beamline from downstream with bellows.

The  $\text{Li}_2\text{B}_4\text{O}_7$  target is slanted by  $45^\circ$  with respect to the beam axis. The position and size of the interaction region were measured by a pixel detector at the end of the beam pipe as shown in Fig. 2.47. The beam spot size was 6 mm in  $\sigma$ , and it was displaced from the center of the  $xy$  plane by 5 cm and 1 cm in the  $x$  and  $y$  directions, respectively.

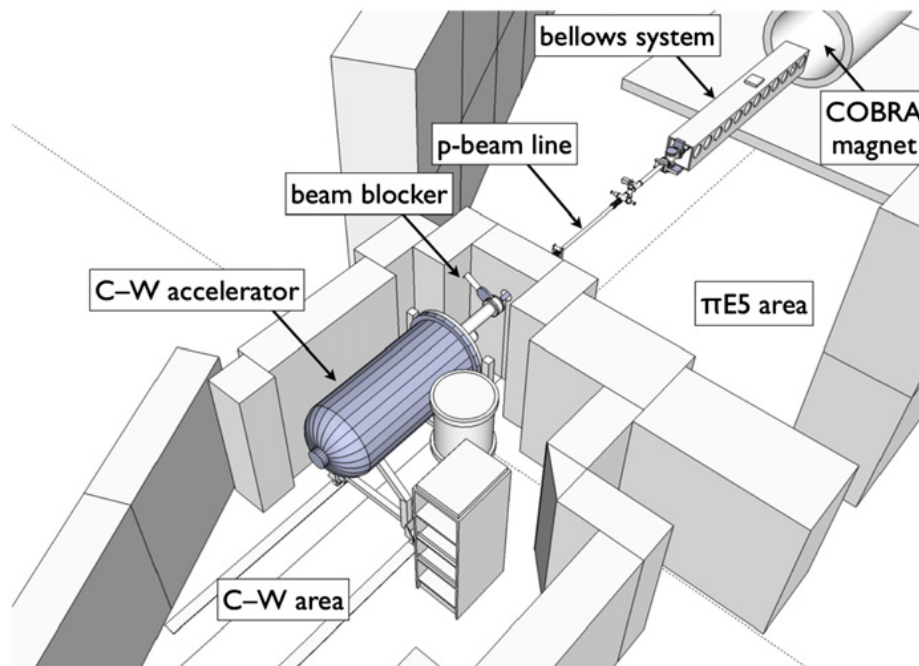


Figure 2.46: Beamline of Cockcroft–Walton accelerator in the downstream of the MEG II system.

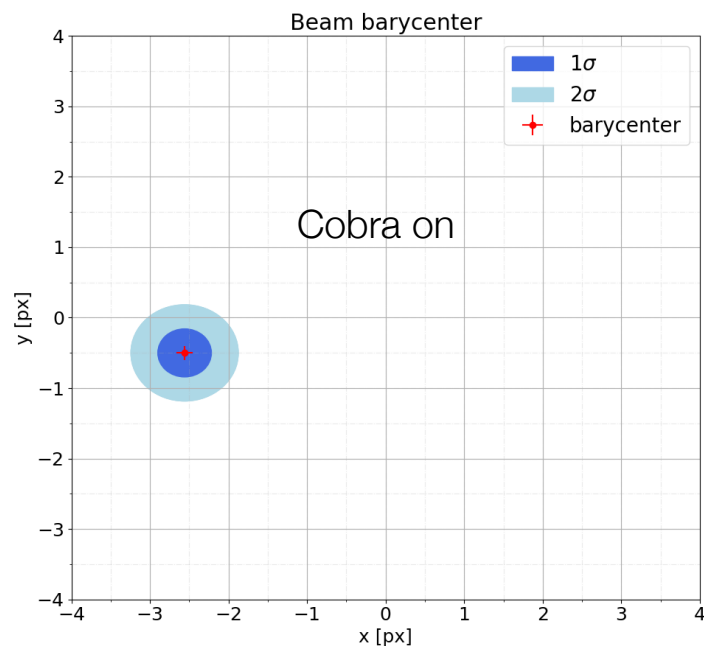


Figure 2.47: CW proton beam vertex position measured with a pixel detector at the end of the beam pipe. The  $x$ - and  $y$ -axis of the plot correspond to the  $x$ - and  $y$ -position in the pixel detector in the unit of the pixel size (2 cm).

## 2.7 Data acquisition system

Given the need for suppression of accidental background events in the  $\mu^+ \rightarrow e^+\gamma$  search, it is desirable to have a fast waveform digitizer that works at a high sampling frequency.

A new DAQ module, WaveDREAM<sup>\*1</sup>, was developed for MEG II. It is equipped with a fast waveform digitizer, Domino Ring Sampler (DRS) [60]. As shown in Fig. 2.48, the trigger functions, basic DAQ functions, and HV supplies for SiPMs are integrated into a single WaveDREAM board. Thanks to this integrated design, the experiment can read out signals from the granular readouts with a manageable number of cables. The number of readout channels in the MEG II is three times larger than that in the MEG experiment, as shown in Table 2.8.

Fig. 2.49 shows the principle of the waveform digitization by the DRS. Each capacitor stores voltage information by means of a sampling signal generated by an inverter delay chain. When triggered, this sampling signal stops, and the voltage value at that point is stored in the shift register. The DRS chip can be operated at sampling frequencies from 0.5 to 5 GHz. In the 2021 run, the data were acquired at 1.4 GHz for all readout channels except for the CDCH readout channels (1.2 GHz). The sampling frequency was determined considering the latency of the trigger system. It is high enough to achieve a good timing resolution and low enough to

<sup>\*1</sup> Waveform Drs4 REadout Module

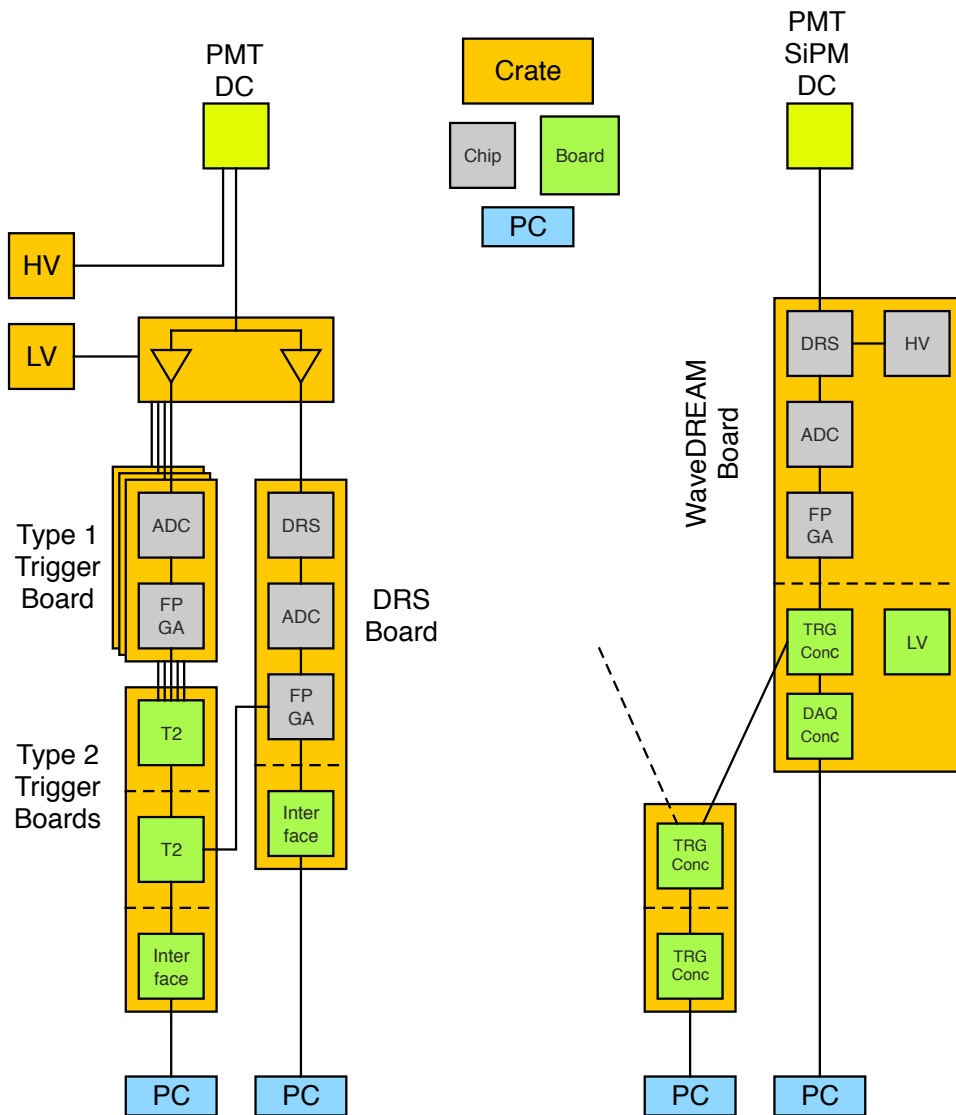


Figure 2.48: Comparison of the DAQ system in the MEG (left) and MEG II (right). See the legend at the top for the color of the boxes. A WaveDREAM board has basic trigger functionality and a slot for an HV card to apply bias voltages to the SiPMs.

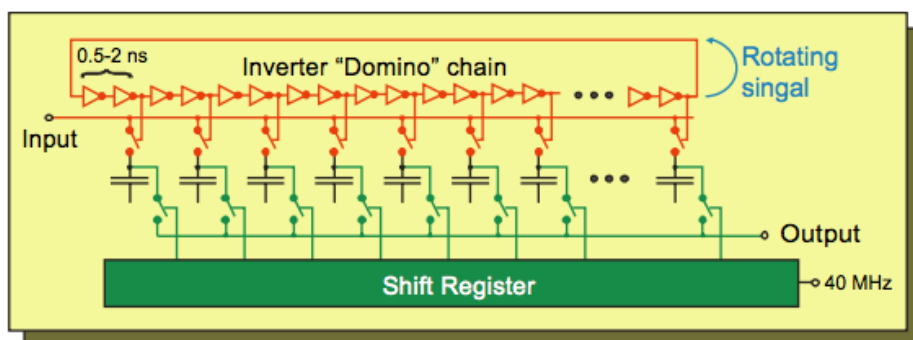


Figure 2.49: Working principle of a DRS chip [59].



Figure 2.50: WaveDREAM boards in a crate. A WaveDREAM crate has 16 slots for WaveDREAM boards and two slots for a DCB and a TCB.

secure a reasonable margin of 100 ns before the pulse, which is necessary to unfold the pileup pulse before the main pulse.

Since SiPMs generally have lower gain than PMTs, the readout electronics have amplifiers for compensation. The two stages of switchable amplifiers with a gain of 10 and programmable attenuators are implemented for each channel. They allow setting the overall input gain in a range from 0.5 to 100 in eight steps. The high gain of 100 is used to calibrate the photosensors with small signal waveforms. The low gain of 1–5 is used to collect high-energy gamma-ray events. In the 2021 run, the amplifier gain was set to 5 for MPPC readout channels and 2.5 for PMT channels. This is high enough to have a good online timing resolution, while the amplitude of the waveform is within the dynamic range of the readout electronics for a large fraction of events. The amplifier gain of 100 was used for MPPC calibration that requires a higher S/N ratio to measure  $\mathcal{O}(1)$  photoelectrons.

Table 2.8: The number of readout channels of MEG and MEG II detectors.

Detector	MEG	MEG II
LXe detector	846	4,760
Positron timing counter	120	1,024
Drift chamber	1,728	3,456
Radiative decay counter	(0)	100
Total	2,690	~10,000

A single WaveDREAM board can read out 16 channels. A single WaveDREAM crate (Fig. 2.50) has 16 slots for WaveDREAM boards. Since 10,000 channels are used, 36 crates (19 for the LXe detector, 4 for pTC, 10 for CDCH, and 3 for other systems, such as RDC, BGO, pre-shower, and beam monitoring detectors) are used.

The WaveDREAM crate also has one slot each for Trigger Concentrator Board (TCB) and

Data Concentrator Board (DCB). The DCB bridges the WaveDREAM boards and the DAQ system. It is responsible for the configuration of the boards, the distribution of the master clock and trigger signals, and the readout of waveform data from each board. The upper limit of the data rate that can be processed by the DCB is 130 MB/s. The TCB is designed for online data processing. The trigger system made up of TCBs reconstructs the physics variables such as momenta, relative timing, and direction of positrons and gamma-rays. The collected data are transferred to the online computer and compressed by the pbzip library.

The data acquisition and the slow control of the detectors are controlled by the MIDAS system [61].

## 2.8 Trigger

Table 2.9: Trigger logics used for this thesis.

Logic	Purpose
Pedestal trigger	Monitoring of the noise condition.
LED trigger	Calibration with LEDs.
EGamma trigger	Measure the LXe detector response
Alpha trigger	Calibration with $^{241}\text{Am}$ sources.
MEG trigger	Search for $\mu^+ \rightarrow e^+\gamma$ .
$\pi^0$ trigger	$\pi^0$ run.

A variety of trigger logics are prepared for the data acquisition as shown in Table 2.9.

### 2.8.1 Pedestal trigger

The pedestal trigger is fired periodically, and so independently of the detector signals. The pedestal data is useful to estimate the noise level and the event-by-event fluctuation of the baseline.

### 2.8.2 LED trigger

As described in Sec. 2.3.6, two kinds of LEDs are installed in the LXe detector. For both systems, a trigger signal in synchronous with the driver signal for the LEDs is provided from the driver module to the trigger system. The LEDs are flashed by 0.1 Hz with the beam and  $\mathcal{O}(10)$  Hz in dedicated calibration measurement, and the trigger is fired when the trigger signal is larger than a given threshold.

### 2.8.3 EGamma trigger

A self-trigger of the LXe detector called “EGamma” trigger is used to take  $\gamma$ -ray events with a given threshold. The online  $\gamma$ -ray energy is reconstructed using a weighted sum of the photosensor waveforms. The trigger is fired when the amplitude of the weighted sum waveform exceeds the threshold. The weights of each photosensor are calculated from the calibration parameters such as gain, ECF, and PDE. The scale of the online  $E_\gamma$  was calibrated by 17.6 MeV gamma-ray from the CW-Li setup.

### 2.8.4 Alpha trigger

A dedicated trigger is implemented to take  $\alpha$  events from the  $^{241}\text{Am}$  sources. The trigger is fired when the sum of the sensor waveforms of PMTs exceeds a given threshold. A particle identification based on the waveform shape is used to improve the purity of  $\alpha$  events by rejecting gamma rays and cosmic rays.

### 2.8.5 MEG trigger

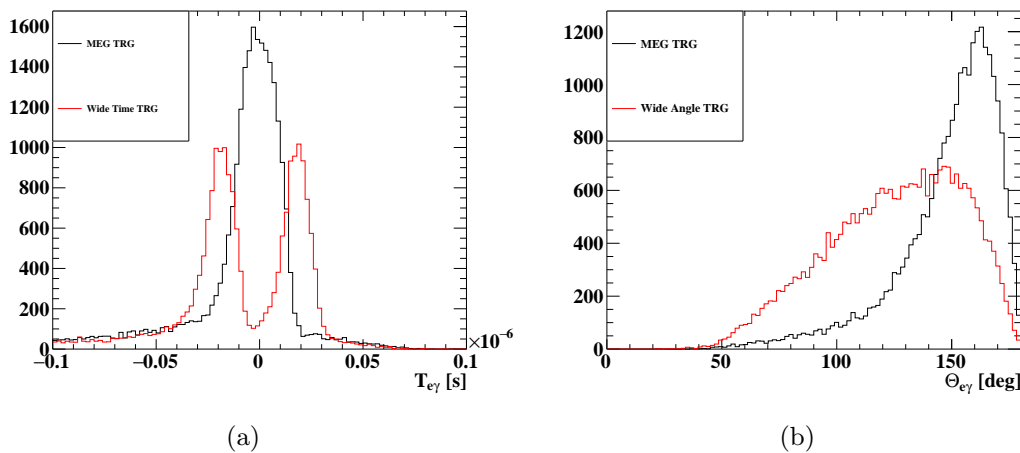


Figure 2.51: (a)  $t_{e+\gamma}$  and (b)  $\Theta_{e+\gamma}$  distribution of the events collected by the MEG trigger (black) and ancillary trigger with a loose constraint (red). The  $t_{e+\gamma}$  window of the MEG trigger was 25 ns in the 2021 run. Events with a large opening angle are collected with the direction matching.

The trigger logic for the  $\mu^+ \rightarrow e^+\gamma$  search called “MEG trigger” is composed of three independent conditions, as listed below.

- Coincidence trigger of gamma and positron
- Back-to-back position selection (Direction matching).
- EGamma trigger

In addition to the main trigger, three ancillary triggers with a wide time window, a lower  $E_\gamma$  threshold, and a loose direction match constraint are prepared to evaluate the trigger efficiency. In the 2021 run, the trigger rate was 5–20 Hz depending on the beam rate and the threshold values.

### 2.8.5.1 Coincidence trigger

A coincidence trigger is designed to select a pair of a positron and a gamma ray produced at the same time. The trigger is fired when the difference between the time of a gamma-ray measured by the LXe detector and the time of a positron measured by the positron timing counter is smaller than a certain threshold. In the 2021 run, the online gamma-ray time was defined as the time when the amplitude of the summed waveform of the MPPCs exceeded a certain threshold. The online  $t_\gamma$  resolution was limited by the time walk and was about 3 ns. The positron timing was reconstructed using the timing of pTC hits.

The center of the coincidence time window was defined by the  $t_{e+\gamma}$  peak of RMD events. In 2021, the width of the window was 25 ns so that the RMD peak was completely included by taking the online time resolution ( $\sim 5$  ns) into account, as shown in Fig. 2.51a.

### 2.8.5.2 Direction matching

As shown in Fig. 2.31, MPPCs are clustered so that  $4\times 4$  MPPCs are read out by a single WaveDREAM board. The direction of gamma-rays is reconstructed by finding the WDB that has the largest signal of all boards connected to MPPCs. The online position resolution for the gamma-ray is  $\sim 3$  cm. The direction of positrons is reconstructed by a hit pattern of a positron in the pTC. Fig. 2.51b shows the distribution of the opening angle  $\Theta_{e+\gamma}$ . Events with  $\Theta_{e+\gamma} \sim 180^\circ$  are collected by the MEG trigger.

## 2.8.6 $\pi^0$ trigger

Four trigger logics were prepared for the  $\pi^0$  run.

- Coincidence of the LXe detector, pre-shower, and BGO detector.
- Coincidence of the LXe detector and BGO detector with a veto by the pre-shower counter.
- A self trigger of the BGO detector
- A self trigger of the pre-shower counter

The first two coincident triggers are fired when the following three conditions are met.

- Online gamma-ray position is inside a given region called “patch”.
- The reconstructed timing by the LXe detector and the timing of the hit of the BGO detector are within the coincidence window.
- The reconstructed timing by the pre-shower counter is inside or outside the coincidence window, depending on the trigger type.

The self-trigger of the BGO detector is fired when the amplitude of the summed waveform of the BGO detector exceeds a given threshold. The dataset with this trigger is useful to calibrate the BGO detector with CW-Li  $\gamma$ -rays in advance of the  $\pi^0$  run and to evaluate the detection efficiency of the LXe detector. The self-trigger of the pre-shower counter is fired when a discriminator of an MPPC readout is fired. It was used for the calibration and performance evaluation of the pre-shower counter.

## 2.9 Detector simulation

### 2.9.1 Overview

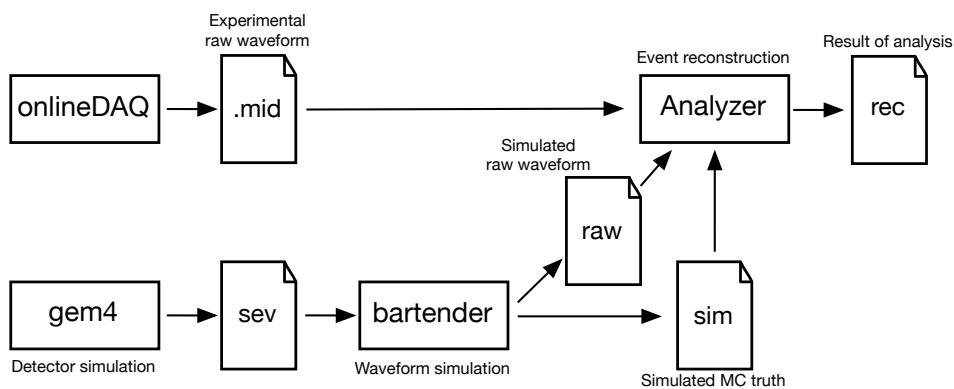


Figure 2.52: MEG II software framework. The online DAQ system saves the data in .mid files. The detector simulation generates .sev files that contain the time and amplitude of the readout channels. bartender simulates the waveforms by taking .sev files as inputs. Then the simulated waveforms are processed by analyzer so that the variables of gamma rays and positrons are reconstructed.

A detector simulation framework has been developed to understand the detector response and performance. Fig. 2.52 shows the overview of the simulation framework together with the analysis flow of the data.

The detector simulation is carried out in a Geant4 [62] based software gem4. Geant4 (Version 4.10.06.p03) is a particle simulation framework with Monte Carlo methods. It generates an event with a given initial condition, such as the type, momentum, and position of particles, the geometry of the detectors, and the electromagnetic field of the simulation volume. For each event, the generated particles are propagated based on a list of the particle interactions called “Physics list”. The geometry of the experimental apparatus is reproduced in gem4. The output of gem4 is stored in “sev” files and used for the following waveform simulation.

Waveform simulation is performed in software called “bartender”. The main function of the bartender is event mixing and electronics simulation. Multiple events are mixed at a certain event rate to simulate pileup effects and stored in “sim” files. The waveform of readout channels is simulated with the response template and stored in “raw” files with the same format as the

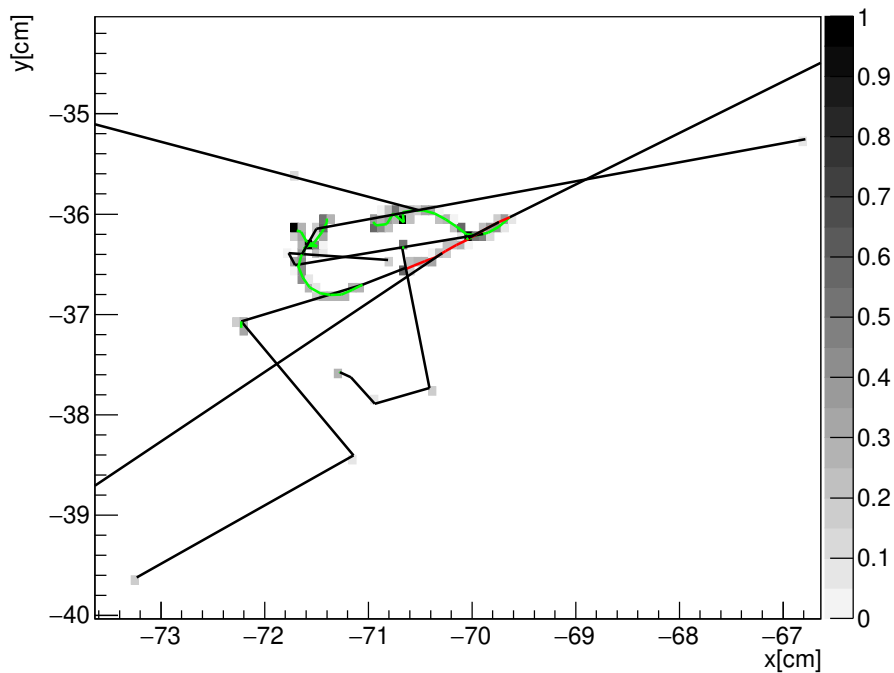


Figure 2.53: Simulation of an electromagnetic shower produced by an impinging gamma ray from the upper right. Particle tracks are shown as lines (black:  $\gamma$ , red:  $e^+$ , green:  $e^-$ ). The energy deposit on each point is overlaid. The scale of the gray bar is in the unit of MeV [2].

real data.

Finally, the “analyzer” analyzes the waveforms with the same algorithm as the data. Bartender and analyzer are based on the ROME framework [63].

## 2.9.2 LXe detector simulation

Here we describe the configuration of the detector simulation of the LXe detector and discuss the difference between the simulation and reality. Table 2.10 summarizes the standard configuration of the simulation.

In the detector simulation, an electromagnetic shower produced by an incident particle is simulated as shown in Fig. 2.53. VUV scintillation photons are generated at each energy deposit in LXe with a given scintillation time constant. The number of generated scintillation photons is calculated from the energy deposit divided by the W-value of LXe, taking the Poisson fluctuation into account. The reflection on the detector material, attenuation by the impurities, and the Rayleigh scattering in the LXe are implemented.

The angular dependence of the MPPC PDE is simulated based on that of the reflection at the sensor surface, which is calculated from a complex refractive index of Silicon and LXe in gem4.

In the waveform simulation, waveforms are formed in a way that the single photoelectron response of each photosensor is summed up with the time distribution of the arriving photons

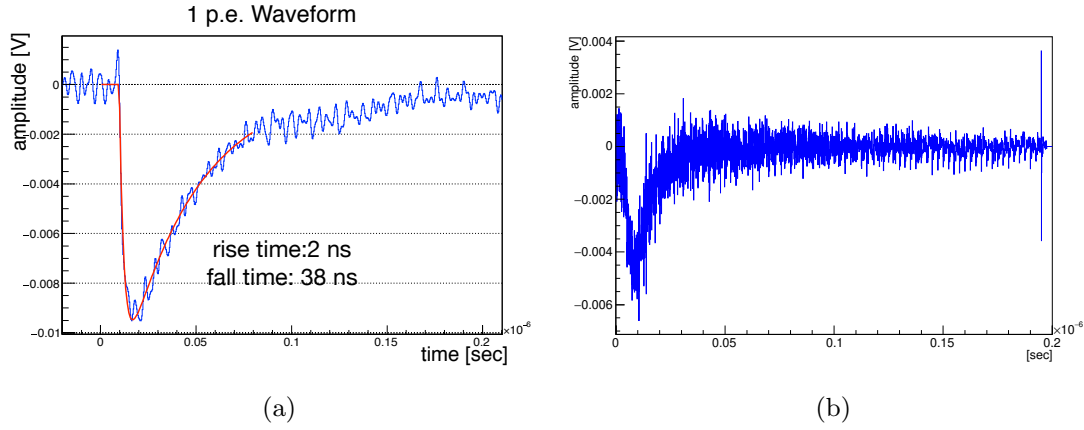


Figure 2.54: Waveform templates of (a) MPPC and (b) PMT used for waveform simulation [2]. The waveform template of the MPPC is obtained by one photo-electron waveform, and that of the PMT is obtained by deconvoluting gamma ray waveform by estimated scintillation signal defined by the scintillation time constant.

simulated in the gem4. Fig. 2.54 shows the single photoelectron response derived from the data. The single photoelectron response of MPPCs is obtained from the template waveform of single photoelectron events in data for MPPCs. That of PMTs was obtained by deconvoluting gamma-ray waveforms by scintillation time distribution since the single photoelectron peak can not be resolved in the charge distribution.

The MPPC characteristics such as crosstalk, after-pulsing, and saturation are simulated in the bartender. In the simulation of the crosstalk, each fired pixel in an MPPC can fire another adjacent pixel with a given probability. To simulate the afterpulse, a fired pixel can also trigger another hit on the same pixel with a given probability and time constant. To simulate saturation, when more than one photon hits the same pixel, the waveform from the second photon is reduced as a function of the elapsed time from the first photon. The individual differences in the gain, ECF, PDE, and QE of the MPPCs and PMTs are not taken into account.

The response of readout electronics is applied to reproduce the signal waveforms. A white noise of a given standard deviation (0.7 mV) is added to the waveform of each readout. The simulated waveform is digitized by a sampling frequency of 1.4 GHz, and the waveform outside the dynamic range of the DRS chip (from  $-950$  mV to  $+50$  mV) is cut.

#### Source of a discrepancy between data and MC

There are several sources of discrepancy between the data and the MC, as listed as follows.

- Reflectivity of the inner wall and the surface of the photosensors.
- Attenuation length and Rayleigh scattering length of scintillation light in LXe.
- Liquid level.
- Incident angle dependence of the PDE of the photosensors.

Table 2.10: Standard configuration of simulation for the LXe detector.

gem4	
Geant4 version	4.10.06.p03
Physics list	G4EmStandardPhysics
W-value for electron [eV]	21.6
W-value for $\alpha$ -particle [eV]	19.6
Scintillation Wavelength (mean) [nm]	175
Rayleigh scattering length [cm]	45
Absorption length [cm]	500
Refractive index of LXe	1.69
Reflectivity of PMT holder	0.5
PDE (MPPC / PMT)	0.12/0.16
Scintillation time constant [ns]	22 (fast) / 45 (slow)
bartender	
Sampling frequency [GHz]	1.4
Gain (MPPC / PMT)	$1.5 \times 10^6$ / $0.8 \times 10^6$
Cross-talk probability	0.15
After-pulsing probability	0.15
After-pulsing time constant [ns]	50
The amplitude of white noise [mV]	0.7

The reflectivities of the detector materials in the MC simulation are defined by the material properties in literature, and they can be different from the real reflectivity because of the actual surface conditions of the material. The discrepancy of the reflectivity has a large impact on the light distribution. The Rayleigh scattering length of scintillation light in LXe is set to 45 cm, which is the measured value in Ref. [64], while it is deviated from the theoretical prediction (35 cm) [42]. The discrepancy of the Rayleigh scattering length also can affect the light distribution. The absorption length was set to 500 cm, which is sufficiently long with respect to the detector size. This is because the light yield saturated with the liquid purification at the beginning of the beam time, and because the distance dependence of the number of photons was consistent with the simulation with 500 cm absorption length as later discussed in Sec. 4.5. The detector is completely filled with LXe in the simulation, but it was found that the level is below the topmost PMTs in the 2021 run. The light distribution close to the level should have been affected by the reflection at the interface between LXe and gaseous xenon.

## Chapter 3

# Run 2021

After the LXe detector was installed in 2017, a series of commissioning runs were performed from 2017 to 2021. The situation of the commissioning runs from 2017 to 2020 is summarized in Appendix A. This chapter focuses on the goal, schedule, and data-taking condition in the 2021 run.

### 3.1 Overview

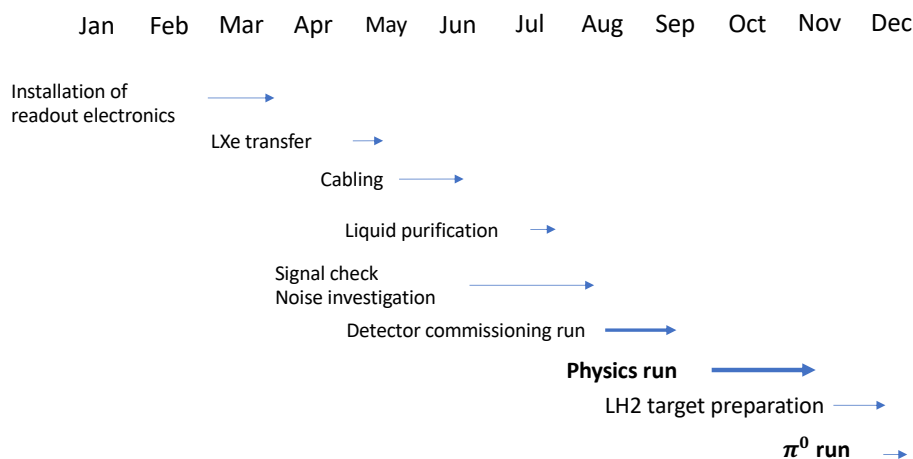


Figure 3.1: Timeline of the 2021 run. The beam time started at the middle of August after a series of preparations. After one month of the detector commissioning run, the physics data acquisition started at the end of September. At the end of year, the  $\pi^0$  run was performed to measure the performance of the LXe detector.

The goal of the 2021 run was to prove that all detectors and hardware were ready for the physics run and to collect physics data for a short period. To achieve this goal, the following requirements needed to be fulfilled.

- The full system of readout electronics must operate stably and with low noise enough to achieve good detector resolutions.

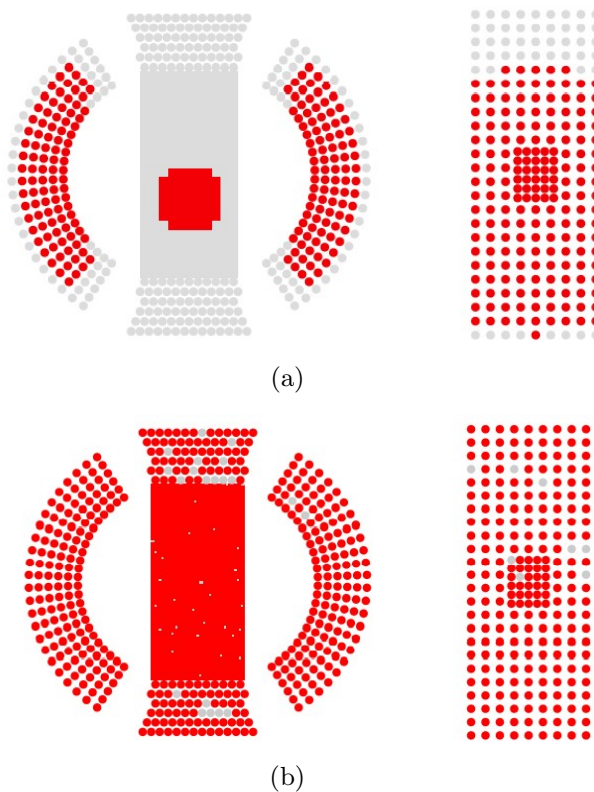


Figure 3.2: Development view with readout region in (top) the 2020 run and (bottom) 2021 run shown in red. While the number of readout channels was limited to  $\sim 1000$  until the 2020 run, the full readout electronics were installed for the 2021 run. Inactive channels are shown in grey.

- All detectors must operate stably in a muon beam environment.
- The trigger for the  $\mu^+ \rightarrow e^+\gamma$  search must be established.
- The detector performance and their stability and uniformity are understood to analyze the dataset.

The timeline of the 2021 run is shown in Fig. 3.1. The detector commissioning run started in the middle of August after the preparation such as the installation of the readout electronics, LXe transfer to the detector, and signal check of the photosensors. The physics data acquisition started in late September and continued until the middle of November. At the end of the year, the  $\pi^0$  run was performed to measure the performance of the LXe detector.

## 3.2 Preparation for physics run

While the number of readout channels was limited to  $\sim 1000$  until the 2020 run, as shown in Fig. 3.2a, the full readout electronics were installed in March 2021 (Fig. 3.2b).

As a result of the signal check, 23 MPPCs and 22 PMTs were found to be unavailable for measurements, as shown in Fig. 3.2b, with the following reasons.

- The short circuit of the photosensor or the cables connected to the photosensors.

- The malfunctioning of the HV supply of the PMTs.
- The malfunctioning of the photosensor.

The unavailable channels causes the non-uniformity of the energy reconstruction, which will be discussed in Sec. 7.2. The noise in the readout electronics was found to be negligible with offline noise reduction as later described in Sec. 4.2.

The liquid purification was performed from 22nd July to 26th July until the light yield reached the plateau. The light yield of the LXe after the liquid purification was  $93\pm 5\%$  of the MC simulation based on the calibration measurements with  $^{241}\text{Am}$  sources. The light yield was stable within a few % till the end of the 2021 run. The monitoring of the light yield will be discussed in Sec. 4.6.

The level of LXe in the detector was  $y = 83$  cm based on the measurement with the  $\alpha$  sources, later discussed in Sec. 4.5. The reflection of the scintillation photons at the interface between LXe and gXe causes the non-uniformity of the light collection efficiency in the detector. Its impact on the energy reconstruction and the correction will be discussed in Sec. 7.2.

The detector commissioning with the muon beam started in the middle of August. The detector calibration with and without muon beam was established in this preparation period. Table 3.1 shows the routine of the calibration in the 2021 run. A series of calibration measurements were performed without the beam twice per day. In addition to the dedicated calibration measurements without the beam, the LED data were mixed with the in-beam data-taking with 0.1 Hz to monitor the photosensor response under a high-intensity environment. Since we had the plan to carry out the  $\pi^0$  run at the end of the year, the beam rate was needed to be defined so that the PDE of the MPPCs did not decrease below 0.04, where the degradation of the resolutions was suggested by the simulation [2]. The beam rate at the beginning of the 2021 run was set to  $3 \times 10^7$  /s based on the measured PDE of the MPPCs.

The MEG trigger was developed in parallel with the detector commissioning. The direction matching and the time coincidence between positrons and gamma rays were developed. The coincidence window of gamma rays and positrons was aligned with the  $t_{e+\gamma}$  distribution of the RMD events collected at low intensity ( $1 \times 10^6$  /s).

### 3.3 Physics run

The physics data-taking started in late September after the MEG trigger was set up. When starting the physics data acquisition, the critical issue was that the data rate with the MEG trigger was too high to collect all triggered events. The data size of the entire waveform of all readout channels was 9 MB per event after the compression. Since the trigger rate was 16 Hz at the beam intensity of  $3 \times 10^7$  /s, the data rate was 150 MB/s to collect all triggered events. However, it was not feasible because it exceeded the upper limit of the data rate offered by the hardware, 130 MB/s. Furthermore, the high data rate was not feasible in terms of the size of the data storage. The 1.6 PB data storage of the MEG II collaboration would be shortly used up if we continue taking the data at such a high data rate.

Table 3.1: Calibration routine in the 2021 run. The dedicated calibration measurements were performed twice per day (morning and afternoon).

Type	Duration [min]	Statistics [events]
Morning		
Random trigger	10	$5 \times 10^3$
LED	15	$4 \times 10^3$
Alpha	20	$1 \times 10^4$
Afternoon		
Random trigger	10	$5 \times 10^3$
LED	40	$2.2 \times 10^4$
Alpha	20	$1 \times 10^4$
Neutron generator	12	$2.4 \times 10^4$
Cosmic	20	$9 \times 10^3$
CW Li $\gamma$ -ray	60	$3 \times 10^4$

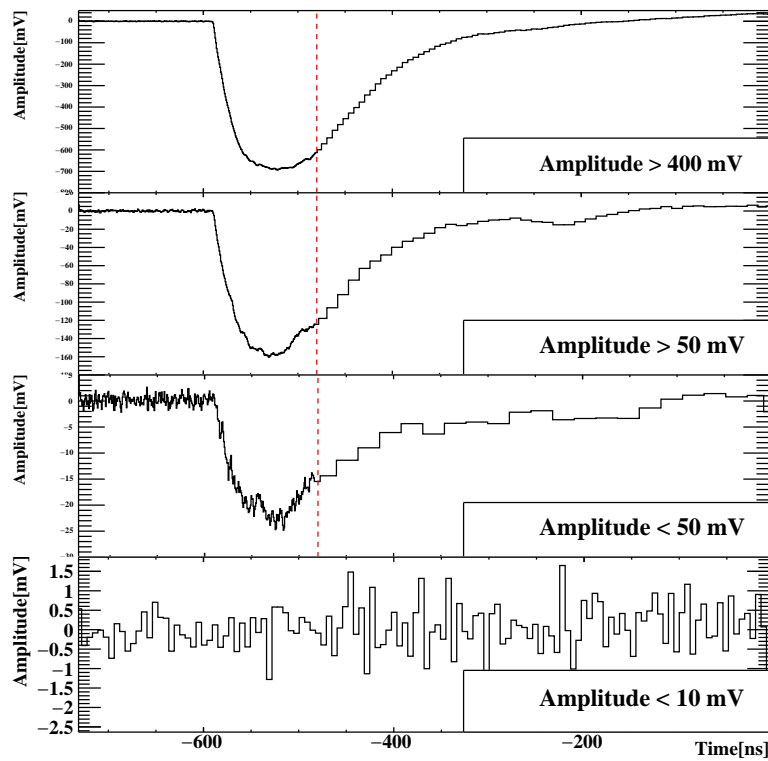


Figure 3.3: MPPC waveforms of a gamma-ray event with different rebinning configurations.

This issue was solved in two ways. One was data reduction by zero-suppression or rebinning of the waveform. The reduction of the data size from the readout of the LXe detector has a large impact because the data of the LXe detector readout is 40% of the whole data size due to a large number of readout channels. Though the rising part of the pulse is important to reconstruct the timing, the charge integration does not require fine sampling. Furthermore, the waveform with a small pulse is not used for the timing reconstruction so that the entire waveform can be rebinned. Therefore, the rebinning of the waveform was implemented as follows. The reduction power for each waveform was determined by the peak-to-peak amplitude of the waveform,  $A_{\text{pk}}$ .

- $A_{\text{pk}} < 10$  mV: fully rebinned by eight.
- $10 \text{ mV} < A_{\text{pk}} < 50$  mV: tail part of the waveform is rebinned by 32.
- $50 \text{ mV} < A_{\text{pk}} < 400$  mV: tail part of the waveform is rebinned by 16.
- $400 \text{ mV} < A_{\text{pk}}$ : tail part of the waveform is rebinned by 8.

The rebinned waveforms are shown in Fig. 3.3. The data size of the LXe detector was reduced to 40% of the original size.

The other solution was the improvement of the uniformity of the online reconstruction of  $E_\gamma$ . In the initial phase of the physics run, there was 10% non-uniformity on the online  $E_\gamma$  reconstruction, particularly in the  $v$  direction. The online  $E_\gamma$  threshold was set to a low value of  $\sim 40$  MeV at the center of the detector in order to secure  $\approx 100\%$  efficiency for  $> 48$  MeV gamma-ray for the whole acceptance of the detector. Since the event rate of accidental background decreases rapidly with gamma-ray energy, the higher and uniform online  $E_\gamma$  threshold help reduce the trigger rate without losing the efficiency of the  $\mu^+ \rightarrow e^+\gamma$  events. The online  $E_\gamma$  reconstruction was improved by the optimization of the weights used for the EGamma trigger, as described in Appendix B. Fig. 3.4 shows the  $v$  dependence of the EGamma trigger threshold before and after the optimization. The online  $E_\gamma$  threshold was raised up to 44 MeV without losing the trigger efficiency.

Table 3.2: Beam rate of 2021 run.

Period	Beam rate [ $10^7$ /s]	Purpose
15 Aug - 15 Oct	3.22	Detector commissioning
25 Sep - 15 Oct	3.22	Physics data acquisition
15 Oct - 28 Oct	1.92	Physics data acquisition
28 Oct - 2 Nov	3.24	Physics data acquisition
2 Nov - 10 Nov	4.01	Physics data acquisition
10 Nov - 18 Nov	4.93	Physics data acquisition
10 Nov - 18 Nov	$\sim 0.1$	Detector commissioning

These solutions were developed and implemented by late October. They made it possible to take physics data with the MEG trigger at the higher muon beam intensities up to  $5 \times 10^7$  /s. The beam rate was increased in steps up to  $5 \times 10^7$  /s until the end of the muon beam time, in

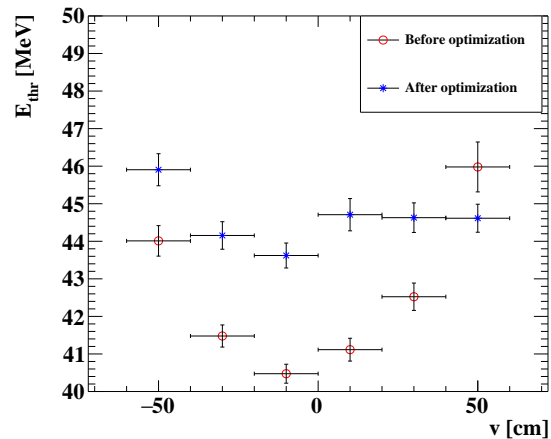


Figure 3.4: Online  $E_\gamma$  threshold as a function of the  $v$  position of the gamma ray. The threshold values before (red) and after the optimization (blue) are shown.

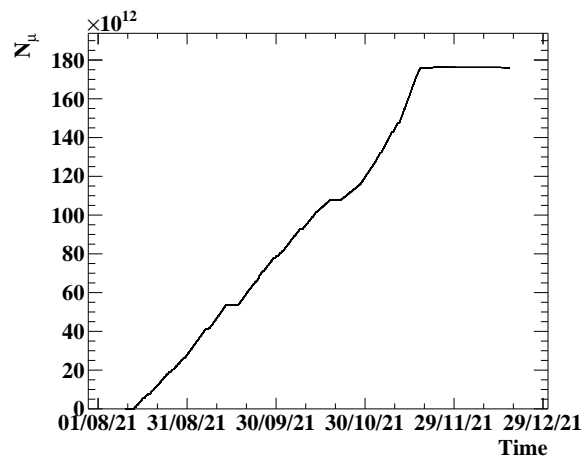


Figure 3.5: The time evolution of  $N_\mu$  in the 2021 run.

order to test the data collection and the stability and to study performance of the detectors at higher intensities. The beam rate in the 2021 run is summarized in Table 3.2. At the end of the muon beam time, a dataset was taken to understand the  $t_{e+\gamma}$  distribution with a reduced beam intensity. Fig. 3.5 shows the time evolution of the number of stopped muons  $N_\mu$  in the 2021 run.

The total live time in the 2021 physics run was  $2.9 \times 10^6$  s, which was 63% of the time elapsed from the beginning to the end of the physics run. The dead time came from the time dedicated to the calibration measurements, the dead time of the trigger, and the time to transition to a new set of the data-acquisition. The total live time in the 2021 physics run is 8.5% of the projected total live time in the MEG II experiment, assuming the physics data will be collected for another three years (2023–2025).

### 3.4 $\pi^0$ run

The goal of the 2021  $\pi^0$  run was to investigate the uniformity of the energy and time resolutions over the detector. As shown in Fig. 3.6, the readout of the inner face was divided into  $3 \times 8$  sections (“patches”). The data were collected for each patch position separately to obtain back-to-back two gammas from a  $\pi^0$  decay. The BGO detector was moved to the opposite direction of each patch position using rails in the  $z$  and  $\phi$  direction.

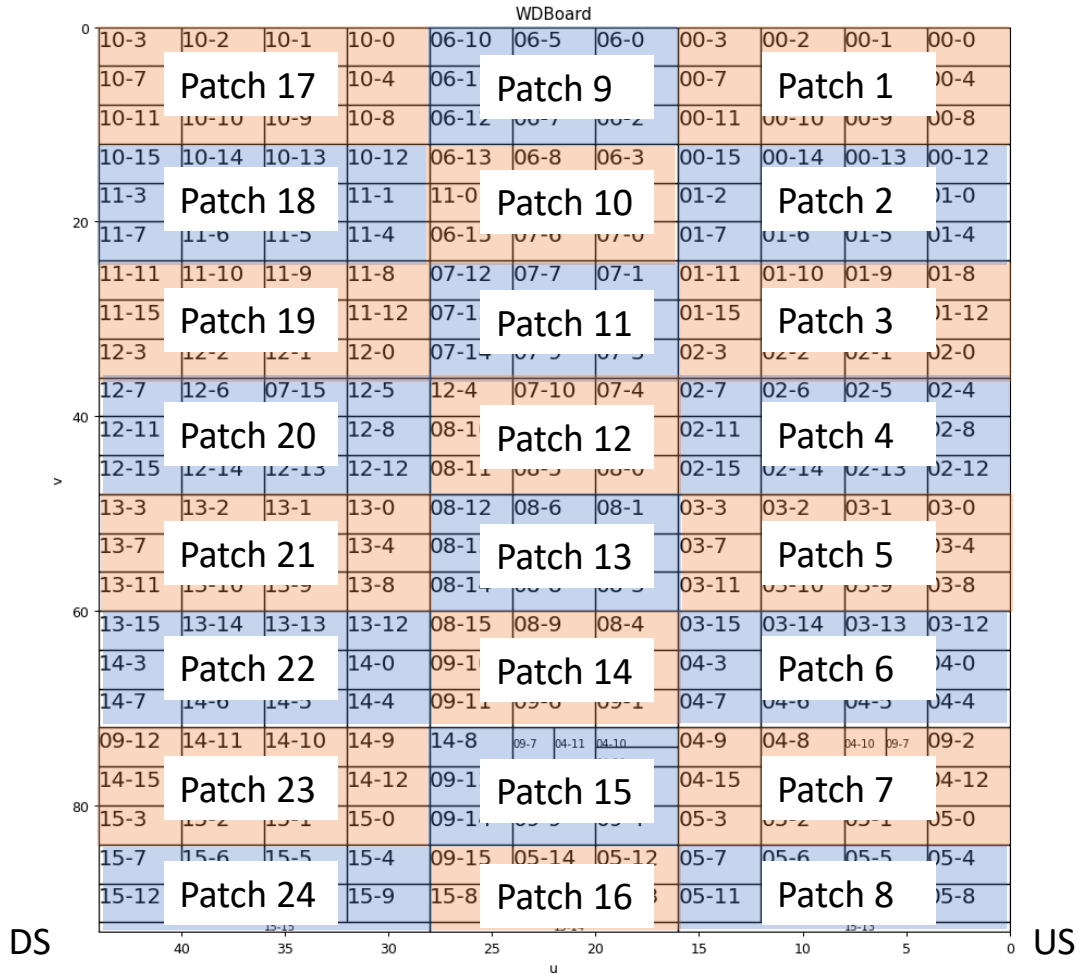


Figure 3.6: The 24 patches for the 2021  $\pi^0$  run. The size of patches in the middle row (Patch 9–16) is  $18 \times 18 \text{ cm}^2$ , and that of other patches is  $24 \times 18 \text{ cm}^2$ . The labels of the  $x$ - and  $y$ - axis are the column and row number of the MPPCs, respectively.

The difficulty of the 2021  $\pi^0$  run was the instability of the new  $\text{LH}_2$  target because it was not filled completely due to a shortage of cooling power. Fig. 3.7 shows the time variation of the temperature of the  $\text{LH}_2$  cell and the pressure of  $\text{gH}_2$  during the run. The plot indicates that the pressure did not fall down to 1.2 bar, which is the pressure when the cell is fully filled by  $\text{LH}_2$ . It took a long time (a few hours) to have a sufficient amount of  $\text{LH}_2$  in the cell to start data acquisition after switching to a new liquid helium bottle once per day. The lower  $\text{LH}_2$  level than

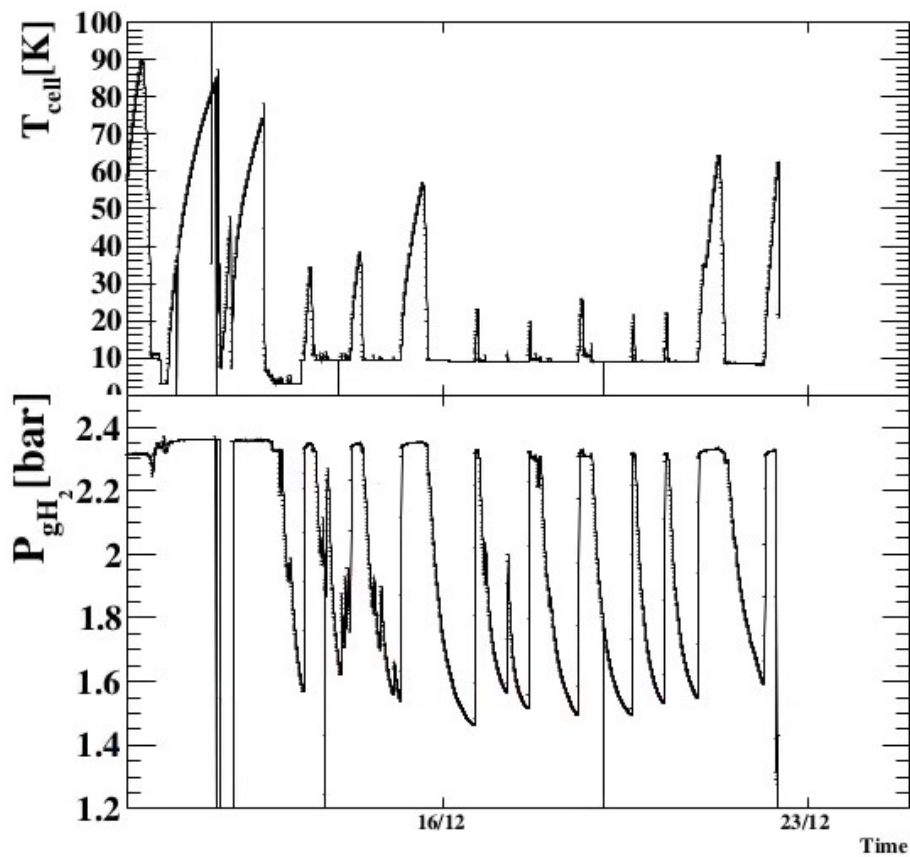


Figure 3.7: Temperature of LH<sub>2</sub> cell (top) and pressure of GH<sub>2</sub> volume (bottom). The target was being filled with LH<sub>2</sub> when the pressure of the GH<sub>2</sub> volume decreased. The pressure of the GH<sub>2</sub> volume jumped when the helium bottle was exchanged.

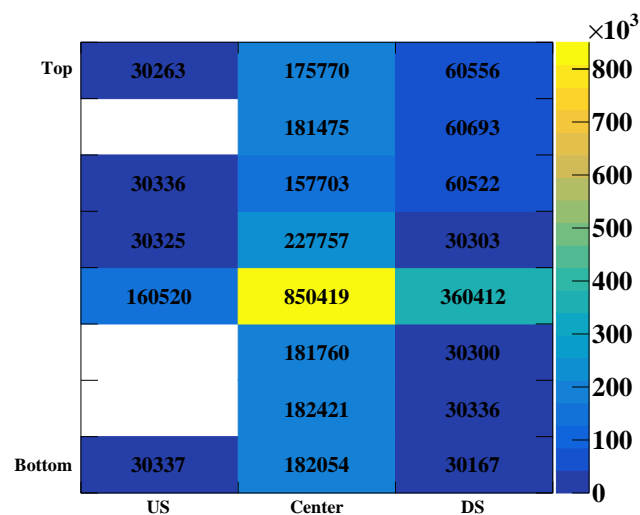


Figure 3.8: The number of events acquired for each patch in the 2021  $\pi^0$  run. No data were acquired for patches 2, 6, and 7 because of the experimental limitation.

the full coverage of the beam spot caused two difficulties on the  $\pi^0$  run. One is the increase of the background gamma rays from pions stopped at the back of the target, and the other is the decrease in the rate of the  $\pi^0 \rightarrow \gamma\gamma$  in the target. When this LH<sub>2</sub> target became ready for the  $\pi^0$  run, there was only one week left until the end of the beamtime.

For the reasons above, the original measurement plan to take sufficient data for all patches was forced to be changed. The  $\pi^0$  run was performed from 16th December to 22nd December based on the following priorities. The first priority was to measure the detector performance in the central part of the detector to confirm the previous performance evaluation carried out in 2020  $\pi^0$  run. The second priority was to measure the uniformity of the performance in the  $u$  and  $v$  directions. The middle row in the  $z$ -direction (Patches 9–16) was scanned first, then patches in the downstream side (Patch 17–24) and upstream side (Patch 1, 4–6, 8) were scanned subsequently. More data were collected for patches 5 and 21 to measure the uniformity of the detector response in the  $u$  direction. The  $\pi^0$  run ended before completing the scan for patches 2, 3, and 7. Fig. 3.8 shows the number of events obtained for each patch.

## Chapter 4

# Calibration and Monitoring of the Liquid Xenon Detector

### 4.1 Overview

For a long-term run, it is essential to keep the quality of a gamma-ray measurement by monitoring and calibrating the detector. The MEG II experiment is planning to take data for five months each year; the stability of the photosensors and the optical properties of LXe must be monitored throughout the beam time. The response of the photosensors can easily be time-varying due to radiation damage, operating conditions, and the optical properties of LXe, such as light yield and absorption. The light yield of LXe might change because it depends on the purity of LXe and must be monitored.

Fig. 4.1 represents the simplified reconstruction chain from the waveform of 4,760 photosensors to the position, timing, and energy of the gamma ray. The left-top part shows the analysis for each photosensor. The raw waveform data is processed to reduce the noise by subtracting noise templates defined for each readout channel. The corrected waveform is used to calculate the charge and timing of the pulse.

The number of photo-electrons  $N_{\text{phe}}$  and the detected number of photons  $N_{\text{pho}}$  are calculated from the integrated charge  $Q$  with an integration range of 150 ns as

$$N_{\text{phe}} = \frac{Q}{G \times F_{\text{EC}}} \quad (4.1)$$

$$N_{\text{pho}} = \frac{N_{\text{phe}}}{\epsilon_{\text{PD}}} \quad (4.2)$$

$$G = G_{\text{FE}} \times G_{\text{ps}} \quad (4.3)$$

where  $G_{\text{FE}}$  is the gain of the amplifier mounted on the frontend electronics (WaveDREAM board),  $G_{\text{ps}}$  is the gain of each photosensor,  $F_{\text{EC}}$  is the excess charge factor (ECF) that represents the fake amplification factor by correlated noises (crosstalk and after-pulsing) and  $\epsilon_{\text{PD}}$  is the PDE of the MPPCs or the QE of the PMTs.

The left-bottom part of Fig. 4.1 shows the reconstruction phase of the gamma ray. The position, energy, and timing of the incident gamma ray are reconstructed based on  $N_{\text{pho}}$  and

$N_{\text{phe}}$ , and the timing of the pulse at each photosensor.

The right panel of the figure summarizes the sensor calibration used for the analysis. In addition to the noise templates and the conversion factor from  $Q$  to  $N_{\text{pho}}$  and  $N_{\text{phe}}$ , the position and time offset of MPPCs are necessary to reconstruct the position and time, respectively. The gamma-ray position measurement requires that the positions of MPPCs are aligned with a precision of  $\sim 500 \mu\text{m}$  to take advantage of the good expected resolution of 2.5 mm. The alignment will be described in Sec. 4.7. The calibration of the time offset will be later described in Sec. 8.1.

As summarized in Table 4.1, various methods are prepared to calibrate the detector. Some of them are complementary, while others are redundant for backups and crosschecking. Calibration measurements were frequently carried out in the 2021 run (see Table 3.1).

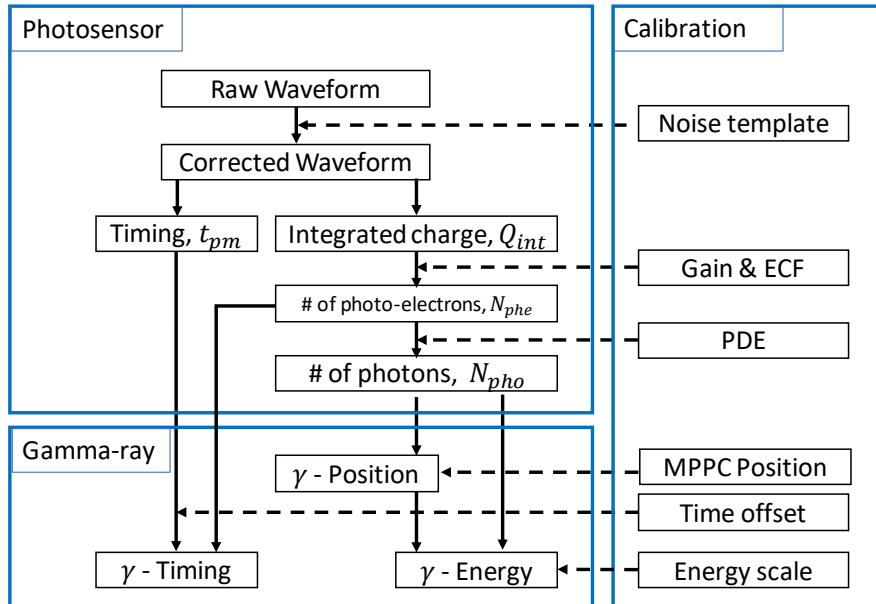


Figure 4.1: Reconstruction chain of gamma-ray. The left-top part shows the analysis of a photosensor. The raw waveform of a photosensor is corrected by noise templates and the corrected waveform is analyzed to calculate  $N_{\text{phe}}$ ,  $N_{\text{pho}}$ , and  $t_{\text{pm}}$ . The left-bottom part shows the gamma-ray reconstruction using the calculated  $N_{\text{phe}}$ ,  $N_{\text{pho}}$ , and  $t_{\text{pm}}$  of the photosensors. The right part shows the calibration parameters necessary for the analysis. The pileup analysis is not included in this figure for simplicity.

Table 4.1: Calibration measurements

Type	Purpose	Source	Energy
Random trigger	Noise calibration	-	0
LED	Gain calibration	blue light	460 nm
$^{241}\text{Am}$	PDE calibration	$\alpha$	5.5 MeV
Cosmic ray	Light-yield monitor	$\mu$	a hundred MeV
CW proton	Light-yield monitor	$\gamma$	17.6 MeV
Thermal neutron capture	Light-yield monitor	$\gamma$	9 MeV
$\pi^0$	resolution & efficiency measurement	$\gamma$	54.9–82.9 MeV
$^{57}\text{Co}$	MPPC Alignment	$\gamma$	124 keV

## 4.2 Noise reduction

Offline noise reduction for both low- and high-frequency noises is important to calculate the charge and timing of the pulse for each photosensor. A high-frequency noise can deteriorate the time resolution. A low-frequency noise whose wavelength is close to the charge integration time window (150 ns) affects the charge measurement, and it leads to worse energy and position resolutions. Fig. 4.2 shows the summed waveform of all the MPPC channels with and without the noise reduction described in this section. The high-frequency noise and the slope of the baseline as well as the offset are reduced.

For 2021 data, four types of noise reduction are applied. While the first three had been developed before the 2021 run, the last one is newly developed for the 2021 run data to suppress the noise identified after the installation of the full readout electronics.

### Cell pedestal

The voltage response of the DRS cells is calibrated by measuring multiple reference voltages within the dynamic range of the ADC. This DRS voltage calibration is applied online when the waveform data is read out and stored on hard disks. However, it is incomplete, and each DRS cell has a residual voltage offset (cell pedestal). This residual offset generates low-frequency noise in the DRS waveform. The template of the cell pedestal can be made from a random trigger dataset by accumulating the waveform as a function of the DRS cell, and it is subtracted from the data.

### High-frequency noise templates

A common clock signal with the same phase is distributed to WaveDREAM boards in order to align the timing of all boards. However, it generates high-frequency noise synchronously with the clock phase. This type of noise can be reduced by subtracting a noise template synchronized

to the clock timing. The template can be made from a random trigger dataset by accumulating the waveform with respect to the clock timing.

### Temperature dependent noise

The DRS cells have a small leakage current which depends on the temperature of the DRS chip. Because the voltage reduction due to the leakage current depends on the hold time until the readout, the temperature dependence of the leakage current shows up in the DRS waveform as a slope of the baseline. The relation between the slope and the temperature was measured and corrected with random trigger datasets collected at different temperatures.

### Start-cell dependent noise

The coherent noise correlated with the “startcell”, the first DRS cell of the waveform, was found at the beginning of the 2021 run. Fig. 4.3a shows that the reconstructed energy of the pedestal waveform has a clear dependence on the startcell. The reason for the dependence remains unknown, but the noise is reduced by making and subtracting a startcell-dependent waveform template. Fig. 4.3b shows the distribution of reconstructed energy for random trigger events. While the energy offset and spread are large ( $\mathcal{O}(1)$  MeV) without any correction, they are significantly reduced down to  $\mathcal{O}(10\text{--}100)$  keV by applying all types of correction. The RMS of the reconstructed energy distribution is 0.26 MeV with all corrections except for the startcell correction, and it is 0.08 MeV with all corrections. The spread corresponds to 0.16% of the signal  $\gamma$ -ray energy, and thus it is totally negligible for energy resolution.

Fig. 4.4 shows the stability of the offset and fluctuation of the reconstructed energy for the random trigger events. The energy spread was 0.15 MeV at maximum through the run, and the energy offset during the 2021 run had only 0.02 MeV as RMS (Fig. 4.5), which is negligible for the gamma-ray measurement.

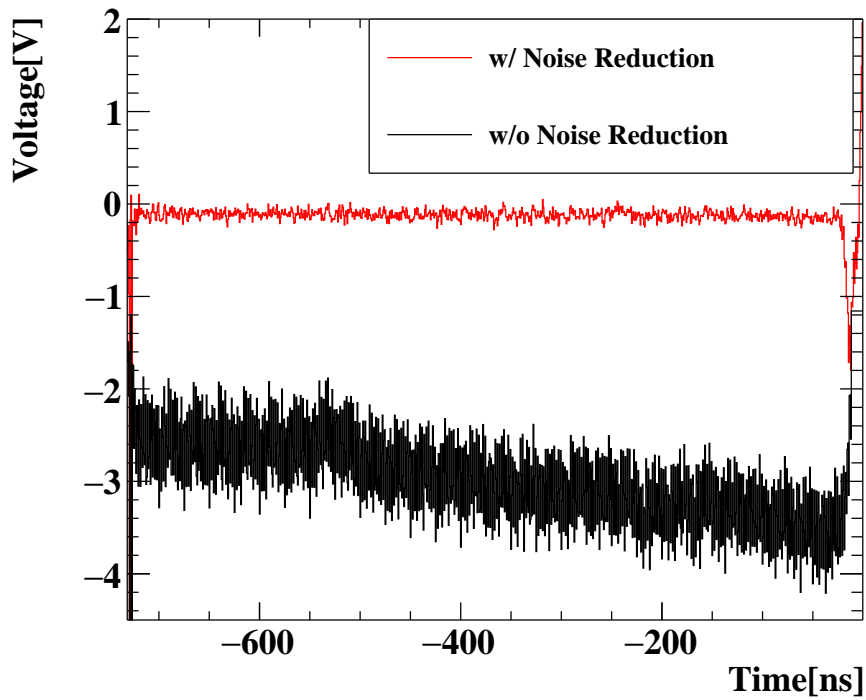


Figure 4.2: Summed waveform of MPPC channels with (red) and without (black) noise reduction. The raw waveform has an offset of 3 V, low- and high-frequency noises, but all of them are reduced by offline noise reduction. The edges of the waveform are noisy and not used for the waveform analysis.

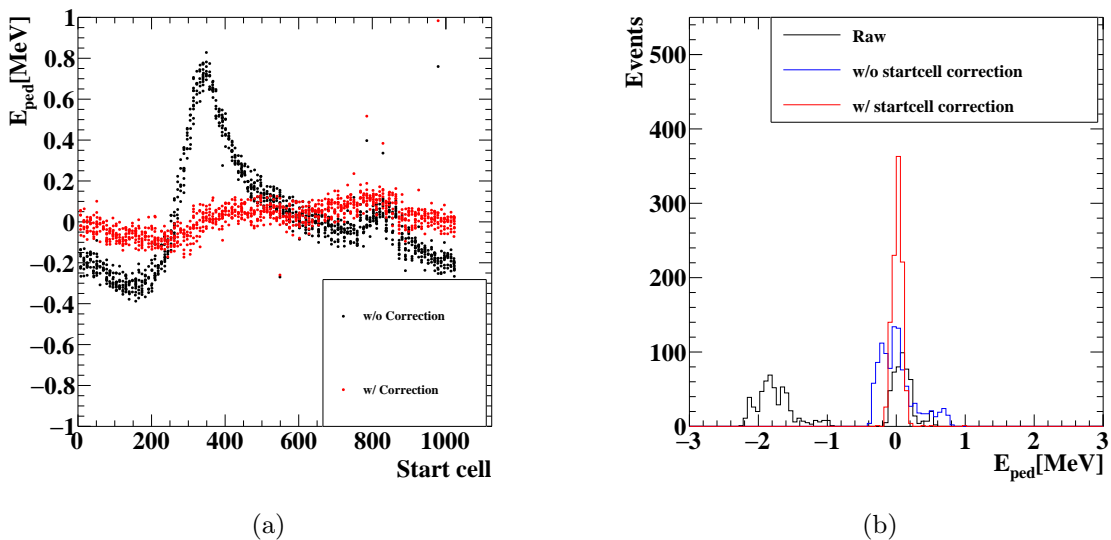


Figure 4.3: (a) Reconstructed energy for random trigger events as a function of the startcell. (b) The distribution of reconstructed energy for a single random trigger dataset. While the energy offset and spread are large without correction (black), they are significantly reduced with correction (red).

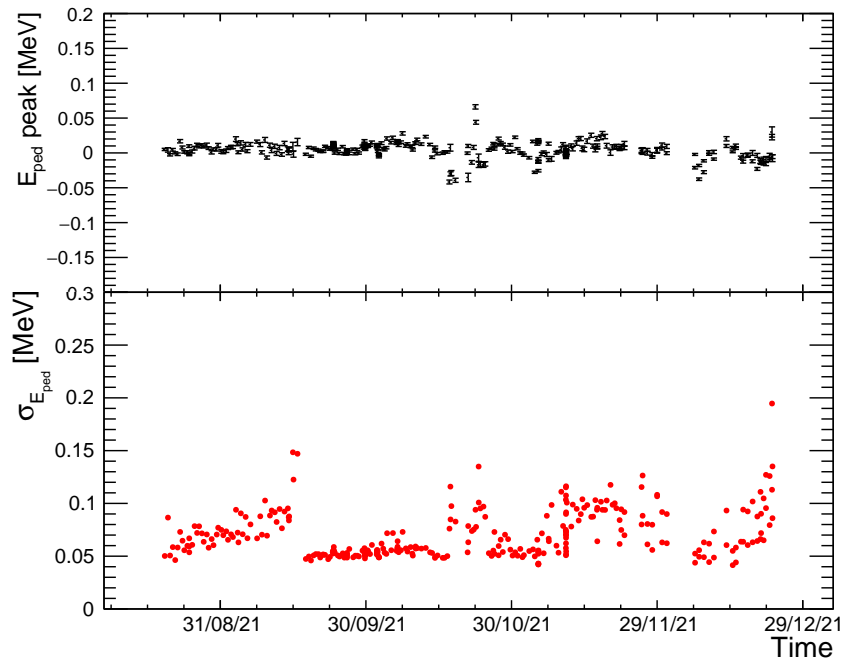


Figure 4.4: (top) Energy offset and (bottom) the pedestal fluctuation measured with random trigger datasets collected in the 2021 run.

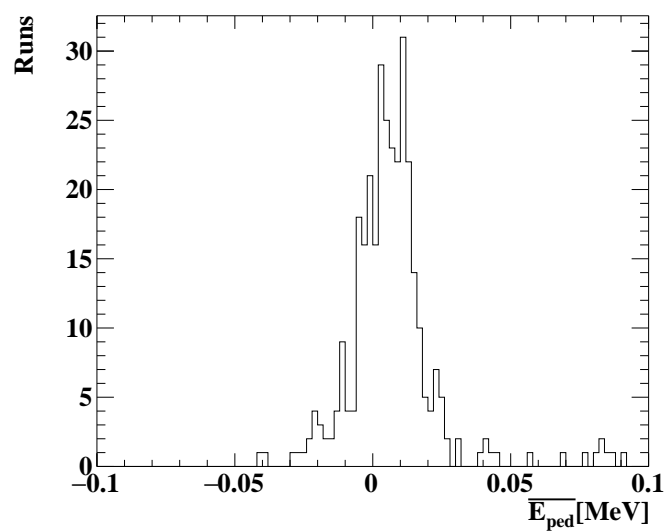


Figure 4.5: Energy offset measured with random trigger datasets collected in the 2021 run.

### 4.3 MPPC gain and ECF calibration

The gain and ECF of the MPPCs were measured by the charge spectrum for low-intensity LED light (Fig. 4.6). Two LEDs on the outer face at the same vertical position were flashed simultaneously in a run. The intensity of the LEDs was adjusted so that the MPPCs close to the LEDs detect about one photoelectron on average. This adjustment allows the charge spectrum of MPPCs to have both zero and one photoelectron peaks with a reasonable fraction of events. The amplifier gain of MPPC readout channels was set to 100 to have the best S/N ratio to separate the peaks.

The sum of two Gaussian functions was fitted to the zero and one photo-electron peaks, and the gain was estimated by the distance between the peaks. Since the S/N ratio with an integration range longer than  $\sim 120$  ns was not good enough to separate the two peaks, the total gain was estimated by the gain values from the analysis of the charge spectra with multiple short integration ranges. The integration range dependence of the gain values was fitted with an effective function,  $G(t) = G \times (1 - \exp(-(t - t_0)/\tau_{\text{fall}}))$ , where  $\tau_{\text{fall}}$  is the time constant of the tail of single photo-electron response and  $t_0$  is the timing offset, as shown in Fig. 4.7b. The scale of the function was regarded as the total gain for one photoelectron.

The ECF can be measured from the charge spectrum as,

$$F_{\text{EC}} = \bar{Q}_{\text{measured}}/Q_{\text{expected}} \quad (4.4)$$

$$= \bar{Q}_{\text{measured}}/G\lambda, \quad (4.5)$$

where  $\bar{Q}_{\text{measured}}$  is the average of measured charge. The expected charge without correlated noises  $Q_{\text{expected}}$  is the product of the gain  $G$  and the expected number of photo-electrons  $\lambda$ . If there is no correlated noise, the detected number of photoelectrons from an LED follows a Poisson distribution with the mean  $\lambda$ . Since the number of zero photoelectron events  $N_{\text{pedestal}}$  is not affected by the correlated noise,  $\lambda$  is estimated using the fraction of  $N_{\text{pedestal}}$  as,

$$N_{\text{pedestal}}/N_{\text{total}} = \exp(-\lambda) \rightarrow \lambda = -\log(N_{\text{pedestal}}/N_{\text{total}}), \quad (4.6)$$

where  $N_{\text{total}}$  is the total number of events in the charge spectrum. As we did for the gain,  $\lambda$  was estimated with the measured  $\lambda$  with the multiple short integration ranges as shown in Fig. 4.7a.

Fig. 4.8a shows the MPPC gain and ECF as a function of the serial number. The gain of the photosensor  $G_{\text{ps}}$  was  $(1.3\text{--}1.7)\times 10^6$  and had a small production lot dependence. The precision of the absolute gain measurement was 2.5% from the statistical uncertainty of the fitting of the spectrum. On the other hand, the ECF was 1.3–2.5 and had a large dependence on production lots. Even though a large variation was observed, this is still acceptable as long as we can measure it correctly. The dominant uncertainty of the ECF measurement came from the statistical uncertainty of  $\lambda$ , which was 1–5% depending on  $\lambda$ . It should be noted that the uncertainty of the absolute gain and ECF becomes the uncertainty of the PDE measurement, but they do not affect the conversion factor from the integrated charge to  $N_{\text{pho}}$  since the PDE was calibrated with the measured gain and ECF of each photosensor.

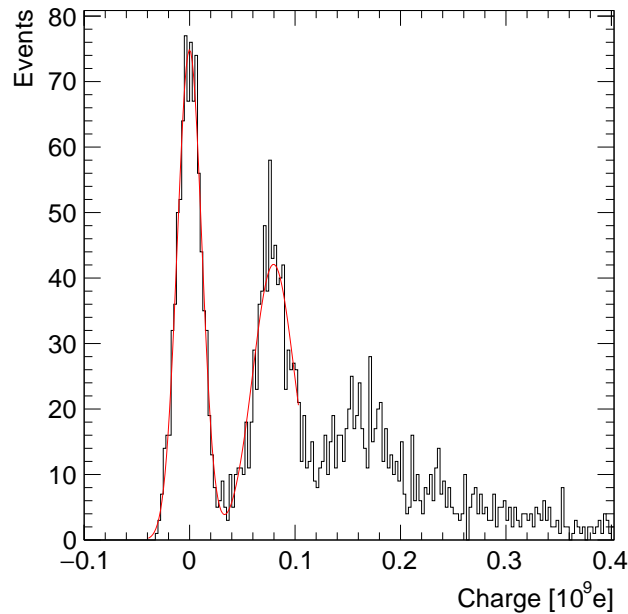


Figure 4.6: Charge spectrum under low-intensity LED light. The red line is the sum of the two Gaussian functions fitted to the data. The charge integration range is 70 ns.

The time variation of the gain and ECF was monitored by using the charge under stable LED light. The integrated charge under LED light can be described as

$$Q = N_{\text{pho}} \times G \times F_{\text{EC}} \times \epsilon_{\text{PD}}^{\text{vis}}, \quad (4.7)$$

where  $\epsilon_{\text{PD}}^{\text{vis}}$  is the detection efficiency for visible light. By using this charge, the relative time variation of the gain and ECF can be traced together with  $\epsilon_{\text{PD}}^{\text{vis}}$  with good precision, though it does not provide an accurate measurement of their absolute values since the number of incoming photons cannot be accurately estimated. A Gaussian function was fitted to the charge distribution of  $\mathcal{O}(10^3)$  LED events, and the mean value was used in order to monitor the sensor response for the visible light.

Fig. 4.9 shows the time variation of the average  $Q$  under the LED light in the 2021 run. The average  $Q$  of the MPPCs gradually decreased by 4% during the 2021 run. This decrease was correlated with the decrease of the PDE for the VUV light due to the radiation damage later discussed in Chapter 5. The sharp decrease of  $\sim 1\%$  in early November was due to the temperature instability as explained in Sec. 2.3.4.5. The temperature of LXe increased by 1 K, and the breakdown voltage increased by 0.8% because of the temperature dependence (56 mV/K). Since we applied a constant bias voltage to each MPPC, the increase in the breakdown voltage resulted in a decrease in the overvoltage. The MPPC response decreased by 1.3% since the overvoltage dependence of the ECF is more than linear, while the gain is proportional to the overvoltage.

Another observation was that the charge in the beam was smaller than that without the beam.

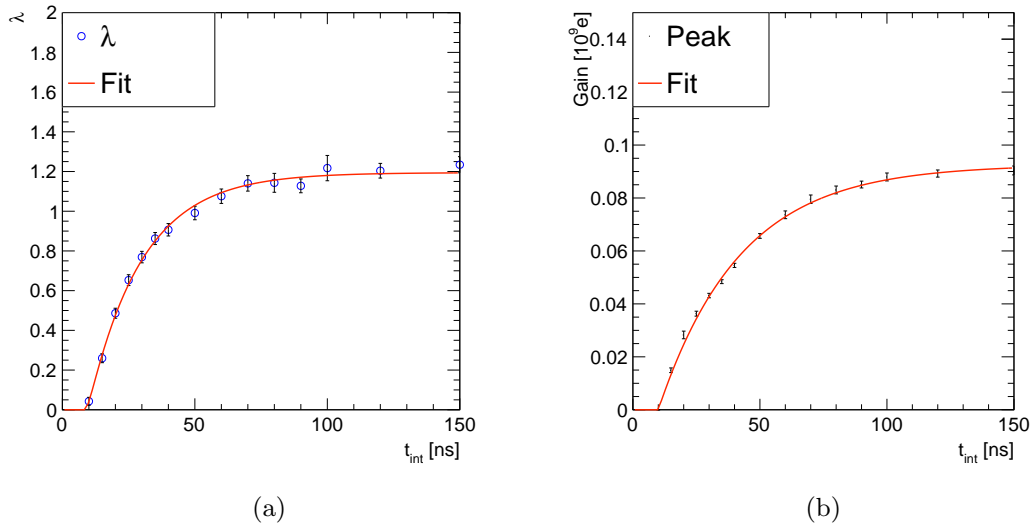


Figure 4.7: (a)  $\lambda$  and (b) gain estimated by the charge spectra with multiple integration ranges. Red lines show the fitting functions defined by a scale  $C$ , the time offset  $t_0$ , and a time constant  $\lambda$  as  $F(t) = C \times \{1 - \exp(-(t_{\text{int}} - t_0)/\lambda)\}$ .

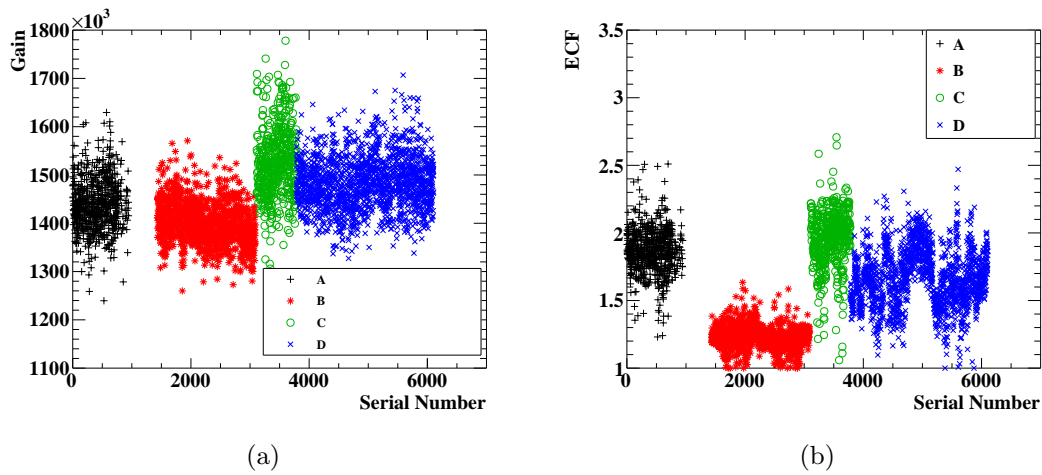


Figure 4.8: Measured (a) gain and (b) ECF of MPPCs as a function of the serial number. The colors of each point show the production lot of the MPPC.

The effect was 0.2% under  $3 \times 10^7/s$  muon beam and 1.0% during the  $\pi^0$  run. This is likely due to the voltage drop by the induced current under a high-intensity environment. Fig. 4.10 shows the current of one MPPC channel in the center of the entrance face. The current value was 0.5–1.4  $\mu\text{A}$  depending on the beam intensity in the muon beam period and 2–2.5  $\mu\text{A}$  in the  $\pi^0$  run. The effect of the induced current on the gain was foreseen in the design phase, and a small resistance of 2 k $\Omega$  in the series connection with the MPPC chip was adopted to reduce it [47]. The measured dependence in the actual detector was 0.2–0.4%/ $\mu\text{A}$ , as was expected.

The time variation of  $Q$ , as shown in Fig. 4.9, was used to correct the time variation of gain

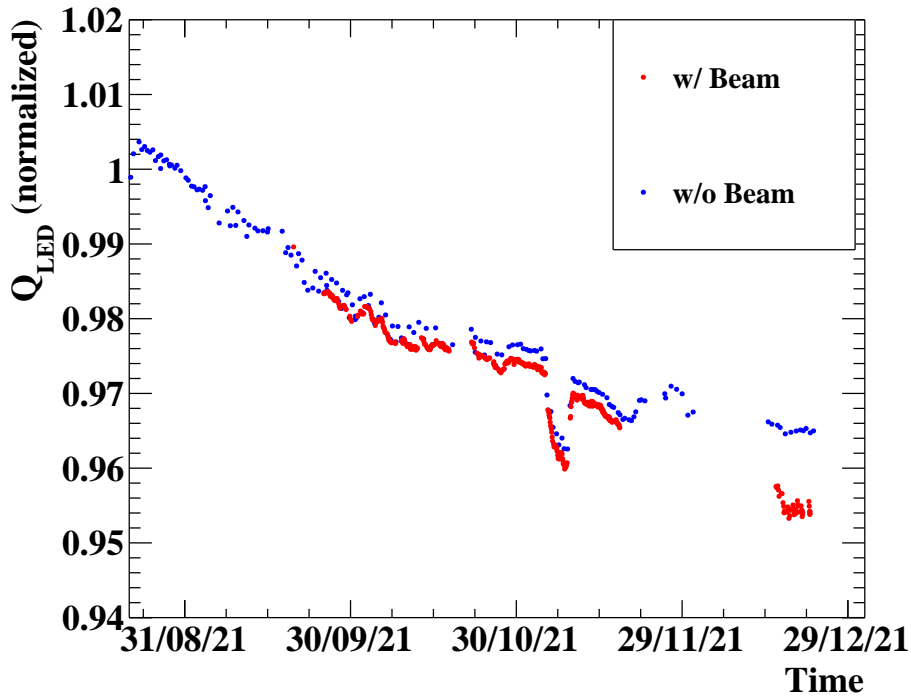


Figure 4.9: Average MPPC charge under LED light of a fixed intensity with and without beam (red and blue, respectively) as a function of time. The average of all MPPCs is shown. The gradual decrease in charge is due to the decrease in the  $\epsilon_{\text{PD}}^{\text{vis}}$ . The sharp drop at the beginning of November is due to the temperature instability.

and ECF of each photosensor. The time variation of  $Q$  is normalized with the absolute gain measured in the middle of the 2021 run. In this method, the time variations of gain and ECF are corrected together with the  $\epsilon_{\text{PD}}^{\text{vis}}$ .

After all the gain calibrations were applied, the peaks of LED events mixed in physics data-taking showed good stability. Fig. 4.11a–4.11b show the time variation and distribution of the LED peak position of  $N_{\text{phe}}$  of a single MPPC, and Fig. 4.12a and 4.12b show those of the sum for all MPPCs. The sigma of the distribution was 0.2% and 0.02% for a single MPPC and all MPPCs, respectively. This is good enough to achieve <0.5% stability so that the stability does not limit the energy resolution.

## 4.4 PMT gain calibration

The PMT gain was calibrated by using the photo-electron statistics of LED light. The average of the integrated charge can be written as

$$\bar{Q} = G \cdot e \cdot \bar{N}_{\text{phe}}, \quad (4.8)$$

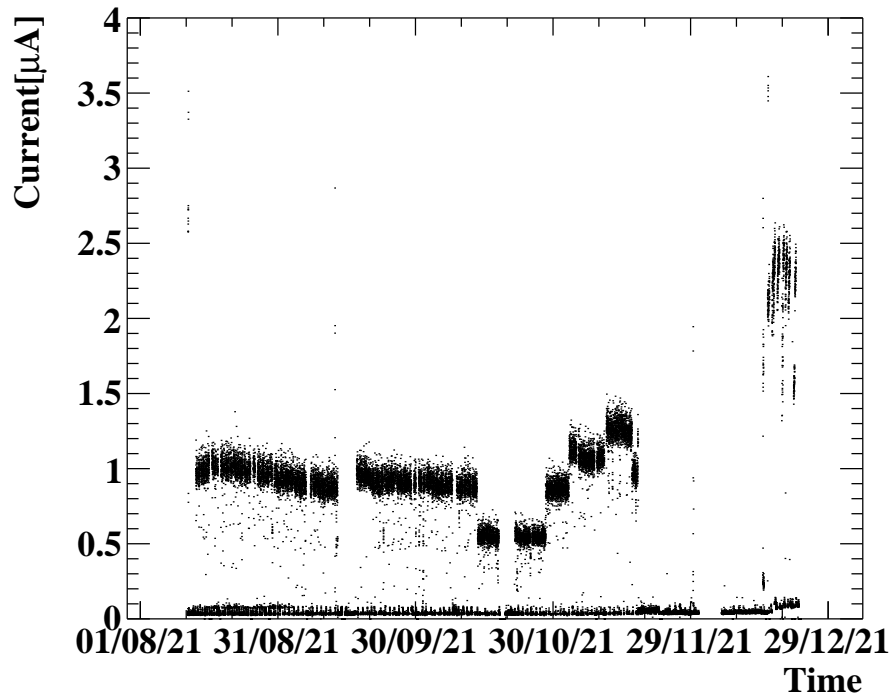


Figure 4.10: The readout current of an MPPC in the central region of the inner face as a function of time in the 2021 run. The readout current was  $0.5 \mu\text{A}$ – $1.5 \mu\text{A}$  in the muon beam period depending on the muon beam rate. The current in the  $\pi^0$  run was 2.0–2.5%. The current without beam was  $0.05 \mu\text{A}$ .

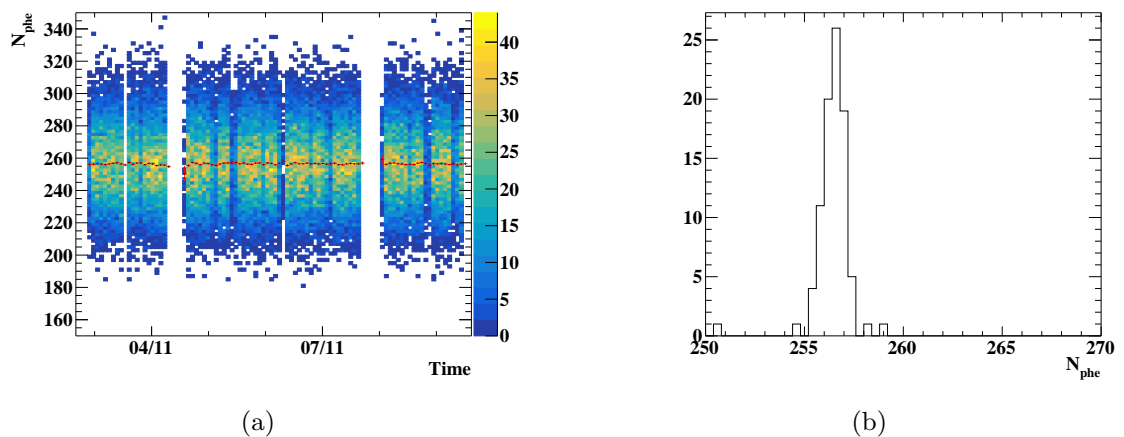


Figure 4.11: (a) The time variation and (b) distribution of LED peaks of a single MPPC in the 2021 physics run.

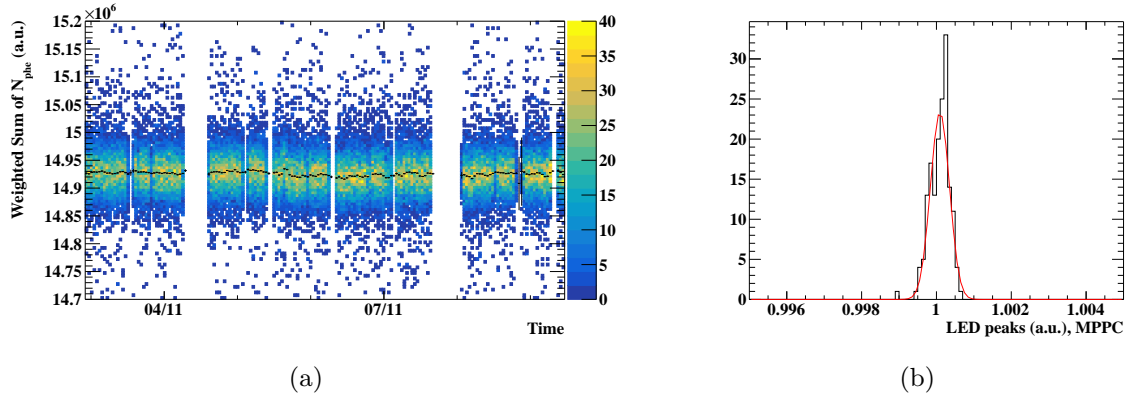


Figure 4.12: (a) The time variation of LED peaks mixed in the 2021 physics run. (b) Distribution of LED peaks in the 2021 physics run. A Gaussian fit function with 0.02% sigma is shown in red line.

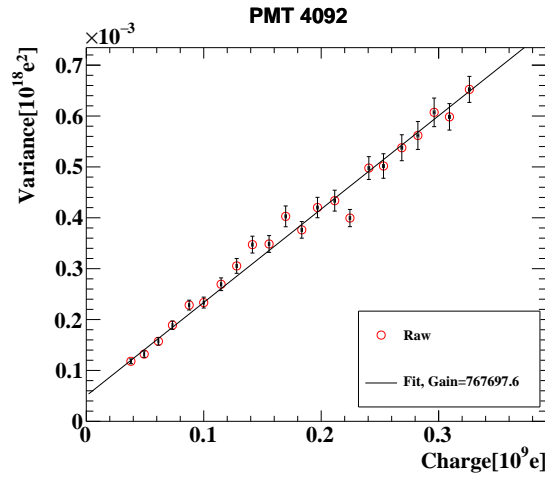


Figure 4.13: Measured relation between the variance and mean of the charge spectrum under LED light with various intensity.

where  $\bar{N}_{\text{phe}}$  is the average number of photoelectrons, and  $e$  is the elementary charge. The variance of the charge distribution can be expressed as

$$\sigma_Q^2 = (G^2 + \sigma_G^2) \cdot e^2 \cdot (\sigma_{\text{phe}}^2 + \sigma_{\text{LED}}^2) + \sigma_0^2 \quad (4.9)$$

where  $\sigma_0$  is the noise of the readout electronics,  $\sigma_{\text{LED}}$  is the fluctuation of the LED pulsar output, and  $\sigma_G$  is the resolution for a single photo-electron. Assuming that the gain fluctuation is small with respect to the gain ( $\sigma_G \ll G$ ), that the LED is sufficiently stable ( $\sigma_{\text{LED}} \ll \sigma_{\text{phe}}$ ), and that the distribution of the number of detected photo-electrons  $N_{\text{phe}}$  follows a Poisson distribution,  $\sigma_{\text{phe}}^2 = \bar{N}_{\text{phe}}$ , the variance of the charge distribution  $\sigma_Q^2$  can be described as follows.

$$\sigma_Q^2 = G^2 \cdot e^2 \cdot (\sigma_{\text{phe}}^2) + \sigma_0^2 \quad (4.10)$$

$$= G^2 \cdot e^2 \cdot \bar{N}_{\text{phe}} + \sigma_0^2 \quad (4.11)$$

$$= G \cdot e \cdot \bar{Q} + \sigma_0^2 \quad (4.12)$$

Eq. 4.12 means that the variance  $\sigma_Q^2$  can be expressed as a linear expression of the mean of the charge  $\bar{Q}$ . The charge distribution was measured at several LED intensities, and the mean and variance are plotted as shown in Fig. 4.13. The absolute PMT gain can be calculated by fitting this correlation between the mean and variance. This calibration method is called “intensity scan”.

At the beginning of the 2021 run, the gains were adjusted to  $8 \times 10^5$  for the following reasons,

- Equalize the PMT performance, such as timing response.
- Keep a pulse height within the dynamic range of the readout electronics.

The bias voltage of each PMT was determined by the relation between the voltage and the gain,  $G \propto (V - V_0)^k$ , where  $V_0$  was 100 V, and  $k$  was 9.5. These values were empirically determined from the experience of the commissioning runs. Fig. 4.14a and 4.14b show the distribution of the PMT gain and the bias voltage after the adjustment, respectively. The gain distribution has the mean value of  $8.4 \times 10^5$  and 3% standard deviation after the adjustment.

Fig. 4.15 shows the time variation of the PMT gain without the beam measured in two methods, the intensity scan and the charge under stable LED light. The absolute gain from the intensity scan decreased by 14% through the beam time, while the charge for LED light decreased by 11%. The reason for the discrepancy might be the systematics of the intensity scan. If  $\sigma_G$  or  $\sigma_{LED}$  has a non-negligible impact on the gain calibration, it could explain the discrepancy.

The time variation of the gain was corrected by the time variation of charge, and the absolute value was normalized by the absolute gain measured by the intensity scan in the middle of the 2021 run. Fig. 4.16a shows the time variation of the LED peaks mixed in the physics run after the gain correction. The fluctuation of the LED peaks was only 0.02%, as shown in Fig. 4.16b.

As mentioned in Sec. 2.3.3, the impact of the gain shift during the data-taking was negligible in the 2021 run because the data-taking of the physics run started a few minutes after the beam blocker was opened, while the main time variation of the gain shift has  $\mathcal{O}(10)$ s time constant. As shown in Fig. 4.17, the time variation of the number of photons collected by PMTs  $N_{PMT}$  after opening the beam blocker is just 0.03%, which is acceptable. Therefore, no correction is applied to correct the effect of the gain shift.

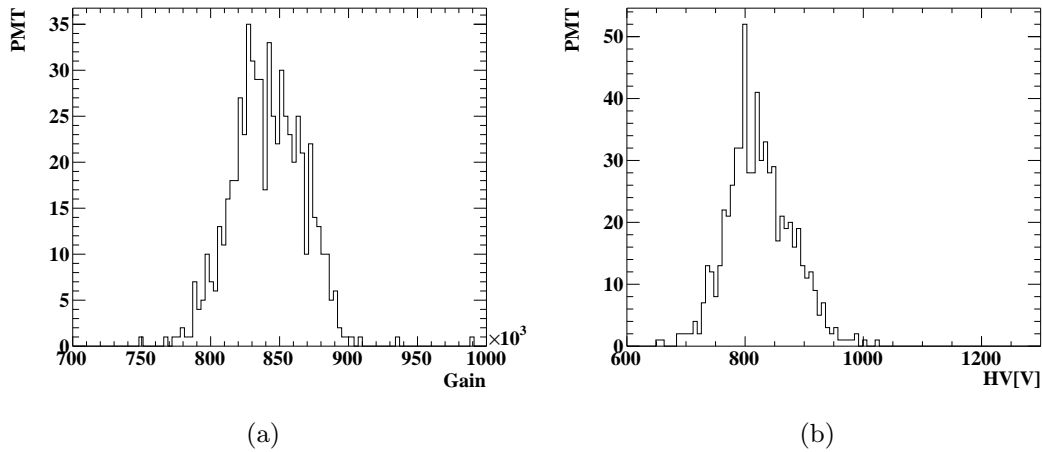


Figure 4.14: (a) Gain and (b) bias voltage of PMTs at the beginning of the 2021 run. The gain of all PMTs is adjusted to be  $8.4 \times 10^5$ .

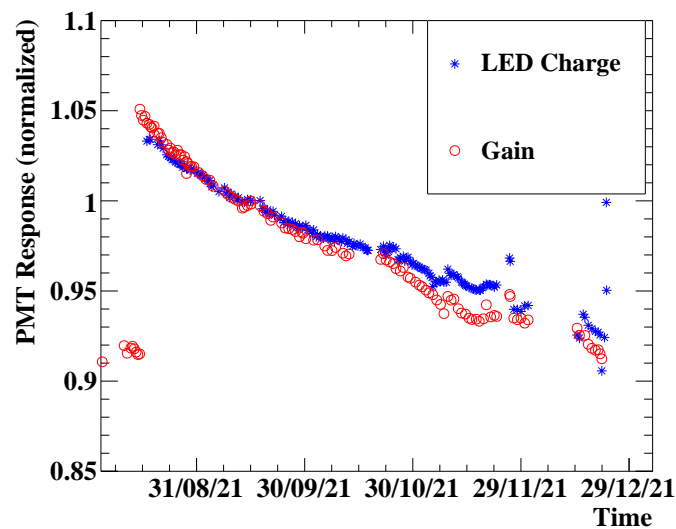


Figure 4.15: PMT gain measured with the intensity scan (red) and charge (blue) as a function of time. The average values of all PMTs are shown. The difference between the two measurements is considered to be due to the systematic error of the gain measurement by the intensity scan.

## 4.5 PDE and QE calibration

The PDE of MPPCs and the QE of PMTs were estimated by using the  $^{241}\text{Am}$  sources. Since the positions of the installed sources and the energy of the emitted alpha ray are known, the number of photoelectrons observed by each photosensor can be calculated by means of MC simulation. The PDE and QE were extracted from the comparison between the measured photoelectrons and the calculated ones by the MC. The wavelength of scintillation light from alpha particles is the same as that from gamma rays. Thus, the estimated PDE and QE from

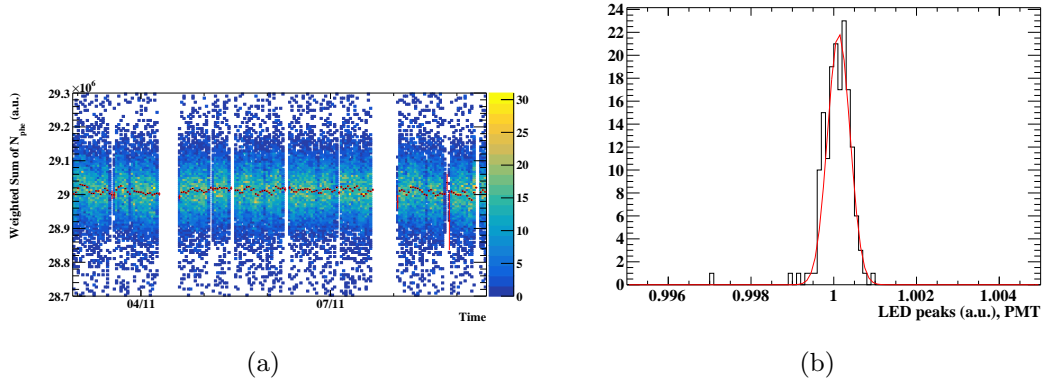


Figure 4.16: (a) LED signal amplitude of PMTs during the physics run and the time variation of the peak (red) and (b) the distribution of the LED peak.

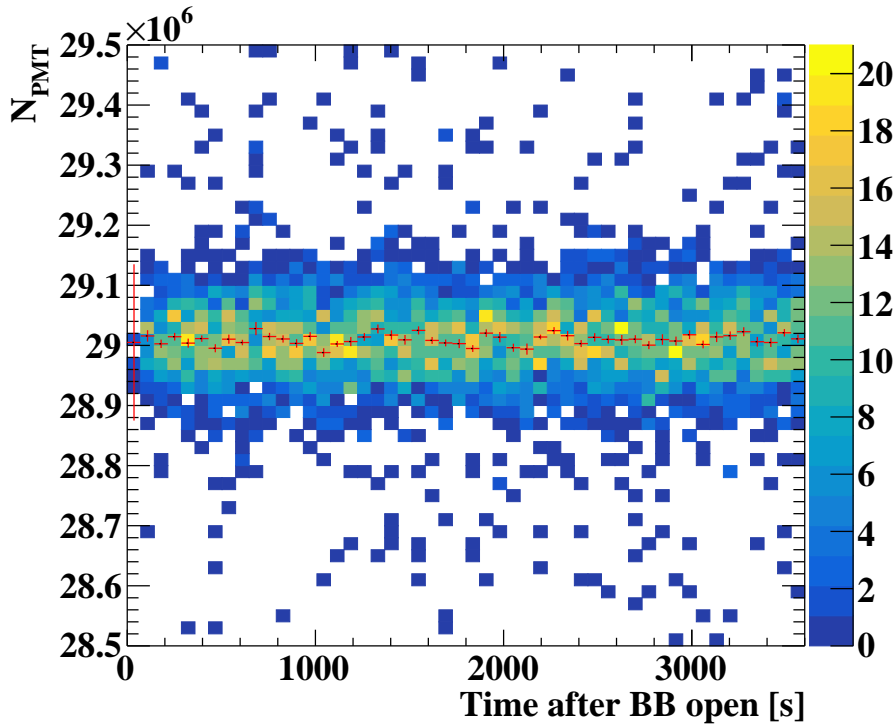


Figure 4.17:  $N_{\text{PMT}}$  of the LED events as a function of the elapsed time after the beam blocker was open. The mean value of the  $N_{\text{PMT}}$  distribution in the finite period is shown in red.

alpha sources can be directly used for the gamma-ray reconstruction.

The main background of the calibration is cosmic-ray events. A particle identification was carried out by pulse shape discrimination. Fig. 4.18 shows the ratio between the charge and amplitude of the summed waveform of all PMTs. The events whose ratio is larger than a given threshold were rejected as they originated from cosmic-ray.

The source spot that generated the  $\alpha$ -ray in each event was identified with the light distribution of the PMTs. The wire of the source was determined by comparing the total number of detected

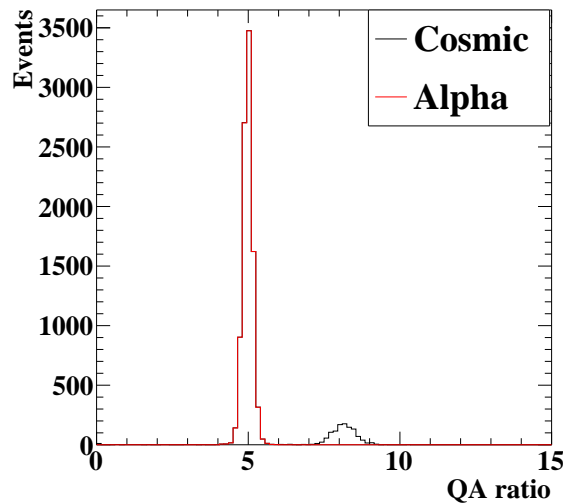


Figure 4.18: Ratio between charge and amplitude of the summed waveform of all PMTs in a dataset collected by the alpha trigger. The peak at 5 (red) corresponds to the  $\alpha$ -ray events, and that at 8 (black) corresponds to cosmic-ray events.

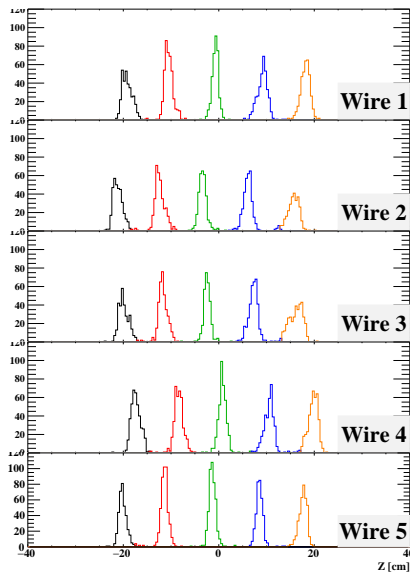


Figure 4.19: Reconstructed  $z$  position of five alpha source spots for wire 1 (top)–5 (bottom). The distribution of five source spots is shown in different colors.

photons in 32 PMTs in the downstream and upstream faces around each wire. Then, the spot was identified with the average  $z$ -position of the PMTs weighted by  $N_{\text{pho}}$ . Fig. 4.19 shows the reconstructed  $z$  position for each wire. Five peaks corresponding to the source spots on a wire were well separated for all the wires, indicating that the spot can be uniquely identified.

Fig. 4.20 shows the correlation between  $\overline{N}_{\text{phe,Data}}$ , the average number of detected photoelectrons in data, and  $\overline{N}_{\text{phe,MC}}$ , that in a dedicated MC simulation for each source. The PDE

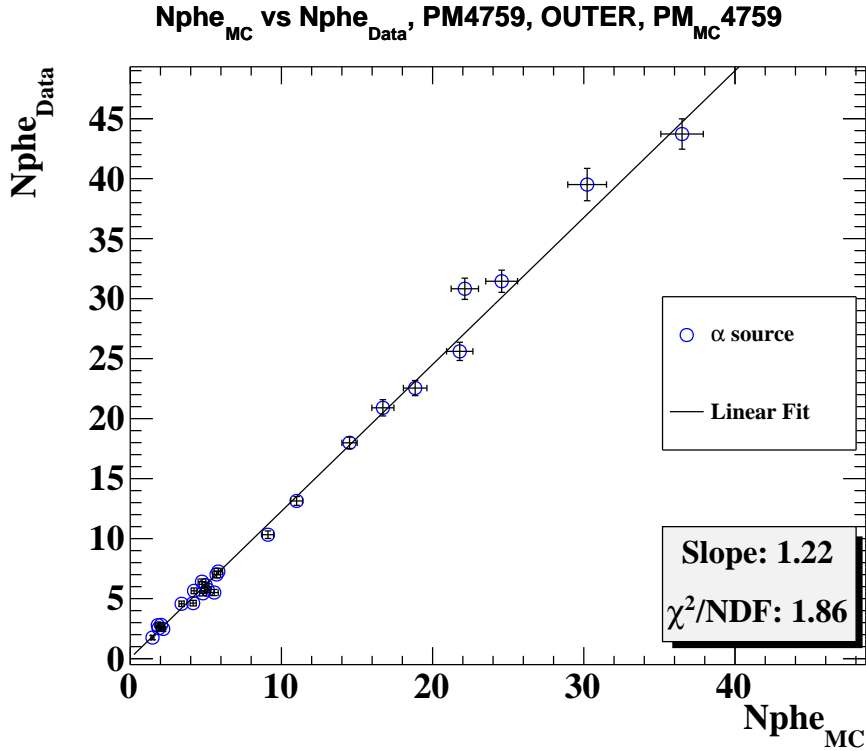


Figure 4.20: Correlation of  $N_{\text{phe,Data}}$  and  $N_{\text{phe,MC}}$  for a PMT. Each data point corresponds to a source spot. The slope of the linear fit function was used for the PDE calibration.

in data  $\epsilon_{\text{PD}}^{\text{Data}}$  is calculated as,

$$\epsilon_{\text{PD}}^{\text{Data}} = \epsilon_{\text{PD}}^{\text{MC}} \times R \times F_{\text{LY}}, \quad (4.13)$$

where  $R$  corresponds to the slope of the correlation between  $\overline{N}_{\text{phe,Data}}$  and  $\overline{N}_{\text{phe,MC}}$  and  $F_{\text{LY}}$  is the light yield of liquid xenon.  $\epsilon_{\text{PD}}^{\text{MC}}$  was 0.12 for MPPCs and 0.16 for PMTs in the MC simulation.  $F_{\text{LY}}$  was adjusted so that the mean of all PMT QEs takes 0.16.

There are several sources of the uncertainties of the PDE (QE) measurement as summarized in Table. 4.2. The uncertainty of the gain and ECF is a source of the systematic uncertainty because it becomes the uncertainty of the  $\overline{N}_{\text{phe,Data}}$ . The reflection at the walls increases  $N_{\text{phe}}$  of each photosensor. Hence, the difference in the reflectivity of the walls between data and MC simulation becomes the systematic error of the PDE (QE) and light yield. In particular, the PMT holder covers a large area of the wall, and its reflectivity has a large impact on light distribution. The reflectivity was estimated as  $50 \pm 10\%$  by comparison of the light distribution between the data and simulation. The light distribution of several sets of MC simulations with different reflectivities was compared with the measured light distribution, and the simulation with 50% reflectivity reproduced the measured distribution best. The uncertainty of the PDE (QE) and the light yield from the uncertainty of the reflectivity was estimated to be 5%.

Another source of systematic uncertainty is the absorption of scintillation photons in LXe. The absorption induced by impurities decreases  $N_{\text{phe}}$ , particularly when a photosensor is distant from the source spots. Fig. 4.21 shows the ratio between  $\overline{N}_{\text{phe,Data}}$  and  $\overline{N}_{\text{phe,MC}}$  as a function

of the distance between a  $^{241}\text{Am}$  source spot and a photosensor. The distance dependence indicates that the absorption in data was not significant with respect to MC simulation with a long absorption length (500 cm). The increased  $R$  for distant sources ( $>80$  cm) is likely due to the difference in the reflectivity of the wall between data and MC. The uncertainty of the light yield from the absorption is  $<1\%$  and negligible with respect to the uncertainty from the reflection.

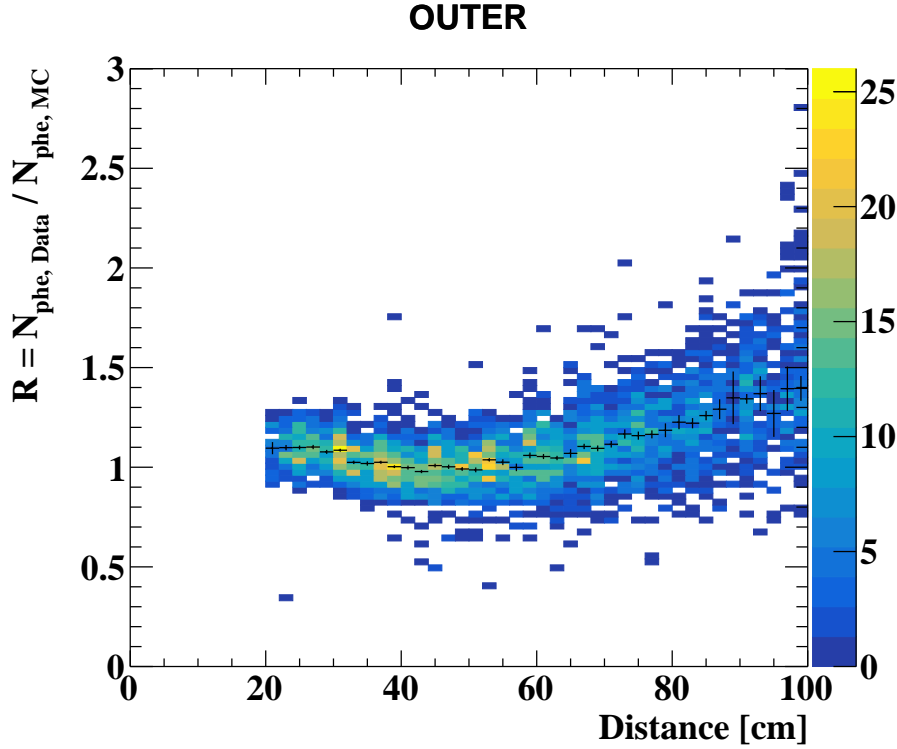


Figure 4.21: Ratio between  $\bar{N}_{\text{phe,Data}}$  and  $\bar{N}_{\text{phe,MC}}$  as a function of the distance between  $^{241}\text{Am}$  source and a photosensor. PMTs on the outer face and 25 sources are overlaid. The black points show the distance dependence of the averaged ratio.

Though the uncertainties of the light yield and the PDE (QE) are large, it does not become a problem for the gamma-ray measurements, because the energy scale and the non-uniformity of the reconstructed energy will be determined and corrected by using the gamma-ray dataset.

Fig. 4.22 shows the PDE distribution of all channels in the development view, and Fig. 4.23a and Fig. 4.23b show the distribution of the PDE of MPPCs and PMTs, respectively. The average PDE of MPPCs at the end of the 2021 run was 0.06. The low PDE with respect to the reported PDE in the phase of the development (0.18–0.20) [47] is due to the unexpected radiation damage, and it will be discussed in Chap. 5. The large position dependence comes from the systematic errors of the PDE calibration and the position dependence of the radiation damage. The MPPCs used until the 2020 run are surrounded by red lines in Fig. 4.22 and had been damaged particularly.

Fig. 4.24 shows the QE of the PMTs as a function of the  $y$  position of PMTs. While it is

Table 4.2: Uncertainties of PDE (QE) measurement.

Source	Relative uncertainty
Gain	2.5% (MPPC) / 2% (PMT)
ECF	1–5% (MPPC)
Reflection at the walls	5%
Absorption	$\mathcal{O}(1)\%$
Liquid level	$\mathcal{O}(1)\%$ ( $y < 50$ cm) / $\mathcal{O}(10)\%$ ( $y > 50$ cm)
Light yield	5%
Total uncertainty	10%

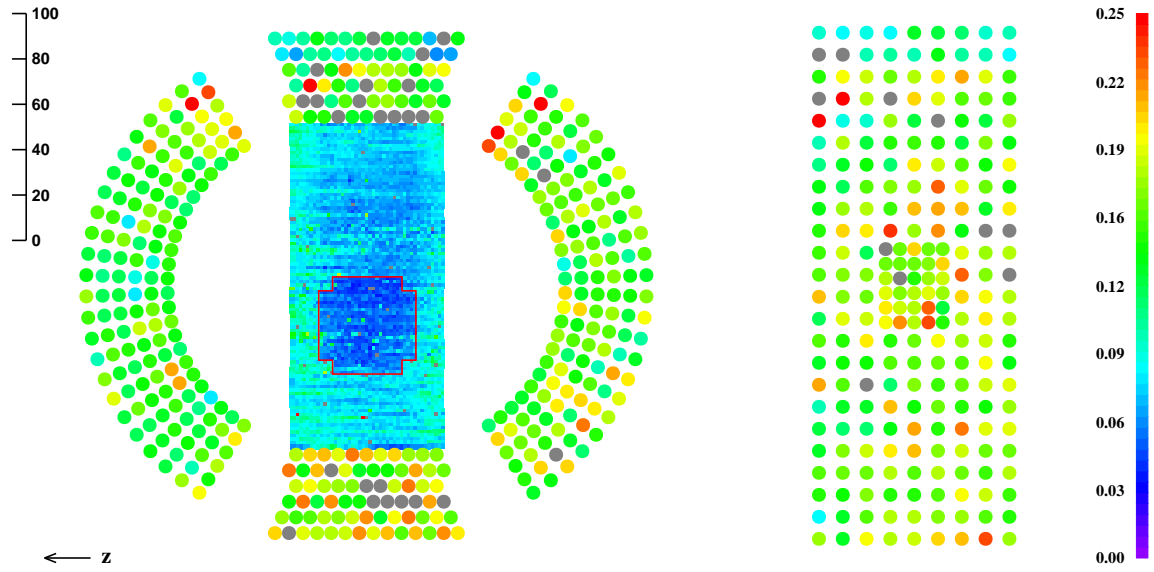


Figure 4.22: PDE (QE) distribution at the end of the 2021 run in the development view. The MPPCs surrounded by red lines were used until the 2020 run.

generally uniformly distributed along the  $y$ -axis, a lower QE is measured for PMTs at  $y > 83$  cm. Furthermore, the QE of some PMTs slightly below 83 cm was up to twice higher than other PMTs. This indicates that the liquid surface (the boundary surface with gas xenon) was around  $y=83$  cm. The reflection at the liquid surface due to a mismatching of the refractive index between LXe (1.69) and gXe ( $\sim 1$ ) reduced the number of photons detected by the PMTs above the liquid surface. It also explains that the QE of the PMTs slightly below the liquid surface was high, as the reflection increased the number of detected photons. Since the measured QE for PMTs close to the liquid level had a relatively large systematic error up to 10%, the PMTs with  $y > 50$  cm were excluded from the PMTs for the light yield normalization.

Fig. 4.25a shows the time variation of the average MPPC PDE during the 2021 run. The average MPPC PDE gradually decreased from 0.082 to 0.060. Considering the monitoring with gamma rays or cosmic rays indicated that the total number of photons detected by the MPPCs increased during the beam time, the degradation measured with alpha might be overestimated.

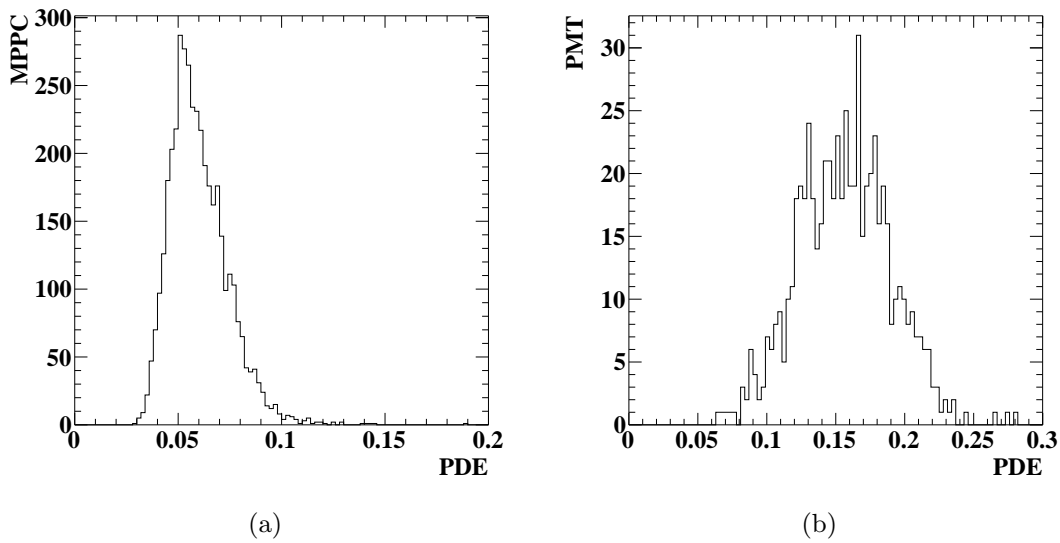


Figure 4.23: (a) Distribution of the PDE of the MPPCs and (b) the QE of the PMTs at the end of the 2021 run.

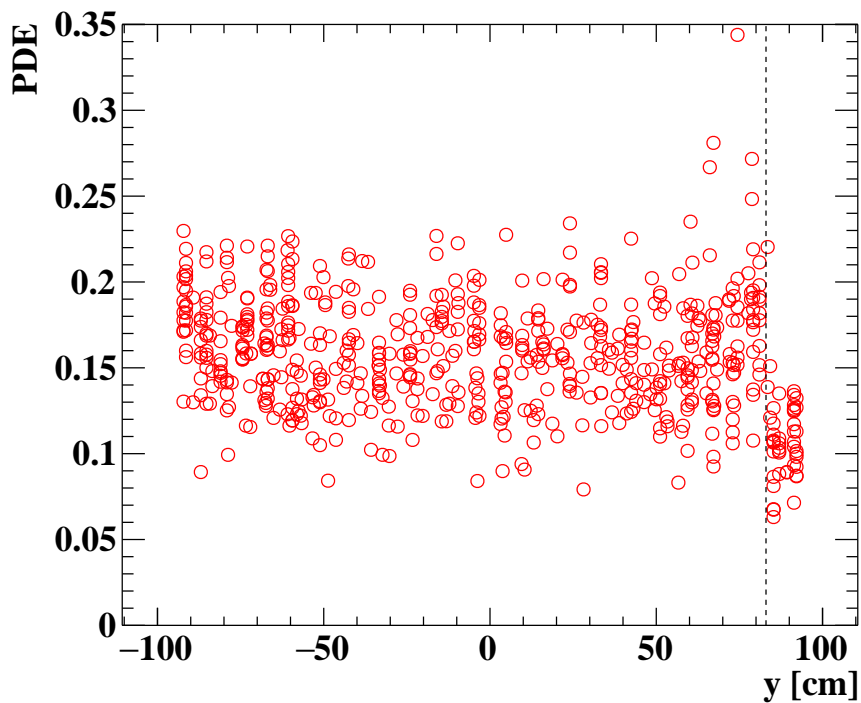


Figure 4.24: QE as a function of the  $y$  position of the PMT. The dashed line shows the estimated LXe level (83 cm). The QE of the PMTs above this level is obviously lower than that of the PMTs below.

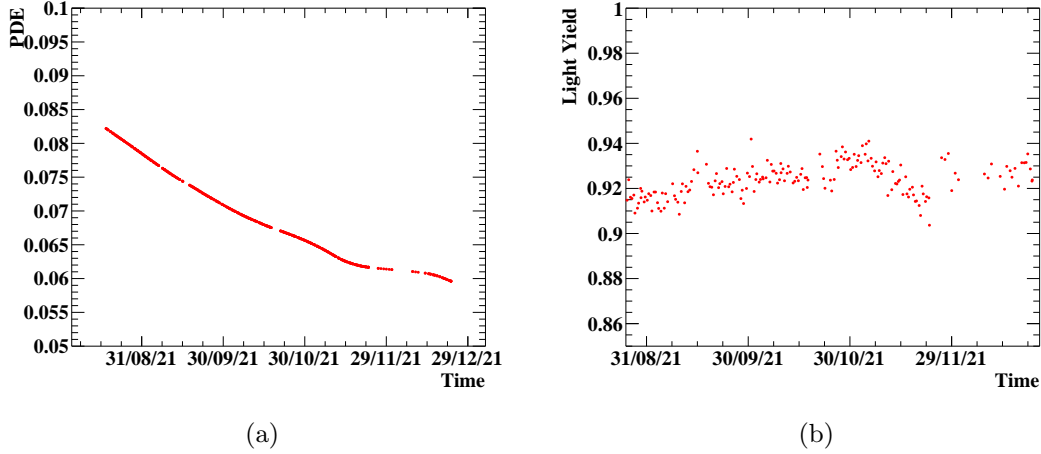


Figure 4.25: (a) Average MPPC PDE and (b)  $F_{LY}$  in the 2021 run.

Fig. 4.25b shows the time variation of the light yield,  $F_{LY}$ . The absolute light yield value is  $93 \pm 5\%$  of the MC simulation. The time variation of the light yield will be discussed in the next section.

## 4.6 Light yield and energy scale

The energy of the gamma-ray  $E_\gamma$  is calculated by using the weighted sum of the  $N_{\text{pho}}$  of the MPPCs  $N_{\text{MPPC}}$  and that of the PMTs  $N_{\text{PMT}}$  as

$$E_\gamma = C \times F(u, v, w) \times T(t) \times (N_{\text{MPPC}} \times r_{\text{MPPC}}(t) + N_{\text{PMT}}) \quad (4.14)$$

where  $C$  is the energy scale to convert the number of photons to the energy,  $F(u, v, w)$  is a uniformity correction function,  $T(t)$  is a function to correct the time variation of the energy scale, and  $r_{\text{MPPC}}(t)$  is a function to correct the time variation of the  $N_{\text{MPPC}}$  with respect to the  $N_{\text{PMT}}$ . The uniformity correction of the energy scale and the weights for the MPPCs and the PMTs to calculate the  $N_{\text{MPPC}}$  and  $N_{\text{PMT}}$  are summarized in Sec. 7.1. Here we focus on the correction functions of the time variation  $T(t)$  and  $r_{\text{MPPC}}(t)$  to discuss the stability of the energy scale. The time variation of the energy scale comes from the time variation of the properties of LXe, such as the light yield and the absorption length. Since the  $N_{\text{PMT}}$  was stable in the MEG, it was used to monitor the light yield. The  $r_{\text{MPPC}}(t)$  and  $T(t)$  were determined by a procedure as follows.

1. Determine  $r_{\text{MPPC}}(t)$  and  $T(t)$  based on the monitoring with the 17.6 MeV gamma-ray from the CW-Li setup and the cosmic-ray .
2. Update  $T(t)$  in the physics run based on the energy scale estimated by the energy spectrum of the background gamma-ray collected by the MEG trigger.

## CW-Li gamma

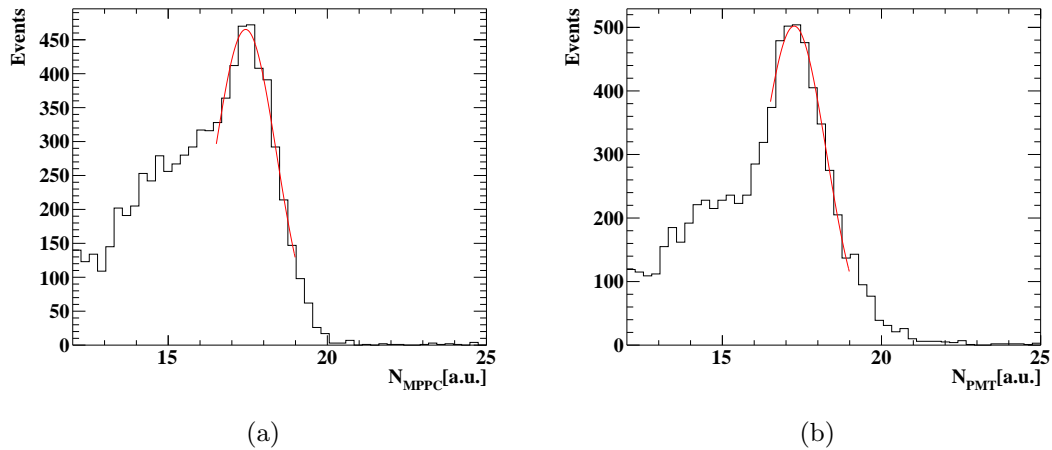


Figure 4.26: The spectrum of the (a)  $N_{\text{MPPC}}$  and (b)  $N_{\text{PMT}}$  for 17.6 MeV gamma rays. The red lines are Gaussian fitting functions to estimate the energy peak for the monitoring. The values are normalized so that the peak comes to around 17.6.

Since the CW-Li gamma-rays are monochromatic (17.6 MeV), the distribution of  $N_{\text{MPPC}}$  and  $N_{\text{PMT}}$  has a peak with a simple non-uniformity correction in the  $w$  direction. Fig. 4.26 shows the distribution of  $N_{\text{MPPC}}$  and  $N_{\text{PMT}}$ . A Gaussian function was fitted to the distribution to monitor the  $N_{\text{MPPC}}$  and  $N_{\text{PMT}}$  with the mean value of the Gaussian.

## Cosmic-ray

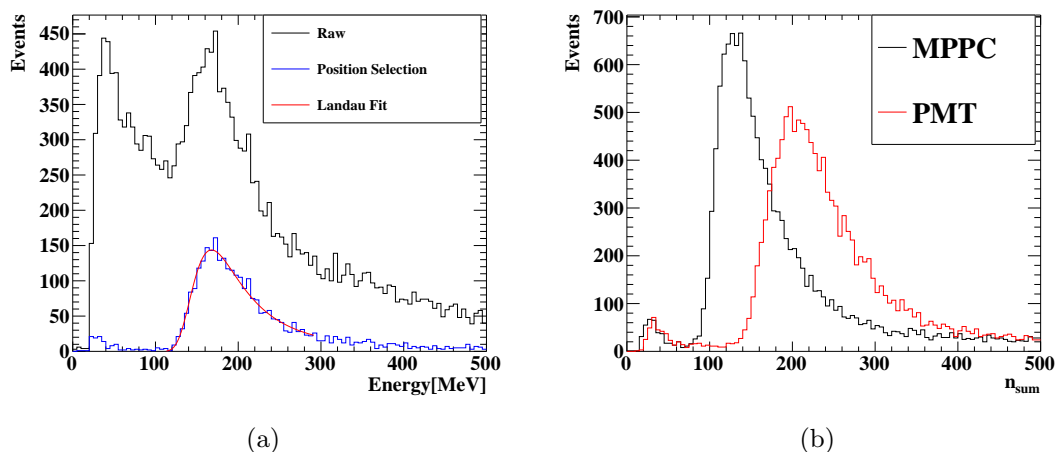


Figure 4.27: (a) The energy spectrum of the cosmic-ray with (blue) and without (black) event selection. The red line shows a landau function fitted to the spectrum with the selection. (b) The  $N_{\text{MPPC}}$  (black) and  $N_{\text{PMT}}$  (red) distribution of the cosmic-ray with the event selection.

The energy deposit by a cosmic ray in the LXe detector depends on the path length in the LXe volume. By selecting the cosmic rays which passes through the entrance face and makes a peak there in the light distribution with the selection criteria as below, a  $\sim 170$  MeV peak was clearly separated from low-energy events that come from cosmic-ray events with a short path length in LXe volume, as shown in Fig. 4.27a.

- $|u| < 20$  cm,  $|v| < 65$  cm,  $w < 10$  cm.
- $N_{\text{MPPC}}/N_{\text{outer}} < 1.6$

where  $N_{\text{outer}}$  is the weighted number of collected photons by PMTs in the outer face. Fig. 4.27b shows the distribution of  $N_{\text{MPPC}}$  and  $N_{\text{PMT}}$  for the cosmic-ray events. A Landau function was fitted to the peak of the distributions to monitor the relative time variation of the energy scale.

The time variations of the  $N_{\text{PMT}}$  monitored with alpha, CW-Li gamma-ray, and cosmic-ray are summarized in Fig. 4.28a. The fluctuation of the  $N_{\text{PMT}}$  was within a few percent in the 2021 run. The time variation of the  $N_{\text{PMT}}$  represents the time variation of the light yield of LXe, considering that the QE of the PMT was stable in the MEG experiment. The time variation of the  $N_{\text{MPPC}}$  shown in Fig. 4.28b indicated that the  $N_{\text{MPPC}}$  gradually increased. The discrepancy is likely due to the difference in the distance and the incident angle from the light source to the sensor between the calibration measurements. The reciprocal of the time variation of the  $N_{\text{PMT}}$  normalized at the beginning of the  $\pi^0$  run was used as the  $T(t)$ , and the  $r_{\text{MPPC}}(t)$  was calculated by interpolating the ratio  $(N_{\text{PMT}}^{\text{norm}} - N_{\text{PMT}})/N_{\text{MPPC}}$  where  $N_{\text{PMT}}^{\text{norm}}$  stands for the  $N_{\text{PMT}}$  at the normalization of the  $T(t)$ . The data points were interpolated by a smooth line to mitigate the statistical fluctuation of the individual measurement, and the line was used for correction to keep the energy scale stable during the beam time.

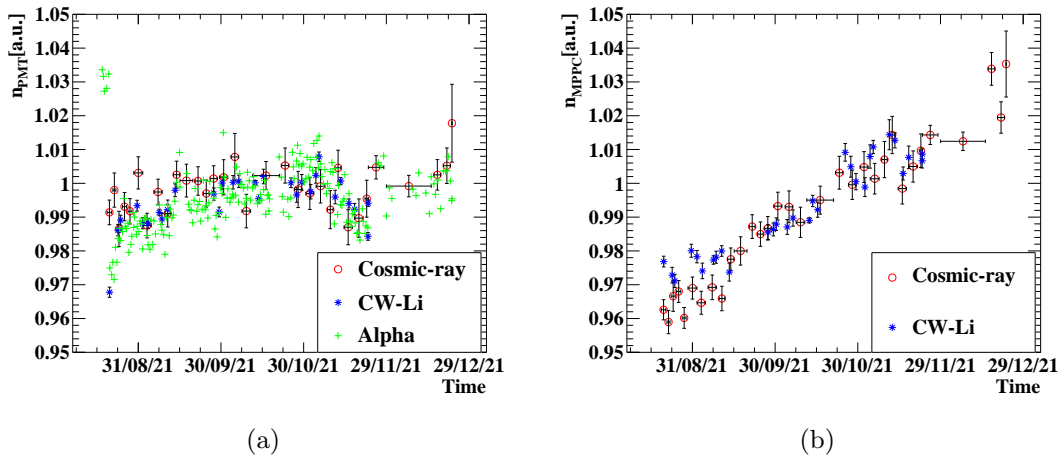


Figure 4.28: (a)  $N_{\text{PMT}}$  and (b)  $N_{\text{MPPC}}$  as functions of time. The results with CW-Li gamma-ray (blue), cosmic-ray (red), and alpha (green) are shown.

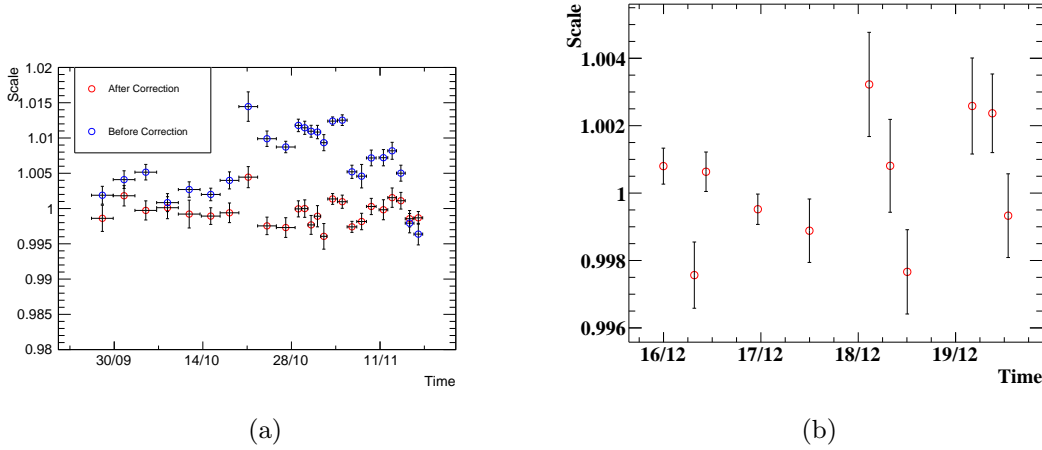


Figure 4.29: (a) Time variation of the energy scale measured with the BG gamma-ray spectrum. The energy scale with the  $T(t)$  estimated by the cosmic-ray and CW-Li gamma-ray is shown in blue. The energy scale with the updated  $T(t)$  by the BG gamma-ray spectrum is shown in red. (b) Time variation of the energy scale measured with the 55 MeV gamma-ray spectrum in the  $\pi^0$  run. The fluctuation of the energy scale was 0.1% for the  $\pi^0$  run period.

## BG gamma-ray spectrum

Fig. 4.29a shows the time variation of the energy scale monitored by the background gamma-ray in the time sideband<sup>\*1</sup> of the physics dataset after the correction with  $r_{\text{MPPC}}(t)$  and  $T(t)$  based on the cosmic-ray and the CW-Li gamma-ray. The dataset of the time sideband was divided into subsets based on the periods, and the energy scale in each period was estimated by fitting an expected  $E_\gamma$  spectrum to the measured  $E_\gamma$  spectrum in the time sideband. The  $E_\gamma$  spectrum was estimated by smearing the energy spectrum in the MC simulation and adding the measured cosmic-ray energy spectrum. Fig. 4.29a shows the time variation of the energy scale with the corrections. The systematic uncertainty of the energy scale that comes from the monitoring was estimated to be 0.36% based on the difference between the  $T(t)$  estimated by the cosmic-ray and CW-Li gamma-ray (the first step) and that by the background gamma-ray in the second step.

## 55 MeV gamma-ray from $\pi^0$ decay

The time variation of the energy scale during the  $\pi^0$  run was corrected based only on the cosmic-ray dataset because the CW beamline is not compatible with the LH<sub>2</sub> target for the  $\pi^0$  run. The correction during the  $\pi^0$  run was validated with the 55 MeV peak of gamma-rays from the  $\pi^0 \rightarrow \gamma\gamma$ . Fig. 4.29b shows the time variation of the 55 MeV peak during the  $\pi^0$  run

<sup>\*1</sup> See Sec. 11.1 on the definition of the time sideband

after the correction. The time variation of the energy peak was limited to 0.1%, thanks to the correction.

## 4.7 Alignment of MPPC

The position of the MPPCs was measured by two complementary methods. One method is a direct optical alignment at room temperature in the construction phase and the other method uses a collimated and well-aligned gamma-ray beam after the detector is filled with LXe.

### 4.7.1 Alignment at room temperature

The surface of the arrays of the MPPCs was surveyed by a laser scanner (Faro Edge ScanArm [65]) in the construction phase [66] as shown in Fig. 4.30a. The scanner was inserted from the side of the detector and it measured the surface structure of the MPPC array by triangulation, which measures the position of the object from the reflected light of the irradiated laser. Fig. 4.30b shows the data points measured with the scanner for several MPPCs. The colors of the data points show the contour of the surface structure. While the four chips and the gap between them are clearly visible for the MPPC in the center, data points are missing from the upper half of the MPPC on the left (white region). The positions of the MPPCs were reconstructed using the gap between the four MPPC chips. A symmetric function was fitted to the data points in the central part of an MPPC to reconstruct the center position of the MPPC. All MPPCs were surveyed, and the three-dimensional position of 426 MPPCs was reconstructed with good quality. While the reconstruction was successful for the MPPCs well within reach of the scanner's arm, it failed for MPPCs far from the support of the arm due to the diffused reflection at the surface.

Since the MPPCs are mounted on the PCBs precisely with the same interval (15.1 mm), the resolution of the measurement was estimated from the distribution of the distance between adjacent MPPCs, as shown in Fig. 4.31. The resolution was estimated to be  $120\ \mu\text{m}$  based on the sigma of the distribution.

The position of all MPPCs was interpolated by the measured positions of the limited number of MPPCs by the following procedures separately for all CFRPs.

1. Fit a cylindrical surface to the reconstructed points of the MPPC center with six parameters, five for the core axis and one for the radius.
2. Project the array of the 3D reconstructed data points to the cylindrical surface.
3. Fit the projected array of reconstructed data points with a lattice assuming equal spacing.
4. Calculate the position of all MPPCs as lattice points.
5. Reconstruct the 3D position of all MPPCs with the parameters of the cylinder and the position of all MPPCs.

The reconstructed position was consistent with the measured position to an accuracy of  $180\ \mu\text{m}$

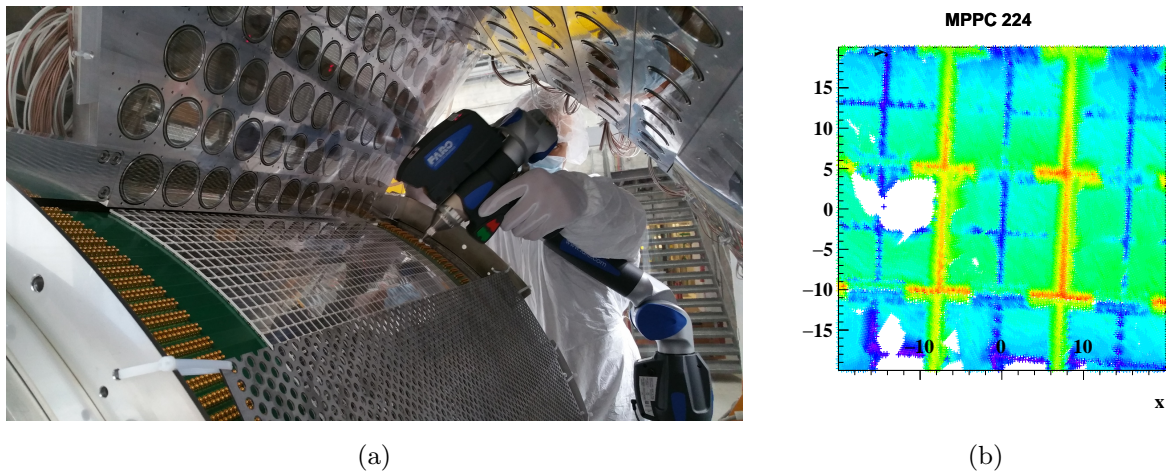


Figure 4.30: (a) Survey with a Faro laser scanner. The scanner was inserted from the upstream or downstream of the detector, and the surface structure of the MPPC array was surveyed. (b) Measured data points around an MPPC with the laser scanner. The color of each data point shows the contour. The orange and red points show the ceramic package of the MPPCs, and most of the blue points show the gap between MPPC chips. The white region on left and bottom show the region where no data are collected by the scanner.

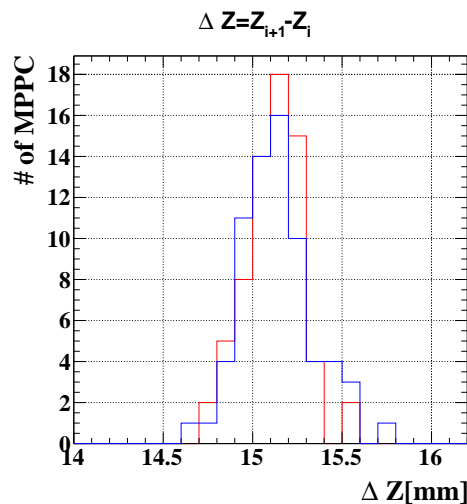


Figure 4.31: Distance between adjacent MPPCs. The distribution of the distance between the position of odd channel – even channel is shown in red and that between even channel – odd channel in blue.

based on the deviation between them. The interpolated positions by the above procedures were used to combine the positions measured by the other method, later discussed in Sec. 4.7.3.

#### 4.7.2 Alignment with gamma-ray beam

The positions of the MPPCs are affected by thermal contraction and by cryostat deformations due to the fact that the detector is filled with the cold (169 K) and heavy (2.7 t) LXe. Since

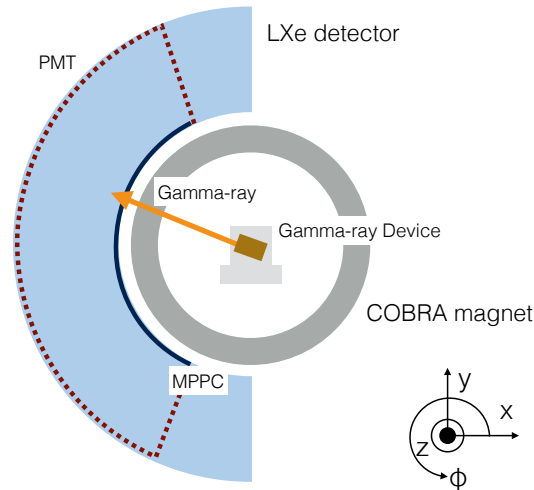


Figure 4.32: Schematic side view of the MPPC position measurement with the low-energy gamma-ray beam. The gamma rays emitted from the collimator in the center of the COBRA magnet are used for the position measurement of the MPPCs.

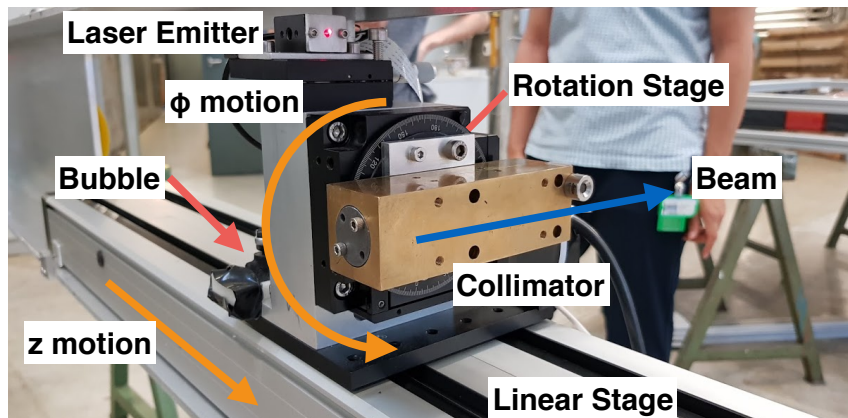


Figure 4.33: Brass collimator where the  $^{57}\text{Co}$  is installed inside and the two stages to control the gamma-ray beam position at the entrance face.

neither of the two effects can be precisely modeled, it is difficult to estimate the actual position of the MPPCs from the measured positions at room temperature. Therefore, the measurements for the in-situ positions of the MPPCs are necessary.

Fig. 4.32 shows the schematics of the measurement. In order to measure the position of MPPCs at LXe temperature, a low-energy gamma-ray ( $\sim 100$  keV) beam is a suitable probe because it penetrates the material in front of LXe and also interacts at the very shallow region ( $\mathcal{O}(1)$  mm) in the LXe volume. The source of scintillation photons is so close to the MPPC surface that the photon distribution is concentrated to a few MPPCs. The rate of the MPPC signal is quite sensitive to the beam position in the entrance face. By scanning the entrance face along  $z$  and  $\phi$  with the gamma-ray beam, the 2D positions of the MPPCs on the entrance face can be measured. MPPCs with large  $|z|$  cannot be scanned by this technique because the

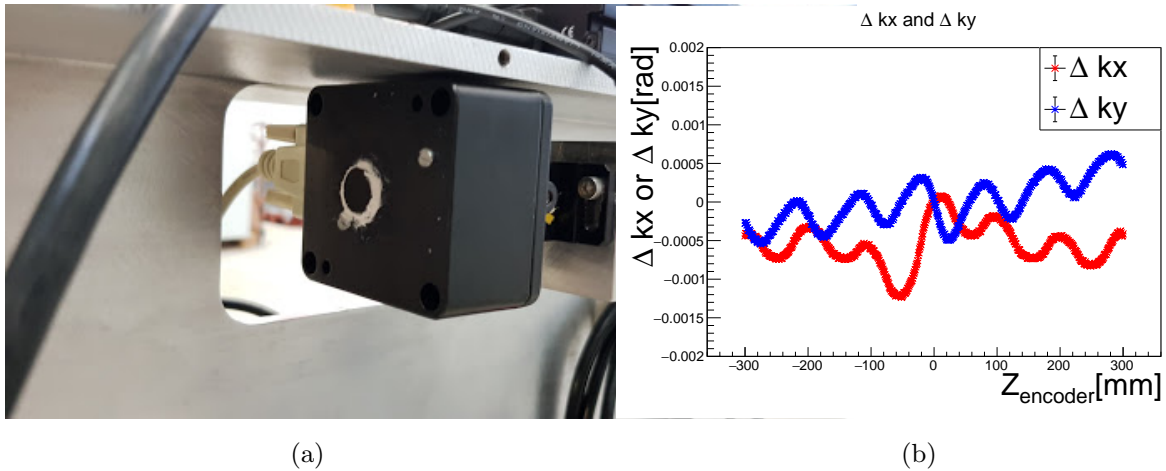


Figure 4.34: (a) Quadrant Photo Diode mounted on the support structure. The spot of the emitted laser from the emission device mounted to the rotation stage is measured to monitor the rotation of the stage about  $x$  and  $y$  axis. (b) The rotation angle around  $x$  (red) and  $y$  (blue) axes monitored with the QPD as a function of the  $z$  position of the collimator. The wavelike structure comes from the imperfections in the drive screw in the translation stage.

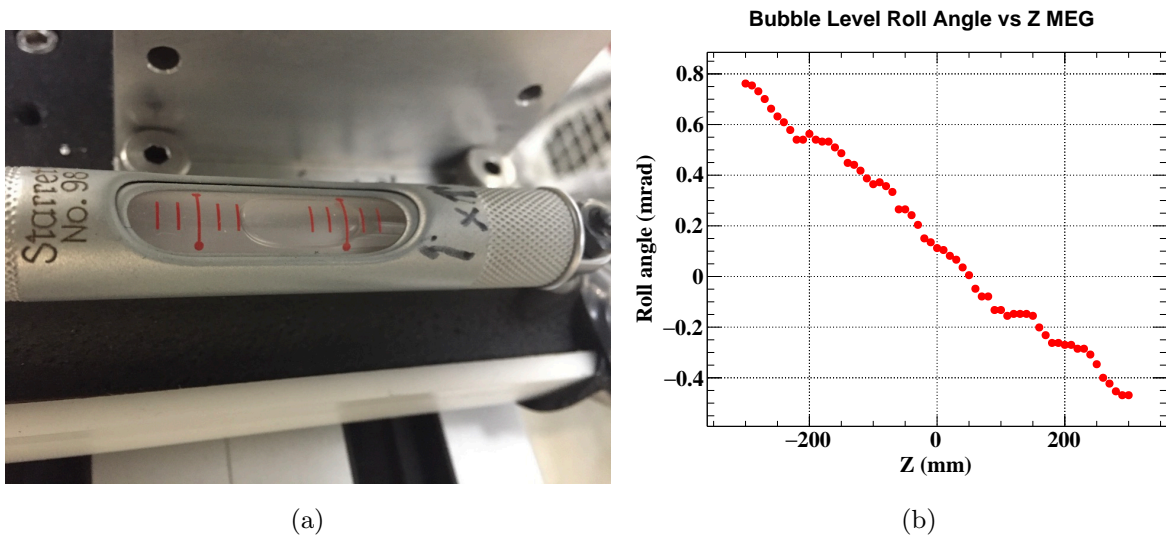


Figure 4.35: (a) Bubble level mounted on the rotational stage. A picture of the level is taken for each measurement position and it is used to monitor the rotation angle about the  $z$  axis. (b) Rotation angle about the  $z$  axis monitored by the level.

gamma-rays can not penetrate the COBRA magnet outside of the thin window ( $|z| > 120$  mm).

Fig. 4.33 shows a picture of the gamma-ray measurement device. A commercial  $^{57}\text{Co}$  dot source was selected as a probe. The decay of  $^{57}\text{Co}$  has two emission lines at 122 keV ( $\approx 80\%$ ) and 136 keV ( $\approx 10\%$ ). The activity of the source was high enough ( $3 \times 10^{10}$  Bq) to perform the measurement within a reasonable time. The source was fixed in a  $38 \times 38 \times 116$  mm<sup>3</sup> brass collimator with a  $0.15 \times 5.0$  mm<sup>2</sup> slit. The size of the beam spot was  $1.5 \times 40$  mm<sup>2</sup> at the entrance

face of the detector. The collimator was mounted on a rotational stage around the  $z$ -axis on a linear stage along the  $z$ -axis. The linear stage allowed precise and delicate movement with a step of  $25\ \mu\text{m}$  in the  $z$  direction. The rotational stage allowed rotation with a step of  $25\ \mu\text{m}$  around the  $z$  axis. The linear stage was fixed to a rigid support structure that can be mounted between both ends of the COBRA magnet.

The gamma-ray beam position at the entrance face was aligned with several alignment instruments. An optical survey of the collimator with a laser tracker (Leica Absolute Tracker [67]) was performed at multiple positions in  $z$ . The precision of the optical survey was  $0.1\ \text{mm}$  in  $z$  and  $0.15\ \text{mrad}$  in  $\phi$ . The rotation of the stage around the  $x$ - and  $y$ -axis, which affects the  $z$  position of the beam at the entrance face, was monitored by a Quadrant Photo Diode (QPD, Fig. 4.34a). The irradiated position of the infrared laser from an emission device mounted on the rotational stage was detected by a QPD to measure the rotation of the rotational stage. Fig. 4.34b shows the measured rotation angle around the  $x$  and  $y$  axis as a function of  $z$  position of the collimator. The wavelike structure comes from the imperfections in the drive screw in the translation stage because the spacing between the peaks is almost equivalent to one turn of the drive screw. The uncertainty of the correction for the  $z$  position of the gamma-ray beam in the entrance face was  $0.03\ \text{mm}$ . A bubble level and a camera are equipped with the back of the rotational stage to monitor the rotation of the stage around the  $z$ -axis (Fig. 4.35), which affects the  $\phi$  position of the gamma-ray beam. The uncertainty of the  $\phi$  correction from this monitoring was  $0.08\ \text{mrad}$  based on the reproducibility during the data-taking period.

The data-taking was performed twice, in 2017 and 2018. Fig. 4.36 shows the measured MPPC positions in 2017 and 2018. In the first data-taking in 2017, 1900 MPPCs were scanned by measuring the trigger rate of each MPPC with a certain threshold. The second data-taking in 2018 was performed by recording the waveform and reducing the background mainly from the cosmic-ray events. In 2018, 700 MPPCs were scanned. A subset of the MPPCs was scanned twice to measure the reproducibility of the measurement.

Fig. 4.37 shows the measured gamma-ray event rate as a function of the beam  $z$  position. A symmetric function that has a flat top and Gaussian tail on both sides is fitted to the distribution. The MPPC position is reconstructed as the center of the function. The resolution of the measurement is estimated to be  $0.1\ \text{mm}$  by using the spacing between the measured position of adjacent MPPCs.

The validation of the alignment was performed using 16 lead strips attached to the entrance face of the cryostat (Fig. 4.38). The lead strips ( $1 \times 1 \times 25\ \text{mm}^3$ , Fig. 4.38a) were capsulated by plastic packages and attached to the outer wall of the entrance face of the LXe detector, and aligned by the laser tracker with a precision of  $\sim 100\ \mu\text{m}$ . When an MPPC that is the back of a lead strip is scanned by the gamma-ray beam, the measured signal rate is significantly reduced at the position of the strip as shown in Fig. 4.39. The reconstructed positions of the lead strips with the gamma-ray measurement agree with the optical survey with standard deviations of  $\sigma_z = 0.43\ \text{mm}$  and  $\sigma_\phi = 0.68\ \text{mrad}$ .

Table 4.3 summarizes the uncertainty of the alignment with the gamma-ray beam. The dom-

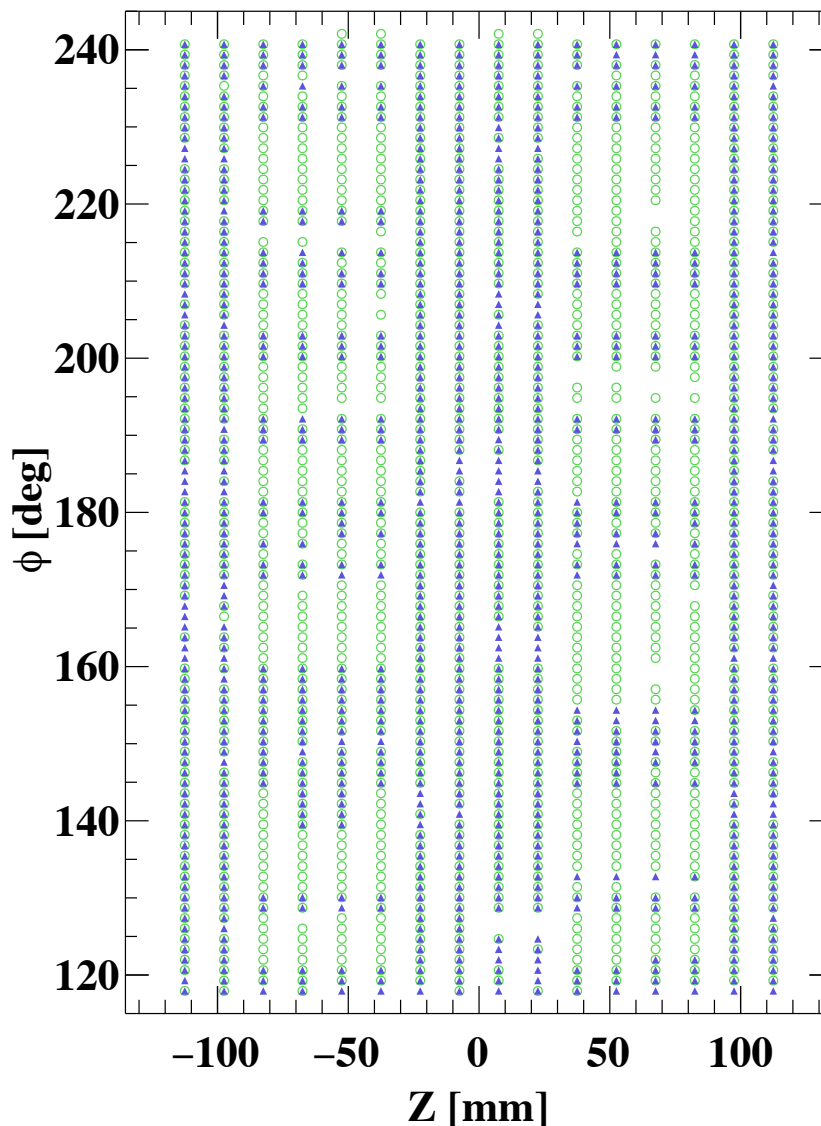


Figure 4.36:  $z$ - $\phi$  positions of MPPCs measured by the gamma-ray beam measurements in 2017 (open green circles) and in 2018 (solid blue triangles).

inant uncertainty comes from the consistency of the lead strip position and the reproducibility.

### 4.7.3 Combination of two methods

The 3D positions of the MPPCs at the low temperature in the coordinate system of the MEG II experiment are estimated by combining the two complementary measurements. The measurement with the laser scanner gives the 3-D positions of MPPCs, but the detector was at room temperature. On the other hand, the measurement with the low-energy gamma-ray beam gives the  $(z, \phi)$  positions of the MPPC on the incident plane in the coordinate system of the MEG II experiment, but the radial position is not known. Assuming that the MPPCs contract

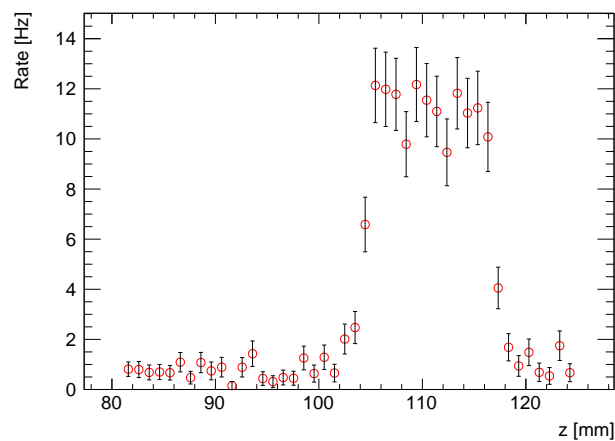
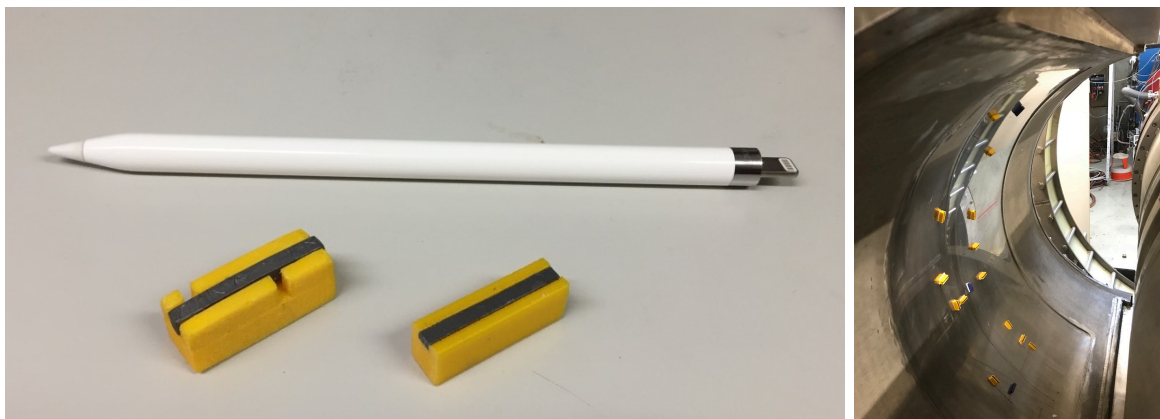


Figure 4.37: Gamma-ray event rate measured by an MPPC as a function of  $z$  position of the beam. The rate is significantly high where the beam position is pointed to the MPPC.



(a)

(b)

Figure 4.38: (a) Lead strip fixed in a plastic groove. (b) The entrance face of the detector with lead strips mounted.

Table 4.3: Uncertainties of the MPPC position measurement

Source	Z Unc. [mm]	$\phi$ Unc. [mrad]
Beam alignment	0.10	0.21
QPD corrections	0.03	-
Bubble-level corrections	-	0.08
Statistical uncertainty	0.15	0.18
MPPC spacing dispersion	0.25	0.55
Lead strip consistency	0.43	0.68
Reproducibility	0.57	-

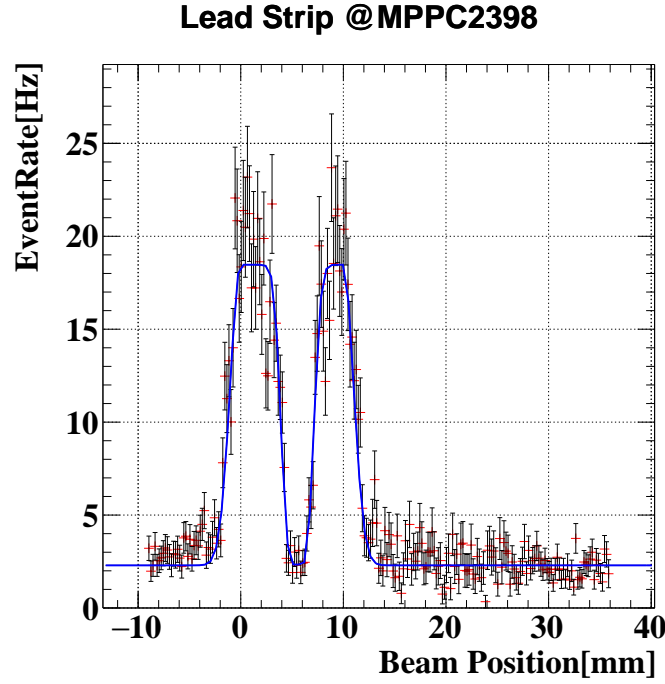


Figure 4.39: Gamma-ray event rate of an MPPC with a lead strip as a function of the beam position (red). A clear dip is observed at the position where a lead strip is mounted. A fitting function to estimate the position of the lead strip is shown in blue.

uniformly, the 3D in-situ position of an MPPC can be written as follows,

$$\vec{x}_{\text{exp}} = (1 - s)R\vec{x}_{\text{FARO}} + \vec{x}_{\text{offset}}, \quad (4.15)$$

where  $s$  is the scaling parameter to correct the thermal contraction,  $R$  and  $\vec{x}_{\text{offset}}$  are the rotation matrix and position offset to align the global rotation and offset of the measured position at room temperature  $\vec{x}_{\text{FARO}}$  with respect to that at LXe temperature  $\vec{x}_{\text{exp}}$ . The parameters  $s$ ,  $R$ ,  $\vec{x}_{\text{offset}}$  are estimated by minimizing the following  $\chi^2$ ,

$$\chi^2(s, R, \vec{x}_{\text{offset}}) = \sum_i [(z_{\gamma,i} - z_{\text{exp},i})^2/\sigma_z^2 + (\phi_{\gamma,i} - \phi_{\text{exp},i})^2/\sigma_\phi^2], \quad (4.16)$$

$$\sigma_x = \sqrt{\sigma_{\text{exp}}^2 + \sigma_\gamma^2} \quad (x = z, \phi) \quad (4.17)$$

where  $z_\gamma$  and  $\phi_\gamma$  are the measured position in the gamma-ray measurement, and  $z_{\text{exp}}$  and  $\phi_{\text{exp}}$  are the expected position defined by Eq. 4.15. The uncertainty  $\sigma_x$  ( $x = z, \phi$ ) is calculated by combining the uncertainty of each measurement. The MPPCs that were scanned with the gamma-ray measurement with good quality are used for the computation of the  $\chi^2$ . The precision of the combination of the two measurements is estimated by the distribution of the difference between the measured position by the gamma-ray measurement  $z_\gamma, \phi_\gamma$  and the expected position after the fitting  $z_{\text{exp}}, \phi_{\text{exp}}$ . Fig. 4.40 shows the distribution  $\Delta z = z_\gamma - z_{\text{exp}}$  and  $\Delta\phi = \phi_\gamma - \phi_{\text{exp}}$ . The sigma of the distribution is  $250 \mu\text{m}$  and  $0.38 \text{ mrad}$ , respectively. A part of this spread comes from the resolution of the gamma-ray beam measurement ( $150 \mu\text{m}$  in  $z$  and  $0.18 \text{ mrad}$  in  $\phi$ ),

which is included in the uncertainties summarized in Table 4.3. The residual ( $0.20 \mu\text{m}$  in  $z$  and  $0.33 \text{ mrad}$  in  $\phi$ ) can be explained by the non-uniformity of the thermal contraction. Therefore, the total uncertainty of the MPPC position measurement consists of the non-uniformity of the thermal contraction and the uncertainty of the measurement with the gamma-ray beam, and it is  $0.60 \text{ mm}$  in  $z$  and  $0.75 \text{ mrad}$  in  $\phi$ . The combined position of the 2018 gamma-ray measurement and the optical survey is used for the gamma-ray position reconstruction.

To understand the thermal contraction, the thermal expansion coefficient  $\alpha_t$  is calculated using the relation

$$s = \alpha_t \Delta T, \quad (4.18)$$

where  $\Delta T$  is the change in temperature,  $123 \pm 10 \text{ K}$ , between the survey performed at room temperature ( $293 \pm 10 \text{ K}^{*2}$ ) and the gamma-ray survey performed at LXe temperature ( $170 \text{ K}$ ). The calculated  $\alpha_t$  in 2017 and 2018 measurements are shown in Table 4.4. The calculated  $\alpha_t$  agrees well with the theoretical value of the coefficient of the thermal contraction of the PCB material ( $16 \pm 1 \text{ ppmK}^{-1}$ ) used for mounting the photodetectors.

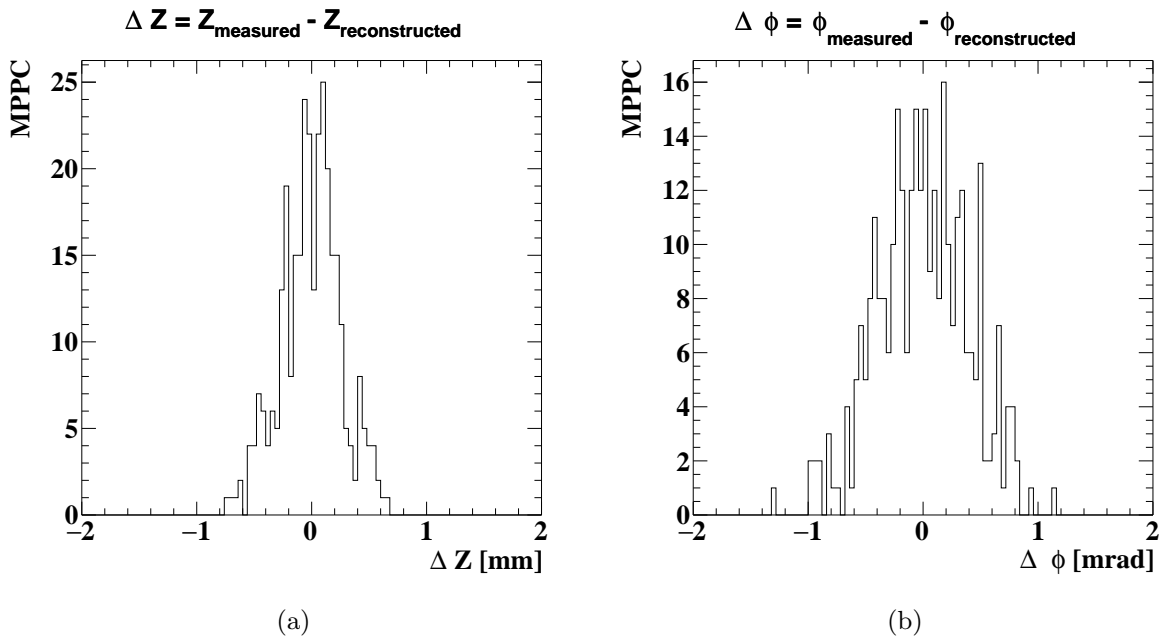


Figure 4.40: The distribution of the difference between the expected position  $x_{\text{exp}}$  and the measured position by the gamma-ray measurement  $x_{\gamma}$  in (a)  $z$  and (b)  $\phi$ . The sigma of the distribution was  $0.25 \text{ mm}$  in  $z$  and  $0.38 \text{ mrad}$  in  $\phi$ .

The position dependence of the signal rate is helpful to estimate the non-uniformity of the material budget in the entrance face. The space between the support structure and the cryostat is filled with LXe. The signal rate is sensitive to the material budget before the LXe volume. Fig. 4.41a shows the signal rate for each MPPC. The signal rate is relatively high at the edges of the CFRP because each CFRP is fixed to the inner wall at the four corners and the thickness

<sup>\*2</sup> The large uncertainty is assigned because the temperature in the measurement was not recorded.

Table 4.4: Thermal expansion coefficient of the MPPC array

Year	s	$\alpha_t[\text{ppmK}^{-1}]$
2017	0.0019	$15.1 \pm 1.6$
2018	0.0021	$17.1 \pm 1.9$

of the LXe volume is small there. On the other hand, the LXe volume is thick in the middle of each CFRP. The thickness of the LXe volume was calculated from the signal rate as

$$d_{\text{LXe}} = -\lambda_{\text{LXe}} \ln(R_\gamma/R_{\gamma,\text{norm}}), \quad (4.19)$$

where  $d_{\text{LXe}}$  is the thickness of LXe,  $\lambda_{\text{LXe}}$  is the attenuation length of LXe for  $\sim 120$  keV gamma-ray (2.8 mm),  $R_\gamma$  is the signal rate of each MPPC,  $R_{\gamma,\text{norm}}$  is the signal rate without attenuation by LXe volume.  $R_{\gamma,\text{norm}}$  is estimated from the signal rate of MPPCs around the boundary between CFRP 1 and CFRP 2 because the CFRPs are fixed firmly to the cryostat there according to the record of the construction. Fig. 4.41b shows  $d_{\text{LXe}}$  as a function of the  $v$  position of the MPPCs.  $d_{\text{LXe}}$  is 1.8 mm on average, and the inefficiency for the signal gamma-ray due to this LXe volume is 1.8%.

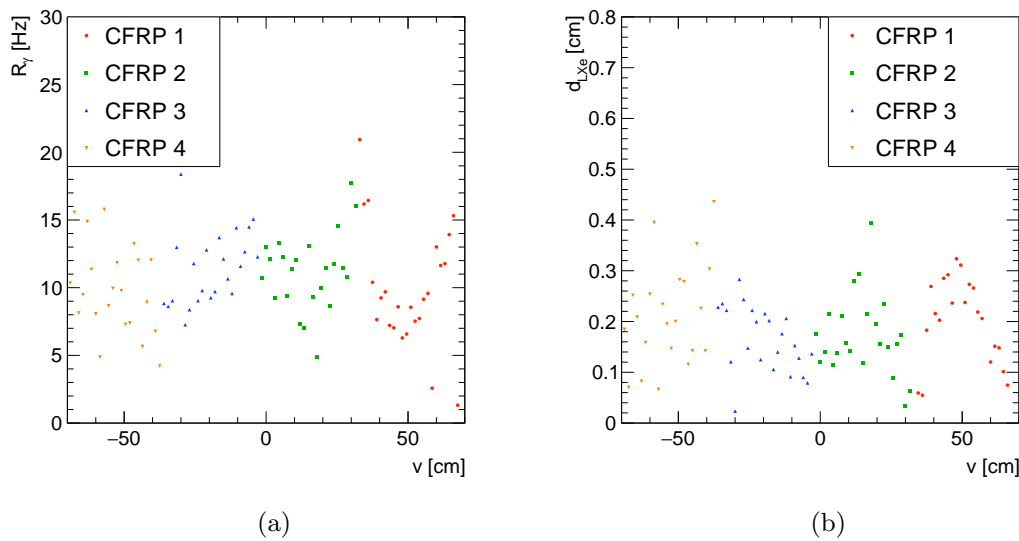


Figure 4.41: (a) The signal rate of gamma-ray measurement as a function of the  $v$  position of the MPPCs. The color of the data points corresponds to the CFRP on which MPPC is fixed. (b) The measured  $d_{\text{LXe}}$  as a function of the longitudinal position of the MPPC.

## Chapter 5

# Radiation Damage to VUV-MPPC

In this chapter, the observations of the unexpected radiation damage to the new VUV-MPPC in a series of commissioning runs are discussed. In five years of the beam time,  $4.2 \times 10^{14}$  muons had been stopped at the target as summarized in Table 5.1. In the meantime, the calibration measurements revealed that the PDE of MPPC decreased due to radiation damage. The radiation environment of the MPPC will be described in Sec. 5.1, and the observed radiation damage to the MPPC will be summarized in Sec. 5.2. In Sec. 5.3, the recovery of PDE by annealing is described. In Sec. 5.4, the impact of radiation damage on the experiment is discussed based on the previous study [2].

Table 5.1: Muon beam intensity  $R_\mu$  and the total accumulated number of stopped muons at the target,  $N_\mu$  in the beam time in each year.

Year	$R_\mu$ [ $10^7/s$ ]	$N_\mu$ [ $10^{12}$ ]
2017	7	55
2018	7	40
2019	7	60
2020	3	90
2021	2–5	175

### 5.1 Radiation environment for MPPC

Two types of radiation damage are known for MPPC [68]. One is bulk damage due to Non-Ionizing Energy Loss (NIEL), and the other is surface damage due to Ionizing Energy Loss (IEL). The bulk damage is primarily produced by high-energy particles (protons, pions, electrons, and photons) and neutrons, displacing atoms out of their lattice site and generating crystal defects. An increase in leakage current and a decrease in the signal are reported as consequences of the bulk damage [69, 70, 71, 72]. According to the reports, the damage occurs above  $1 \times 10^8 / \text{cm}^2$  (1 MeV neutron equivalent). Electrons and photons with energies below the threshold for bulk defects ( $\sim 300$  keV) generate only defects in the dielectrics at the interface between

the passivation layer (typically  $\text{SiO}_2$ ) and the silicon layer. This is called surface damage. A large dark current was reported as a consequence of the surface damage after irradiation of  $\mathcal{O}(10^2)$  Gy [73].

Fig. 5.1 illustrates the radiation environment during the muon beamtime. The MPPCs were irradiated with gamma-rays, neutrons, and VUV photons.

The gamma-ray dose from the beginning of the 2017 run to the end of the 2021 run is estimated to be  $1.2 \times 10^{-4}$  Gy with a dedicated MC simulation of RMD gamma-rays.

The photon fluence during the beamtime is calculated based on MPPC current and MC simulation. The MPPC current is expressed as

$$I = R_{\text{pho}} \times G \times F_{\text{EC}} \times \epsilon_{\text{PD}} \times c_{\text{elec}}, \quad (5.1)$$

where  $R_{\text{pho}}$  is the rate of incident photon for the MPPC,  $c_{\text{elec}}$  is the calibration parameter of the readout electronics ( $\approx 6.5^{*1}$ ). In the 2019 run, the MPPC current was  $1 \mu\text{A}$  on average at  $7 \times 10^7$  /s muon beam intensity. The photon rate in data is calculated as  $R_{\text{pho}} = 4.4 \times 10^6$  /s based on the sensor parameters given by the calibration measurements ( $G=1.5 \times 10^6$ ,  $F_{\text{EC}}=1.9$ ,  $\epsilon_{\text{PD}} = 0.08$ ). The MC simulation of RMD gamma rays from the target gives the number of detected photoelectrons for each single RMD decay. By using the branching ratio of the RMD and the muon beam intensity, the average value of the number of photons per event is translated to the photon rate. The photon rate based on the MC simulation is  $3.3 \times 10^6$  /s. By a combination of both results, the fluence to VUV photons by the end of the 2021 run is estimated to be  $4(1) \times 10^{11}$  / $\text{mm}^2$  at the center of the detector.

Fig. 5.2 shows the position dependence of the estimated exposure for VUV photon and gamma-ray in the  $u$  direction. Since the LXe detector and the COBRA magnet are designed to have a reduced material budget only in the acceptance region ( $|u| < 23.9$  cm), the radiation exposure induced by muon decay at the target is expected to be smaller outside the acceptance.

Neutrons come from the hadronic interaction of the primary proton beam with the pion production target. The production target is located upstream  $\sim 20$  m away from the MEG II detectors. From a neutron flux measurement in the MEG experimental area [28], the total neutron fluence by the end of the 2021 run is estimated to be less than  $2 \times 10^7$  / $\text{cm}^2$ .

The estimated neutron fluence and the gamma-ray dose are much smaller than the level where the NIEL damage has been reported. The radiation damage to SiPMs by the VUV irradiation has never been reported.

## 5.2 Decrease in MPPC PDE

Though the absolute scale of the MPPC PDE has 10% systematic uncertainty as discussed in Sec. 4.5, it is omitted from the discussion below since the relative decrease is important to discuss the radiation damage. Fig. 5.3 shows the time variation of the MPPC PDE from 2017

---

\*1 This parameter is calculated by taking the ratio of the current readout value of an MPPC by the electronics to the expected current value based on the measured charge and the frequency to flash the LEDs

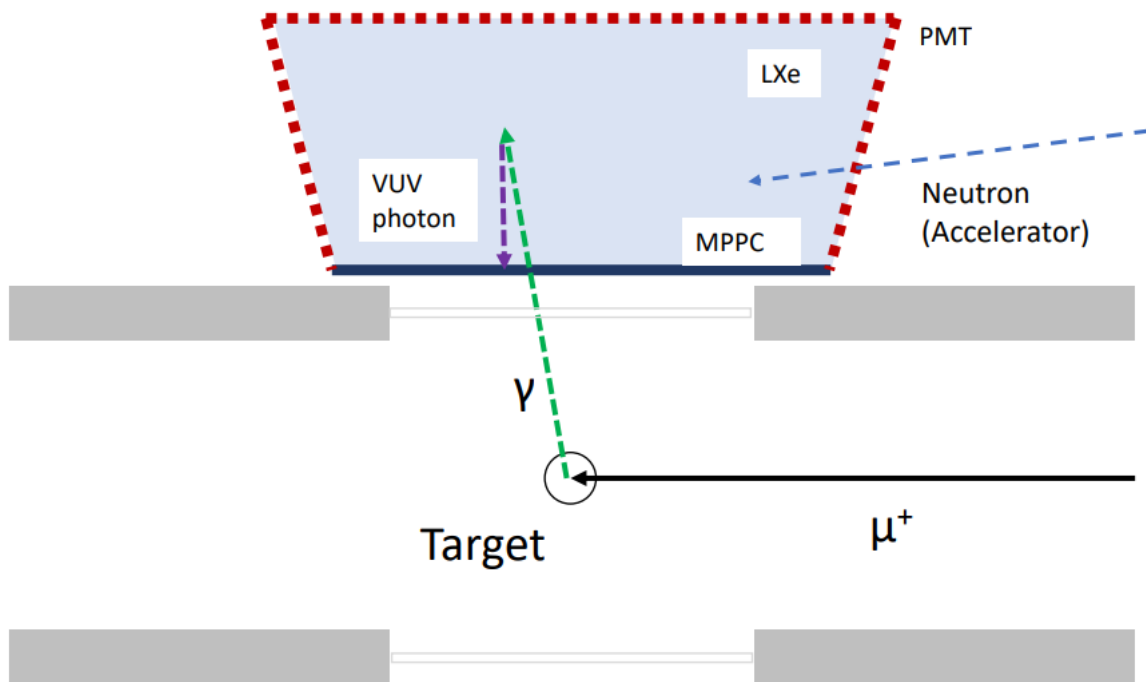


Figure 5.1: Radiation environment of the detector. MPPCs are exposed to gamma rays, VUV photons, and neutrons. Gamma rays come from muon decays, VUV photons come from the xenon scintillation induced by incoming gamma rays, and neutrons come from the pion production target in the upstream.

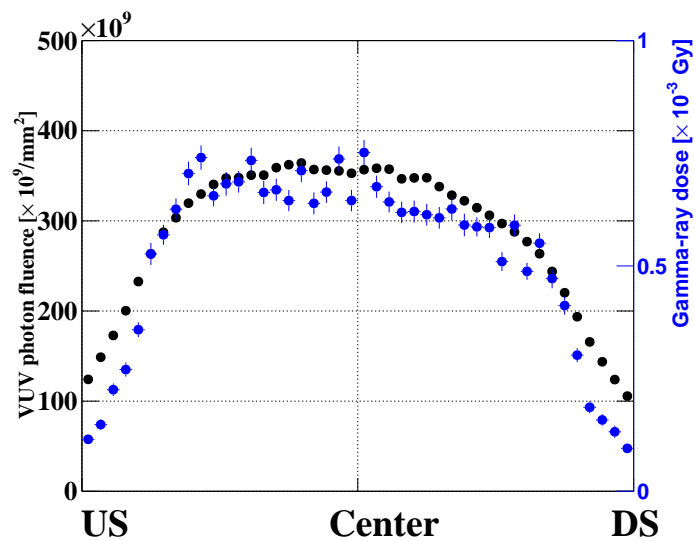


Figure 5.2: Estimated radiation exposure of VUV photons (black) and gamma ray (blue) by MC simulation as a function of  $u$  position of MPPCs.

Table 5.2: Exposure to radiation from 2017 to 2021

Particle	Dose / Fluence
Gamma-ray	$7 \times 10^{-4}$ Gy
Neutron	$2 \times 10^7$ cm <sup>-2</sup> (1 MeV equivalent)
VUV photon	$4 \times 10^{11}$ mm <sup>-2</sup>

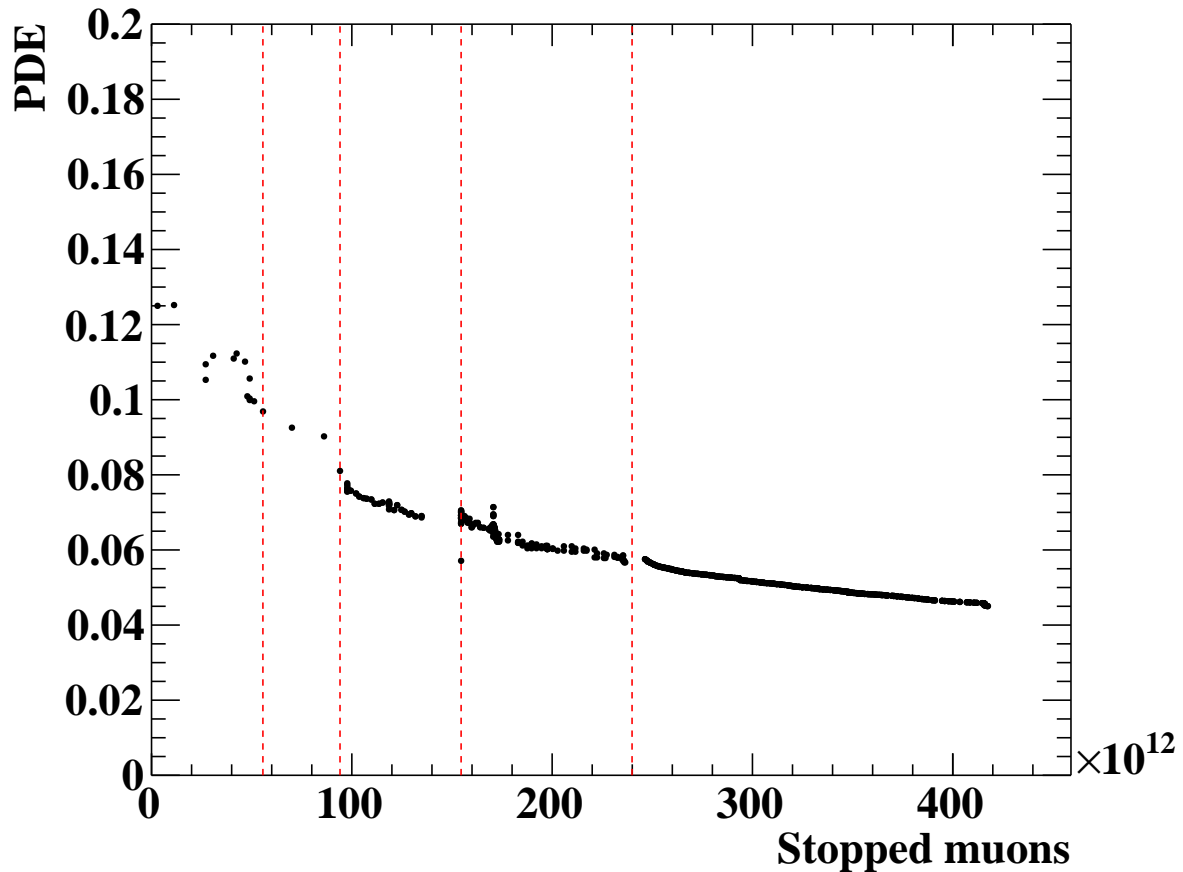


Figure 5.3: The degradation of the MPPC PDE on average as a function of the accumulated number of stopped muons from 2017 to 2021. The red dashed lines show the starting point of each year. The calibration data were collected frequently from the 2019 run after the decrease of the PDE was realized.

to 2021 as a function of  $N_\mu$ . The time variation of the averaged PDE for the MPPCs read out through all the beam times is shown. The figure shows that the MPPC PDE decreased from 0.13 to 0.04 as  $N_\mu$  evolved up to  $4.2 \times 10^{14}$ . This damage is categorized as radiation damage because the decrease during the long shutdown period between the beam time was negligible compared to the decrease during the beam time. This radiation damage was not expected, considering that the level of radiation was small compared to the previous studies of the radiation damage of SiPMs. Another observation is that the degradation slowed down as the MPPCs were damaged.

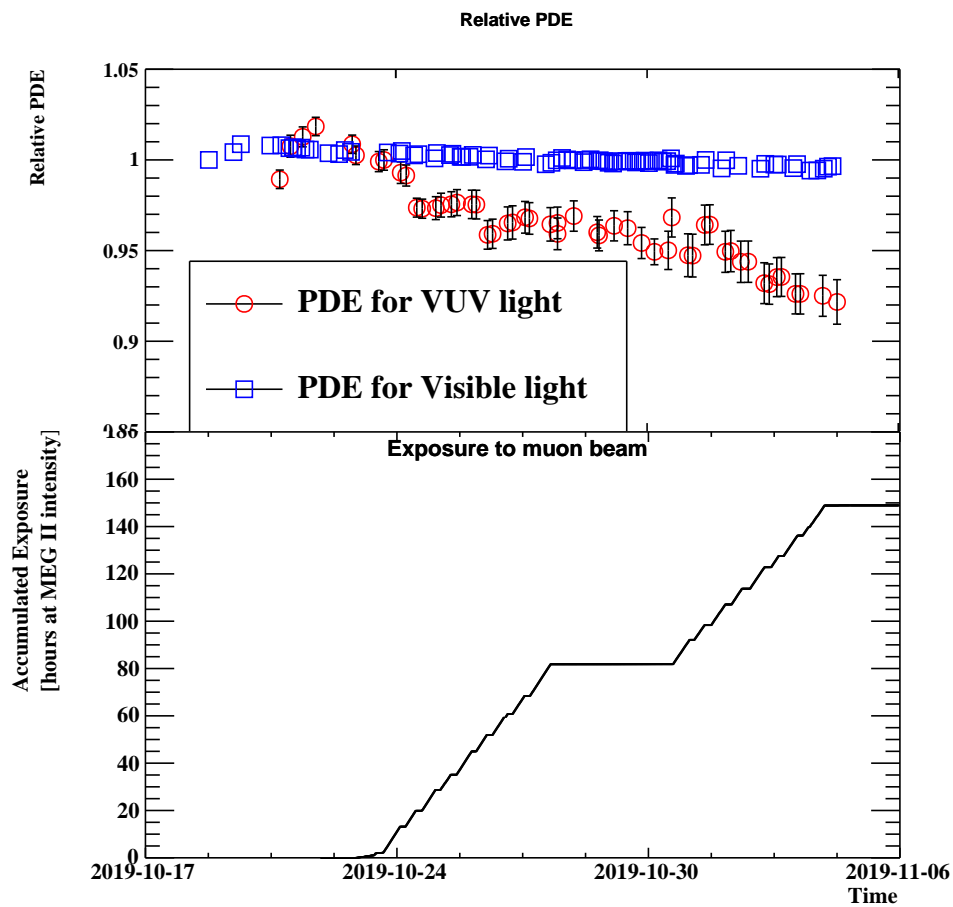


Figure 5.4: (top) Average MPPC PDE for visible light (blue) and VUV light in 2019 beam time. (bottom) Accumulated time of the muon beam usage period.

The PDE decreased from 0.125 to 0.080 at the beginning of a series of the commissioning runs as  $N_\mu$  evolves from zero to  $1 \times 10^{14}$ , while the PDE degradation in the latter half of the 2021 run was 0.052 to 0.045 as  $N_\mu$  evolved from  $3.2 \times 10^{14}$  to  $4.2 \times 10^{14}$ .

Compared to the decrease in the PDE for VUV light ( $\lambda = 175$  nm), the decrease of the PDE for visible light ( $\lambda = 430$  nm) was one order smaller, as shown in Fig. 5.4. Considering that the VUV-MPPC detects VUV photons by using avalanche amplification of the e-h pairs created in the vicinity of the interface, the observed damage is likely categorized as surface damage.

Fig. 5.5 shows the measured PDE at the beginning of 2021 as a function of the  $u$  position of the MPPCs. Since the PDE of MPPCs did not have a position dependence right after the construction of the detector, the observed position dependence shows the position dependence of the radiation damage from the installation. The magnitude of radiation damage has a large  $u$ -dependence, which looks correlated to the position dependence of VUV photon and gamma-ray dose based on MC simulations shown in Fig. 5.2. This implies that this radiation damage is caused directly or indirectly by radiation coming from the muon-stopping target. Neutrons are unlikely to be the source of the radiation damage because they come from upstream.

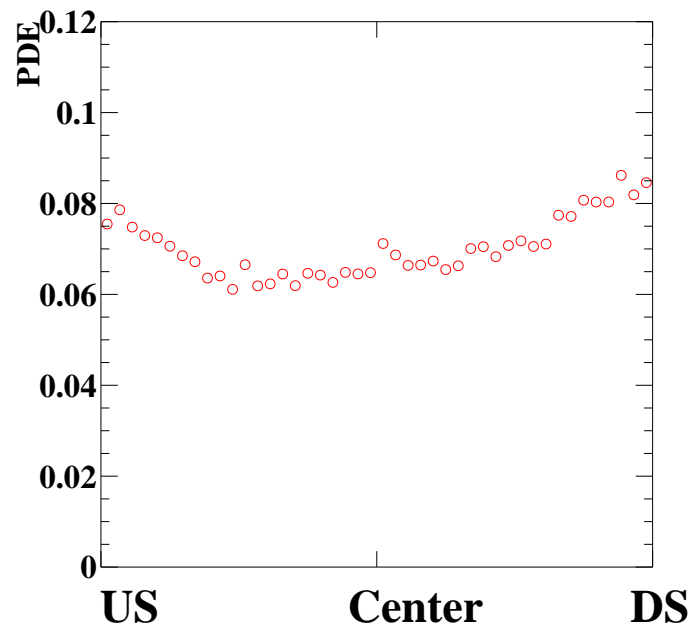


Figure 5.5: Average  $\epsilon_{\text{PD}}^{\text{VUV}}$  as a function of the  $u$  position of the MPPCs in the middle of the 2021 run. The MPPCs that were not read out in the commissioning runs until the 2021 run were used to calculate the average PDE at each  $u$  position.

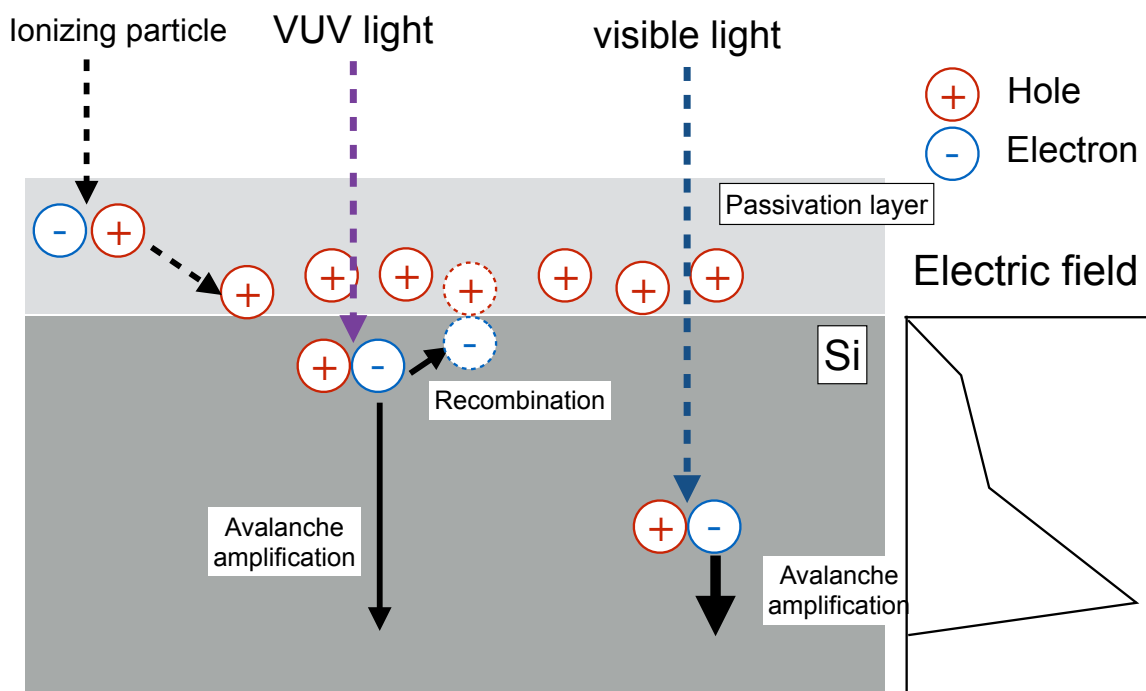


Figure 5.6: Schematic view of surface damage. Ionization makes e-h pairs in the passivation layer, and a fraction of holes remain in the layer (left). The remaining holes distort the electric field around the interface and enhance recombination (middle). This effect has little impact on visible light detection due to the long attenuation length (right).

Fig. 5.6 illustrates a suspected mechanism of the PDE degradation by the surface damage. Injection of the ionizing particles generates e-h pairs in the passivation layer, and a certain fraction of the holes remain while most electrons leave the passivation layer because of their high mobility and low trapping probability. The electric field around the interface is distorted by the remained holes, and it causes recombination with an electron produced by another incident photon. Since the VUV light creates e-h pairs in the vicinity of the interface due to its short attenuation length ( $\sim 6$  nm), recombination around the interface deteriorates the detection efficiency. On the other hand, the recombination probability is smaller for the e-h pairs created by visible light because of its relatively long attenuation length ( $\sim 180$  nm). If this hypothesis is correct, thermal annealing has the potential to recover the PDE. As in Ref. [74], the thermal excitation can de-trap the holes in the interface state and restores the interface states so that the electrons from e-h pairs generated in the vicinity of the interface can reach the amplification region again.

Several irradiation tests were performed to reproduce and understand the radiation damage in a lab [3, 75, 76]. In these tests, neutrons, VUV photons, and gamma-rays were irradiated to VUV-MPPCs. However, a rapid decrease in the MPPC PDE was not reproduced as observed in the LXe detector. Therefore, it is not yet identified which particle induces the radiation damage, and the mechanism of the damage remains unknown.

### 5.3 Thermal annealing

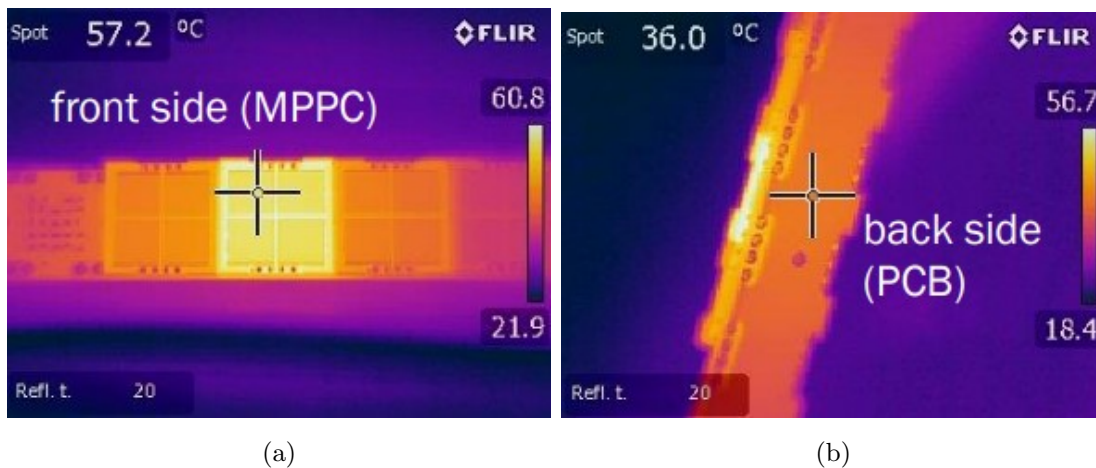


Figure 5.7: Images of (a) MPPC and (b) PCB taken by the thermal camera during the feasibility test of the thermal annealing. The temperature of the MPPC surface increased up to  $57.2^{\circ}\text{C}$  when that of the back of the PCB was heated to  $36.0^{\circ}\text{C}$ .

The strategy of thermal annealing was to raise the temperature of the MPPCs by using Joule heat produced by the current flowing through the MPPC. A combination of high reverse bias voltage and continuous intense LED light can produce high photo-electric current and heat on the MPPCs by Joule heat.

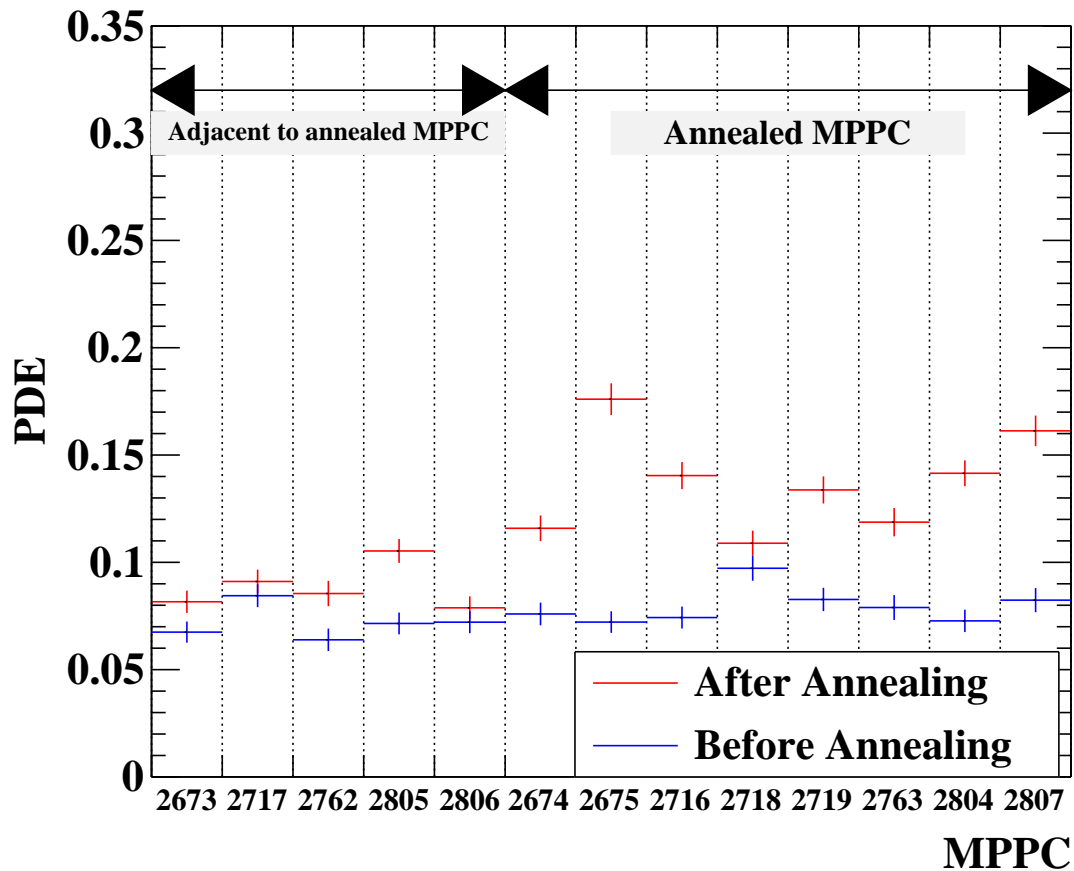


Figure 5.8: PDE of MPPCs before (blue) and after (red) the annealing in 2020. Five MPPCs on left were adjacent to the annealed MPPCs and moderately heated by the Joule heat of the annealed MPPCs. Eight MPPCs on right were annealed by applying high bias voltage and flowing high current.

One concern was the heat damage to the surrounding material. The CFRP that supports PCBs can be damaged when they are heated over  $45^{\circ}\text{C}$ . To avoid this damage, a feasibility check was carried out in a lab and then annealing tests for several damaged MPPCs in the detector were performed. In the following sections, the feasibility check including the annealing tests for damaged MPPCs is presented in Sec. 5.3.1 and the mass annealing for  $\sim 4,000$  MPPCs will be presented in Sec. 5.3.2.

### 5.3.1 Feasibility test

A spare MPPC was attached to a spare PCB to reproduce the setup in the LXe detector, and it was illuminated by a room light with a bias voltage applied. Its temperature was measured by a thermal imaging camera (FLIR E50 [77]) as shown in Fig. 5.7a and Fig. 5.7b. It was found that the MPPCs can be heated to  $62^{\circ}\text{C}$  with the bias voltage of 65 V and the induced current of 20 mA, while keeping the back side of the PCB to  $39^{\circ}\text{C}$ .

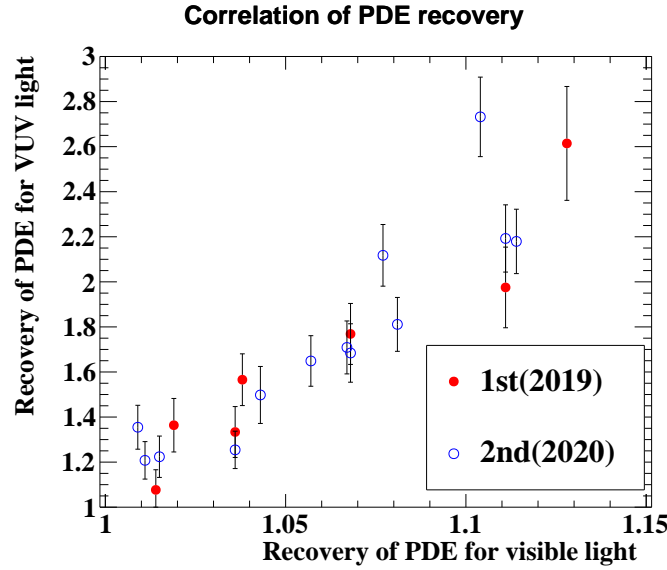


Figure 5.9: Correlation between the recovery of  $\epsilon_{\text{PD}}^{\text{VUV}}$  and  $\epsilon_{\text{PD}}^{\text{vis}}$ . The results of the first annealing in 2019 and the second annealing in 2020 are shown in red and blue, respectively.

Table 5.3: Configuration of annealing before the 2020 run.

MPPC ID	current	voltage	time
2763	15–21 mA	67–69 V	488 hours
2716	15–21 mA	68 V	215 hours
2807	22 mA	69 V	126 hours
2718	20 mA	67 V	69 hours
2719	22 mA	69 V	84 hours
2804	20–22 mA	68–69 V	302 hours
2674	20 mA	67 V	61 hours
2675	21 mA	68–69 V	157 hours

Before the beam time in 2019 and 2020, annealing tests were performed for a small number of damaged MPPCs in the LXe detector. During the test, the LXe was transferred to a storage tank, and the detector was filled with gXe at room temperature. The bias voltage was applied to each MPPC by a dedicated HV module that can supply sufficient current ( $> 20$  mA), and the LEDs in the cryostat were used as light sources. Seven MPPCs in 2019 and eight MPPCs in 2020 were annealed one by one at different bias voltages. The annealing condition in 2020 is summarized in Table 5.3. After the detector was filled with LXe, the PDE for VUV light  $\epsilon_{\text{PD}}^{\text{VUV}}$  was measured. It was difficult to measure the PDE with alpha sources at room temperature due to the large dark current.

A significant recovery of the PDE was observed for the annealed MPPCs, as shown in Fig. 5.8. The amount of the recovery was correlated to the applied current and duration of the annealing. The PDE after annealing was 0.11–0.18 for annealed MPPCs, while the PDE before the annealing

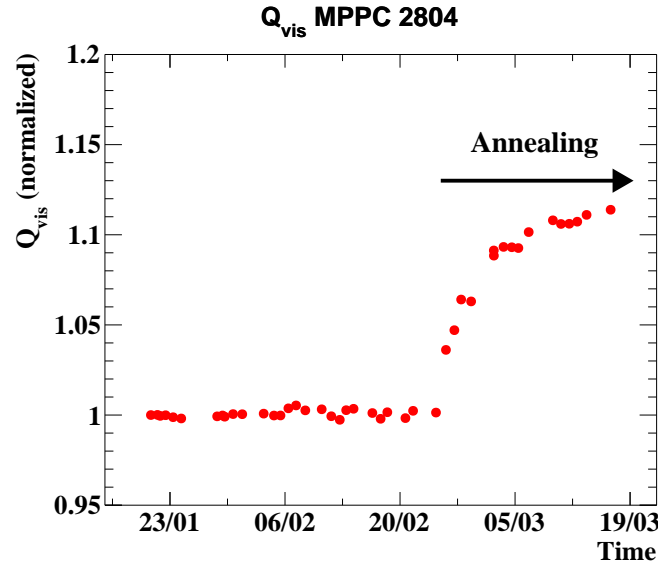


Figure 5.10: MPPC charge ( $Q_{\text{vis}}$ ) with stable LED light in the annealing period. The annealing started on 25th February and ended on 19th March because of the limitation of time. The value is normalized to one at the beginning of the annealing.  $Q_{\text{vis}}$  increased by thermal annealing.

was 0.07.

The recovery of the  $\epsilon_{\text{PD}}^{\text{VUV}}$  was also correlated with the recovery of the  $\epsilon_{\text{PD}}^{\text{vis}}$ , as shown in Fig. 5.9. This correlation can be explained by a hypothesis that the restoration of the surface state gives more impact on the VUV light detection but less on the visible light detection because a fraction of visible light generates an e-h pair close to the interface between Si and the passivation layer. The recovery of  $\epsilon_{\text{PD}}^{\text{vis}}$  was about 10% of the recovery of  $\epsilon_{\text{PD}}^{\text{VUV}}$ . This ratio is comparable with the ratio between the decrease of  $\epsilon_{\text{PD}}^{\text{vis}}$  and  $\epsilon_{\text{PD}}^{\text{VUV}}$  under the muon beam shown in Fig. 5.4. At the second annealing test in 2020, the recovery of the charge under stable LED light was monitored and used to monitor the progress of the annealing as shown in Fig. 5.10.

Fig. 5.11 shows the time variation of PDE for annealed MPPCs. The PDE degradation of the annealed MPPC was not faster than that of non-annealed MPPCs, considering the PDE of the annealed MPPC decreased from 0.11 down to 0.08 as the  $N_{\mu}$  evolved up to  $2 \times 10^{14}$  after the annealing whereas the PDE of the MPPCs decreased from 0.125 to 0.060 as the  $N_{\mu}$  evolved to the same number.

### 5.3.2 Mass annealing

The 2022 physics run was the first long-term run, and in order to take full advantage of the beamtime to acquire physics data, it was necessary to recover the MPPC PDE significantly from its value at the end of 2021 (0.045) by annealing.

An alternative method of annealing using warm water was tested during the shutdown period before the 2022 beamtime. This method delivers heat to the MPPCs by circulating warm water of about 45°C through a liquid nitrogen circulation line attached directly to the outer surface

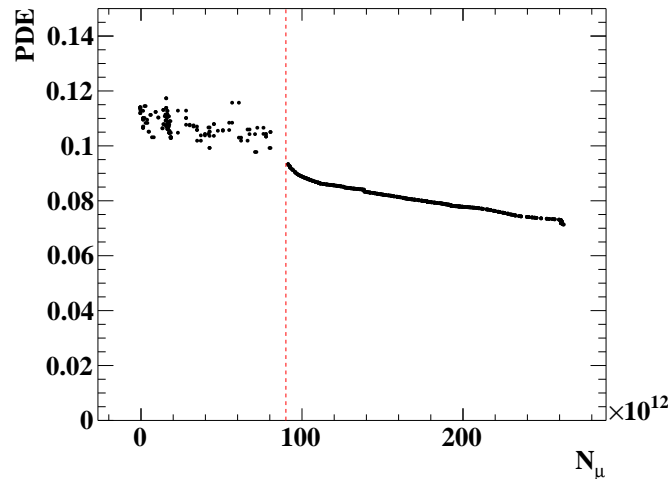


Figure 5.11: Average PDE of annealed MPPCs as a function of the accumulated number of stopped muons at the target after the annealing. A red dotted line indicates the beginning of the 2021 run.

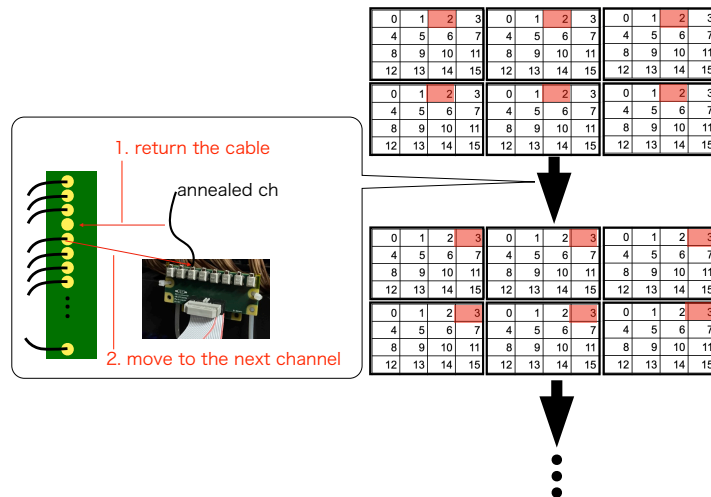


Figure 5.12: Cabling scheme of the Joule annealing. Eight MPPC channels that have the same channel number in WaveDREAM boards are bundled to the same port of the current source and annealed at once.

of the inner cryostat of the detector. The temperature of the detector was monitored by the thermometers installed in the detector. The potential advantage of this method was that it might recover the PDE of most MPPCs quickly and at once. The warm water annealing was carried out from 20th January to 30th March. The temperature of the detector reached from room temperature (17°C) to 45°C in late February. The recovery of the PDE of the MPPC was estimated indirectly by measuring the time variation of charge under LED light. The average PDE for the annealed MPPCs recovered from 0.057 to 0.075. However, since the recovery rate was too slow to reach a sufficient level ( $\sim 15\%$ ) to complete a long-term run in 2022, the warm

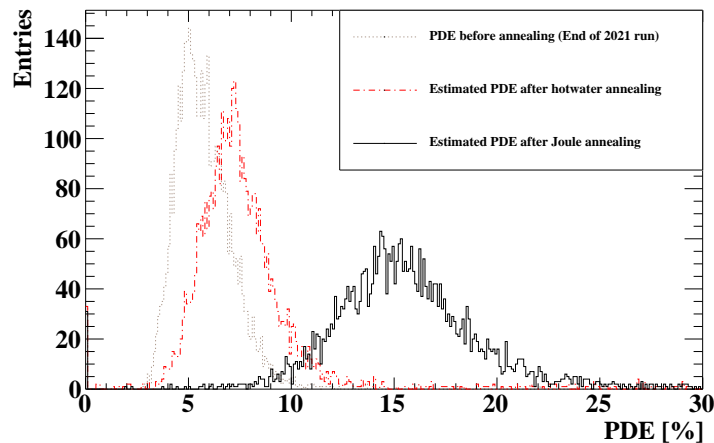


Figure 5.13: MPPC PDE before the annealing (grey), after the warm water annealing (red), and after the Joule annealing (black). The PDE was estimated by the charge for the LED light.

water annealing was stopped to start the Joule heat annealing. The slow recovery rate was probably because the temperature of the annealing was too low.

A dedicated current source was prepared to anneal many MPPCs at once. The specification of the current source is summarized in Table 5.4. Since the current of 30 mA is required to anneal a single MPPC, and a single port can provide 250 mA current at maximum, eight channels connected in parallel can be annealed by the output of a single port at the same time. This scheme allows us to anneal 240 MPPCs simultaneously. By repeating a set of the annealing for 240 MPPCs by 16 times, most MPPCs were annealed except for some MPPCs that remain non-annealed for reference. The scheme of the cabling is shown in Fig. 5.12. An MPPC from each WaveDREAM board was annealed in one set of annealing. This scheme was advantageous from a safety point of view because it allowed to avoid overheating the MPPCs and their support structure by selecting MPPCs distant from each other. A set of the annealing process consists of 26 hours of annealing, 5.5 hours for cabling and cooling for the measurement, and 0.5 hour of data acquisition. In the data acquisition, the charge under a fixed intensity of the LED light was measured by the standard DAQ system to monitor the recovery of the PDE indirectly.

Table 5.4: Specification of the current source for the Joule annealing.

The number of ports	30
Voltage [V]	60–80
Current [mA]	0–250
Manufacturer	Araki Denki inc.

As a result, the PDE recovered from 0.075 to 0.14 on average, as shown in Fig. 5.13. Thanks to this significant recovery, the MPPCs can be operated with  $\text{PDE} > 0.04$  at a beam rate of  $5 \times 10^7$  for five months based on the degradation rate in 2017–2021 runs shown in Fig. 5.3.

## 5.4 Impact on the experimental sensitivity

The impact of the low MPPC PDE on the detector performances was already discussed in Ref. [2]. Fig. 5.14 shows the position resolution in the simulation at different MPPC PDE. The degradation of the position resolution is expected mainly for deep gamma-ray hits. This is because the contribution from the statistical uncertainty becomes larger for the deep events due to the smaller number of photoelectrons on the inner face, while the contribution from the event-by-event fluctuation depending on the direction of the shower development is dominant for the shallow events.

Fig. 5.15 shows the energy resolution as a function of the PDE. Since the measured energy resolution is limited by an unknown term of 1.5%, it is added to the simulated energy resolution. The MPPC signal contributes to one-third of the total energy, and the statistical fluctuation is only 0.2%. Since the statistical contribution to the energy resolution is small compared to the unknown term (1.5%) and the expected resolution (1.0%), the impact of the degradation of the energy resolution is limited.

With a low PDE, the worse S/N ratio and the larger statistical fluctuation deteriorate the timing resolution of a single photosensor. The degradation of the S/N ratio can be recovered to some extent by using the amplifier mounted on the WaveDREAM board. Since the noise on the input of the amplifier is limited, the noise level is not proportional to the amplifier gain, and the relative noise level is better with amplification. Fig. 5.16a shows the time resolution defined only by the MPPCs as a function of the MPPC PDE, together with the resolution defined only by the PMTs. When the MPPC PDE is lower than 0.10, the timing resolution defined by the PMTs (55 ps) is better than the resolution defined by the MPPCs and dominates the overall resolution. As a result, the impact of the PDE degradation on the overall resolution is moderate, as shown in Fig. 5.16b.

Fig. 5.17 shows the experimental sensitivity evaluated in Ref. [2] as a function of MPPC PDE. The impact of the PDE degradation on the sensitivity is limited to a few percent as long as PDE is larger than 0.04. If the MPPC PDE can be recovered up to 0.15 by annual annealing before the data-taking of each year, the MPPC PDE can stay higher than 0.04 for the whole year when the muon beam intensity is lower than  $5 \times 10^7/s$ . With this beam intensity, the number of stopped muons will be increased up to  $3.9 \times 10^{14}$ . In conclusion, the impact of the radiation damage of the MPPC PDE on the physics performance of the MEG II experiment is less than a few percent.

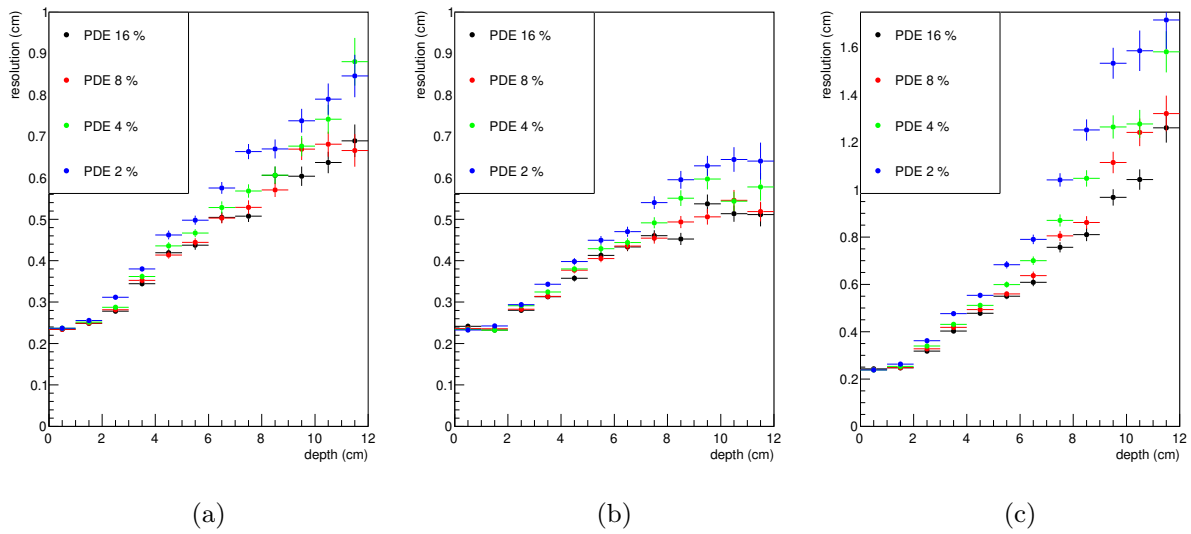


Figure 5.14: Position resolution in the simulation as a function of the conversion depth at various PDE for (a) u, (b) v, and (c) w direction [2].

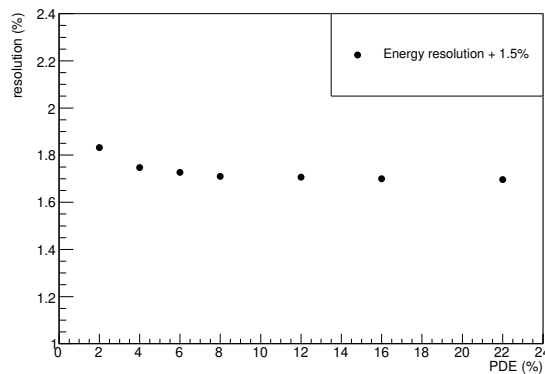


Figure 5.15: Energy resolution as a function of the MPPC PDE [2]

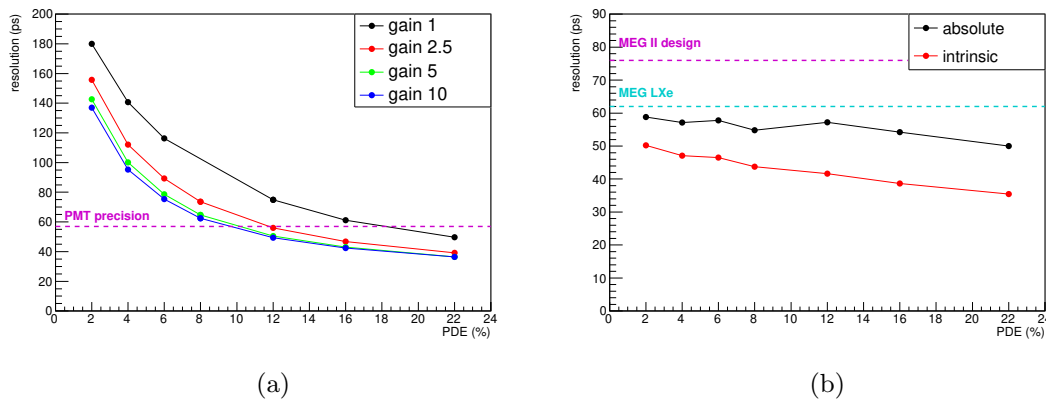


Figure 5.16: (a) Timing precision with all the MPPCs as a function of the MPPC PDE [2]. (b) Expected timing resolution as a function of the MPPC PDE [2].

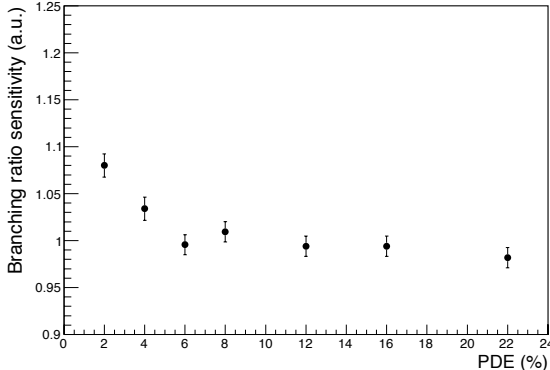


Figure 5.17: Experimental sensitivity as a function of the MPPC PDE [2].

## Chapter 6

# Position Resolution

The high-resolution measurement of the opening angle  $\Theta_{e+\gamma}$  requires a good position resolution of the LXe detector. The direction of a gamma ray is determined from the vertex position at the target given by the reconstructed positron track and the position of the gamma ray measured by the LXe detector. The MEG II LXe detector is expected to have a better position resolution than the MEG LXe detector thanks to the granular readout of the inner face by the new small VUV-MPPCs. This chapter describes the evaluation of the position resolution of the LXe detector by a combination of an MC simulation and measurement using a collimator with thin slits. In Sec. 6.1, the position reconstruction method is explained. In Sec. 6.2, the method and results of the position resolution measurement using the collimator and the 17.6 MeV CW-Li gamma rays are explained.

### 6.1 Position Reconstruction

The position of the first conversion point of the gamma ray  $\vec{x} = (u_{\text{hit}}, v_{\text{hit}}, w_{\text{hit}})$  in the LXe detector is reconstructed by the light distribution of the MPPCs.

Firstly, the hit position is reconstructed by a method called “projection fitting”. In this method, a symmetric function is fitted to the projected  $N_{\text{pho}}$  distribution in the  $u$  and  $v$  direction. It provides a quick reconstruction of the gamma-ray position for the subsequent reconstruction with a method called “chi-square fitting”.

In the chi-square fitting method, an expected light distribution is fitted to the light distribution around the peak such that the following  $\chi_{\text{pos}}^2$  is minimized.

$$\chi_{\text{pos}}^2(\vec{x}) = \sum_{i \in \text{region}} \frac{(N_{\text{pho},i} - C \times \Omega_i(\vec{x}))^2}{\sigma_{\text{pho},i}^2} \quad (6.1)$$

$$\sigma_{\text{pho},i} = N_{\text{pho},i} / \sqrt{N_{\text{phe},i}} \quad (6.2)$$

where  $C$  is the scale of light distribution,  $\Omega_i(\vec{x})$  is the solid angle at position  $\vec{x}$  subtended by the photosensor,  $\sigma_{\text{pho},i}$  is the uncertainty of  $N_{\text{pho}}$  for each photosensor and defined as Eq. 6.2. Fig. 6.1a shows the distribution of the measured  $N_{\text{pho}}$  and the expected number of photons  $N_{\text{exp}} = C \times \Omega(\vec{x})$ .

Table 6.1: The criteria of the MPPCs used for the fitting. The MPPCs in a circular region with a radius of the distance threshold around the position reconstructed by the projection fitting were used for the chi-square fitting.

Reconstructed $w$	Distance threshold
$0 < w < 3$ cm	3 cm
$3$ cm $\leq w < 5$ cm	5 cm
$5$ cm $\leq w < 7$ cm	7 cm
$7$ cm $\leq w < 9$ cm	9 cm
$9$ cm $\leq w < 12$ cm	12 cm
$12$ cm $\leq w < 38.5$ cm	15 cm

The MPPCs in a circular region around the calculated position from the projection fitting with a certain radius are used for the chi-square fitting as shown in Fig. 6.1b. The radius of the circular region depends on the reconstructed  $w$  as shown in Table 6.1. This is because the width of the peak in the light distribution depends on  $w$ . Only MPPCs close to the hit are used for a shallow gamma-ray hit with a narrow peak, while a large number of MPPCs are used for a deep gamma-ray hit with a broad peak.

This fitting is based on the assumption that the number of detected photons by each photosensor is proportional to the solid angle at the interaction point subtended by the photosensor. In reality, the source of scintillation photons has a finite size because an electromagnetic shower is formed in a correlated direction with the direction of the incoming gamma-ray. The position from the fitting,  $(u_{\text{fit}}, v_{\text{fit}}, w_{\text{fit}})$  is biased in the direction of the shower development as shown in Fig. 6.2. Two corrections are applied to the position from the fitting to take this effect into account.

One is called “global correction”, which corrects position-dependent biases. Since the shower development is correlated to the gamma-ray momentum, the deviation  $\Delta u = u_{\text{fit}} - u_{\text{hit}}$  is correlated with  $u_{\text{fit}}$  as shown in Fig. 6.3a. The relation between the deviation and the fit position is corrected by the relation in the MC simulation.

The other correction is “shower correction”, which corrects the bias from the event-by-event fluctuation of shower development. Fig. 6.3b shows the relation between the deviation  $\Delta u = u_{\text{fit}} - u_{\text{hit}}$  and the fit position with different ranges. As with the global correction, the event-by-event shower fluctuation is corrected with the relation in MC.

This reconstruction method provides uniform position resolutions over the detector. Fig. 6.4 shows the position dependence of the position resolution for the signal gamma ray in the MC simulation. The variation of the position resolutions in all three dimensions was 0.01 cm in RMS in the acceptance region ( $|u| < 23.9$  cm,  $|v| < 67.9$  cm), which is small compared to the position resolution.

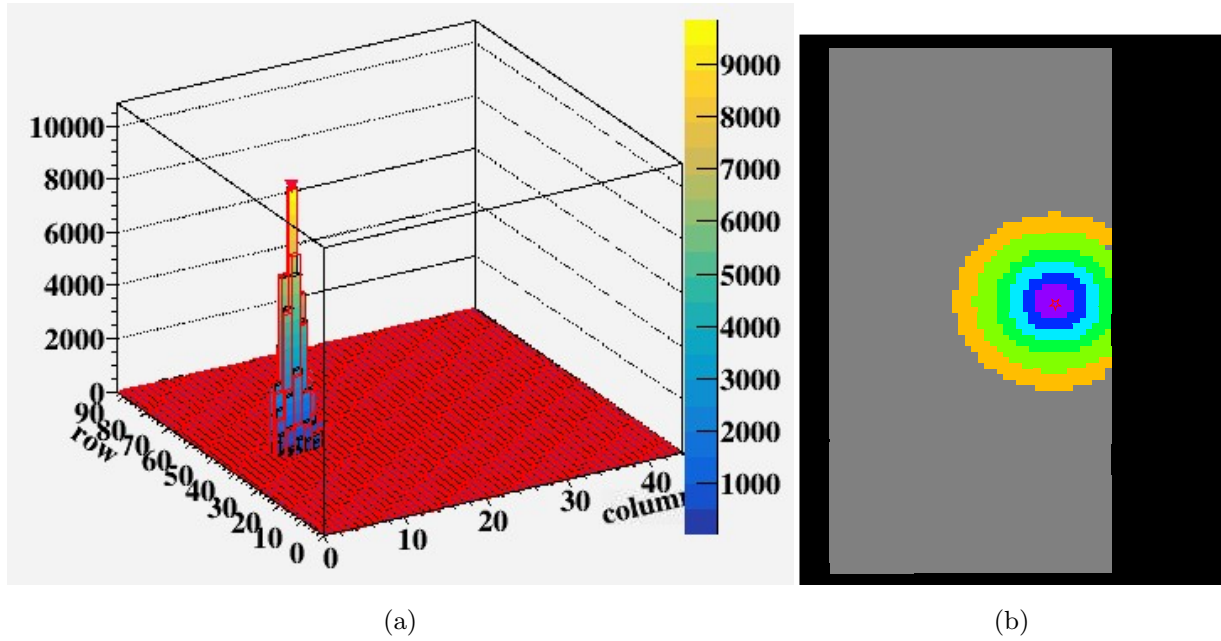


Figure 6.1: (a) Measured  $N_{\text{pho}}$  distribution and the expected (red) distribution from the chi-square fitting. (b) The MPPC region for the chi-square fitting of the  $N_{\text{pho}}$  distribution for a gamma-ray event. The MPPCs in the circular region around the reconstructed position from the projection fitting (red) are selected.

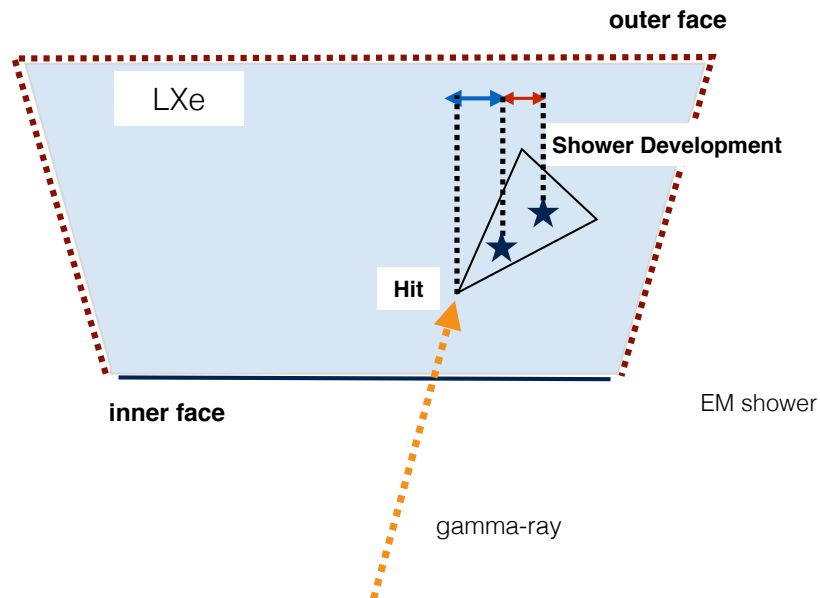


Figure 6.2: Shower development in the detector. An electromagnetic shower develops in a correlated direction with the momentum of the incoming gamma-ray, and the fit position is biased to the direction. The distance between the hit position  $x_{\text{hit}}$  and the position from the fitting  $x_{\text{fit}}$  (blue arrow) is calculated with the global correction with  $x_{\text{fit}}$  and the distance between the positions from different fit regions (red arrow).

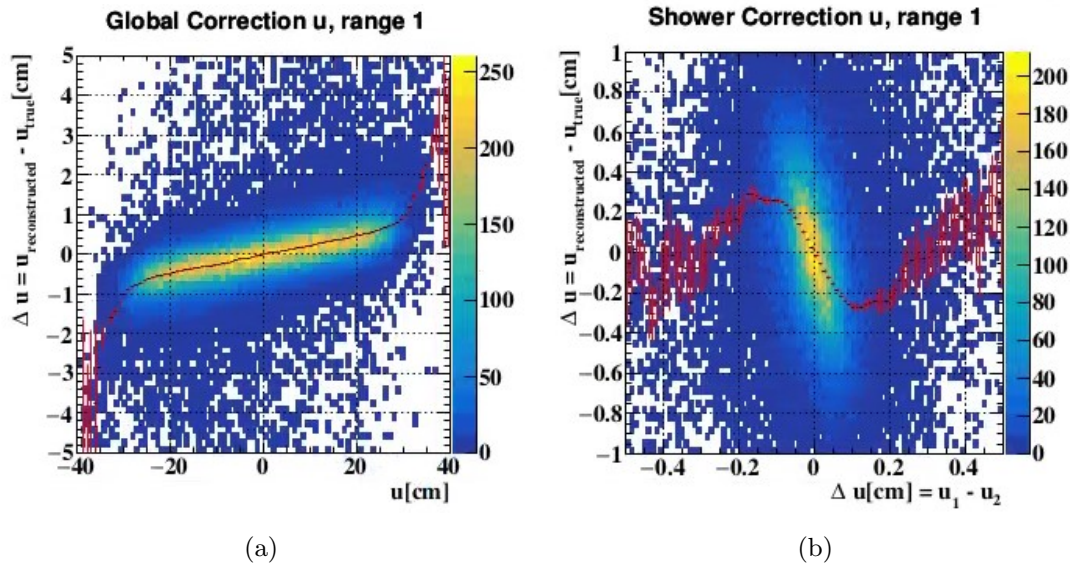


Figure 6.3: The (a) global and (b) shower correction for  $u$  position. The global correction is applied based on the position from the fitting  $u_{fit}$ , and the shower correction is based on the difference of the position fitted with different ranges.

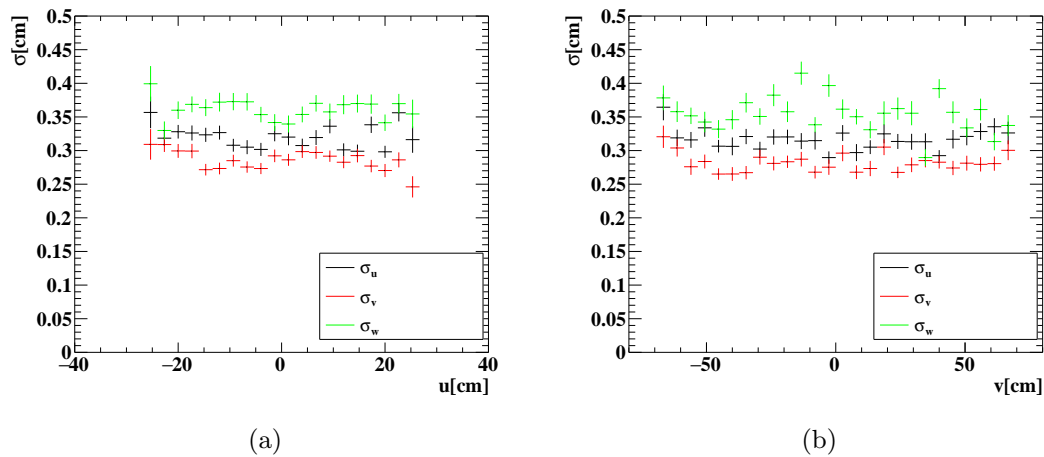


Figure 6.4: The position resolution for the signal gamma ray in  $u$  (black),  $v$  (red), and  $w$  (green) direction as a function of (a)  $u$  and (b)  $v$  in MC simulation.

## 6.2 Resolution Measurement

### 6.2.1 Principle

The position resolution was measured using a collimator and the 17.6 MeV gamma ray from the CW-Li setup. Fig. 6.5 shows the schematics of the resolution measurement. The position distribution of incoming gamma rays is shaped with the collimator installed between the detector

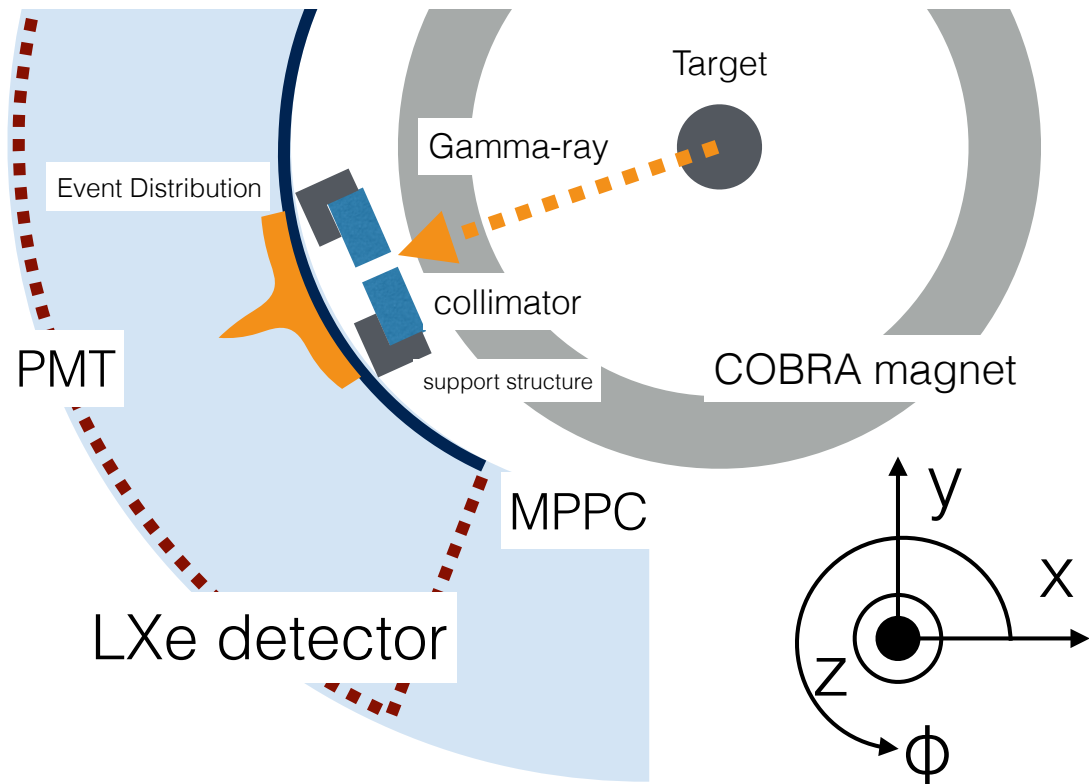


Figure 6.5: Schematic view of the position resolution measurement. The collimator is installed between the detector and the magnet. The position distribution of gamma rays (orange) has a peak structure for each slit.

and the COBRA magnet. Since the observed position distribution  $F(x_{\text{rec}})$  can be expressed as,

$$F(x_{\text{rec}}) = F(x_{\text{true}}) \oplus \sigma_x, \quad (x = u, v) \quad (6.3)$$

where  $x_{\text{true}}$  is the hit position distribution estimated from an MC simulation with the measured geometry of the setup, and  $\sigma$  is the position resolution. The resolution can be extracted by fitting the  $x_{\text{true}}$  distribution smeared by a certain resolution  $\sigma_x$  to the measured distribution  $F(x_{\text{rec}})$ .

## 6.2.2 Measurement setup

This method was also adopted in the MEG experiment. Fig. 6.6 shows the collimator used in the MEG experiment. It had wide slits of 1 cm and narrow spacing between slits. The overlap between the peak structures in the position distribution would prevent the precise measurement of the position resolution.

A new lead collimator was designed as shown in Fig. 6.7 and created as shown in Fig. 6.8. The new collimator was  $240 \times 240 \times 25 \text{ mm}^3$  and had eight parallel slits. Each slit was 5 mm wide and 80 mm long, and the slit spacing was 50 mm so that the peak structures at the slits ( $\sigma \sim 2 \text{ mm}$ ) would not interfere with adjacent peaks when the peak is smeared by the detector resolution. The collimator was designed to measure the local dependence of the position resolution. The

slit spacing was not an integer multiple of the MPPC size (15 mm), and the two slit rows were offset from each other by 2.5 mm to locate the slits in the different positions with respect to the MPPC grid. The resolution in both  $u$  and  $v$  directions can be measured by changing the orientation of the collimator by  $90^\circ$ .

The collimator was installed between the COBRA magnet and the detector using a rigid support structure, as shown in Fig. 6.9. The collimator was fixed by screws and tapes to the support structure, and the support structure was fixed to the lateral flanges of the detector by screws. The collimator and the detector were aligned with a laser tracker (Leica, AT960 [67]) with a precision of  $\sim 100 \mu\text{m}$ . Then the detector was moved back by 8 cm from the ordinary position to avoid a conflict between the collimator and the magnet.

The geometry of the gamma-ray production vertex at the target, collimator, and the LXe detector was reproduced in a dedicated MC simulation for position resolution evaluation. The configuration of the MC simulation is summarized in Table 6.2.

Table 6.2: Configuration of the MC simulation for the resolution evaluation.

Energy of gamma-ray	17.62 MeV (72%) / 14.8 MeV (28%)
Range of emission angle $\phi_\gamma$	$185^\circ < \phi_\gamma < 205^\circ$
Range of emission angle $\theta_\gamma$	$-0.15 < \cos \theta_\gamma < 0.15$
Center position of vertex (x,y,z)[mm]	(-5, -1, -5)
Spread of vertex [mm]	6
Total number of simulated events	$1 \times 10^6$ ( $u$ ) / $4 \times 10^6$ ( $v$ )



Figure 6.6: Collimator for the position resolution measurement in the MEG experiment.

The advantage of using the gamma-ray from the CW-Li setup is that the vertex size is smaller than those for other gamma-ray sources, as shown in Table 6.3. The peak width of the position distribution is dominated by the vertex spot size if it is far larger than the slit width of 5 mm. It would make it difficult to estimate the position resolution since the uncertainty of the vertex size becomes another source of the uncertainty of the position resolution.

The measurement was performed at the end of the 2018 run. During the measurement,  $8 \times 10^4$  events were collected with a configuration to measure the resolution in the  $u$  direction, and  $2 \times 10^5$  events with the collimator rotated by  $90^\circ$  to measure the resolution in the  $v$  direction. A trigger was issued based on the amplitude of the summed waveform of 144 MPPCs back of the

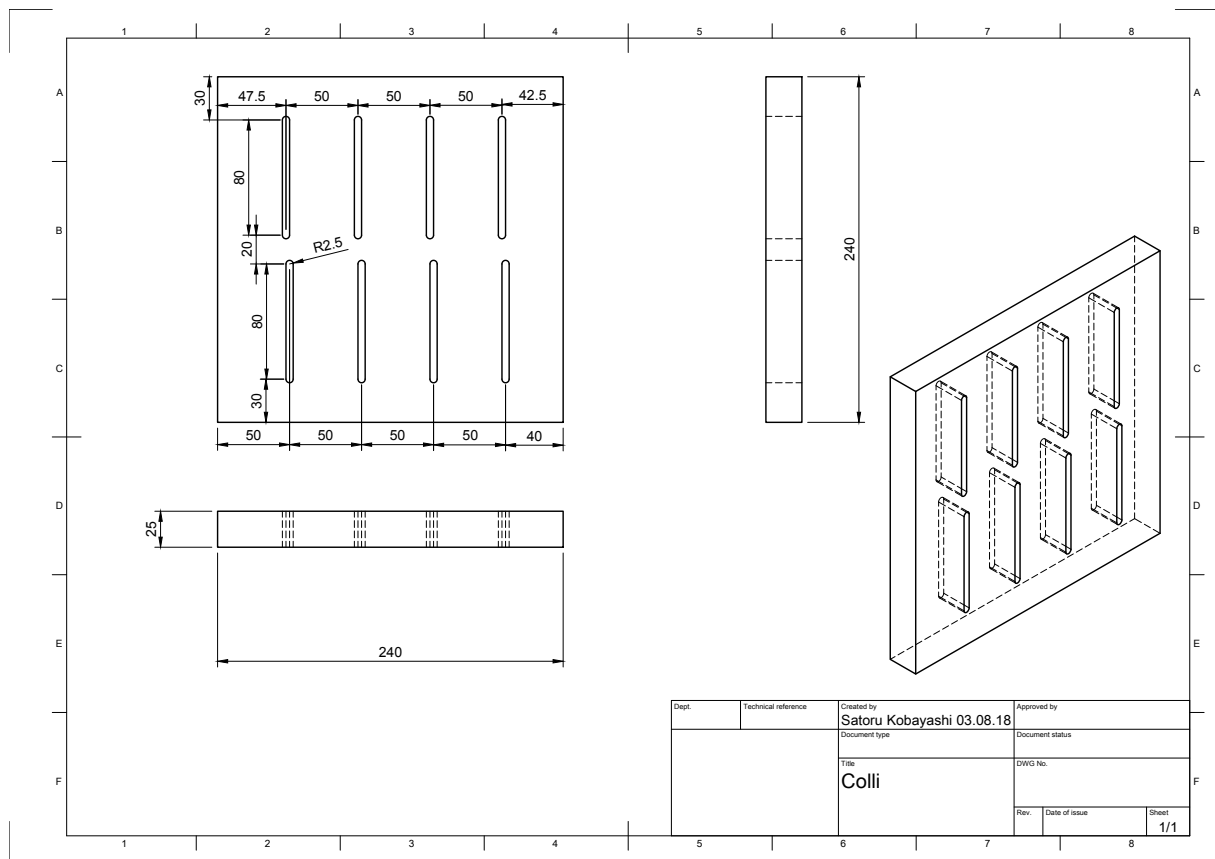


Figure 6.7: Design of the collimator for the position resolution measurement. The  $240 \times 240 \times 25$  mm<sup>3</sup> lead collimator had eight parallel slits.

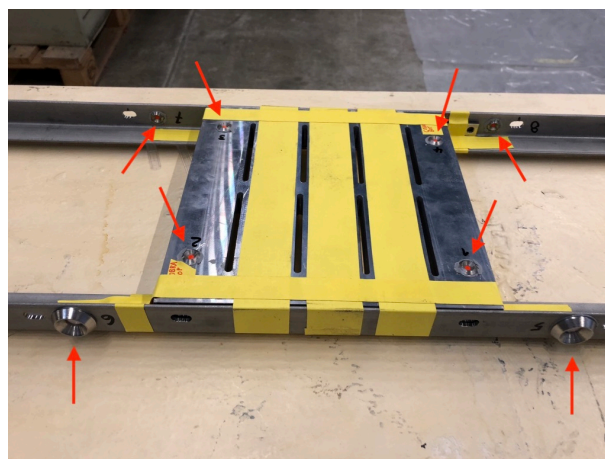


Figure 6.8: Collimator for the position resolution measurement. The collimator is fixed to the support structure by yellow tapes. The red arrows show the sockets for corner cubes to align the collimator with a laser tracker.



Figure 6.9: Installed collimator between the COBRA and the detector. The collimator was fixed by screws and tapes to the support structure, and the support structure was fixed to the lateral flanges of the detector by screws.

Table 6.3: Beam spot size of gamma-ray sources.

Source	$\sigma_{x,y}$ [cm]	$\sigma_z$ [cm]
CW-Li	0.6	0.6
$\pi^0 \rightarrow 2\gamma$	0.6	1
BG $\gamma$ -ray from muon decay	1	5

collimator to collect the gamma rays emitted in the direction of the collimator. Fig. 6.10 shows the 2D position distribution with the collimator in the horizontal and the vertical direction, respectively. The readout region covered four peaks formed by the collimator slits.

### 6.2.3 Resolution

Fig. 6.11a shows 1D-position distribution across a peak. The position resolution is evaluated by fitting a smeared distribution of the hit position  $F(x_{\text{true}})$  in the MC with a resolution  $\sigma_x$  to the measured distribution  $F(x_{\text{rec}})$  by a binned-likelihood method.

Fig. 6.11b shows the resolution in the  $v$  direction for each slit as a function of the depth  $w$ . The measured resolutions and their depth dependence for the four slits are consistent within the statistical uncertainties.

Fig. 6.12 shows the depth dependence of the  $u$  and  $v$  resolutions. The average resolutions for all four slits are shown. The uncertainty of the resolution consists of the statistical uncertainty of the fitting and the systematic uncertainty estimated from the variations among the results with the four slits. The measured position resolution and expected resolution from the MC simulation are consistent within the statistical uncertainty for the shallow region ( $w < 4$  cm). The measured resolution in the shallow region is twice better than the resolution with the MEG LXe detector, which used 2-inch PMTs for the scintillation readout of the inner face. The granular scintillation readout by the small VUV-MPPCs improves the position resolution for

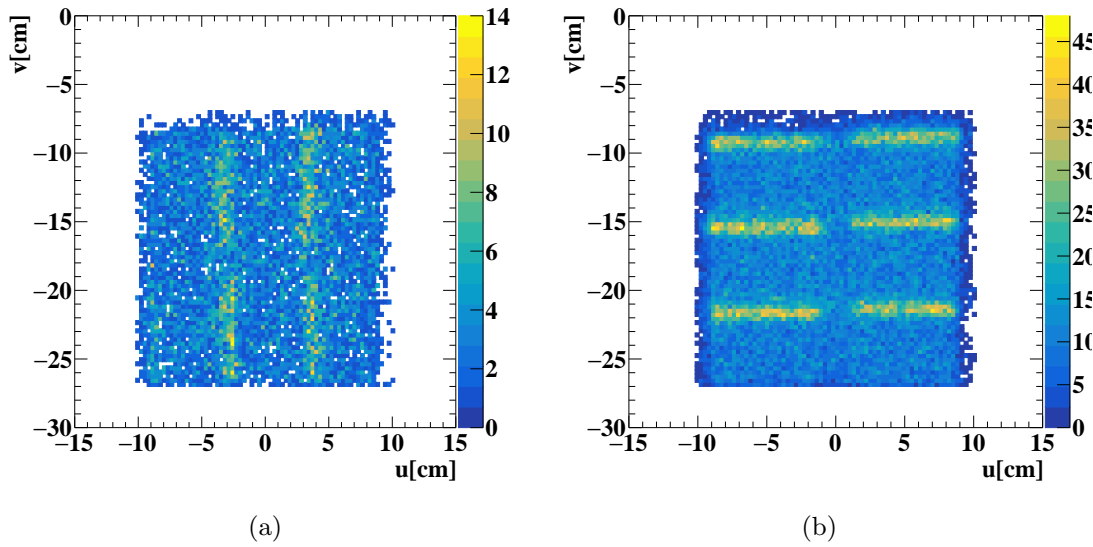


Figure 6.10: Position distribution in UV plane with the collimator with (a)  $u$  orientation and (b)  $v$  orientation. The readout region covers four or six peaks formed by the collimator slits.

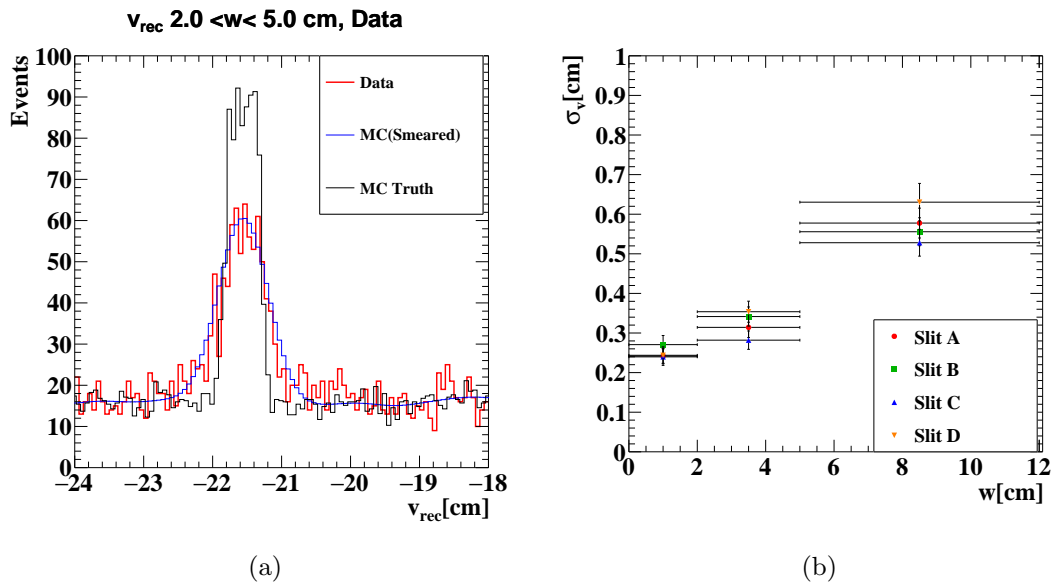


Figure 6.11: (a)  $v$  distribution at a slit of the collimator. The simulated position distribution (black) was smeared to fit the measured position distribution (red). (b) The position resolution measured with the peaks at four slits as a function of the conversion depth. The different colors show the different slits of the collimator.

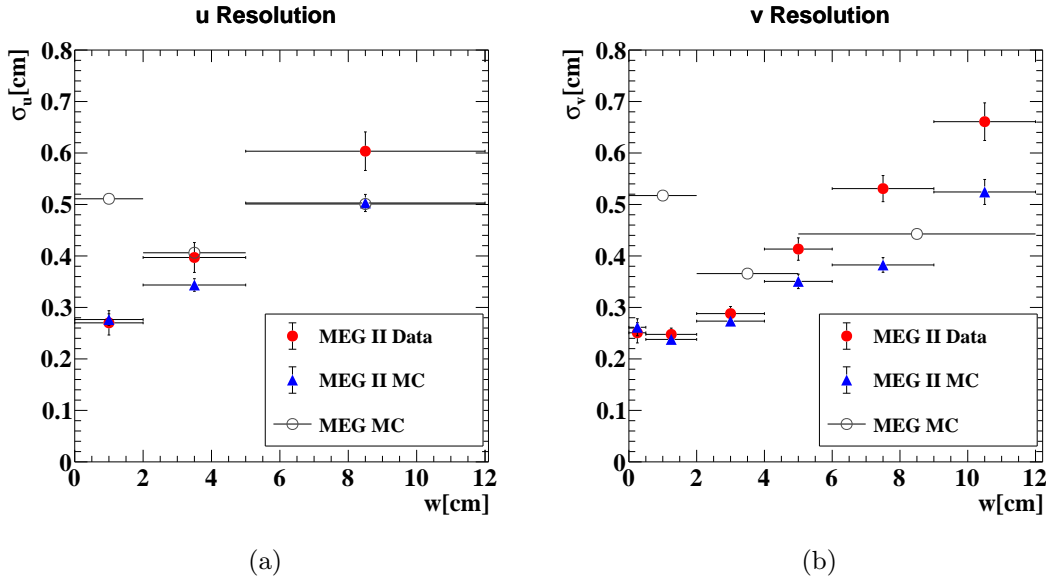


Figure 6.12: The position resolution in the (a)  $u$  and (b)  $v$  direction as a function of  $w$ . The resolutions measured at all four slits are combined. The measured resolution of the MEG II LXe detector (red) is worse than the expected resolution from the simulation (blue), but significantly better than the resolution in the MEG (black).

the gamma ray as expected. However, the resolution in the deep region ( $w > 4$  cm) is worse than the expected resolution. Fig. 6.13 shows the squared difference of the resolution between data and MC as a function of the conversion depth. The magnitude of the discrepancy is consistent between the two directions within the statistical uncertainty. The reason for the discrepancy is not understood. If the following situation is different between data and MC simulation, it might explain the worse resolution.

- Scattering or absorption in LXe.
- Reflection at the PMT holder.
- Size of the gamma-ray vertex at the target.

The degraded PDE of the MPPCs does not explain the disagreement of the position resolution. As shown in Fig. 5.14a–5.14c, the position resolution does not deteriorate with MPPC PDE  $> 0.04$ . Since the average PDE of MPPCs at the measurement was 0.08 at the measurement in 2018, the impact on the position resolution is too small to explain the disagreement.

Though the resolutions for  $u$  and  $v$  were measured, the measurement does not give the resolution in the  $w$  direction. Considering the depth-dependent discrepancy between MC and data is observed for both  $u$  and  $v$  direction, the resolution in  $w$  direction is likely to be worse than the simulated resolution as well. Therefore, the  $w$  resolution is estimated by adding the  $w$ -dependent discrepancy of the position resolution in  $u$  and  $v$  (Fig. 6.13) to the simulated position resolution in the  $w$  direction.

The position resolutions for the signal gamma-ray are estimated by using the resolution for

the signal gamma-ray in an MC simulation and the depth-dependent difference between the measured and expected resolution (Fig. 6.13). The position resolution for the signal gamma-ray in MC simulation is evaluated by fitting a sum of two Gaussian functions to the distribution of the position difference ( $\Delta x = x_{\text{rec}} - x_{\text{true}}$ ), as shown in Fig. 6.14. The estimated resolutions for signal gamma-ray in all directions ( $u, v, w$ ) are summarized in Fig. 6.15.

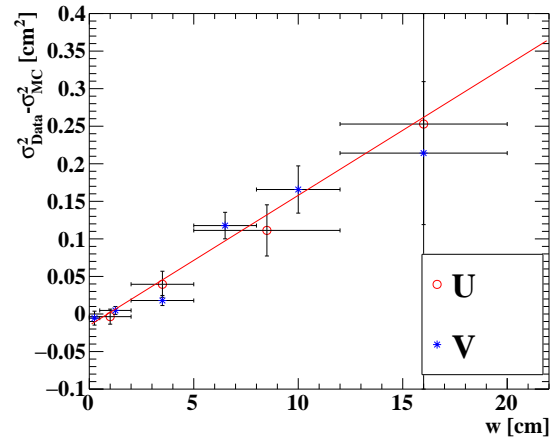


Figure 6.13: The squared difference of the position resolutions in the  $u$  (red) and  $v$  (blue) between data and MC as a function of the conversion depth  $w$ . The red line shows a linear fit to the dependence.

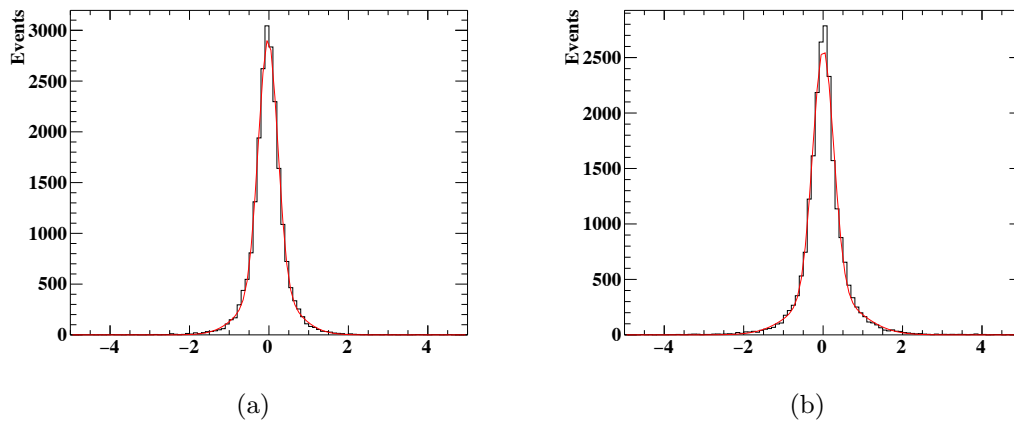


Figure 6.14: The distribution of the (a)  $\Delta u$  and (b)  $\Delta w$  for the signal gamma ray in the signal MC simulation. The red lines show the sum of Gaussian functions fitted to the distributions.

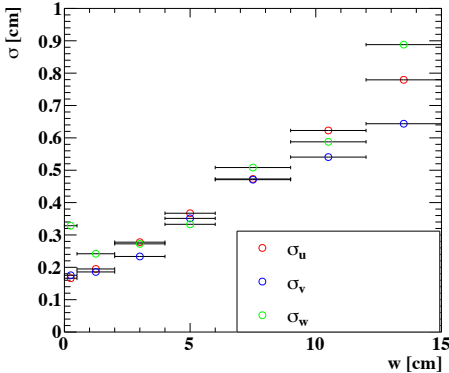


Figure 6.15: The core resolutions in  $u$  (blue),  $v$  (red), and  $w$  (green) directions as a function of  $w$ .

## Chapter 7

# Energy Resolution

In this chapter, the evaluation of the energy resolution with the datasets collected in 2021 is described. In Sec. 7.1, the energy reconstruction method is presented. In Sec. 7.2, the non-uniformity correction of the energy is discussed. In Sec. 7.3, the evaluation of the energy resolution using monochromatic gamma rays is discussed. In Sec. 7.4, the systematic uncertainties of the energy reconstruction is discussed. In Sec. 7.5, the summary of this chapter is given.

### 7.1 Reconstruction Algorithm

The basic idea of the reconstruction of gamma-ray energy  $E_\gamma$  is to sum up the number of photons collected by photosensors, correct the non-uniformity and the time variation, and scale it with an energy scale as

$$E_\gamma = C \times T(t) \times F(u, v, w) \times N_{\text{sum}} \quad (7.1)$$

$$N_{\text{sum}} = (r_{\text{MPPC}}(t) \times N_{\text{MPPC}} + N_{\text{PMT}}) \quad (7.2)$$

$$N_{\text{MPPC,PMT}} = \sum_{i \in \text{MPPC,PMT}} A_i \times F_{\text{face},i}(u, v, w) \times N_{\text{pho},i}, \quad (7.3)$$

where  $C$  is the energy scale from the number of photons to the energy and  $F(u, v, w)$  is a function to correct the position dependence. The weighted sum of the number of photons  $N_{\text{sum}}$  is given with the  $N_{\text{MPPC}}$  and  $N_{\text{PMT}}$  by Eq. 7.2.  $A_i$  is a constant correction factor of the light collection efficiency defined by the size of the insensitive area around each sensor divided by the size of its sensitive area.  $F_{\text{face},i}(u, v, w)$  is the weight assigned to each face to improve the uniformity, called face factor. The correction functions related to the time variation of the energy scale ( $T(t)$  and  $r_{\text{MPPC}}(t)$ ) were already discussed in Sec. 4.6.

In practice, the summation in Eq. 7.3 is carried out using a weighted sum waveform. Waveforms of all MPPCs and PMTs are separately summed up with given weights ( $w_i = \frac{A_i F_{\text{face},i}}{GF_{\text{EC}} \epsilon_{\text{PD}}}$ ), and pulses from off-timing pileup gamma-rays are identified and subtracted as later described in Sec. 10.1. The integrated charge of the weighted summed waveform with pileup subtracted is regarded as  $N_{\text{MPPC}}$  and  $N_{\text{PMT}}$ .

$F(u, v, w)$  and  $F_{\text{face},i}(u, v, w)$  are functions to correct the non-uniformity of energy response

in the detector. They were optimized using monochromatic gamma-rays as described in the following section.

## 7.2 Uniformity

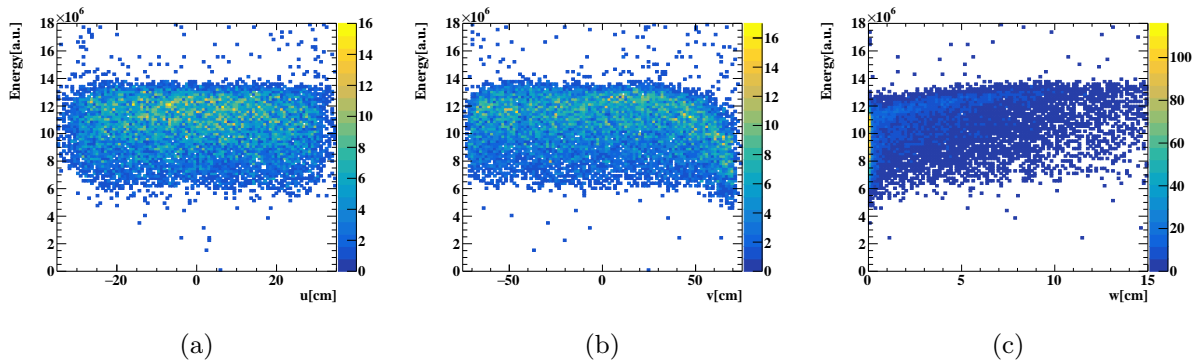


Figure 7.1: Position dependence of the reconstructed  $N_{\text{sum}}$  in (a)  $u$ , (b)  $v$ , and (c)  $w$  directions for the CW-Li gamma ray without any corrections.

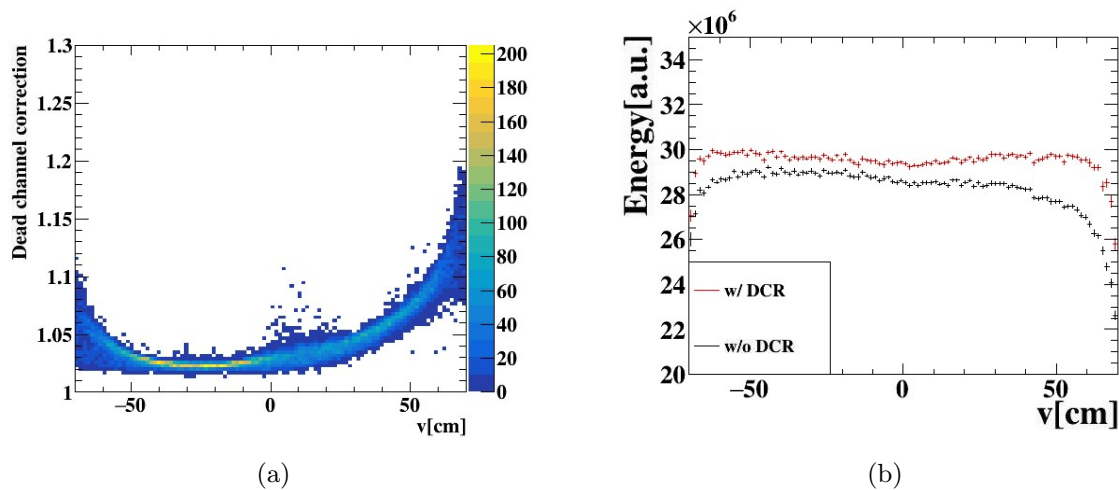


Figure 7.2: (a) The ratio of the reconstructed  $N_{\text{sum}}$  with to that without DCR as a function of the  $v$  position of 52.8 MeV gamma rays in an MC simulation. The ratio is enhanced at large  $v$  because the top face has relatively many unavailable PMTs. (b) Reconstructed  $N_{\text{sum}}$  peak as a function of the  $v$  position of the signal gamma ray in MC simulation with DCR (red) and without DCR (black).

Fig. 7.1 shows the position dependence of the  $N_{\text{sum}}$  with active photosensors without any non-uniformity correction. In other words,  $F(u, v, w) = 1$  and  $F_{\text{face},i}(u, v, w) = 1$  and  $n_{\text{pho},i}$  is zero for dead photosensors. There is a large asymmetric non-uniformity, particularly in the  $v$  direction. The reconstructed  $N_{\text{sum}}$  close to the top face is lower than that in the central part by  $\sim 40\%$ . The non-uniformity of the reconstructed  $N_{\text{sum}}$  comes from several reasons, such as the

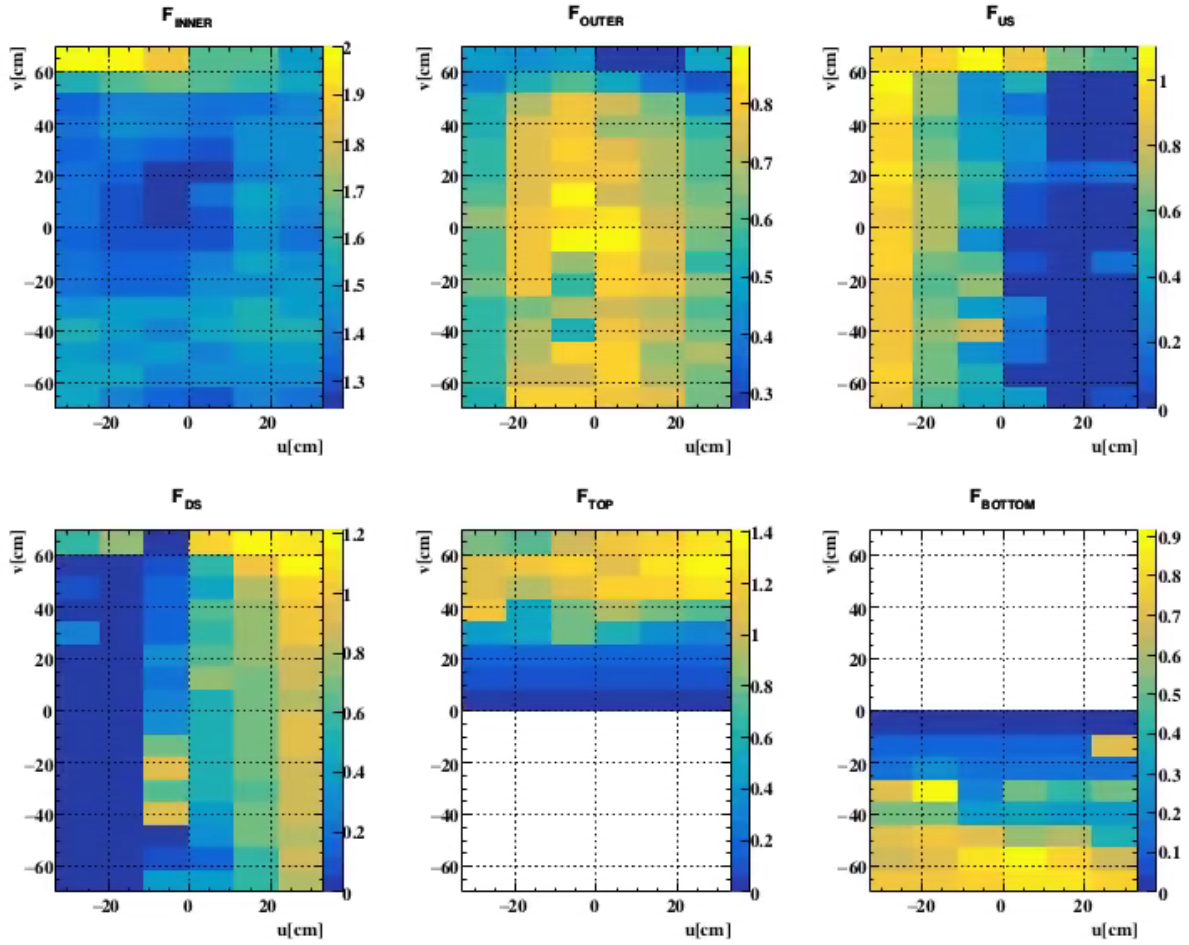


Figure 7.3: The position dependence of the face factor of all faces on  $u$ - $v$  plane. The CW-Li dataset is divided into  $6 \times 16$  sections depending on the  $(u, v)$  position of gamma rays and a set of the face factors is optimized so that the spectrum of the weighted sum of the  $N_{\text{sum}}$  has a sharp peak. The face factors of the top and bottom faces are set to zero where the gamma-ray position is far from the faces ( $v < 0$  cm for the top face and  $v > 0$  cm for the bottom face).

position dependence of light collection efficiency, the systematic bias of sensor calibration, and the reflection at the liquid level.

One of the major causes of the position dependence of the light collection efficiency is the existence of dead channels. As shown in Fig. 3.2b, the detector had  $\sim 1\%$  dead photosensors in the 2021 run. In particular, the dead channels on the top face are localized in the first row, which would detect more photons than other channels in the same face. To mitigate the non-uniformity from the dead channels, the  $N_{\text{pho}}$  of a dead channel was reconstructed from the  $N_{\text{pho}}$  of the surrounding channels in the same face and closer to the dead channel than 20 cm as

$$N_{\text{pho,dead}} = \Omega_{\text{dead}}(u, v, w) \times \frac{\sum_i N_{\text{pho},i}}{\sum_i \Omega_i(u, v, w)}, \quad (7.4)$$

where  $\Omega_{\text{dead}}(u, v, w)$  is the solid angle at the gamma-ray hit position  $(u, v, w)$  subtended by a dead channel,  $\Omega_i(u, v, w)$  is that by the  $i$ -th surrounding channel, and  $N_{\text{pho},i}$  is the number of

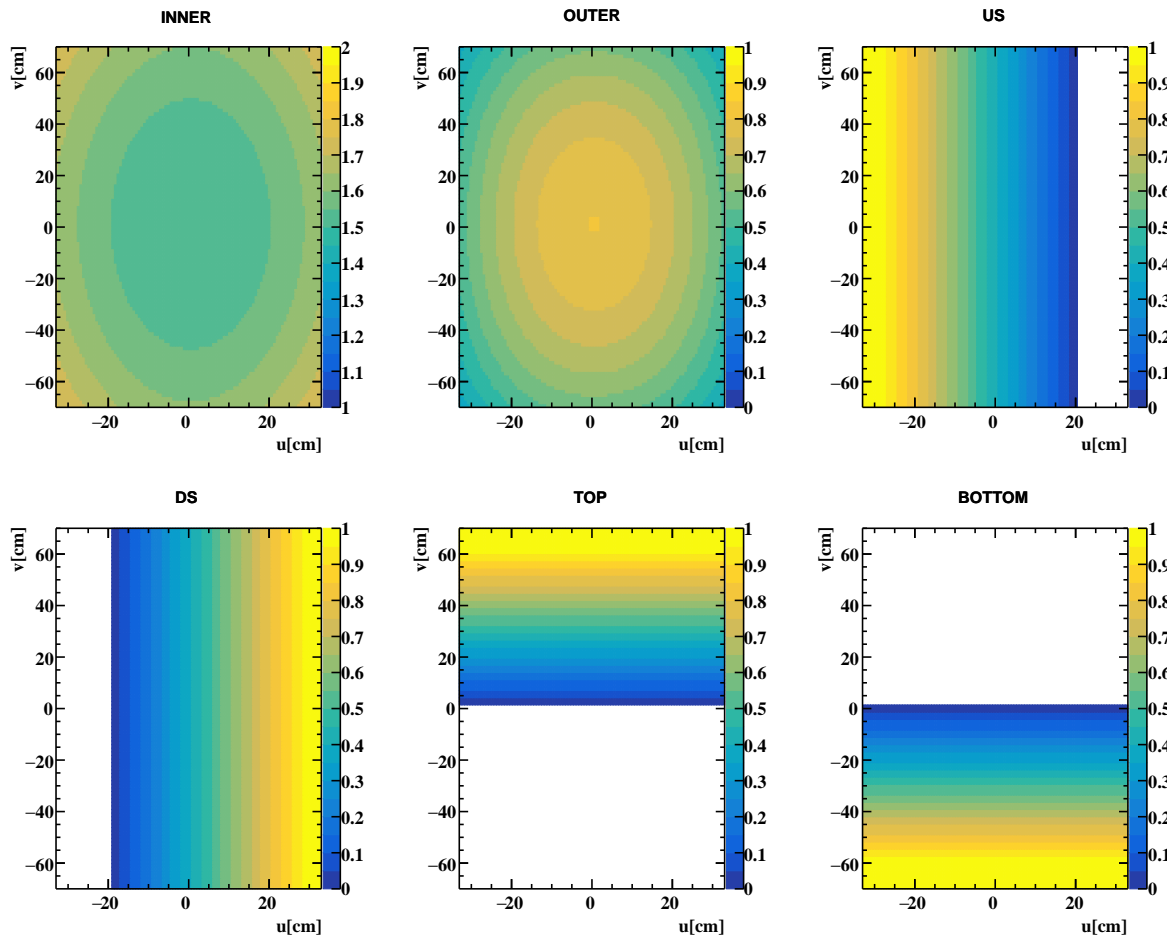


Figure 7.4: Face factor used for the energy reconstruction. The  $u$  and  $v$  dependences in Fig. 7.3 are expressed by a combination of a symmetric function in  $u$  and  $v$ .

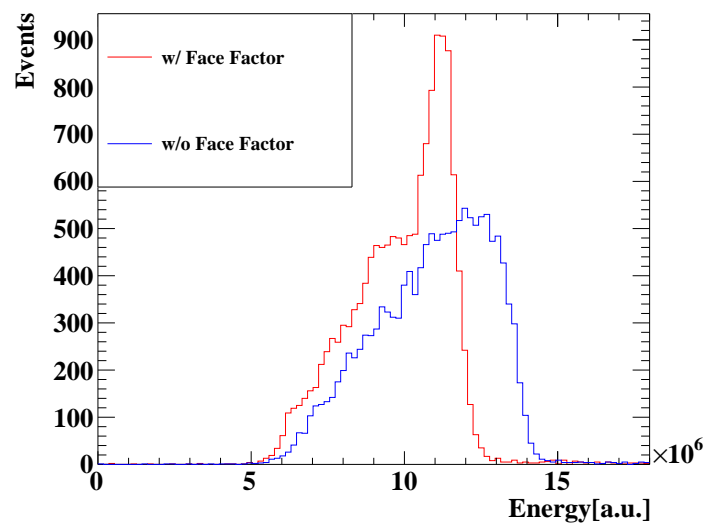


Figure 7.5: Energy spectrum for the CW-Li gamma-ray with (red) and without (blue) face factor. Non-uniformity correction with a correction function  $F(u, v, w)$  is not applied in both cases.

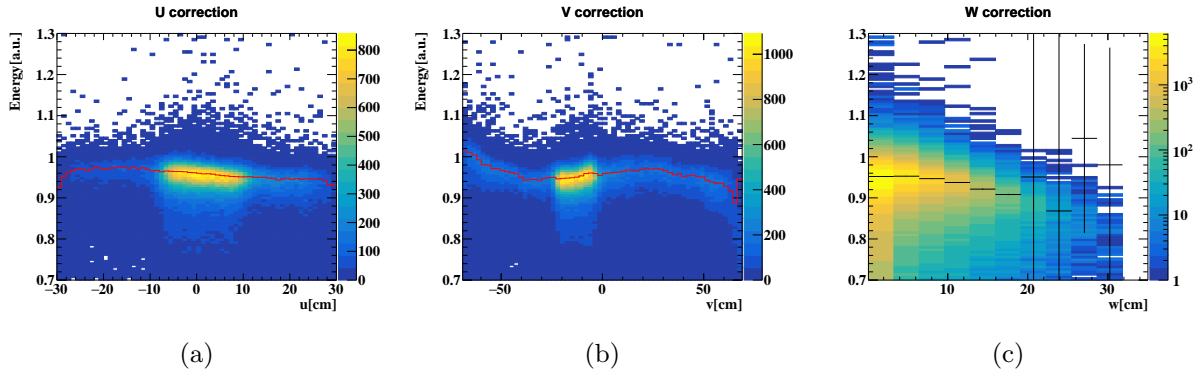


Figure 7.6: The correlation between the reconstructed  $N_{\text{sum}}$  and the (a)  $u$ , (b)  $v$ , and (c)  $w$  positions. Non-uniformity correction functions in  $G_u(u)$ ,  $G_v(v)$ , and  $G_w(w)$  are shown in red and black.

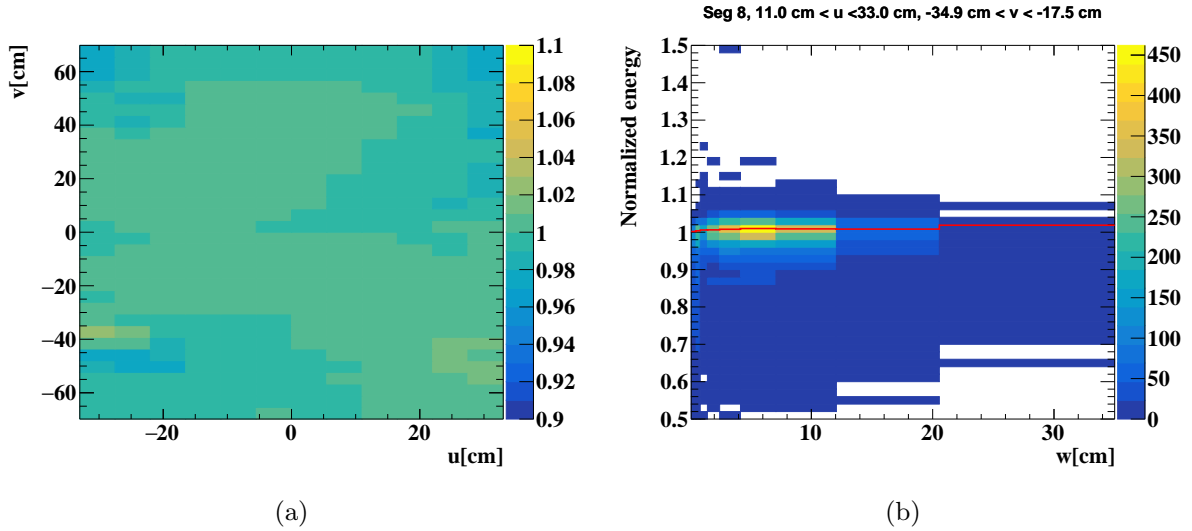


Figure 7.7: Non-uniformity correction function in (a)  $uv$  and (b)  $w$  directions.

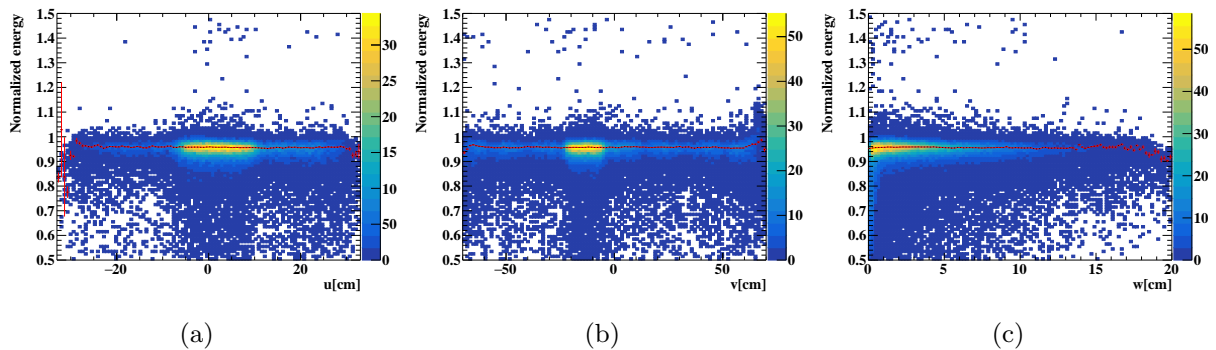


Figure 7.8: Reconstructed energy of the 55 MeV gamma-ray from  $\pi^0 \rightarrow \gamma\gamma$  after the all non-uniformity correction as a function of (a)  $u$ , (b)  $v$ , and (c)  $w$ . The scale of the reconstructed energy is arbitrarily normalized. Red histograms show the position dependences of the 55 MeV energy peak.

photons detected by the  $i$ -th surrounding channel. Let us call this reconstruction dead channel recovery (DCR).

Fig. 7.2a shows the ratio of the reconstructed energy with the DCR to that without the DCR, as a function of  $v$ . The ratio was large near both ends in  $v$  because the top and bottom faces had many dead channels. Fig. 7.2b shows the reconstructed energy peak with and without the DCR as a function of the  $v$ , indicating that the DCR greatly restored uniformity in the  $v$  direction.

The face factor  $F_{\text{face},i}(u, v, w)$  was introduced to mitigate the position dependence of the light collection efficiency. The factor was calculated with the CW-Li gamma-ray. The whole CW-Li dataset was divided into  $6 \times 16$  based on  $(u, v)$  position, and a set of the factors that give the sharpest peak at each subset was calculated. Fig. 7.3 shows the position dependence of the face factor. The position dependence of face factors shows that they are relatively high when the gamma-ray hit is close to each face. Fig. 7.4 shows the position dependence of the face factor actually applied, given by fitting a symmetric function in  $u$  and  $v$  to the distribution in Fig. 7.3. Fig. 7.5 shows the  $N_{\text{sum}}$  distribution for the CW-Li gamma-rays with and without the face factor optimization. The position dependence of energy is mitigated by using the face factor, and the energy spectrum has a relatively sharp peak.

The residual non-uniformity was corrected by optimizing  $F(u, v, w)$  with the energy peak of the 55 MeV gamma-ray from the  $\pi^0 \rightarrow \gamma\gamma$  decay.  $F(u, v, w)$  is composed of several independent correction functions as,

$$F(u, v, w) = G_u(u) \times G_v(v) \times G_w(w) \times L_{uv}(u, v) \times L_w(w|u, v), \quad (7.5)$$

where  $G_u(u)$ ,  $G_v(v)$ , and  $G_w(w)$  are the one-dimensional functions, which correct the global position dependence in each direction, and  $L_{uv}(u, v)$  and  $L_w(w|u, v)$  are additional correction functions which correct the residual non-uniformity.

Fig. 7.6 and Fig. 7.7 show the global correction functions  $G_u(u)$ ,  $G_v(v)$ ,  $G_w(w)$  and the additional correction functions  $L_{uv}(u, v)$  and  $L_w(w|u, v)$  obtained from the 55 MeV peak of the gamma-ray. Fig. 7.8 shows the position dependence of the reconstructed energy of the 55 MeV gamma-ray after all corrections. The distribution of the peaks has 0.1% sigma, and it can be regarded as the precision of the non-uniformity correction.

## 7.3 Resolution

In this section, we will first discuss the energy resolution and its position dependence for the 17.6 MeV gamma-ray from the CW-Li setup and the 55 MeV gamma-ray from the  $\pi^0 \rightarrow \gamma\gamma$  decay. Then, the energy dependence of the resolution will be discussed using the gamma-rays with higher energies.

### 17.6 MeV CW-Li gamma-ray

Fig. 7.9 shows the energy spectrum of the gamma-ray from the CW-Li setup in the 2021 run. The energy resolution is estimated by fitting a Gaussian function to the right side of the energy

spectrum. Fig. 7.10 shows the position dependence of the resolution. The resolution is 2.5% for  $w > 2$  cm and 3.0% for  $w < 2$  cm. A uniform resolution of 2.5% is achieved for  $w > 2$  cm events within the acceptance except for the edges ( $|v| > 60$  cm). The reason for the poor energy resolution at the edge of the detector is likely because of the non-uniformity of the light collection efficiency.

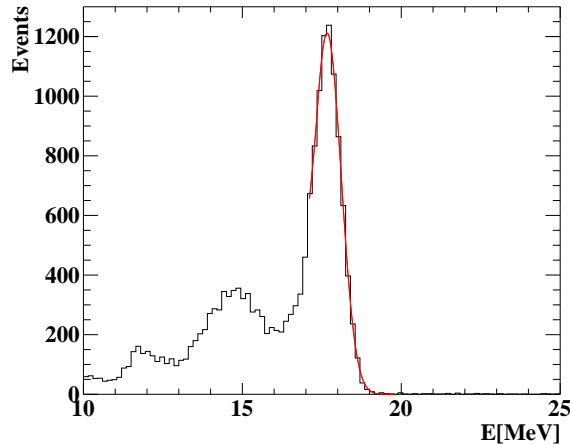


Figure 7.9:  $E_\gamma$  spectrum for the CW-Li gamma-ray ( $w > 2$  cm of the acceptance of the detector) and a Gaussian fit function in red line.

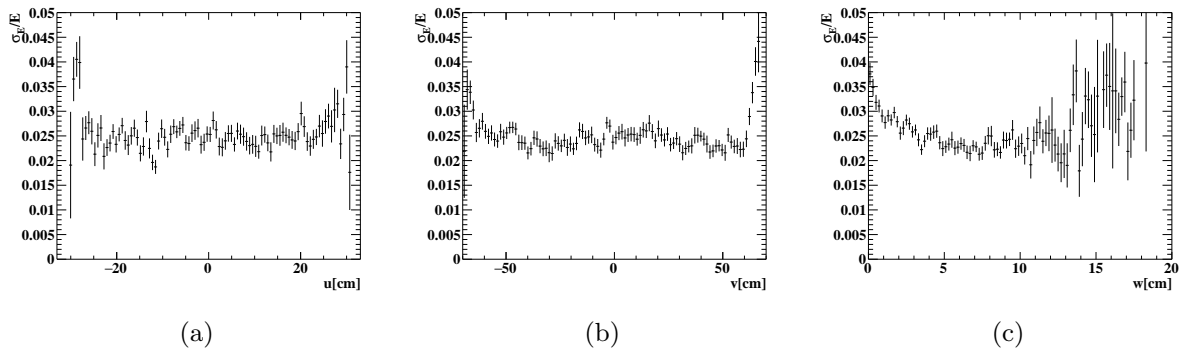


Figure 7.10:  $E_\gamma$  resolution for the 17.6 MeV CW-Li gamma-ray as a function of (a)  $u$ , (b)  $v$ , and (c)  $w$ .

## 2021 $\pi^0$ run

The energy resolution for the 55 MeV gamma-ray is estimated with the  $\pi^0$  run dataset. The following event selections are applied to select the 55 MeV gamma-ray from the  $\pi^0 \rightarrow \gamma\gamma$  decay.

- $65 \text{ MeV} < E_{\text{BGO}} < 90 \text{ MeV}$
- $E_{\text{ps}} < 1 \text{ MeV}$
- $\Theta_{\gamma\gamma} > 170^\circ$

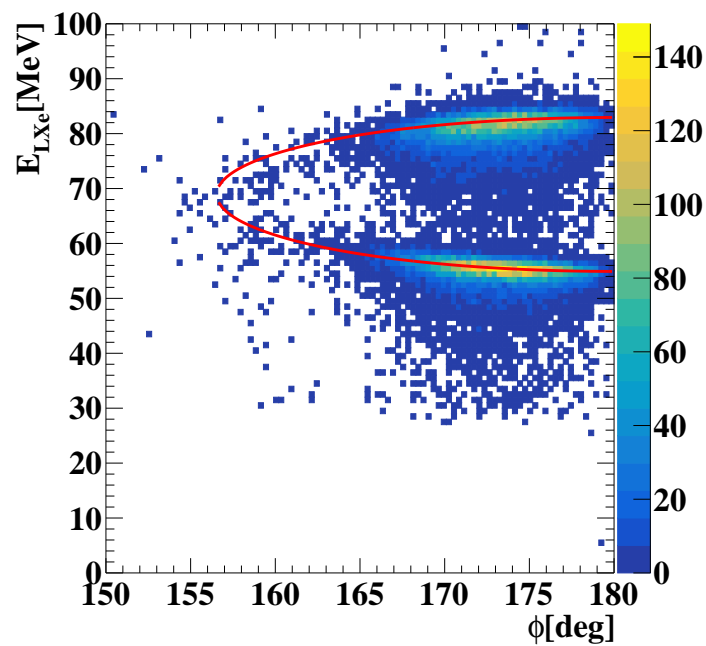


Figure 7.11: Correlation between the opening angle  $\Theta_{\gamma\gamma}$  and the reconstructed energy in the LXe detector. The red line shows the theoretical prediction of the correlation.

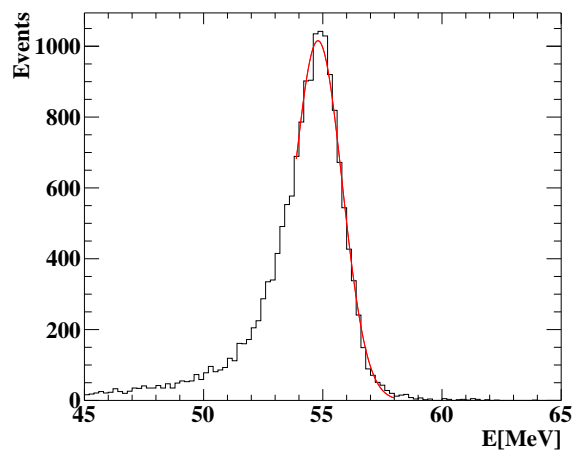


Figure 7.12: Energy spectrum for 55 MeV gamma rays. The  $\Theta_{\gamma\gamma}$  dependence of the energy is corrected. A fitting function that consists of a Gaussian function and an exponential function is shown in red.

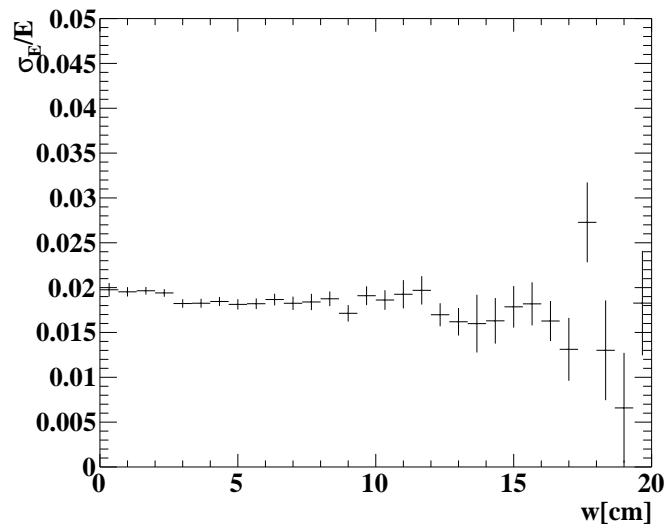


Figure 7.13: Energy resolution at the central part of the detector ( $|u| < 10$  cm,  $-30$  cm  $< v < -10$  cm) for the 55 MeV gamma-ray as a function of the  $w$ .

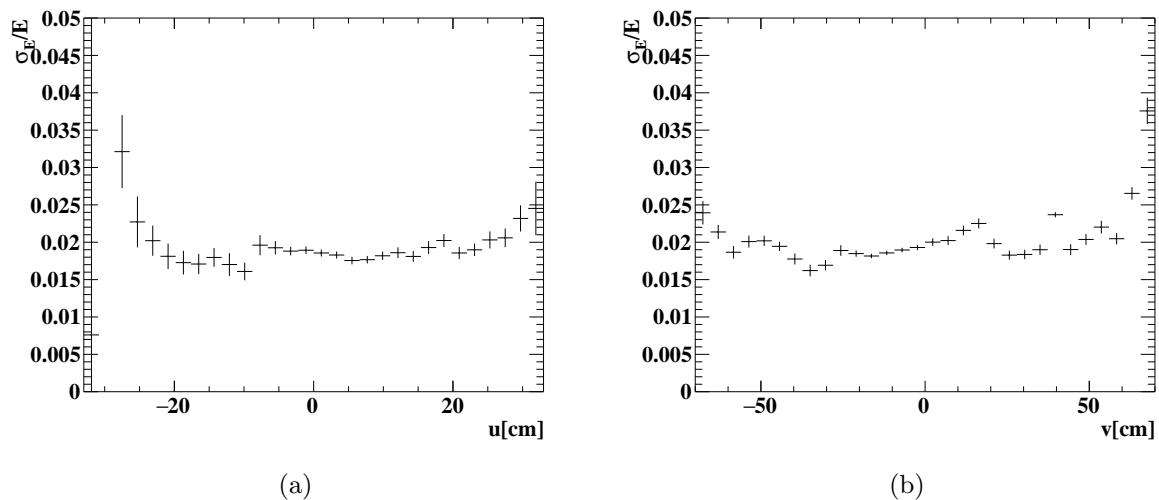


Figure 7.14: Energy resolution for the 55 MeV gamma-ray as a function of (a)  $u$  and (b)  $v$  position.

- $|\Delta t| < 10$  ns
- Single pulse in the summed waveform of the BGO detector.
- Convergence of the pileup analysis (see Sec. 10.1).

where  $E_{\text{BGO}}$  and  $E_{\text{ps}}$  are the reconstructed energies by the BGO detector and the pre-shower counter, respectively, and  $\Delta t$  is the time difference between the LXe detector and the BGO detector,  $\Theta_{\gamma\gamma}$  is the reconstructed opening angle between the two gamma-rays.

Fig. 7.11 shows the correlation between the opening angle and the measured energy by the LXe detector. The measured correlation follows the expected correlation by the kinematics as

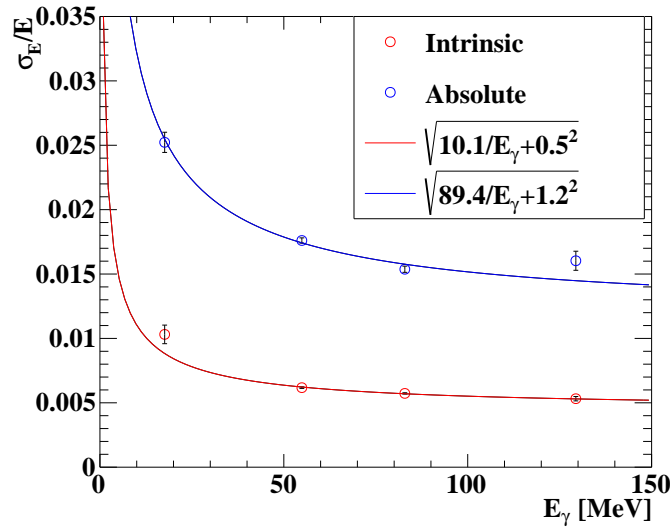


Figure 7.15: The energy resolution as a function of the energy. The intrinsic resolution (red) from the even-odd analysis and the absolute resolution (blue) are shown.

in Eq. 2.15. Due to this correlation, the gamma rays are not exactly monochromatic. The energy difference from the 55 MeV is corrected using the reconstructed opening angle  $\Theta_{\gamma\gamma}$ . The fluctuation of the true energy deposit is 0.4% after the correction is applied. This fluctuation comes from the finite resolution of the opening angle. Since the vertex position had a  $\mathcal{O}(1)$  cm distribution in the LH<sub>2</sub> target and the position resolution of the BGO detector is  $\sim 1$  cm, the resolution of the opening angle is  $1.6^\circ$ .

Fig. 7.12 shows the energy spectrum for the 55 MeV gamma-ray with the  $\Theta_{\gamma\gamma}$  correction. The resolution is estimated by fitting a composite function that uses a Gaussian function for the higher energy part and an exponential function for a tail to the energy spectrum. The two functions are smoothly connected at a transition point lower than the peak energy. Let us call this function the “ExpGaus” function. The contribution of the energy spread due to the opening angle correction (0.4%) is then subtracted in quadrature from the sigma of the Gaussian component.

Fig. 7.13 shows the energy resolution at the central part of the detector ( $|u| < 10$  cm,  $-30$  cm  $< v < -10$  cm) as a function of the depth. The resolution of 1.9/1.8% is achieved for  $w < 2$  cm and  $w > 2$  cm, respectively. Fig. 7.14 shows the resolution as a function of  $u$  and  $v$ . The resolution is distributed between 1.6% and 2.0% within the acceptance except for the edges close to the top and bottom faces ( $|v| > 60$  cm).

Fig. 7.15 shows the energy resolution as a function of the energy. It includes the energy resolution for the 83 MeV gamma-ray from the  $\pi^0 \rightarrow \gamma\gamma$  decay and 129 MeV gamma-ray from the radiative capture  $\pi^- p \rightarrow \gamma n$ . The resolution for the 83 MeV gamma-ray is estimated in the same way as the 55 MeV gamma-ray, by selecting the events with  $40$  MeV  $< E_{\text{BGO}} < 65$  MeV. The resolution for the 129 MeV gamma-ray is estimated by fitting the upper tail of the spectrum with a Gaussian function. At the central part of the detector ( $|u| < 10$  cm,  $|v| < 30$  cm,  $2$  cm  $<$

$w < 10$  cm), the energy dependence is

$$\sigma_E/E \sim \sqrt{89.4/E + 1.2^2}(\%). \quad (7.6)$$

To estimate the contribution of the photoelectron statistics to the resolution, the intrinsic resolution, which is defined by the difference of the reconstructed energies by different parts of the detector, is helpful. The intrinsic resolution  $\sigma_{\text{intrinsic}}$  is calculated by fitting a Gaussian function with the  $\sigma_{\text{intrinsic}}$  to the distribution of the energy difference  $\Delta E_{\text{intrinsic}}$  defined by

$$\Delta E_{\text{intrinsic}} = (E_{\text{even}} - E_{\text{odd}})/2, \quad (7.7)$$

where  $E_{\text{even}}$  and  $E_{\text{odd}}$  are the reconstructed energies by even channels and odd channels, respectively. The intrinsic resolution is composed of the statistical term and the contribution from the position dependence and shower development. The absolute energy resolution can be given as

$$\sigma_{\text{absolute}} = \sigma_{\text{intrinsic}} \oplus \sigma_{\text{coherent}} \quad (7.8)$$

where  $\sigma_{\text{coherent}}$  is the contribution to the energy resolution of the coherent effects such as the noises, the shower development, and the reflection and scattering of scintillation photons. The good intrinsic resolution with respect to the absolute resolution indicates that the energy resolution is not limited by the photoelectron statistics but by the coherent effects as above.

## 7.4 Energy scale

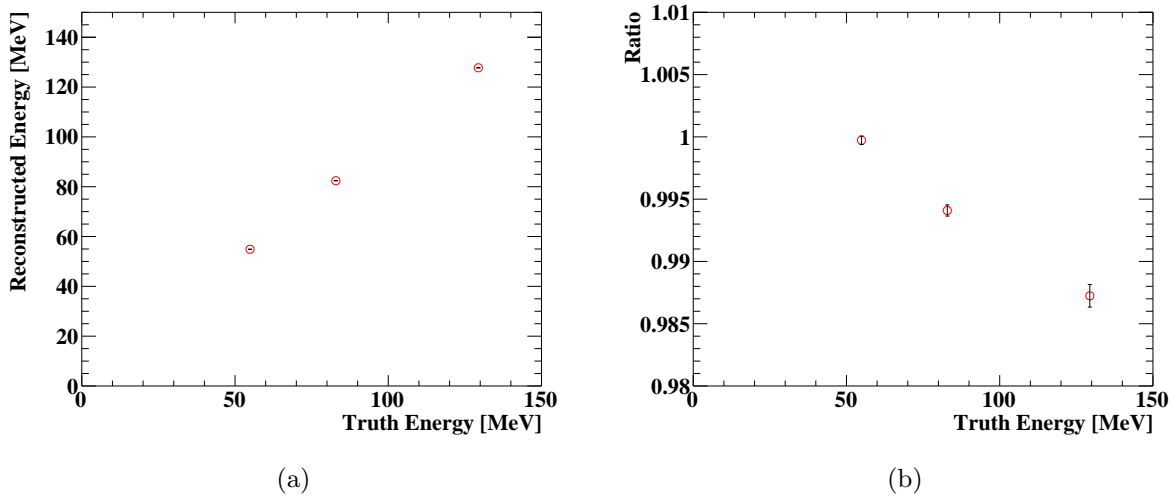


Figure 7.16: (a) The energy peak value and (b) the ratio to the gamma-ray energy as a function of the energy.

The energy scale is determined by the 55 MeV peak in the  $\pi^0$  run. There are several things to be considered: the linearity, stability, and uniformity of the energy scale. Fig. 7.16 shows the energy peak values for different gamma-ray sources and their ratios to the true energy as a function of energy. The nonlinearity of the energy scale of  $\mathcal{O}(1)\%$  is observed. This

might be due to the nonlinearity of the readout electronics or the shower leakage. Since the energy scale is determined by the 55 MeV peak, the impact of the nonlinearity in the analysis region ( $48 \text{ MeV} < E_\gamma < 58 \text{ MeV}$ ) is limited. The uncertainty of the energy scale due to this non-linearity is estimated as 0.1% by the statistical uncertainty.

The systematical uncertainty of the energy scale from the stability is estimated to be 0.4% by the monitoring as discussed in Sec. 4.6. The non-uniformity of the energy scale over the detector volume is 0.1%. The overall uncertainty is 0.4%, dominated by the uncertainty of the precision of the monitoring of the stability.

## 7.5 Summary

The energy resolution of the LXe detector for gamma rays is studied with several gamma-ray sources. The resolution for the 55 MeV gamma ray is 1.9%/1.7% for  $w < 2 \text{ cm}/w > 2 \text{ cm}$  in the region where the optimal energy resolution is achieved. The uniformity of the resolution has been studied using the 17.6 MeV CW-Li gamma-ray and the 55 MeV gamma-ray. The uniform resolution is achieved for the whole acceptance region except for the very edges close to the top and bottom faces ( $|v| > 60 \text{ cm}$ ), where the resolution is limited by the non-uniformity of the light collection efficiency. The uncertainty of the energy scale is estimated to be 0.4% based on the studies of linearity, stability, and uniformity.

## Chapter 8

# Time Resolution

In the 2020  $\pi^0$  run, the time resolution of 81(3) ps was measured [3] while the expected resolution in the design phase was 50–70 ps. The reason for the degraded resolution with respect to the expected resolution was regarded as a systematic error, and a dedicated measurement to suppress the systematic error was performed in the 2021  $\pi^0$  run.

In this chapter, the evaluation of the time resolution in the 2021  $\pi^0$  run is described. First, the time reconstruction method is explained in Sec. 8.1. Then, the evaluation of the time resolution using the 55 MeV gamma-ray dataset collected in the 2021  $\pi^0$  run is presented in Sec. 8.2.

### 8.1 Time Reconstruction

The time of a gamma-ray hit is reconstructed by minimization of the following  $\chi^2$ :

$$\chi^2 = \sum_{i \in \text{MPPC, PMT}} \chi_i^2 \quad (8.1)$$

$$\chi_i^2 = \Delta t^2 / \sigma_i^2 \quad (8.2)$$

$$\Delta t = t_{\text{pm}} - t_{\text{prop}} - t_{\text{walk}} - t_{\text{offset}} - t_\gamma \quad (8.3)$$

where  $t_{\text{pm}}$  is the detected pulse time of each photosensor,  $t_{\text{prop}}$  is the time of propagation of scintillation photons,  $t_{\text{walk}}$  is the delay in the reconstructed pulse time due to the time-walk effect,  $t_{\text{offset}}$  is the time offset of the photosensor with respect to the average offset. The photosensors with large signal ( $N_{\text{phe}} > 50$ ) are used to calculate the  $\chi^2$ . The sensors whose  $\chi_i^2$  is larger than 1.8 are regarded as outliers due to the off-timing pileup and eliminated from the fitting to minimize the impact of the pileup. A set of the fitting and the removal of the outliers is repeated until the reduced chi-square ( $= \chi^2 / NDF$ ,  $NDF$  is the number of degrees of freedom) gets lower than 1.8. Fig. 8.1 shows the sensors used for the time reconstruction of an event, and the color of each sensor indicates its relative time with respect to the reconstructed  $t_\gamma$ . For a signal gamma-ray, a few hundred photosensors are used for the reconstruction.

$t_{\text{pm}}$  is calculated by a constant fraction method to mitigate the time-walk effect, as shown in Fig. 8.2. In this method, the time of each waveform is obtained from the crossing point of the threshold defined by a certain fraction of the pulse amplitude. The constant fraction is set

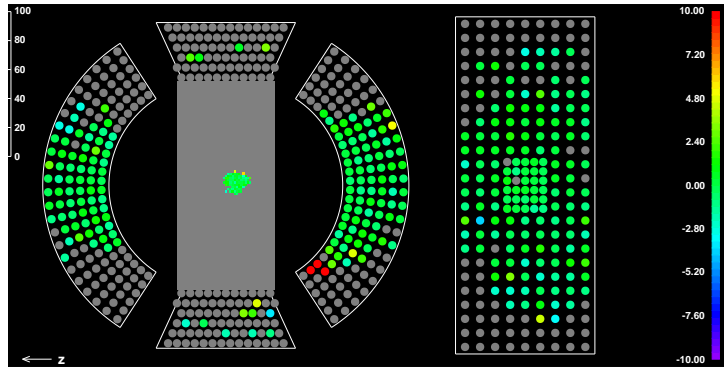


Figure 8.1: Photosensors used for the time fitting of an event in the 2021  $\pi^0$  run. The reconstructed energy is 56.8 MeV, and the depth is 3.4 cm. The color of each sensor indicates its relative time with respect to the reconstructed  $t_\gamma$ .

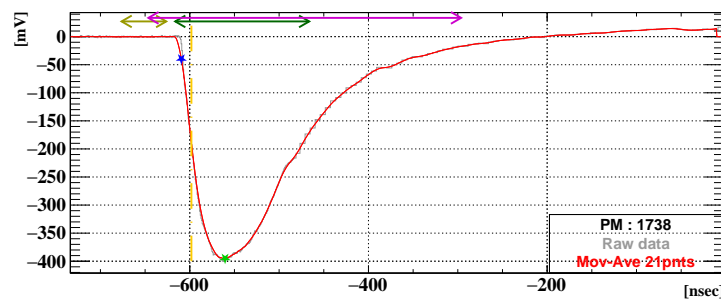


Figure 8.2: MPPC waveform (grey) and shaped waveform with moving average (red) of a gamma-ray event. A green marker shows the amplitude ( $\sim 400$  mV) and time of the peak, and a blue marker shows the crossing point of the waveform and the constant fraction threshold ( $\sim 40$  mV).

to 10% because 5–10% is the best fraction that gives the optimal time resolution in an MC simulation [2]. To suppress the effect of high-frequency noise, the raw waveform is smoothed with a 3-point moving average.

The time walk  $t_{\text{walk}}$  and time offset of each channel were calibrated by using the 55 MeV gamma-rays in the  $\pi^0$  run. The time offset was measured by taking the average of the time difference  $t_{\text{pm}} - t_{\text{prop}} - t_\gamma$ . The  $N_{\text{phe}}$  dependence of  $t_{\text{pm}} - t_{\text{prop}} - t_\gamma$  was calculated and corrected as shown in Fig. 8.3.

## 8.2 Resolution Measurement

### 8.2.1 Principle and setup

The time resolution of the LXe detector  $\sigma_{t_\gamma}$  was measured with the pair of two coincident gamma-rays from the  $\pi^0 \rightarrow \gamma\gamma$  decay collected in the 2021  $\pi^0$  run. The time difference between the measured time by the LXe detector  $t_\gamma$  and that by the pre-shower counter  $t_{\text{ps}}$ , and its spread

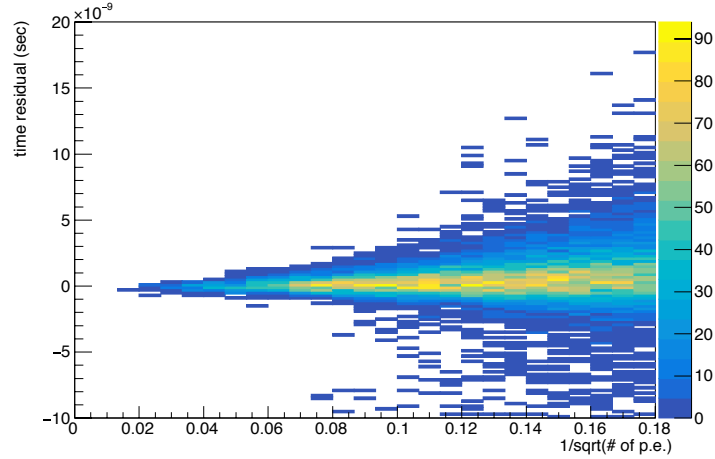


Figure 8.3:  $t_{\text{pm}} - t_{\text{prop}} - t_{\gamma}$  as a function of the number of photoelectrons (MPPC Lot A) [2]. 116 channels  $\times$  1000 events are overlaid.

$\sigma_{\Delta t}$  can be represented as

$$\Delta t = t_{\gamma} - t_{\text{ps}} - t_{\text{TOF}} \quad (8.4)$$

$$\sigma_{\Delta t} = \sigma_{t_{\gamma}} \oplus \sigma_{\text{ps}} \oplus \sigma_{\text{TOF}}, \quad (8.5)$$

where  $t_{\text{TOF}}$  is the time of flight correction,  $\sigma_{\text{ps}}$  and  $\sigma_{\text{TOF}}$  are the spread of  $t_{\text{ps}}$  and  $t_{\text{TOF}}$ , respectively.

The resolution of the pre-shower counter was measured to be  $\sigma_{\text{ps}} = 28.2 \pm 0.2 \text{ ps}$  from the intrinsic time difference between the two scintillator-plate modules, as shown in Fig. 8.4.

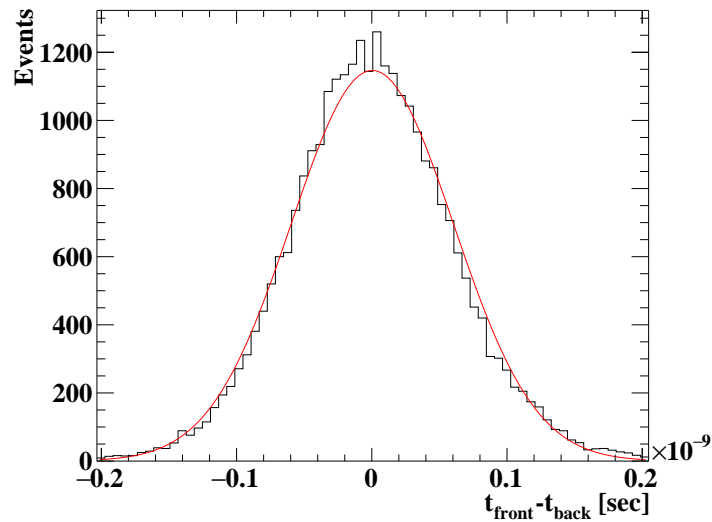


Figure 8.4: Time difference between two pre-shower counter plates. The red line shows the Gaussian fitting function.

The time of flight from the  $\pi^0$  vertex to the interaction point in the LXe detector and in the pre-shower counter is corrected using the reconstructed position of each detector. The dominant

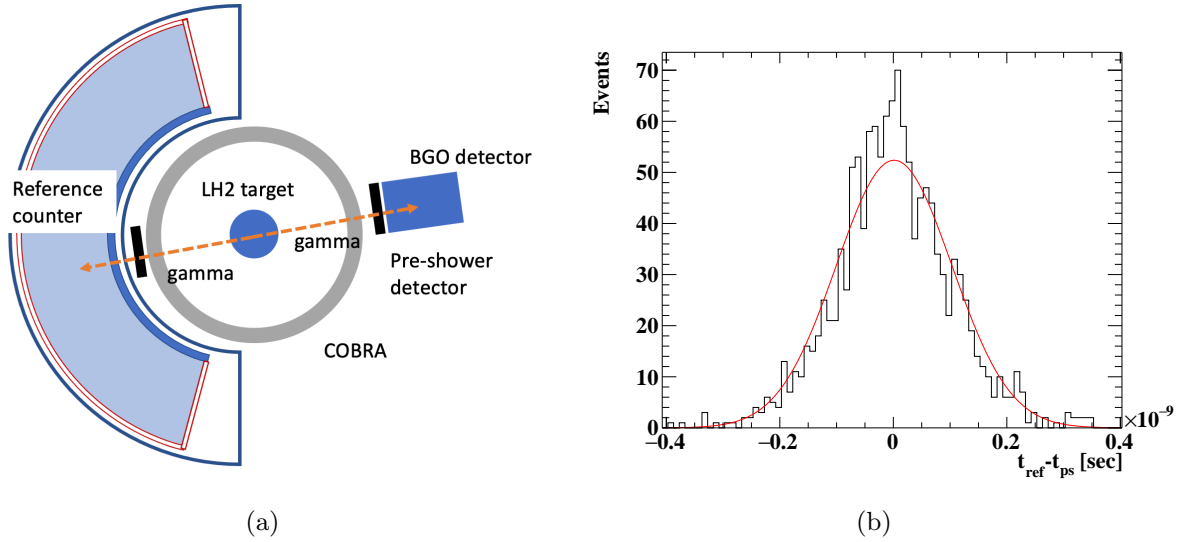


Figure 8.5: (a) Setup of the  $\sigma_{\text{vertex}}$  measurement in 2021. A reference counter with the same design as the pre-shower counter was placed on the opposite side of the pre-shower counter. (b)  $\Delta t_{\text{vertex}}$  distribution in the 2021  $\pi^0$  run. A red line shows the Gaussian fit function.

contribution to  $\sigma_{\text{TOF}}$  comes from the fluctuation of the time difference due to the transverse size of the  $\pi^0$  vertex  $\sigma_{\text{vertex}}$ . The size is estimated as  $\sim 7$  mm in an MC simulation, and the time spread  $\sigma_{\text{vertex}}$  corresponds to the 48(2) ps. However, the poor time resolution in 2020  $\pi^0$  run (81(3) ps [3]) implied that the time resolution was overestimated due to a larger vertex size in reality. In the 2021 run, the  $\sigma_{\text{vertex}}$  was measured by a dedicated measurement with a reference timing counter which has the same design as the pre-shower counter. The setup of the measurement is shown in Fig. 8.5a. The reference counter was placed on the opposite side of the pre-shower counter so that the two counters could measure the time of a pair of back-to-back gamma rays. The  $\sigma_{\text{vertex}}$  can be measured by the relation between the spread of the time difference  $\Delta t_{\text{vertex}} = t_{\text{ref}} - t_{\text{ps}}$  as

$$\sigma_{\Delta t_{\text{vertex}}} = \sigma_{\text{vertex}} \oplus \sigma_{\text{ref}} \oplus \sigma_{\text{ps}} \quad (8.6)$$

where  $\sigma_{\Delta t_{\text{vertex}}}$  is the spread of  $\Delta t_{\text{vertex}}$ ,  $\sigma_{\text{ref}}$  is the time resolution of the reference counter, which was measured using the intrinsic time difference between the two plates as the pre-shower counter. The uncertainty of the  $\sigma_{\text{vertex}}$  measurement is dominated by the statistical uncertainty (6 ps) because of the limited statistics (1600 events) due to the target problem as described in Sec. 3.4. As a result,  $\sigma_{\text{vertex}}$  is estimated to be  $70 \pm 6$  ps.

## 8.2.2 Resolution

Fig. 8.6 shows the measured  $\Delta t$  distribution in the 2021  $\pi^0$  run. The following event selections were applied to estimate the time resolution.

- $50 \text{ MeV} < E_{\gamma} < 58 \text{ MeV}$

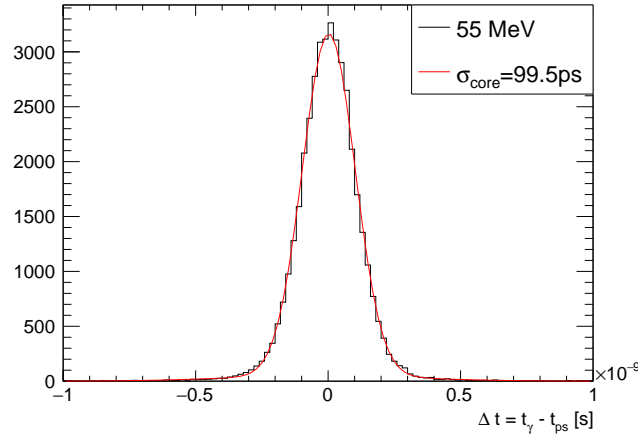


Figure 8.6: Distribution of  $\Delta t$  in the 2021  $\pi^0$  run. The fit function composed of two Gaussian functions is shown in red.

Table 8.1: Summary of time resolution evaluation

Contribution	Spread [ps]
$\sigma_{\Delta t}$ (core)	$99.5 \pm 0.5$
$\sigma_{ps}$	$28 \pm 0.2$
$\sigma_{\text{vertex}}$	$70 \pm 6$
$\sigma_{t_\gamma}$ (core)	$65 \pm 6$

- $\Theta_{\gamma\gamma} > 175^\circ$
- Convergence of the pileup analysis (See Sec. 10.1)

A composite Gaussian function is fitted to the  $\Delta t$  distribution. The sigma of the core part  $\sigma_{\text{core}}$  is  $99.5 \pm 0.5$  ps (98.4%), while the tail part  $\sigma_{\text{tail}}$  is  $338 \pm 8$  ps (1.6%). From these results, the resolution of the LXe detector is calculated to be  $65 \pm 6$  ps. The corrections and their uncertainty are shown in Table 8.1. The dominant uncertainty is the statistical uncertainty of the  $\sigma_{\text{vertex}}$ . The resolution is at the same level as that of the MEG LXe detector (64 ps).

The energy dependence of the time resolution is shown in Fig. 8.7. To discuss the impact of the photoelectron statistics on the time resolution, the intrinsic resolution is defined as  $\sigma_{\text{intrinsic}} = \sigma((t_{\text{odd}} - t_{\text{even}})/2)$  where  $t_{\text{even}}$  and  $t_{\text{odd}}$  are the time reconstructed by even and odd channels respectively. This intrinsic resolution is a part of the absolute resolution and includes a precision of time estimation at each photosensor and electronics. On the other hand, effects such as the precision of the propagation time defined by the gamma-ray hit position resolution, per-event shower development, and the coherent noise over the readout electronics are included only in the absolute resolution. The discrepancy between the intrinsic and absolute time resolutions is 55 ps, and it is considered to be coming from such contributions. The energy dependence of the absolute and intrinsic time resolutions can be given by  $\sigma_{t_\gamma} = \sqrt{255.8^2/E_\gamma + 54.9^2}$  ps and

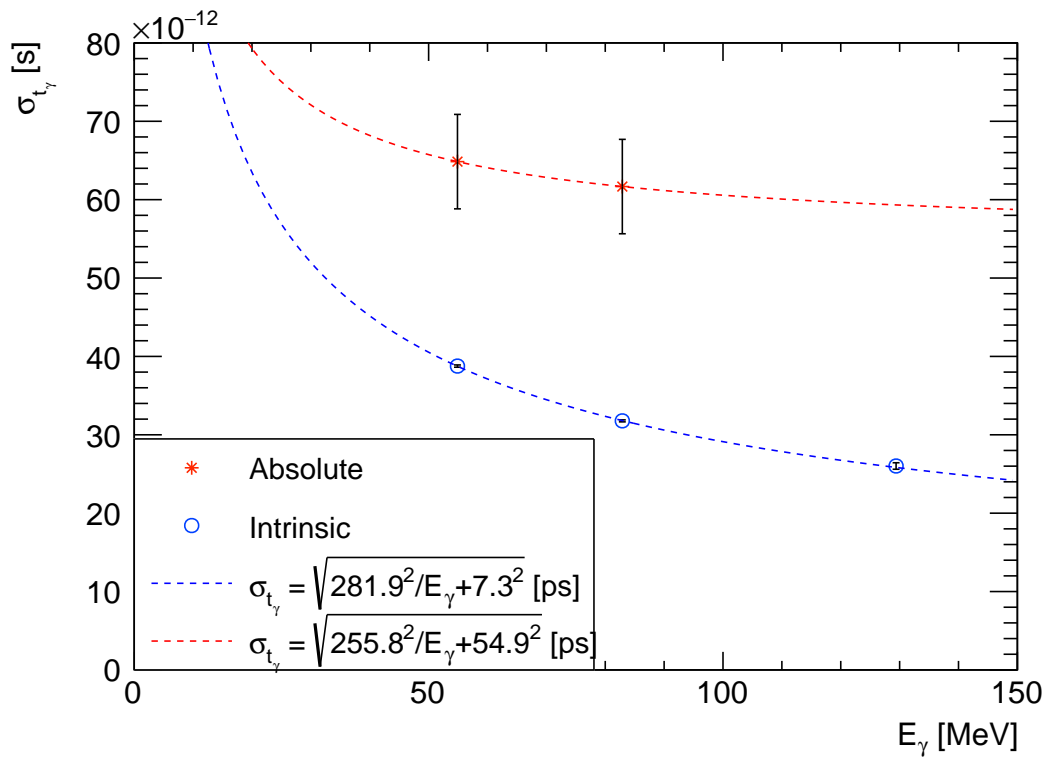


Figure 8.7: The absolute and intrinsic time resolution as a function of  $E_\gamma$ . Red points and a red dotted line show the absolute time resolution and the fitting function, respectively. Blue points and a blue dotted line show the absolute time resolution and the fitting function, respectively.

$\sigma_{t_\gamma} = \sqrt{281.9^2/E_\gamma + 7.3^2}$  ps with a fit, respectively.

Fig. 8.8 shows the position dependence of the  $\sigma_{\Delta t}$ . While the resolution is uniform in the  $u$  and  $v$  direction within the acceptance, the  $\mathcal{O}(10)$  ps non-uniformity in the  $w$  direction is observed. The depth dependence of the time resolution can be explained by the depth dependence of the position resolution because the resolution of the  $t_{\text{prop}}$  is worse with the worse position resolution for the deep gamma-ray hit. The best time resolution is  $61 \pm 6$  ps in  $1 \text{ cm} < w < 5 \text{ cm}$ .

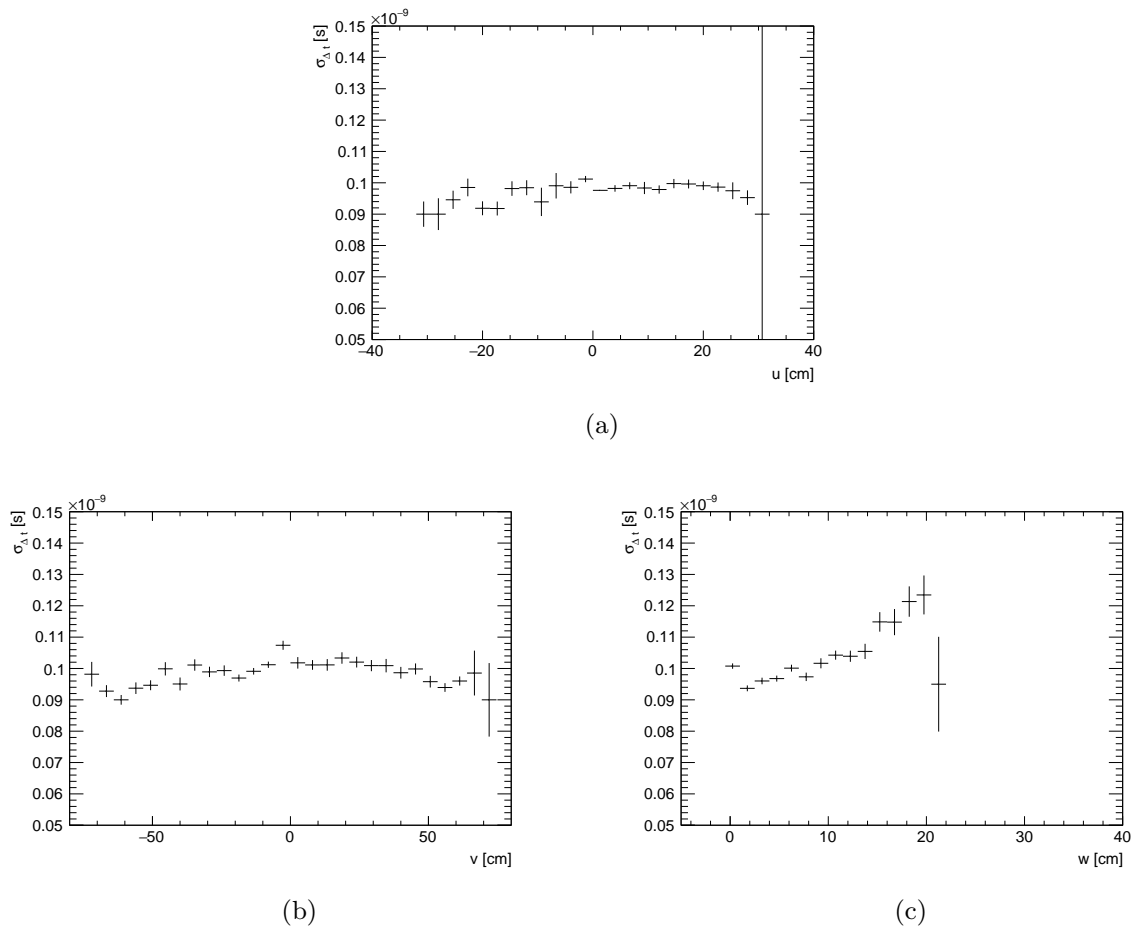


Figure 8.8: Sigma of the  $\sigma_{\Delta t}$  distribution as a function of the (a)  $u$ , (b)  $v$ , and (c)  $w$  position of the 55 MeV gamma ray.

## Chapter 9

# Efficiency

In this chapter, the detection efficiency for the signal gamma ray is estimated. The detection efficiency is defined as the fraction of the detected number of signal gamma-rays  $N_{\text{detected}}$  out of the total number of signal gamma-rays emitted to the acceptance of the detector  $N_{\text{acceptance}}$  as

$$\epsilon_{\gamma} = N_{\text{detected}}/N_{\text{acceptance}}, \quad (9.1)$$

where  $N_{\text{detected}}$  is the number of events that the  $E_{\gamma}$  is larger than a given lower energy threshold  $E_{\gamma}^{\text{threshold}}$ . The analysis efficiency defined by the pileup analysis and event selections will be discussed in Chap. 10.

The LXe detector is thick enough to stop an incoming gamma-ray with  $13.9 X_0$  radiation length, but when the gamma rays are scattered or absorbed before they reach LXe, or energetic secondary particles escape from xenon after the gamma rays reach LXe, the energy deposit in LXe is reduced. The detection efficiency was expected to be 69% in the design phase. This value is better than that of the MEG LXe detector by 9% thanks to the reduced material budget.

The intrinsic detection efficiency for the signal gamma-ray without the analysis efficiency is estimated as

$$\epsilon_{\text{sig}}^{\text{Data}} = \epsilon_{\text{sig}}^{\text{MC}} \times R_{\epsilon} \quad (9.2)$$

where  $\epsilon_{\text{sig}}^{\text{MC}}$  is the efficiency for the signal gamma-ray in MC simulation and  $R_{\epsilon}$  is the ratio of the efficiency in data to that in MC simulation. The ratio is estimated by the efficiencies of 55 MeV gamma rays from  $\pi^0 \rightarrow \gamma\gamma$  in data and MC ( $\epsilon_{\text{CEX}}^{\text{Data}}$  and  $\epsilon_{\text{CEX}}^{\text{MC}}$ , respectively). The evaluation of  $\epsilon_{\text{sig}}^{\text{MC}}$  is described in Sec. 9.1 and that of  $\epsilon_{\text{CEX}}^{\text{Data}}$  and  $\epsilon_{\text{CEX}}^{\text{MC}}$  is described in Sec. 9.2. The estimation of the  $\epsilon_{\text{sig}}^{\text{Data}}$  is discussed in Sec. 9.3.

### 9.1 Efficiency for signal gamma-ray in MC simulation

The  $\epsilon_{\text{sig}}^{\text{MC}}$  is evaluated with an MC simulation. In this MC simulation, the signal gamma-rays were generated from the target in the direction of the LXe detector with the following constraints loose enough to cover the entire LXe volume,

- $|\cos \theta_{\gamma}| < 0.45$

- $110^\circ < \phi_\gamma < 250^\circ$
- $E_\gamma = 52.8 \text{ MeV}$

where  $\theta_\gamma$  and  $\phi_\gamma$  are the polar and azimuthal emission angles of the gamma ray, respectively. Fig. 9.1a is the  $E_\gamma$  spectrum when the gamma ray is emitted to the acceptance. Fig. 9.1b is the efficiency as a function of the lower energy threshold. The efficiency is 0.69 at 48 MeV, which is the lower energy threshold of the MEG II analysis region.

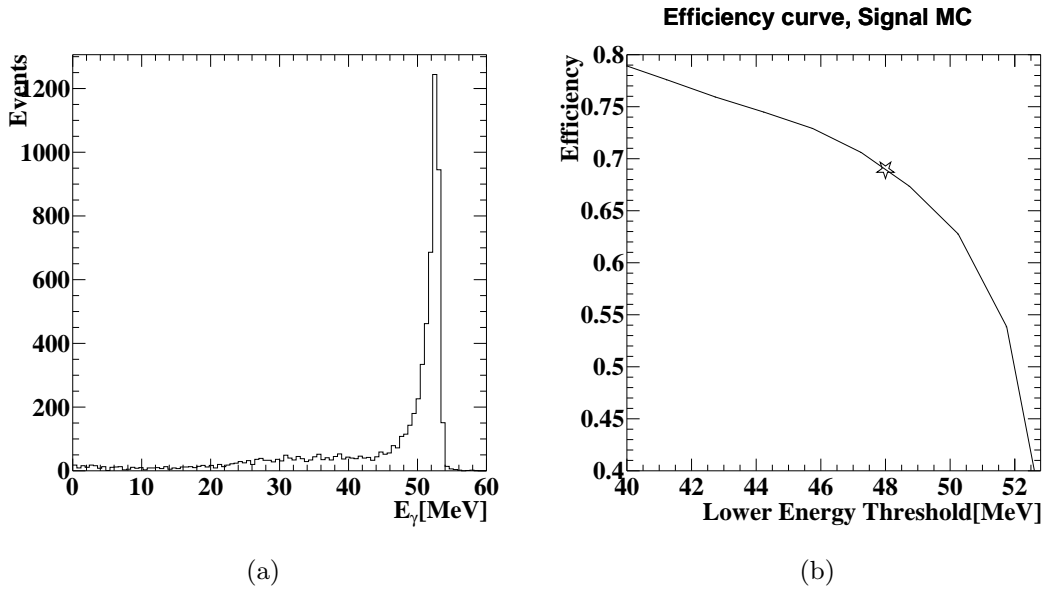


Figure 9.1: (a)  $E_\gamma$  spectrum for the signal gamma-rays emitted to the acceptance of the LXe detector in the MC simulation. (b) The efficiency as a function of lower energy threshold. The efficiency at the  $E_\gamma^{\text{threshold}} = 48 \text{ MeV}$  is shown in a black star.

## 9.2 Efficiency measurement

### 9.2.1 Method

The correlated gamma-ray pairs from  $\pi^0 \rightarrow \gamma\gamma$  are used to estimate the ratio between the efficiency in data and MC. When the BGO detector detects a  $\sim 83 \text{ MeV}$  gamma-ray, a  $\sim 55 \text{ MeV}$  gamma-ray must be emitted in the opposite direction. With this kinematics of  $\pi^0$  decay, the detection efficiency can be defined as  $\epsilon_{\text{CEX}} = N_{\text{LXe}}/N_{\text{BGO}}$ , where  $N_{\text{BGO}}$  is the number of gamma-ray events around  $E_{\text{BGO}} \sim 83 \text{ MeV}$  and  $N_{\text{LXe}}$  is the number of such events with  $E_\gamma > E_\gamma^{\text{threshold}}$ . The data-taking with the BGO self-trigger that collects events with  $E_{\text{BGO}} > 20 \text{ MeV}$  was mixed with the standard data-taking of the  $\pi^0$  run at each BGO position.

The background of this measurement comes from the radiative capture of negative pion  $\pi^- p \rightarrow \gamma n$  in the LH<sub>2</sub> target. As shown in Fig. 9.2a, a peak of the 129 MeV gamma-ray in the BGO energy spectrum has a long low-energy tail so that it interferes the signal region of the efficiency analysis ( $65 \text{ MeV} < E_{\text{BGO}} < 90 \text{ MeV}$ ). In these background events, neutrons are emitted in the

opposite direction of the 129 MeV gamma-ray.

The analysis flow of the efficiency evaluation was as follows.

1. Make a template of the  $E_\gamma$  spectrum of the  $E_{\text{BGO}} > 100$  MeV events.
2. Fit an “ExpGaus” function to the 129 MeV peak of the  $E_{\text{BGO}}$  spectrum.
3. Make the energy spectrum of the LXe detector for the events in the analysis window ( $65 \text{ MeV} < E_{\text{BGO}} < 90 \text{ MeV}$ ).
4. Scale the template spectrum of the LXe detector from the first step using the area under the “ExpGaus” function in the second step.
5. Subtract the scaled template from the energy spectrum of the LXe detector.
6. Count the number of events with  $E_\gamma > E_\gamma^{\text{threshold}}$ .

Fig. 9.2a shows the energy spectrum of the BGO crystal with the BGO self-trigger. The BGO and LXe configuration is the nominal configuration with the largest statistics (Patch13). The low-energy events in the  $E_{\text{BGO}}$  spectrum are likely from the RMD of the negative muon ( $\pi^- \rightarrow \mu^- \nu_\mu, \mu^- \rightarrow e^- \bar{\nu}_e \nu_\mu \gamma$ ). In this case, the low-energy background does not affect the evaluation of the efficiency because the energy of the RMD gamma-ray has an upper limit of 52.8 MeV.

Fig. 9.2b shows the energy spectrum of the LXe detector with BGO energy cut  $65 \text{ MeV} < E_{\text{BGO}} < 90 \text{ MeV}$ , together with the scaled template of the radiative capture background. The peak around  $E_\gamma \sim 0$  MeV corresponds to gamma-rays absorbed or scattered before reaching the LXe volume.

## 9.2.2 MC simulation

The  $\epsilon_{\text{CEX}}^{\text{MC}}$  is calculated with a dedicated MC simulation. In this simulation,  $1 \times 10^4 \pi^0 \rightarrow \gamma\gamma$  events were generated with a constraint to generate either one of the two gamma-rays in the direction of the BGO detector. The difference in the material budget of the LH<sub>2</sub> target between data and MC would cause systematic uncertainty. The LH<sub>2</sub> target is implemented with the material budget summarized in Table 2.6.

## 9.2.3 Result

The dominant uncertainty of the efficiency measurement comes from the statistical uncertainty of the number of radiative capture backgrounds (1%). Fig. 9.3 shows the measured efficiency as a function of the energy lower bound. The  $\epsilon_{\text{CEX}}^{\text{Data}}$  was  $61 \pm 1\%$  where the lower bound is 50 MeV, while the  $\epsilon_{\text{CEX}}^{\text{MC}}$  was 64%. A part of the 4.7% disagreement between the data and MC can be explained by the existence of the LXe volume in the entrance face, as discussed in Sec. 4.7. The LXe volume between the cryostat and the support structure CFRP was estimated as 1.8 mm thick on average, and it causes 1.8% inefficiency based on the attenuation length of LXe. The residual disagreement of 2.9% is not understood. This disagreement implies that the material budget in the measurement is underestimated compared to the MC simulation, but it is not yet identified which apparatus has a larger material budget than expected.

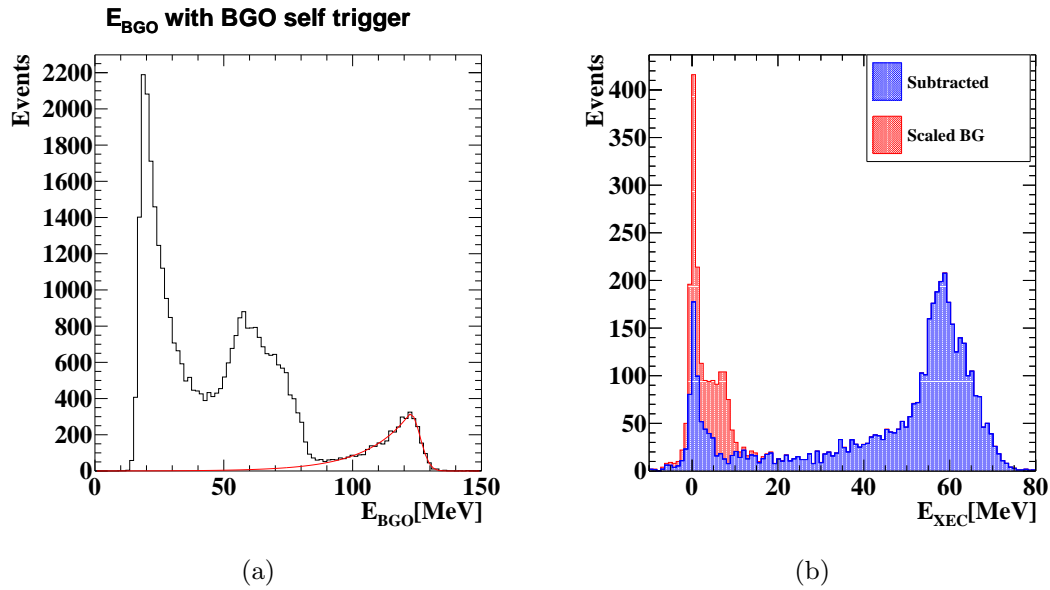


Figure 9.2: (a)  $E_{\text{BGO}}$  spectrum collected by the BGO self trigger. The red line is the fitting function of the 129 MeV peak from the radiative capture. (b)  $E_{\text{LXe}}$  spectrum for the events in the analysis region defined by the  $E_{\text{BGO}}$ . The  $E_{\text{LXe}}$  spectrum of the radiative capture (red) is obtained from the events in the 129 MeV peak. It shows the detector response to 9 MeV neutrons emitted in the opposite direction of 129 MeV gamma rays. The blue spectrum shows the energy spectrum of gamma rays from the charge exchange reaction.

### 9.3 Conclusion

It cannot be concluded if the unidentified disagreement between the  $\epsilon_{\text{CEX}}^{\text{data}}$  and  $\epsilon_{\text{CEX}}^{\text{MC}}$  affects the efficiency of the signal gamma ray or not. If the disagreement is coming from the misunderstanding of the material budget of the  $\text{LH}_2$  target, the disagreement is irrelevant to the efficiency of the signal gamma ray. Otherwise, if the disagreement is coming from the underestimation of the material budget of the entrance face of the LXe detector, the disagreement affects the efficiency of the signal gamma ray. The uncertainty of the  $R_\epsilon$  is estimated to be 0.02 by the statistical uncertainty of the radiative capture background (0.01) and the systematic uncertainty by the disagreement of the  $\epsilon_{\text{CEX}}^{\text{data}}$  and  $\epsilon_{\text{CEX}}^{\text{MC}}$  (0.02). Therefore, the  $R_\epsilon$  is estimated as  $0.97 \pm 0.02$ . The intrinsic detection efficiency for the signal gamma-ray in data is calculated as

$$\epsilon_\gamma = 0.69 \times (0.97 \pm 0.02) = 0.67 \pm 0.02 \quad (9.3)$$

The efficiency is  $0.67 \pm 0.02$ .

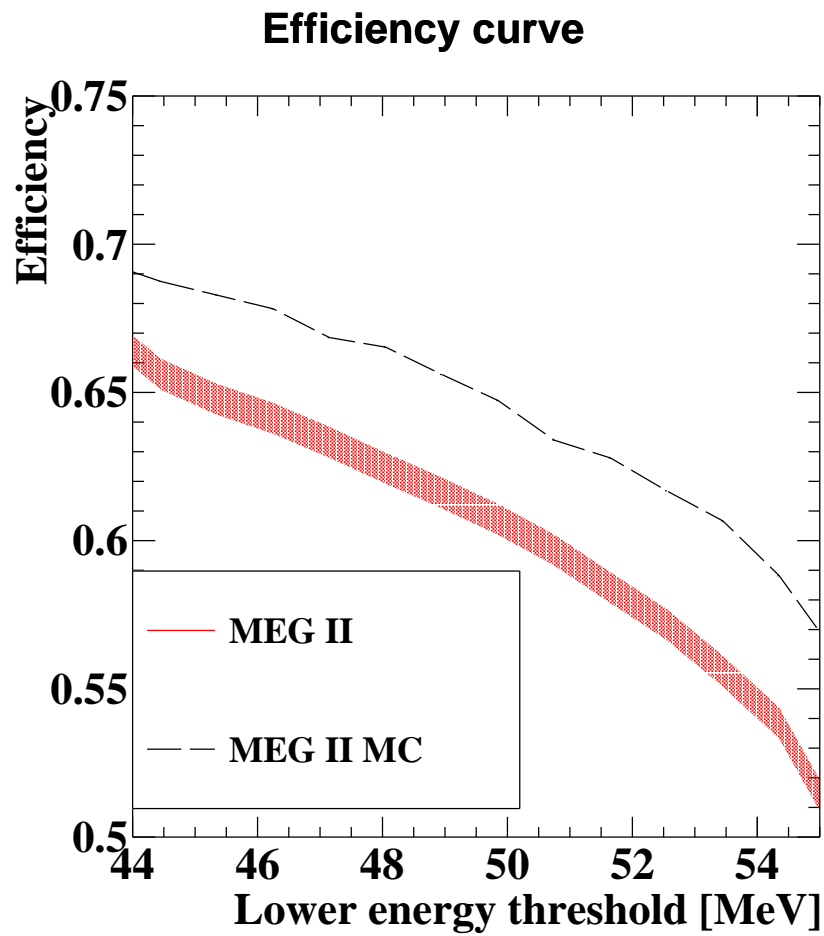


Figure 9.3: Efficiency curve of the LXe detector in the  $\pi^0$  run as a function of the lower bound of the energy. The uncertainty of the curve is shown in red, and the curve in the MC simulation is shown in a black dashed line.

## Chapter 10

# Background

There are two methods to reduce the number of background events in the analysis region. One is to discriminate signal events from background events with good resolutions, and the other is to reject the background events with an event selection. Here we describe two analysis methods to reduce the background events with event selections. One is the pileup analysis that identifies and unfolds the on- and off-time pileup gamma rays and the other is the event selection to reject cosmic rays. In this chapter, the method and performance of the pileup analysis are discussed in Sec. 10.1, and the cosmic-ray rejection is discussed in Sec. 10.2. The rates of the background gamma ray in data and MC simulation are discussed in Sec. 10.3.

### 10.1 Pileup analysis

#### 10.1.1 Source of pileup

Since the LXe detector has a homogeneous LXe volume, when multiple gamma rays impinge on the LXe volume at a close time to a main gamma ray of interest, the measurement of the main gamma ray can be biased.

An off-time pileup gamma ray comes from an accidental gamma ray, mainly from an RMD. The rate of the off-time pileup gamma rays increases with the beam intensity. When the time difference between the off-time pileup gamma ray and the main gamma ray is close, it affects the energy reconstruction of the main gamma ray depending on the time and amplitude of the off-time pileup pulse and deteriorates the effective energy resolution.

The source of the on-time pileup gamma-ray pulse is the AIF of Michel positrons. When both of the two gamma rays from the AIF come to the detector, they are spatially distant and coincident in the detector. This type of event, shown in Fig. 10.1b, is called AIF $2\gamma$  event. In contrast, when only one gamma ray is emitted to the LXe detector, it is called AIF $1\gamma$  (Fig. 10.1a).

The impact on position and time reconstruction is limited, as shown in Fig. 10.2, because only the photosensors close to the main gamma-ray hit are used for the reconstruction. On the other hand, the pileup gamma ray has a major impact on energy reconstruction because the energy is reconstructed by summing up the signal of all photosensors, as presented in Sec. 7.1.

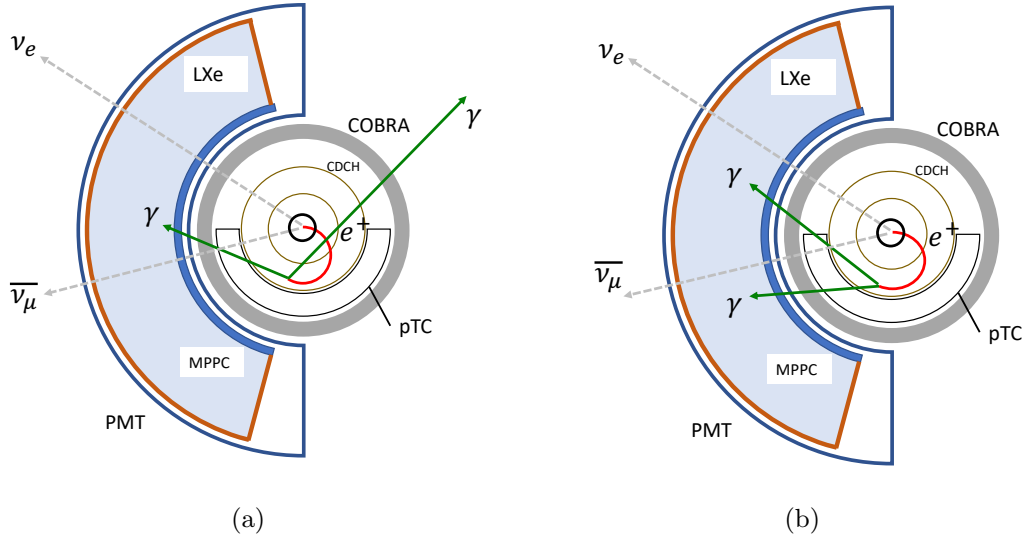


Figure 10.1: Schematic view of the (a) AIF1 $\gamma$  and (b) AIF2 $\gamma$  event. When both two gamma rays produced by the annihilation of a positron are detected by the LXe detector, it is an AIF2 $\gamma$  event. By contrast, only one gamma ray is detected in an AIF1 $\gamma$  event.

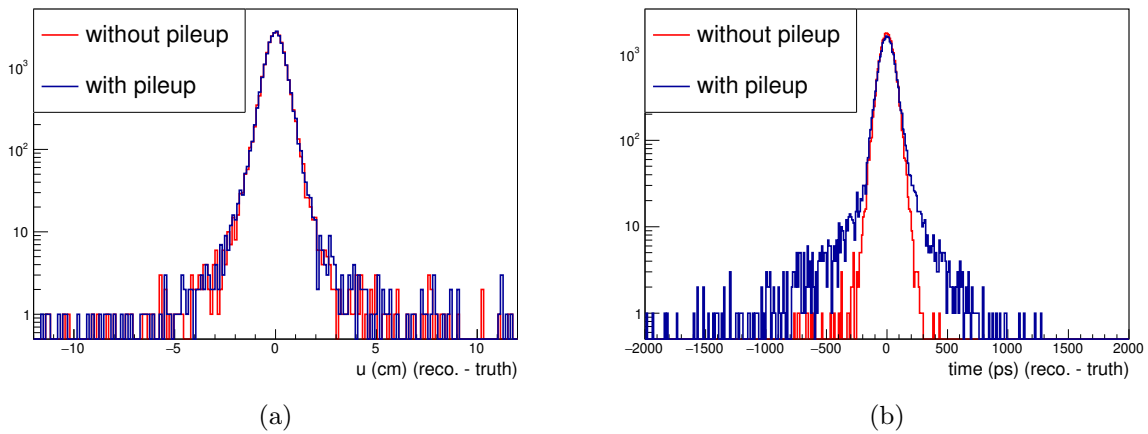


Figure 10.2: Difference between the true and reconstructed (a)  $u$  position and (b) time of signal gamma rays generated in MC simulation [2]. The difference without pileup gamma rays (red) and with pileup gamma rays (blue) are shown.

### 10.1.2 Analysis algorithm

Ref. [3] describes the development of three algorithms to reduce the pileup effect. One is a deep-learning method that uses a deep-learning model trained with an MC simulation to discriminate signal events from background events by using the light distribution of MPPCs. It is not used for the analysis of the 2021 dataset because it was difficult to validate the impact of the systematic difference in the light distribution between data and MC simulation. The second

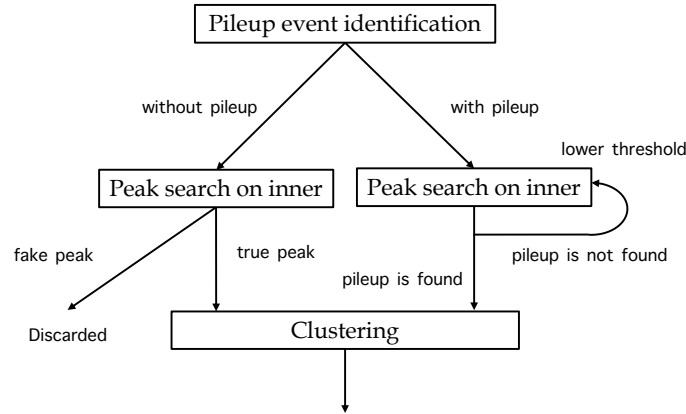


Figure 10.3: Algorithm of the spatial pileup search [3]. First, it is judged if the light distribution has multiple peaks. Then, the peak search on the inner face is performed. A pileup peak with a higher amplitude than certain threshold proceeds to the clustering phase.

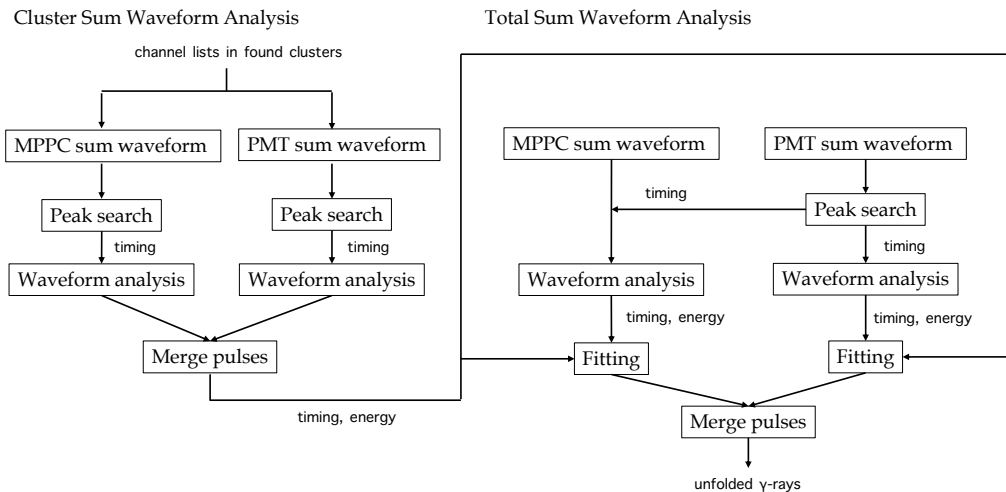


Figure 10.4: Algorithm of the unfolding of sum waveforms [3]. First, MPPC and PMT summed waveforms formed by the clustered photosensors in **PileupClustering** are analyzed to find off-time pileup pulses. Then, the MPPC and PMT summed waveforms formed by all photosensors are fitted based on the estimated pulse time and amplitude in the analysis for summed waveforms with the clustered photosensors.

algorithm is the peak search of the light distribution (Fig. 10.3) called **PileupClustering**, and the last one is the template fit of summed waveforms (Fig. 10.4) called **PileupUnfolding**. The algorithms were developed and tested with MC simulation. In this thesis, further development and performance evaluation of the latter two algorithms with the real dataset are described.

**PileupClustering** searches for spatial pileups in the light distribution of the inner and outer faces. Photosensors whose  $N_{\text{pho}}$  is larger than certain threshold value  $N_{\text{Inner}}^{\text{PLCL}}$  or  $N_{\text{Outer}}^{\text{PLCL}}$  are clustered into groups. When a cluster of photosensors is isolated from the cluster of the main

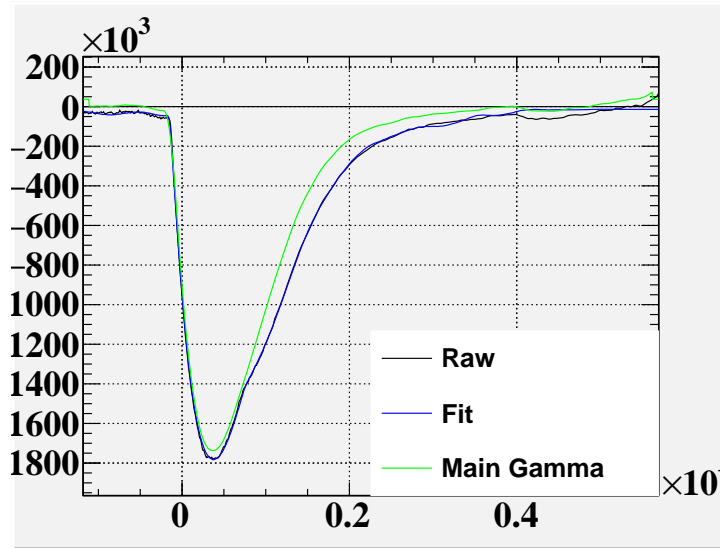


Figure 10.5: MPPC sum waveforms of a gamma-ray event with an off-time pileup pulse. The raw waveform is shown in black, the fitting waveform given by a linear combination of the template waveform is shown in blue, and the estimated main gamma-ray waveform by the pileup analysis is shown in green.

gamma ray, it is recognized as an additional pulse. The position and time of the found pulses are calculated based on the analysis of individual photosensor waveforms in the cluster.

In **PileupUnfolding**, a superimposition of the template waveforms is fitted to the summed waveform of MPPCs and PMTs as shown in Fig. 10.5. Since the MPPCs and PMTs have different pulse shapes, the fitting is performed separately for the MPPCs and the PMTs. The following  $\chi^2_{\text{PLUF}}(\mathbf{p})$  is minimized to find a set of the amplitude and time of the pulses  $\mathbf{p} = (t_i, A_i)$ .

$$\chi^2_{\text{PLUF}}(\mathbf{p}) = \sum_b (h_b - f_b(\mathbf{p}))^2 / \sigma_h^2 \quad (0 \leq b < N_{\text{fit}}), \quad (10.1)$$

$$f_b(\mathbf{p}) = \sum_{i \in \mathbf{p}} A_i g_b(t_i) \quad (10.2)$$

where  $h_b$  represents the  $b$ -th amplitude of the measured waveform,  $f_b(\mathbf{p})$  is that of the expected waveform by a superimposition of the template waveforms  $g_b(t)$  as defined in Eq. 10.2,  $\sigma_h$  is the fluctuation of the waveform due to the noise and the correlated noises, and  $N_{\text{fit}}$  is the number of bins used for the calculation of the  $\chi^2_{\text{PLUF}}$ . The output of the spatial pileup search is used for the initial fitting parameters. If the fitting does not give a small enough  $\chi^2$ , the algorithm attempts to converge the fitting by adding a pulse. The amplitude and time of the additional pulse are estimated from the difference between the waveforms ( $h_b$  and  $f_b(\mathbf{p})$ ) in the fitting. When the estimated amplitude of the additional pulse is above a certain threshold ( $A_{\text{MPPC}}$  and  $A_{\text{PMT}}$  for MPPC and PMT, respectively) and the relative time with respect to the main pulse is outside a coincidence window ( $T_{\text{coinc}}$ ), the additional pulse is accepted and taken into account for the next fitting. This selection of the additional pulse is made to avoid introducing

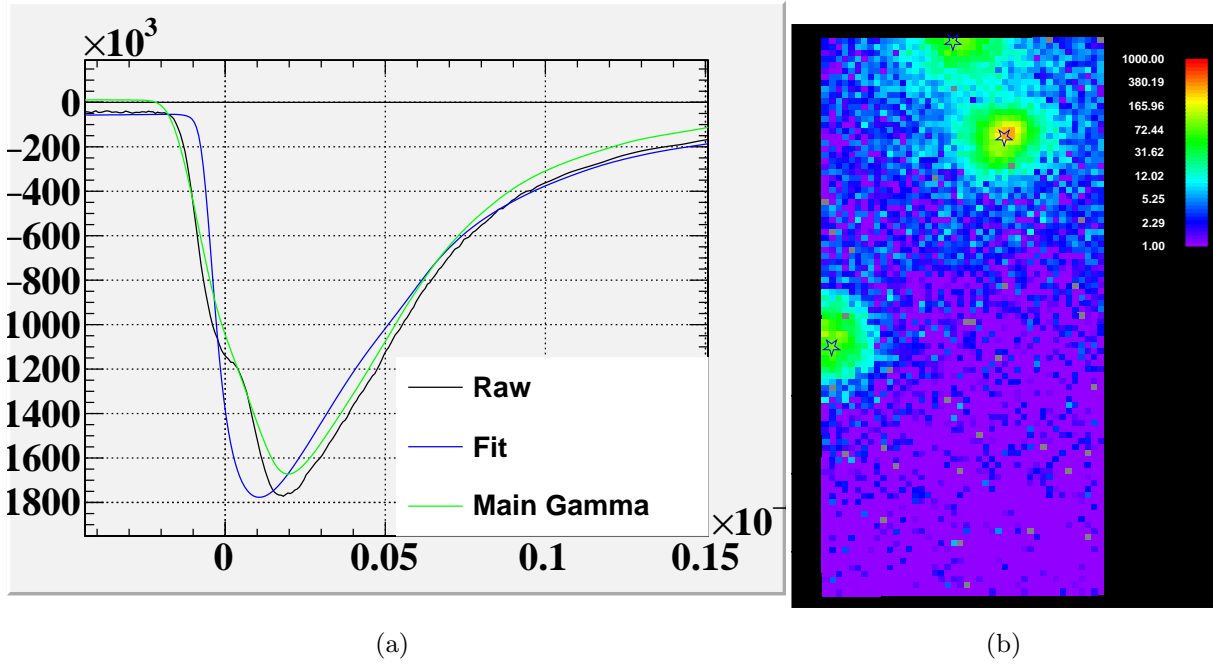


Figure 10.6: (a) Template fit and (b) light distribution of an identical NotConverged event. The template fit failed due to pileup pulses with close time to the main gamma-ray pulse. The light distribution shows the positions of three gamma rays are distant.

a fake pileup gamma-ray pulse, which makes a major error in evaluating the energy of the main gamma-ray pulse. The fitting is iterated until it converges (i.e. the  $\chi^2_{\text{PLUF}}(\mathbf{p})$  is below an upper limit  $\chi^2_{\text{UL}} = 20$ ) or the number of iterations reaches a given threshold (3 times).

The parameters of the pileup analysis are summarized in Table 10.2. The threshold values of the template fit,  $A_{\text{MPPC}}$  and  $A_{\text{PMT}}$ , should be as low as possible to detect pileup pulses as many as possible, but should not be too low to misidentify the fluctuation of the waveform as a fake pulse. Therefore, they were adjusted using the low-intensity muon beam dataset ( $1 \times 10^6 / \text{s}$ ) taken at the last period of the muon beam time in the 2021 run. Since the number of off-time pileups was limited in this dataset, the threshold values were set so that the off-time pileup was hardly detected. The thresholds of the peak search,  $N_{\text{Inner}}^{\text{PLCL}}$  and  $N_{\text{Outer}}^{\text{PLCL}}$ , in **PileupClustering** were adjusted to avoid detecting a fake on-time pileup peak due to the fluctuation of the light distribution and the reflection at the walls.

Events are categorized according to the results of the pileup analysis into four categories summarized in Table 10.1. While NoPileup and Unfolded events are used for the physics analysis, Coincidence and NotConverged events are not used for the analysis. A large fraction of Coincidence events comes from  $\text{AIF}2\gamma$ . Fig. 10.6 shows the result of the **PileupUnfolding** and **PileupClustering** of a NotConverged event. While the **PileupClustering** detected two pileup gamma-ray peaks together with a main gamma-ray peak, the template fit in **PileupUnfolding** failed due to the close off-time pileup pulse. The pileup analysis fails to converge the template fit when the time difference between the main gamma-ray pulse and an off-time pileup pulse

was smaller than the width of coincidence window  $T_{\text{coinc}} = 30$  ns and larger than  $\sim 5$  ns. In this case, the fit failed because the fitting was performed assuming only one pulse in the fit region.

Table 10.1: Event category of the pileup analysis.

Event categorization	Definition
NoPileup	No gamma-ray pulse is found aside from the main gamma ray.
Unfolded	The template fit is converged with off-time pileup.
Coincidence	On-time pileup is found by spatial pileup search.
NotConverged	The template fit is not converged.

Table 10.2: Input parameters of the pileup analysis. See the text for the definition of the parameters.

Parameter	Data
$N_{\text{Inner}}^{\text{PLCL}}$	250
$N_{\text{Outer}}^{\text{PLCL}}$	250
$A_{\text{MPPC}}$	$6 \times 10^4$
$A_{\text{PMT}}$	$6 \times 10^4$
$T_{\text{coinc}}$ [ns]	30
$\chi_{\text{UL}}^2$	20

### 10.1.3 Performance evaluation

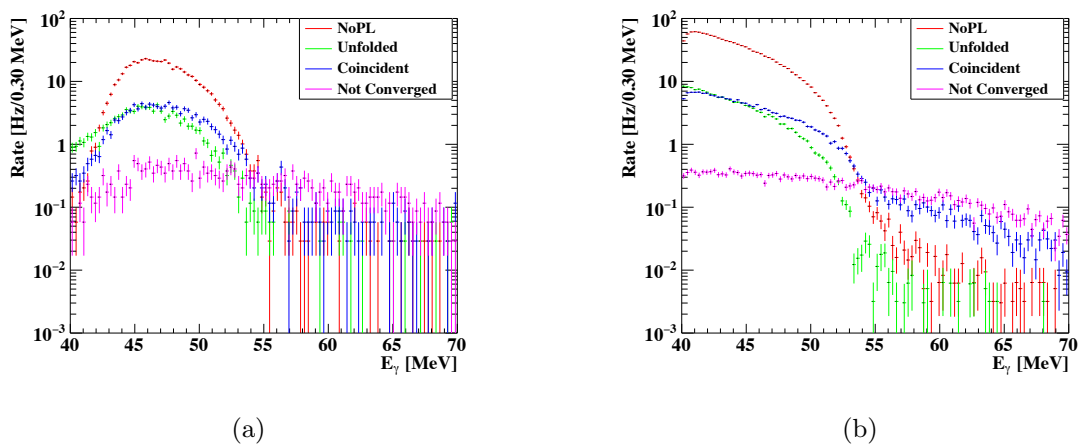


Figure 10.7: Energy spectrum of the accidental gamma ray in (a) data and (b) MC. The spectrums are shown in different colors depending on the categorization of events. NoPileup in red, Unfolded in green, Coincidence in blue, and NotConverged in purple.

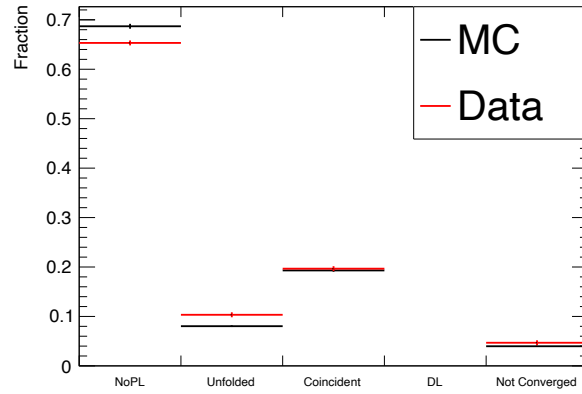


Figure 10.8: Fraction of four event categories for gamma-ray events in the analysis  $E_\gamma$  region ( $48 \text{ MeV} < E_\gamma < 58 \text{ MeV}$ ) in data (red) and in MC (black). Category “DL” is not used because the deep-learning-based analysis algorithm is not used.

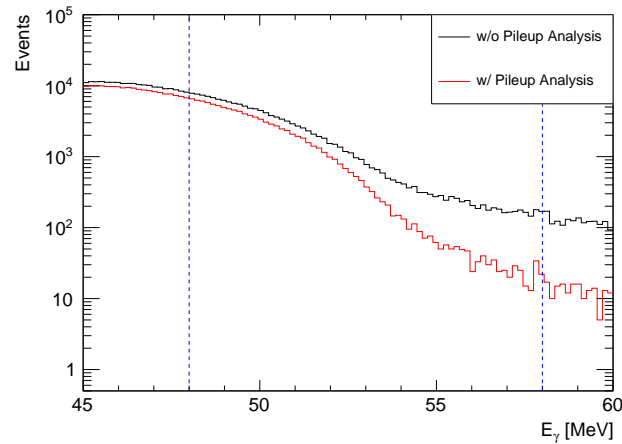


Figure 10.9: Energy spectrum for accidental background gamma rays with (red) and without (black) pileup analysis. The boundary of the analysis region ( $48 \text{ MeV} < E_\gamma < 58 \text{ MeV}$ ) is shown in blue dotted lines.

The key parameters of the pileup analysis are the efficiency of the signal gamma ray and the reduction of the background events in the signal  $E_\gamma$  region around  $52.8 \text{ MeV}$ . The accidental background gamma-ray events collected with the EGamma trigger were used to compare data and MC simulation.

Fig. 10.7 shows the energy spectrum for each event status in data and MC. While the energy spectra for NoPileup events and Unfolded events have sharp falling edges at around the signal energy ( $52.8 \text{ MeV}$ ), that of Coincidence and NotConverged are relatively flat. This is because the events with a pileup pulse at a very close time (within a few ns with respect to the main pulse) to the main gamma ray are categorized into Coincidence events. The Coincidence events

consist of the events with a very close off-time pileup pulse and the events with an on-time pileup gamma ray, such as the AIF2 $\gamma$  events.

Fig. 10.8 shows the fractions of event statuses for background gamma-ray events collected by the EGamma trigger. The fraction of the Coincidence events in data and MC are both 20% and consistent within the uncertainty (0.5%). This observation indicates that the fraction of the on-time pileup was consistent between in data and MC, contrary to the observation in Ref. [2]. Furthermore, the fraction of NotConverged events is also consistent between data and MC.

Fig. 10.9 shows the  $E_\gamma$  spectrum for background gamma rays in the time sideband<sup>\*1</sup> of the analysis region with and without the pileup analyses. The fraction of NoPileup and Unfolded events is 75% of the events that survive the cosmic-ray cut discussed in the next section, which means that the pileup analysis reduces the number of background events in the analysis region by 25%. When we focus on the energy range around the signal gamma ray,  $51.5 \text{ MeV} < E_\gamma < 54 \text{ MeV}$ , 43% of background events are reduced by the pileup analysis. The reduction rate for the background events is 8% worse than the previous study with the MC simulation (51% [3]). This can be explained by the fact that the deep-learning algorithm is not used and that the higher threshold values ( $N_{\text{Inner}}^{\text{PLCL}}$ ,  $N_{\text{Outer}}^{\text{PLCL}}$ ,  $A_{\text{MPPC}}$ ,  $A_{\text{PMT}}$ ) are used in order to cope with the fluctuation of the waveform and the reflection at the walls, which are not taken into account in the MC simulation.

The efficiency for the signal gamma ray is estimated with a dedicated MC simulation of the signal gamma ray with pileup gamma rays. The fraction of Coincidence and NotConverged events in this dataset is 4.7% and 1.4%, respectively. A part of Coincidence events have two peaks in the MPPC light distribution due to a gamma ray which escapes from the main electromagnetic shower. Fig. 10.10 shows an energy deposit of such signal gamma-ray event in the MC simulation. A gamma ray escaping from the main electromagnetic shower is converted in a distant place in the LXe volume and creates the second peak on the inner face. The systematic uncertainty is estimated by the deviation of the event categorization between data (time sideband) and the MC simulation. The overall inefficiency for the signal gamma ray due to the pileup analysis is estimated to be  $6.1 \pm 0.5\%$ .

## 10.2 Cosmic-ray rejection

While the energy spectrum of RMD and AIF events sharply drops with the energy, that of cosmic-ray events is relatively flat in the analysis region ( $48 \text{ MeV} < E_\gamma < 58 \text{ MeV}$ ). The cosmic ray has a large impact on the high-energy side of the analysis region. The position and energy of cosmic rays are reconstructed in the same way as for gamma rays. Cosmic-ray datasets taken without the beam are used to estimate the contribution in the analysis region. Fig. 10.11a shows the two-dimensional position distribution of cosmic-ray events with  $48 \text{ MeV} < E_\gamma < 58 \text{ MeV}$ . The reconstructed positions of most cosmic rays distribute at the edge of the detector because the

---

<sup>\*1</sup> See Sec. 11.1 for the definition of the analysis region and the time sideband.

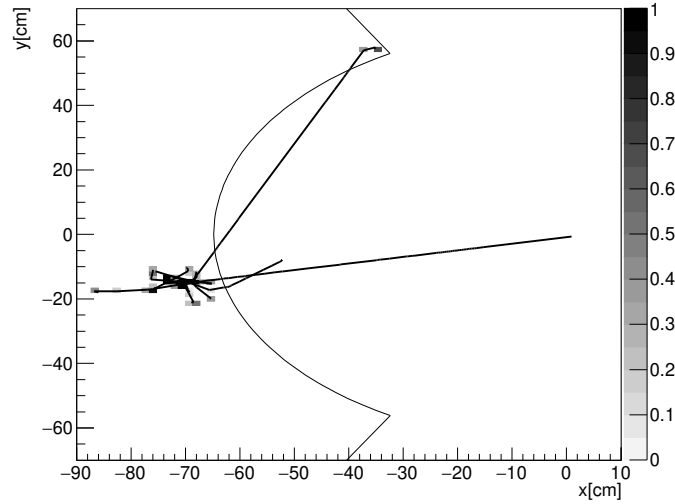


Figure 10.10: Energy deposit of a signal gamma-ray event in the MC simulation that has two peaks in the inner face [2].

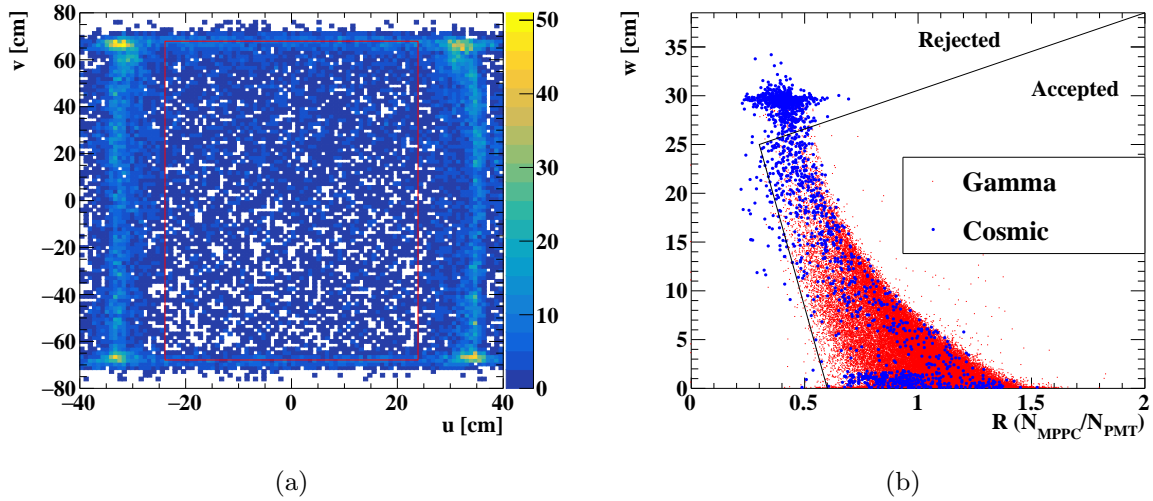


Figure 10.11: (a) Two-dimensional distribution of the reconstructed positions  $u$  and  $v$  in cosmic-ray events with the signal-like energies ( $48 \text{ MeV} < E_\gamma < 58 \text{ MeV}$ ). The position of most cosmic rays is at the edge of the readout region because the low-energy cosmic ray has a short path length in the LXe volume. A red box in the center shows the acceptance of the LXe detector. (b) The distribution of  $R = N_{\text{MPPC}}/N_{\text{PMT}}$  and  $w$  of 55 MeV gamma ray in the  $\pi^0$  run (red) and cosmic-ray (blue). The black solid line shows the event selection to reduce cosmic-ray events defined in Eq. 10.3.

cosmic-ray events reconstructed at low energy have a relatively short path length in LXe.

In order to exclude the cosmic-ray events contained in both the acceptance and analysis  $E_\gamma$  region, the reconstructed conversion depth ( $w$ ) and the ratio  $R = N_{\text{MPPC}}/N_{\text{PMT}}$  are used. The ratio  $R$  tends to be smaller for cosmic-ray events because the cosmic rays do not come from the target. The depth  $w$  is also effective to identify the cosmic rays that scratched the back of the detector. The events that satisfy the following cosmic-ray cut are accepted, as shown in Fig. 10.11b.

$$(w < a_1 \times R + b_1) \wedge (w > a_2 \times R + b_2) \quad (10.3)$$

where  $(a_1, b_1, a_2, b_2)$  are the parameters to define the cut. The parameters were optimized to be  $(a_1, b_1, a_2, b_2) = (7.9, 22.6, -83.3, 50.0)$ . This cut reduces the number of cosmic-ray events by 46.3% while keeping the efficiency for the signal gamma ray to 99.6%.

Since the total analysis efficiency is the product of the efficiency of the pileup analysis ( $93.9 \pm 0.5\%$ ) and the efficiency of the cosmic-ray event selection ( $99.6\%$ ), it is  $93.5 \pm 0.5\%$ .

### 10.3 Background rate

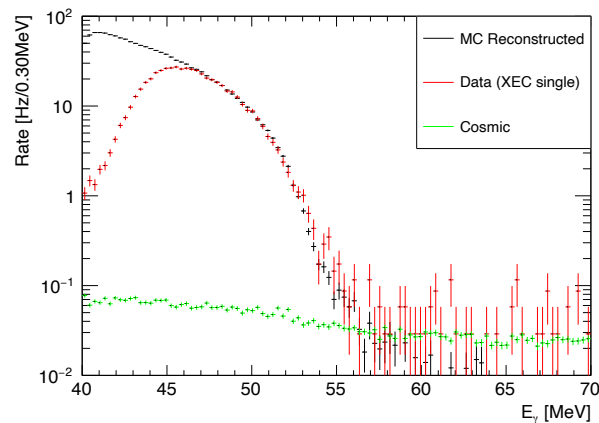


Figure 10.12: Energy spectrum of EGamma trigger events (red). The energy spectrum of background gamma rays in the MC simulation is shown in black, and that of cosmic-rays is shown in green. The trigger threshold was set to 44 MeV to have  $\approx 100\%$  efficiency in the analysis region (48 MeV).

The absolute rate of the background gamma-ray events is studied with the EGamma trigger dataset. Fig. 10.12 shows the energy spectrum of the EGamma trigger dataset at  $3.24 \times 10^7$  /s muon stopping rate together with the expected  $E_\gamma$  spectrum from MC simulation. The rate of background gamma-ray events in the analysis  $E_\gamma$  region of  $48 \text{ MeV} < E_\gamma < 58 \text{ MeV}$  and in the acceptance of the LXe detector is  $(1.40 \pm 0.13) \times 10^2$  Hz. The uncertainty is dominated by systematic uncertainty in the energy scale. The measured rate agrees well with the expected rate  $(1.43 \pm 0.01) \times 10^2$  Hz from the sum of MC  $((1.42 \pm 0.01) \times 10^2$  Hz) and the cosmic-ray

dataset ( $0.8 \pm 0.1$  Hz). This good agreement validates the beam rate estimated by other systems, such as the direct rate measurement by the beam monitoring counter and the hit rate at the pTC.

# Chapter 11

## Sensitivity

In this chapter, the sensitivity of the MEG II experiment is estimated based on the current estimates of the detector resolutions and counting rate. In particular, the position dependencies of the gamma-ray energy and position resolutions are taken into account in the sensitivity estimation. The sensitivity calculation method using the maximum likelihood analysis is explained in Sec. 11.1. The dataset, PDFs, effective number of muons are described in Sec. 11.2–11.5. The sensitivity of the 2021 dataset is estimated in Sec. 11.6. In Sec. 11.8, the improvement of the sensitivity by the detector upgrade and the possible improvements in the future are discussed.

### 11.1 Maximum Likelihood Analysis

In the physics analysis of the  $\mu^+ \rightarrow e^+\gamma$  search, the expected value of the number of signal events in a given analysis region  $N_{\text{sig}}$  is estimated by the maximum likelihood method. The analysis region is defined as

- $48 \text{ MeV} < E_\gamma < 58 \text{ MeV}$
- $52.2 \text{ MeV} < E_{e^+} < 53.5 \text{ MeV}$
- $|t_{e^+\gamma}| < 0.5 \text{ ns}$
- $|\theta_{e^+\gamma}| < 40 \text{ mrad}$
- $|\phi_{e^+\gamma}| < 40 \text{ mrad}$

The likelihood function is described as

$$\mathcal{L}(N_{\text{sig}}, N_{\text{RMD}}, N_{\text{ACC}}) := \frac{e^{-(N_{\text{sig}} + N_{\text{RMD}} + N_{\text{ACC}})}}{N_{\text{obs}}!} e^{-\frac{(N_{\text{RMD}} - \langle N_{\text{RMD}} \rangle)^2}{2\sigma_{\text{RMD}}^2}} e^{-\frac{(N_{\text{ACC}} - \langle N_{\text{ACC}} \rangle)^2}{2\sigma_{\text{ACC}}^2}} \times \prod_{i=1}^{N_{\text{obs}}} (N_{\text{sig}} S(\vec{x}_i) + N_{\text{RMD}} R(\vec{x}_i) + N_{\text{ACC}} A(\vec{x}_i)), \quad (11.1)$$

where  $N_{\text{RMD}}$  and  $N_{\text{ACC}}$  are the expected numbers of RMD and accidental background events in the analysis region, respectively, and  $N_{\text{obs}}$  is the number of observed events.  $\langle N_{\text{RMD}} \rangle$ ,  $\langle N_{\text{ACC}} \rangle$ ,  $\sigma_{\text{RMD}}$ , and  $\sigma_{\text{ACC}}$  are the estimated numbers of RMD and accidental background events and their uncertainties, based on the sidebands of the analysis region.  $S(\vec{x}_i)$ ,  $R(\vec{x}_i)$ , and  $A(\vec{x}_i)$  are the probability density functions (PDFs) of signal, RMD, and accidental background events

as functions of observables  $\vec{x}_i = (E_\gamma, E_{e^+}, t_{e^+\gamma}, \phi_{e^+\gamma}, \theta_{e^+\gamma}, t_{\text{RDC}}, E_{\text{RDC}})$  where  $t_{\text{RDC}}$  and  $E_{\text{RDC}}$  are the time and energy of a positron measured by the RDC. The best estimates of a set of  $(N_{\text{sig}}, N_{\text{RMD}}, N_{\text{ACC}})$  are calculated by maximizing the likelihood function.

The sensitivity that can be achieved in the MEG II experiment is determined by repeating a number of toy-MC experiments only with the background events and calculating the upper limits on  $N_{\text{sig}}$  at the 90% confidence level. The confidence interval of the  $N_{\text{sig}}$  is computed with the Feldman-Cousins approach with the profile likelihood ratio  $\lambda_p(N_{\text{sig}})$  defined below as a test statistic.

$$\lambda_p(N_{\text{sig}}) = \frac{\mathcal{L}(N_{\text{sig}}, \hat{N}_{\text{RMD}}, \hat{N}_{\text{ACC}})}{\mathcal{L}(\hat{N}_{\text{sig}}, \hat{N}_{\text{RMD}}, \hat{N}_{\text{ACC}})}, \quad (11.2)$$

where  $\hat{N}_i$  ( $i = \text{sig}, \text{RMD}, \text{ACC}$ ) is the best estimated value and the  $\hat{N}_i$  is the value that maximizes  $\mathcal{L}$  for the assumed  $N_{\text{sig}}$ . The upper limit of the confidence interval can be calculated either by a full-frequentist method or by an asymptotic method [78]. The full-frequentist method uses toy MC samples generated with a different  $N_{\text{sig}}$  to obtain the distribution of  $\lambda_p$  for a given  $N_{\text{sig}}$ . This method requires a large number of toy MC samples ( $\mathcal{O}(10^4)$  toy experiments for each  $N_{\text{sig}}$ ) and is thus time-consuming. The asymptotic method uses the approximation that the distribution of a test statistic  $-2 \ln(\lambda_p)$  is approximately a chi-square distribution for a large sample [79]. This method is advantageous in terms of computation time because it can estimate the upper limit without the toy MC experiments. The median of the upper limit of the  $N_{\text{sig}}$  divided by the normalization factor  $k$  is defined as the sensitivity.

## 11.2 2021 dataset

Fig. 11.1 shows the two-dimensional distribution in  $t_{e^+\gamma}$  vs  $E_\gamma$  of the 2021 dataset. In order to avoid possible human biases, the events close to the  $\mu^+ \rightarrow e^+\gamma$  signal were blinded so that they can not be used for the calibrations and analyses until all necessary parameters become ready for the likelihood analysis. The blind box is defined by using the  $E_\gamma$  and  $t_{e^+\gamma}$  as

- $48 \text{ MeV} < E_\gamma < 58 \text{ MeV}$ ,
- $|t_{e^+\gamma}| < 1 \text{ ns}$ .

Fig. 11.2 shows the  $t_{e^+\gamma}$  distribution of the energy sideband ( $45 \text{ MeV} < E_\gamma < 48 \text{ MeV}$ ) events. Though the  $t_{e^+\gamma}$  distribution should be flat because a gamma ray and a positron are not correlated in the accidental background events, the  $t_{e^+\gamma}$  distribution has a slope slightly down to the positive time difference in the 2021 dataset. This is because the trigger efficiency depended on the  $t_{e^+\gamma}$  due to the time-walk effect of the MPPC waveform. The slope of the distribution of  $w_\gamma > 10 \text{ cm}$  events is steep because the time-walk effect is enhanced for a small waveform.

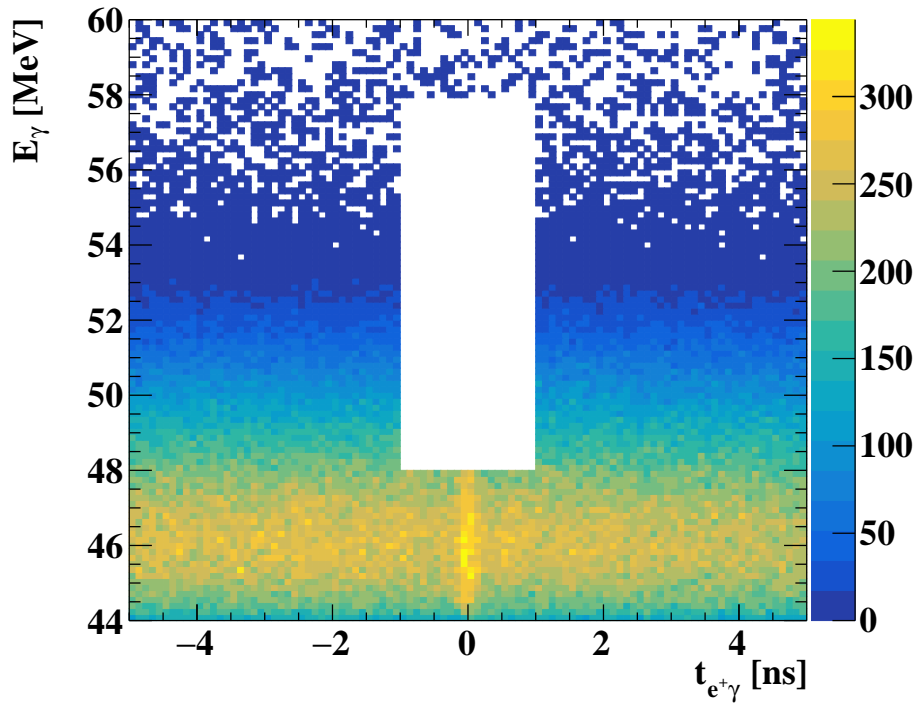


Figure 11.1: Two dimensional event distribution in  $t_{e+\gamma}$  and  $E_\gamma$  collected in the 2021 run. The blank box at the center shows the blind box. The following loose cut is applied for the illustration purpose;  $42 \text{ MeV} < E_{e^+} < 56 \text{ MeV}$ ;  $44 \text{ MeV} < E_\gamma < 60 \text{ MeV}$ ;  $|t_{e+\gamma}| < 5 \text{ ns}$ .

## 11.3 PDF

### 11.3.1 Signal PDF

The PDF of signal events is described as

$$\begin{aligned}
 S(E_\gamma, E_{e^+}, t_{e+\gamma}, \phi_{e+\gamma}, \theta_{e+\gamma}, t_{\text{RDC}}, E_{\text{RDC}} | \vec{r}_\gamma, \vec{y}_i) = & S_1(t_{e+\gamma}) \\
 & \times S_2(E_\gamma | \vec{r}_\gamma) \\
 & \times S_3(\phi_{e+\gamma} | w_\gamma, \vec{y}_i) \\
 & \times S_4(\theta_{e+\gamma} | w_\gamma, \vec{y}_i) \\
 & \times S_5(E_{e^+} | \vec{y}_i) \\
 & \times S_6(t_{\text{RDC}}, E_{\text{RDC}} | E_\gamma),
 \end{aligned}$$

where  $\vec{r}_\gamma$  is the position of the gamma-ray and  $\vec{y}_i$  is a set of reconstructed positron variables, the direction, the decay vertex, and the tracking quality.

$S_1(t_{e+\gamma})$  is estimated with the  $t_{e+\gamma}$  distribution of RMD events in the energy side-band (Fig. 11.3). The sum of two Gaussian functions with a slope is fitted to the  $t_{e+\gamma}$  distribution, and the core sigma of the function is 85 ps. The average  $t_{e^+}$  resolution is estimated to be 50 ps from the intrinsic time difference between the pTC counters with a method described in Ref. [33], and the residual 70 ps is dominated by the  $t_\gamma$  resolution ( $65 \pm 6$  ps).

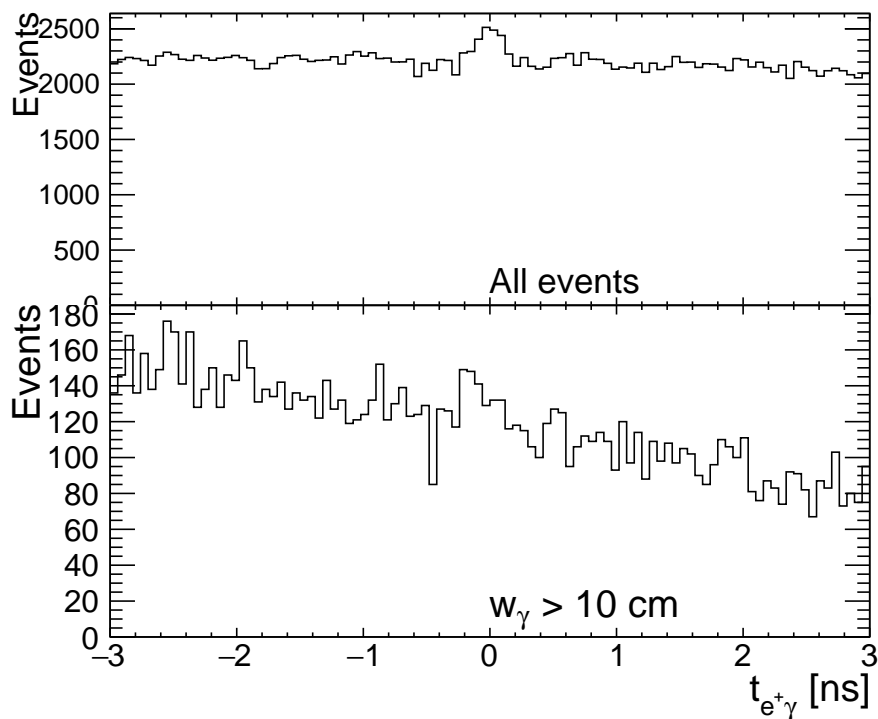


Figure 11.2:  $t_{e+\gamma}$  distribution of the energy sideband events without angular event selection. The distributions of (top) all events and (bottom)  $w_\gamma > 10$  cm events are shown.

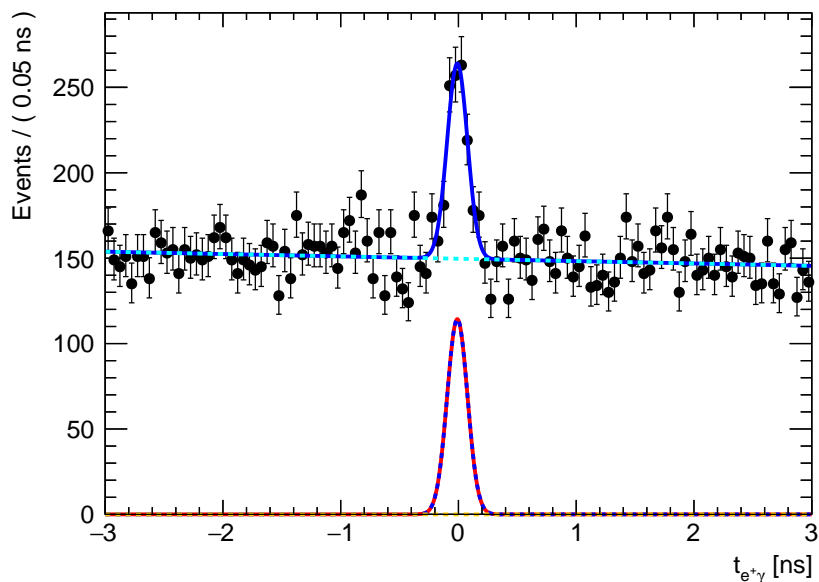


Figure 11.3:  $t_{e+\gamma}$  distribution in the energy sideband. The opening angle between positrons and gamma rays is constrained as  $\cos \Theta_{e+\gamma} < -0.995$ . The blue line shows the fit function that consists of two Gaussian functions and a slope (cyan). The line in red and blue in the bottom shows the function without the slope.

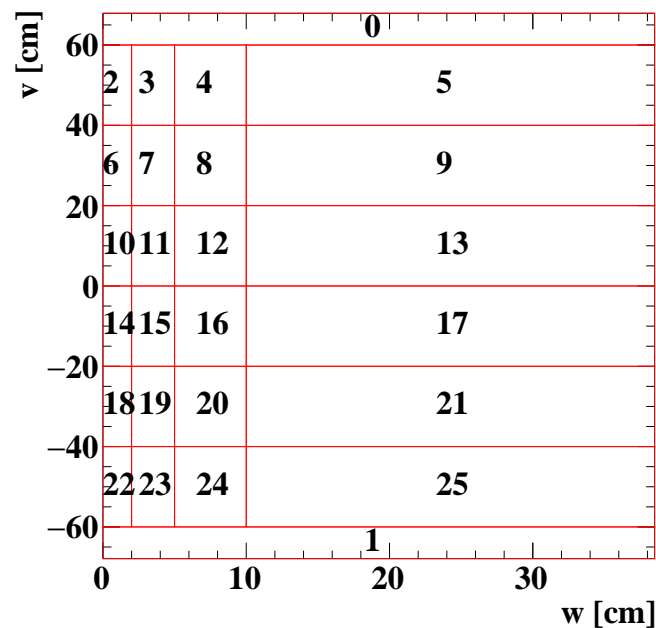


Figure 11.4: Division of the gamma-ray acceptance in the  $w$ - $v$  plane for the signal  $E_\gamma$  PDF.

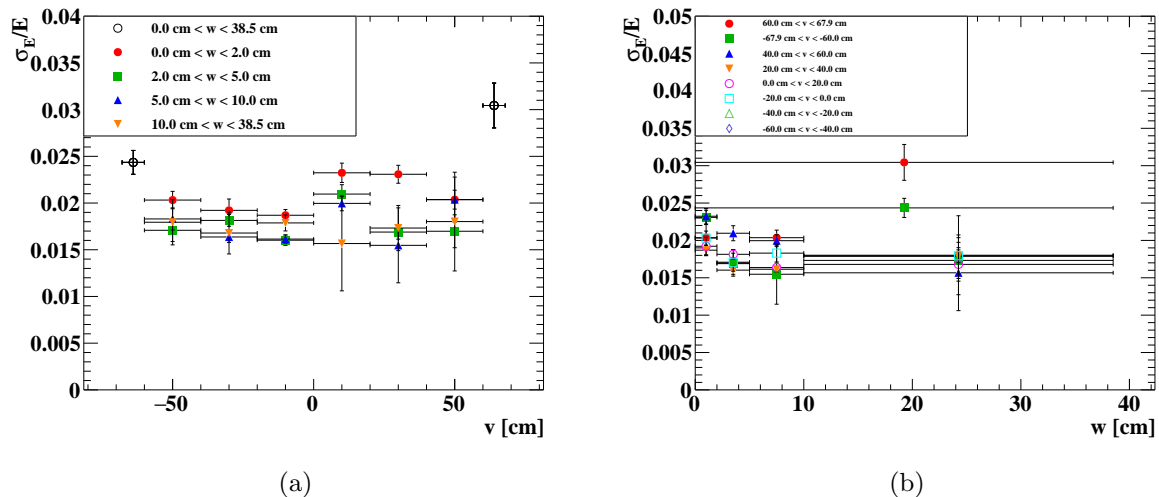


Figure 11.5: Core energy resolutions as functions of (a)  $v$  and (b)  $w$ . The resolutions are estimated by fitting a sum of two ExpGaus functions to the 55 MeV gamma-ray energy spectrum collected in the  $\pi^0$  run. The resolutions are shown in different colors depending on the gamma-ray positions.

$S_2(E_\gamma|\vec{r}_\gamma)$  is determined by the energy spectrum of the 55 MeV gamma ray from the  $\pi^0 \rightarrow \gamma\gamma$  decay. Since the energy resolution mainly depends on  $v_\gamma$  and  $w_\gamma$ , the position dependence of the detector response was taken into account in the PDF. The acceptance of the LXe detector is divided into 26 sections, as shown in Fig. 11.4, and the sum of two ExpGaus functions is fitted to the 55 MeV gamma-ray energy spectrum in each section. Fig. 11.5 shows the position dependence of the core energy resolution.

$S_3(\phi_{e+\gamma})$  and  $S_4(\theta_{e+\gamma})$  are determined by the position resolution for the gamma rays and the positron tracking performance. The  $w_\gamma$  dependences of the  $u_\gamma$ ,  $v_\gamma$ , and  $w_\gamma$  resolutions (Fig. 6.15) are taken into account.

The  $E_{e+}$  response for signal positrons ( $S_5(E_{e+}|\vec{y}_i)$ ) is estimated by fitting a smeared theoretical Michel energy spectrum (Fig. 1.6a) to the energy spectrum of Michel positrons in the time sideband. The signal PDF of RDC observables is created by the time and energy distribution of Michel positrons because only accidental hits by Michel positrons are expected in the signal events.

### 11.3.2 RMD PDF

The PDF for the RMD event is written as

$$\begin{aligned} R(E_\gamma, E_{e+}, t_{e+\gamma}, \phi_{e+\gamma}, \theta_{e+\gamma}, t_{\text{RDC}}, E_{\text{RDC}}|w_\gamma, \vec{y}_i) &= R_1(t_{e+\gamma}) \\ &\times R_2(E_\gamma, E_{e+}, \theta_{e+\gamma}, \phi_{e+\gamma}|u_\gamma, \vec{y}_i) \\ &\times R_3(t_{\text{RDC}}, E_{\text{RDC}}) \end{aligned}$$

$R_1(t_{e+\gamma})$  is the normalized  $t_{e+\gamma}$  distribution for a coincident pair of a positron and a gamma-ray, and thus it is identical to  $S_1(t_{e+\gamma})$ .  $R_2(E_\gamma, E_{e+}, \theta_{e+\gamma}, \phi_{e+\gamma}|u_\gamma, \vec{y}_i)$  is obtained by the convolution of the theoretical spectrum based on the SM and the detector response. The PDF of RDC observables  $R_3$  is the same as the signal PDF because only accidental hits by Michel positrons are expected in the RMD events.

### 11.3.3 Accidental background PDF

The PDF for the accidental background event is written as

$$\begin{aligned} A(E_\gamma, E_{e+}, t_{e+\gamma}, \phi_{e+\gamma}, \theta_{e+\gamma}|\vec{r}_\gamma, \vec{y}_i) &= A_1(t_{e+\gamma}|E_\gamma, E_{e+}, \vec{y}_i) \\ &\times A_2(E_\gamma|\vec{r}_\gamma) \\ &\times A_3(\theta_{e+\gamma}|u_\gamma, \vec{y}_i) \\ &\times A_4(\phi_{e+\gamma}|v_\gamma, \vec{y}_i) \\ &\times A_5(E_{e+}|\vec{y}_i) \\ &\times A_6(t_{\text{RDC}}, E_{\text{RDC}}|E_\gamma) \end{aligned}$$

Since positrons and gamma rays are not correlated with each other in accidental background events, the PDFs can be made based on the time sideband of the analysis region.

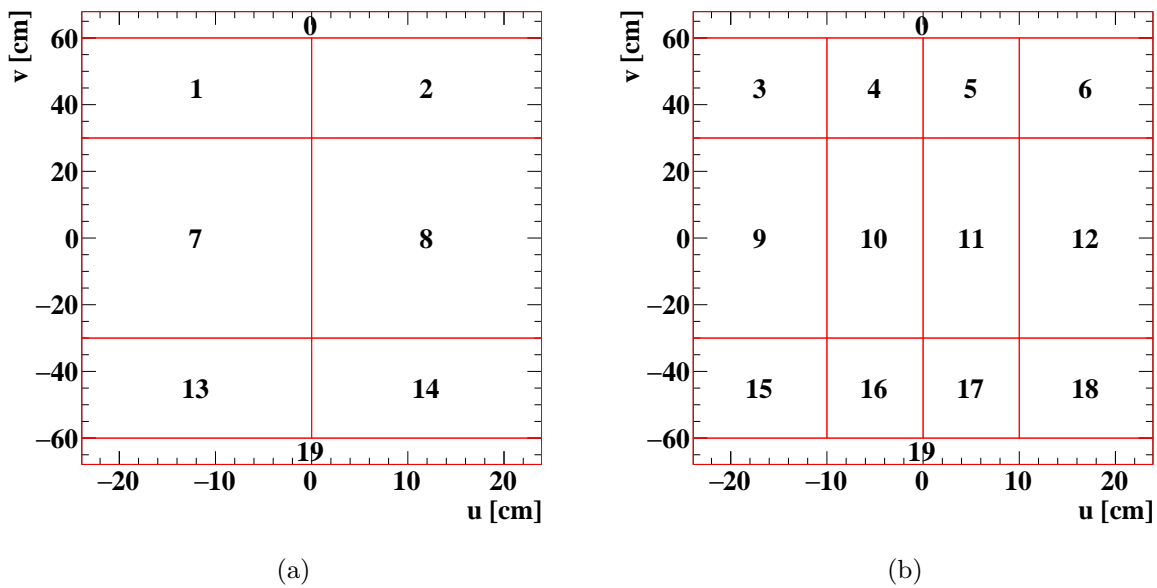


Figure 11.6: Sections to create the accidental background PDF  $A_2(E_\gamma|\mathbf{r}_\gamma)$  for (a) shallow ( $w < 2$  cm) and (b) deep ( $w > 2$  cm) region.

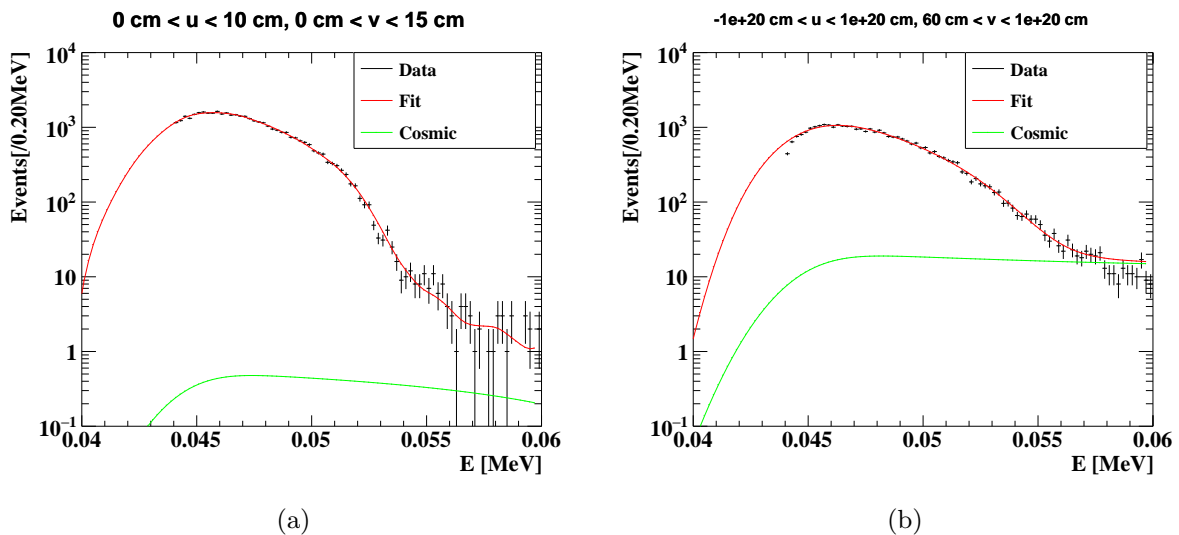


Figure 11.7: Background energy spectrum of the time sideband (a) in the central region of the detector ( $0 \text{ cm} < u_\gamma < 10 \text{ cm}$ ,  $0 \text{ cm} < v_\gamma < 15 \text{ cm}$ ,  $2 \text{ cm} < w_\gamma < 38.5 \text{ cm}$ ) and (b) in the edge region of the detector ( $-23.9 \text{ cm} < u_\gamma < 23.9 \text{ cm}$ ,  $60 \text{ cm} < v_\gamma < 67.9 \text{ cm}$ ,  $0 \text{ cm} < w_\gamma < 38.5 \text{ cm}$ ).

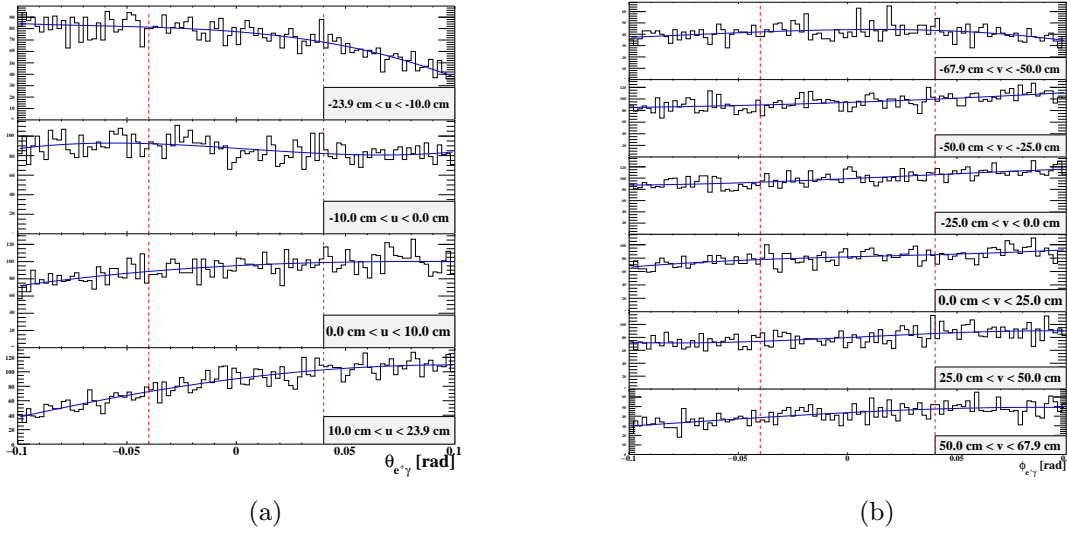


Figure 11.8:  $\theta_{e+\gamma}$  and  $\phi_{e+\gamma}$  distribution in the time sideband. A cubic function was fitted to the distribution to parameterize the distribution. The red lines show the boundary of the analysis region ( $|\theta_{e+\gamma}| < 0.04$  mrad and  $|\phi_{e+\gamma}| < 0.04$  mrad).

As discussed in Sec. 11.2, the  $t_{e+\gamma}$  distribution has a slope in the 2021 dataset. The sensitivity calculation for this thesis nevertheless uses a flat  $t_{e+\gamma}$  distribution as the PDF  $A_1(t_{e+\gamma})$  assuming the impact of the slope is negligible because the fraction of deep gamma-ray events ( $w_\gamma > 10$  cm) where the  $t_{e+\gamma}$  distribution has a steep slope is small (5%) and because the shape of the signal  $t_{e+\gamma}$  PDF is different from the accidental  $t_{e+\gamma}$  distribution of deep gamma-ray events ( $w_\gamma > 10$  cm).

$A_2(E_\gamma|\mathbf{r}_\gamma)$  is determined by the time sideband. The acceptance region of the LXe detector is divided into 20 sections, as shown in Fig. 11.6, and a function to model the accidental background, which consists of the RMD gamma-ray, AIF gamma-ray, and cosmic-ray components, is fitted to the energy spectrum of each section as shown in Fig. 11.7. This is to improve the sensitivity by taking the position dependence of the background distribution and the detector resolution into account. In particular, the fraction of the cosmic-ray background is larger in the edge region in the  $v$  direction as shown in Fig. 11.7b.

Fig. 11.8 shows the  $\theta_{e+\gamma}$  and  $\phi_{e+\gamma}$  distribution with different  $u_\gamma$  and  $v_\gamma$  requirements in the time sideband. The position dependence of the  $\theta_{e+\gamma}$  and  $\phi_{e+\gamma}$  distribution reflects the position dependence on the detection efficiency and the acceptance of positrons. A cubic function was fitted to the distributions and used as the angular PDFs ( $A_3(\theta_{e+\gamma}|u_\gamma, \vec{y}_i)$  and  $A_4(\phi_{e+\gamma}|v_\gamma, \vec{y}_i)$ ) after normalization.

$A_5(E_{e^+})$  is determined by fitting a smeared distribution of the theoretical Michel spectrum with multiple Gaussian functions to the  $E_{e^+}$  spectrum in the time sideband.

The PDF of RDC observables  $A_6(t_{\text{RDC}}, E_{\text{RDC}}|E_\gamma)$  is calculated by using the correlation between RDC observables ( $t_{\text{RDC}}, E_{\text{RDC}}$ ) and  $E_\gamma$  in the time sideband.

Table 11.1 summarizes the current estimates of the detector performance in the 2021 run. The

gamma-ray resolutions are the average values over the acceptance. The position dependencies of the position and energy resolutions are taken into account for the signal and accidental background PDFs.

Table 11.1: Summary of the detector performance in 2021. The efficiencies and the average values of the resolutions are presented. The  $w$  dependence of the position resolution and the  $v, w$  dependence of the energy resolution are taken into account for the sensitivity calculation.

Resolution	
$E_\gamma$ resolution (%)	2.0 ( $w < 2$ cm) / 1.7 ( $w > 2$ cm)
$E_{e^+}$ resolution (keV)	90 (core, 70%) / 310 (tail, 30%)
$\theta_{e^+\gamma}$ resolution (mrad)	8.6
$\phi_{e^+\gamma}$ resolution (mrad)	6.8
$t_{e^+\gamma}$ resolution (ps)	85
Efficiency	
$\epsilon_{e^+}$ (%)	70
$\epsilon_\gamma$ (%)	63
$\epsilon_{\text{sel}}$ (%)	87

## 11.4 Normalization and single event sensitivity with 2021 dataset

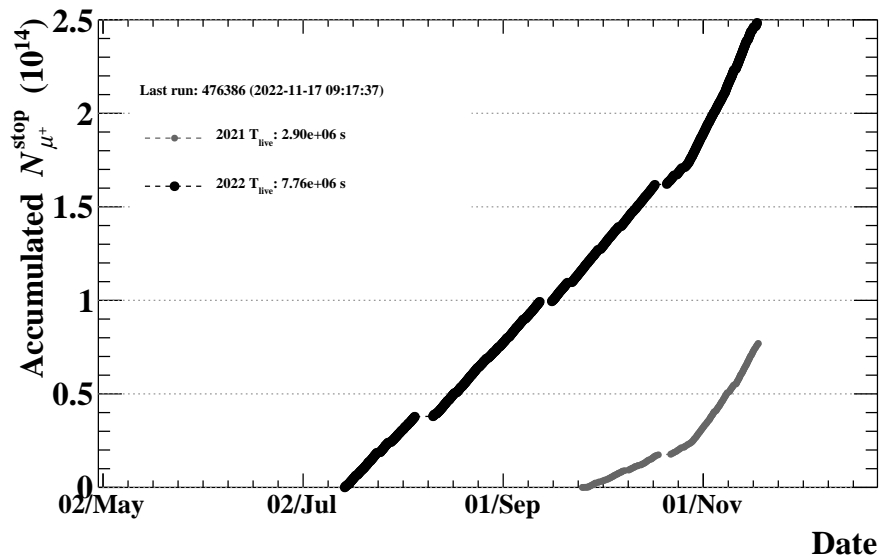


Figure 11.9: The accumulated number of stopped muons at the target  $N_\mu$  calculated by the product of the livetime and the muon stopping rate at the target in the 2021 (grey) and 2022 run (black).

Fig. 11.9 shows the evolution of the  $N_\mu$  in the 2021 run and the 2022 run. In the 2021 run, the  $N_\mu$  during the physics data-taking evolved up to  $8 \times 10^{13}$ . Based on Eq. 1.23, the following

relation stands between the  $N_\mu$  and the effective number of muons for the  $\mu^+ \rightarrow e^+\gamma$  search  $k$ .

$$k = N_\mu \times \Omega \times \epsilon_\gamma \times \epsilon_{e^+} \times \epsilon_{\text{sel}} \quad (11.3)$$

The  $k$  is estimated by using the number of Michel events triggered by the pTC self trigger  $N_{\text{Michel}}$  because the time variations of the beam intensity and the  $\epsilon_{e^+}$  are reflected in the time variation of the number of counted positrons as

$$k = \frac{N_{\text{Michel}}}{\mathcal{B}_{\text{Michel}}} \cdot \frac{P_{\text{MEG}}}{P_{\text{Michel}}} \cdot \frac{\epsilon_{\text{TRG}}^{\text{MEG}}}{\epsilon_{\text{TRG}}^{\text{Michel}}} \cdot \frac{\epsilon_{e^+}}{\epsilon_{e^+}^{\text{Michel}}} \cdot \epsilon_\gamma \cdot \epsilon_{\text{sel}}. \quad (11.4)$$

The definitions of the variables are listed below.

- $\mathcal{B}_{\text{Michel}}$  is the branching ratio of Michel decay in the analysis window.
- $P_{\text{MEG}}$  and  $P_{\text{Michel}}$  are the prescaling factors of the MEG trigger and the pTC alone trigger, respectively.
- $\epsilon_{\text{TRG}}^{\text{MEG}}$  and  $\epsilon_{\text{TRG}}^{\text{Michel}}$  are the efficiency of the MEG trigger and the pTC self trigger, respectively.
- $\epsilon_{e^+}^{\text{Michel}}$  is the detection efficiency of Michel positrons.

The  $k$  in the 2021 run is  $(2.6 \pm 0.1) \times 10^{12}$ .

## 11.5 Estimated number of background events with 2021 dataset

Table 11.2: The definition of the analysis region and sidebands for counting the number of backgrounds.

	Analysis region	Time sideband	Energy sideband
$E_\gamma$ [MeV]	[48, 55]	[48,55]	[45,48]
$E_{e^+}$ [MeV]	[52.2, 53.5]	[52.2, 53.5]	[42, 56]
$t_{e^+\gamma}$ [ns]	[-0.5, 0.5]	[-3.0, -1.0] + [1.0, 3.0]	[-3.0, 3.0]
$\cos \Theta_{e^+\gamma}$	-	-	[-1.0, -0.995]
$\theta_{e^+\gamma}, \phi_{e^+\gamma}$ [mrad]	[-40, 40]	[-40, 40]	-

The number of background events ( $\langle N_{\text{ACC}} \rangle$  and  $\langle N_{\text{RMD}} \rangle$ ) is estimated from the time and energy sidebands defined in Table 11.2, respectively. The  $\langle N_{\text{ACC}} \rangle$  can be calculated by counting the number of background events in the positive and negative time sidebands and scaling it with the ratio of the  $t_{e^+\gamma}$  interval of the analysis region (1 ns) to that of the time sidebands (4 ns). The impact of the slope of the  $t_{e^+\gamma}$  distribution is canceled by using the two sidebands that are symmetric with respect to the analysis region. Since the number of background events in the sidebands is  $249 \pm 16$  events, the  $\langle N_{\text{ACC}} \rangle$  is  $62.3 \pm 3.9$ .

The  $\langle N_{\text{RMD}} \rangle$  is estimated based on the number of RMD events in the energy sideband  $N_{\text{RMD}}^{\text{SB}}$ . From the peak in the  $t_{e^+\gamma}$  distribution in the energy sideband, shown in Fig. 11.3, the number of RMD events ( $N_{\text{RMD}}^{\text{SB}}$ ) is estimated to be  $494 \pm 38$ .

The  $\langle N_{\text{RMD}} \rangle$  can be expressed using the  $N_{\text{RMD}}^{\text{SB}}$  as

$$\langle N_{\text{RMD}} \rangle = N_{\text{RMD}}^{\text{SB}} \times \frac{\mathcal{B}_{\text{RMD}}^{\text{AR}}}{\mathcal{B}_{\text{RMD}}^{\text{SB}}} \times \frac{\epsilon_{\text{TRG,RMD}}^{\text{AR}}}{\epsilon_{\text{TRG,RMD}}^{\text{SB}}}, \quad (11.5)$$

where  $\mathcal{B}_{\text{RMD}}^{\text{SB}}$  and  $\mathcal{B}_{\text{RMD}}^{\text{AR}}$  are effective branching ratios of RMD events in the energy sideband and the analysis region, respectively. The effective branching ratio is calculated by the energy response measured by the 55 MeV gamma-ray from the  $\pi^0 \rightarrow \gamma\gamma$  and the theoretical branching ratio (Eq. 1.18).  $\epsilon_{\text{TRG,RMD}}^{\text{AR}}$  and  $\epsilon_{\text{TRG,RMD}}^{\text{SB}}$  are the trigger efficiencies for the RMD events in the analysis region and energy sideband, respectively. The calculated branching ratios are  $\mathcal{B}_{\text{RMD}}^{\text{SB}} = 1.2 \times 10^{-10}$  and  $\mathcal{B}_{\text{RMD}}^{\text{AR}} = 3.2 \times 10^{-13}$ , respectively. The ratio of the trigger efficiency is determined as  $\frac{\epsilon_{\text{TRG,RMD}}^{\text{AR}}}{\epsilon_{\text{TRG,RMD}}^{\text{SB}}} = 0.78$  by the  $E_\gamma$  dependence of the efficiency of the EGamma trigger and the  $\cos \Theta_{e+\gamma}$  dependence of the efficiency of the direction matching. The  $\langle N_{\text{RMD}} \rangle$  has a large systematic uncertainty because it has a 60% discrepancy between the  $N_{\text{RMD}}^{\text{SB}}$  and the expectation given by a product of the  $k$  and the effective branching ratio ( $312 \pm 12$ ). This discrepancy should be understood before opening the blinding box, though it will not affect the sensitivity calculation because the accidental background is dominant in the analysis region. For the sensitivity calculation in this thesis, an average value in the two expected values is used, and the deviation is assigned as the systematic uncertainty. The  $\langle N_{\text{RMD}} \rangle$  is estimated to be  $1.1 \pm 0.3$ .

## 11.6 Sensitivity with 2021 dataset

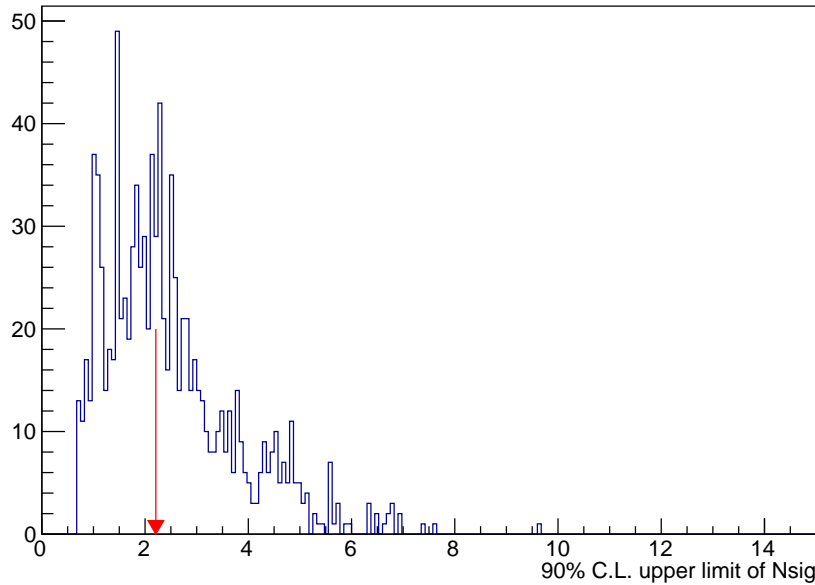


Figure 11.10: The distribution of the 90% C.L. upper limits on  $N_{\text{sig}}$ . The red arrow shows the median value of the distribution (2.2).

Table 11.3: Summary of the sensitivity calculation. The values with \* are the calculated ones based on the livetime and the measured values in the 2021 run. See the text for the detail.

Year	2021	2021+2022	2021–2025
$k$	$(2.7 \pm 0.1) \times 10^{12}$	$(1.3 \pm 0.1) \times 10^{13}$	$(5.0 \pm 0.2) \times 10^{13}$ *
Livetime [s]	$2.9 \times 10^6$	$1.1 \times 10^7$	$3.4 \times 10^7$
$\langle N_{\text{ACC}} \rangle$	$62 \pm 4$	$283 \pm 8^*$	$1360 \pm 20^*$
$\langle N_{\text{RMD}} \rangle$	$1.1 \pm 0.3$	$5.2 \pm 2.5^*$	$20.4 \pm 9.2^*$
The median of 90% U.L. of the $N_{\text{sig}}$	$2.2^*$	$2.6^*$	$4.1^*$
Sensitivity	$(8.1 \pm 0.3) \times 10^{-13}$ *	$(2.1 \pm 0.1) \times 10^{-13}$ *	$(8.1 \pm 0.3) \times 10^{-14}$ *

Table 11.4: Summary of the systematic uncertainties of gamma-ray measurement.

Element	Systematic uncertainty
Alignment of the LXe detector	0.60 mm / 0.75 mrad ( $z/\phi$ )
Center of $t_{e+\gamma}$	7 ps
$E_\gamma$ scale	0.4%

The sensitivity that can be achieved with the 2021 dataset was estimated by  $10^4$  toy experiments with the parameters summarized in Table 11.3. The confidence interval of the  $N_{\text{sig}}$  was calculated by the full-frequentist method with  $4 \times 10^3$  toy MC experiments for 23  $N_{\text{sig}}$  values between 0 and 15. To take the systematic uncertainties of the gamma-ray measurement into account, the PDFs are randomized with the estimated uncertainties as summarized in Table 11.4 when the toy MC experiments are generated for the likelihood ratio ordering. Fig. 11.10 shows the distribution of  $N_{\text{sig}}$  upper limit for the toy experiments. The median of the distribution was 2.2, and the sensitivity was estimated to be  $(8.1 \pm 0.4) \times 10^{-13}$ . The impact of the systematic uncertainties is  $<1\%$ , and it is negligible with respect to the systematic uncertainty of the normalization factor  $k$ . This is because the systematic uncertainties of the gamma-ray direction (0.4 mrad) and time (6 ps) are smaller than the resolutions.

## 11.7 Sensitivities with 2022 run dataset and further

In this section, we discuss the sensitivity by adding the dataset that was already collected in the 2022 run and that is to be collected in 2023–2025 run. In the 2022 run, the data were collected for four months, starting from the middle of July until the middle of November, and the  $N_\mu$  evolved up to  $2.5 \times 10^{14}$  as shown in Fig. 11.9. The muon stopping rate was adjusted to  $2.8 \times 10^7$  /s in the first 3.5 months and then increased to  $5.8 \times 10^7$  /s to speed up the accumulation of the statistics. Assuming that the same detection efficiency and detector performance as the 2021 run were achieved, the normalization factor  $k$  in the 2022 run is estimated to be  $9.7 \times 10^{12}$  using the number of Michel decays as described in Sec. 11.4. The  $\langle N_{\text{ACC}} \rangle$  and  $\langle N_{\text{RMD}} \rangle$  in the combined datasets are calculated by using the measured values of the 2021 dataset, the

accumulated number of  $k$ , and the projected muon stopping rate. The estimated sensitivity will improve to  $(2.1 \pm 0.1) \times 10^{-13}$  with the combined dataset collected in 2021 and 2022. This is 2.5 times better than the sensitivity in the MEG experiment,  $5.3 \times 10^{-13}$ . Therefore, the highest sensitivity for the  $\mu^+ \rightarrow e^+ \gamma$  can be achieved with the dataset that has already been collected.

Assuming that we will collect the physics data for the same livetime ( $7.8 \times 10^6$  s) per year and at the muon stopping rate of  $5 \times 10^7$  /s from 2023 to 2025, the accumulated  $k$  will evolve up to  $(5.0 \pm 0.2) \times 10^{13}$ . The sensitivity will further go down to  $(8.1 \pm 0.4) \times 10^{-14}$  after another three years of data acquisition up to 2025. The parameters and results of the sensitivity calculation of the upcoming datasets are summarized in Table 11.3 together with those of the 2021 dataset. The sensitivity of the MEG II experiment will be six times higher than that of the MEG experiment ( $5.3 \times 10^{-13}$ ). Fig. 11.11 shows the sensitivity of the MEG II experiment as a function of the livetime.

However, the estimated sensitivity is worse than the expected sensitivity in the design phase ( $6 \times 10^{-14}$  [29]). In the design phase, the estimation of the beam rate dependence of the detector performance was optimistic. The analysis efficiency of positrons gets lower at a higher beam rate with the current analysis method, and it is currently preventing the collection of the physics data at a higher intensity than  $5 \times 10^7$  /s. The second reason for the degraded sensitivity is the worse  $E_\gamma$  resolution than expected. The impact of the degraded  $E_\gamma$  resolution on the sensitivity was estimated to be 15% [2].

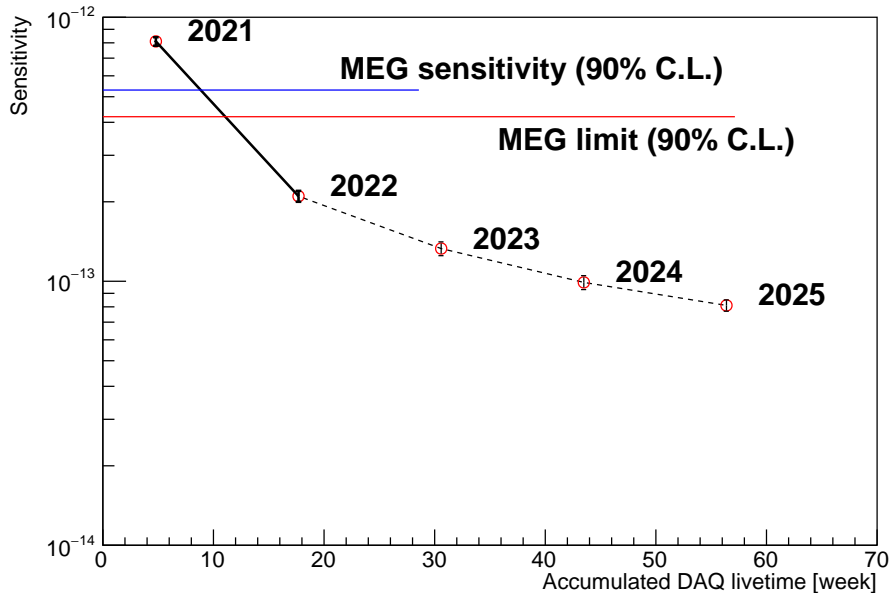


Figure 11.11: Projected sensitivities with the detector performance achieved in the 2021 run. The data points show the sensitivity of the dataset collected by the end of the year. The sensitivity and upper limit of the full dataset of the MEG experiment are shown in blue and red, respectively.

## 11.8 Discussion

### 11.8.1 Impact of the upgrade of the LXe detector from the MEG experiment

Table 11.5: Summary of performances of the LXe detector in MEG [29] and MEG II.

Performance	MEG	MEG II (design)	MEG II (measured)
Position resolution [mm]	5	2.5	2.5
Energy resolution [%] ( $w < 2$ cm / $w > 2$ cm)	2.4% / 1.7%	1.1% / 1.0%	2.0% / 1.7%
Time resolution [ps]	62	50–70	65
Detection efficiency [%]	63	69	63

Table 11.5 summarizes the measured and expected performance of the LXe detector from the MEG to the MEG II. While the position resolution improved by a factor of two, as expected, the energy resolution improved only in the shallow region. To evaluate the impact of the improvement of the gamma-ray measurement, the sensitivity with the performance of the MEG LXe detector is calculated. The signal PDFs ( $S_2$ ,  $S_3$ , and  $S_4$ ) and accidental background PDF  $A_2$  for the physics analysis of the MEG dataset collected in the 2012 run are used for the calculation, while other PDFs are common to the sensitivity calculation for the MEG II. The sensitivity achieved with the performance of the MEG LXe detector is  $1.1 \times 10^{-13}$  with the dataset to be collected by the end of the 2025 run. Therefore, the impact of the improvement of the detector performance is 26%.

### 11.8.2 Possible improvements

We have shown that the highest sensitivity of  $\mu^+ \rightarrow e^+\gamma$  can be achieved with the dataset that has already been collected by the end of the 2022 run and the detector performance achieved in the 2021 run. In this section, possible improvements of the  $\mu^+ \rightarrow e^+\gamma$  sensitivity are shown.

The identification of AIF2 $\gamma$  events through a deep-learning technique is one of the possible improvements. A deep-learning method to discriminate signal events from AIF2 $\gamma$  events was proposed and developed in Ref. [3]. In this method, a deep learning model to calculate the signal likelihood from the light distribution is trained using MC simulation to discriminate signal events from AIF2 $\gamma$  events. However, it is not used because it is difficult to predict how the output of the model would be affected by the systematic deviation of the light distribution of the data from the MC. One way to overcome the deviation of the light distribution is the feature extraction. The momenta of the two gamma rays in an AIF2 $\gamma$  event are correlated with each other, which appears as a correlation between the distance between the peaks and energy of the gamma rays, as shown in Fig. 11.12a. On the other hand, when the signal gamma rays have distant peaks, the correlation of these variables is different from the AIF2 $\gamma$  events. The distribution of the distance between the peaks in the signal events in the MC simulation is shown in Fig. 11.12b. It

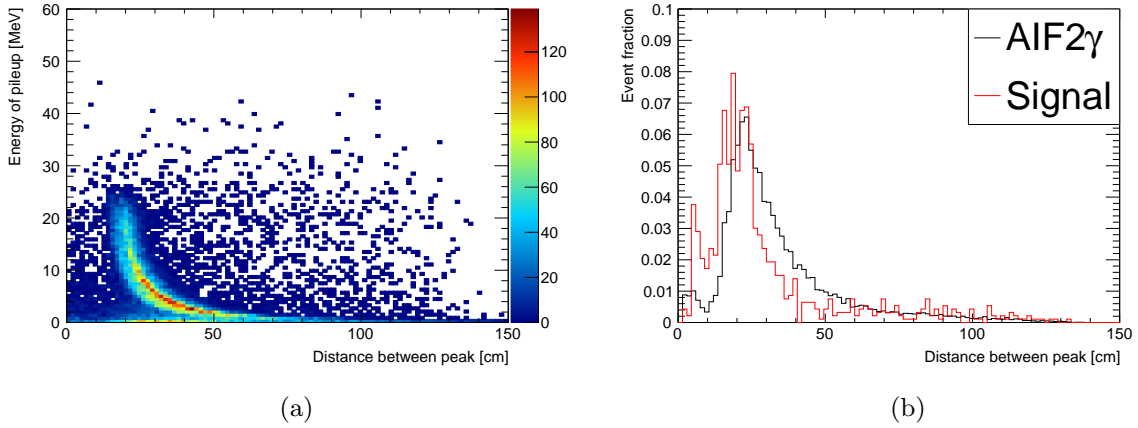


Figure 11.12: (a) Correlation between the distance between peaks in the MPPC light distribution and the reconstructed energy of the pulse of the AIF2 $\gamma$  events in the MC simulation. (b) Distance between peaks in the MPPC light distribution for the signal gamma-ray events and AIF2 $\gamma$  events in the MC simulation.

is likely that such features were extracted indirectly in the training process of the deep learning model. To realize consistent discrimination between data and MC, it would be effective to train the model with the reconstructed position and peak amplitude of the two peaks as the input instead of giving the light distribution. By doing this, it would be easier to develop a robust model that provides consistent identification of the background in data and simulation. The improvement of the analysis of on-time pileups would recover the analysis efficiency of the signal gamma ray up to 3% and improve the identification of AIF2 $\gamma$  events.

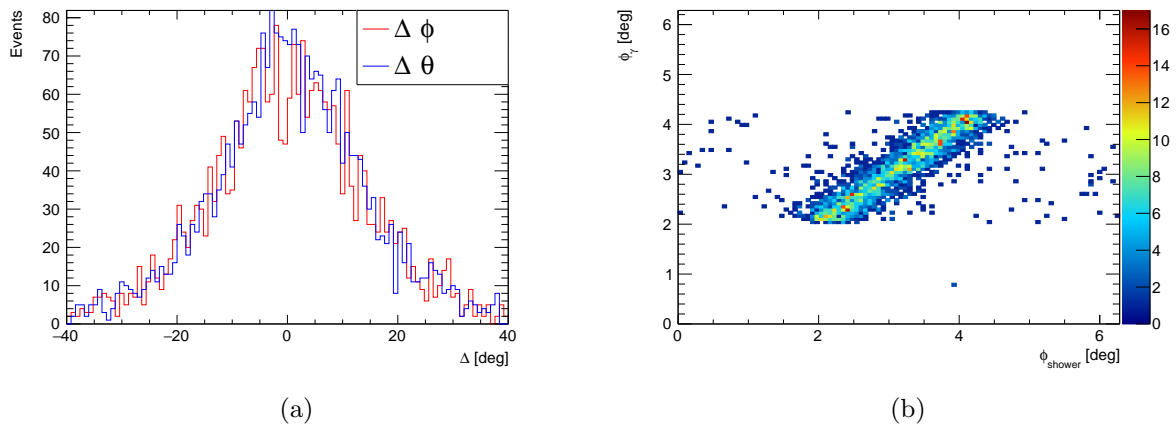


Figure 11.13: (a) Difference between the direction of the shower development and the gamma-ray momentum in  $\theta$  (blue) and  $\phi$  (red). (b) Correlation of the  $\phi$  direction between the shower development and gamma-ray momentum.

Another potential improvement is the identification of the AIF gamma-ray through the re-

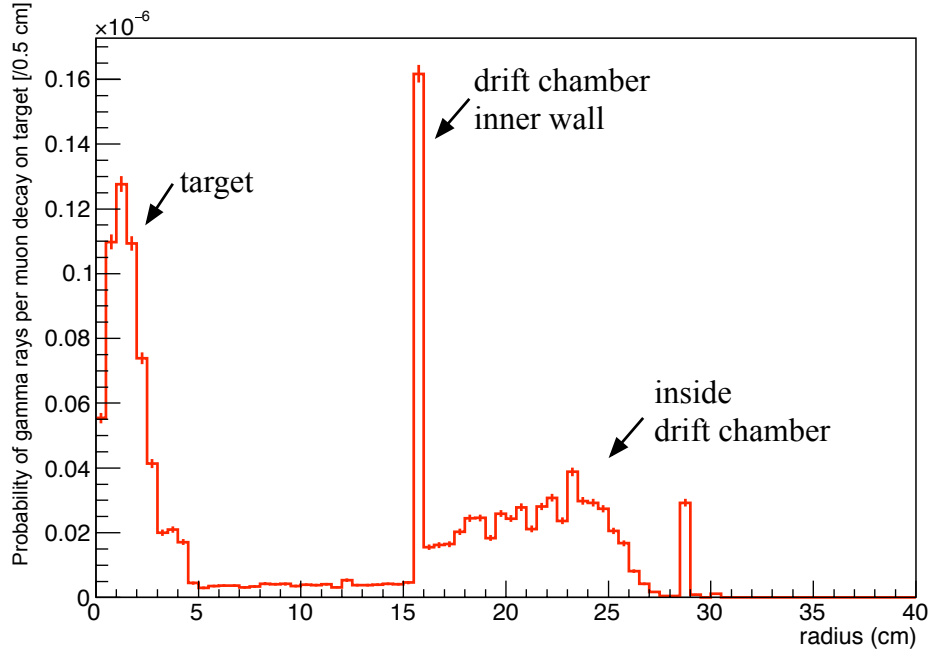


Figure 11.14: Radial distribution where the background gamma-rays ( $E_\gamma > 48$  MeV) are generated from the Michel positrons in the MC simulation [2] (The title of the y axis is added to the original figure). The  $y$ -axis is normalized to the probability per one muon decay on the target.

construction of gamma-ray direction. Let us define a vector of the shower development  $\vec{x}_{\text{shower}}$  in the MC simulation as

$$\vec{x}_{\text{shower}} = \sum_i E_i (\vec{x}_i - \vec{x}_{\text{hit}}) / E_\gamma, \quad (11.6)$$

where  $E_i$  is an energy deposit in the shower and  $\vec{x}_i$  is the position of the energy deposit. The direction of the shower development is correlated with the momentum vector of the incoming gamma-ray, as shown in Fig. 11.13. If we can reconstruct the direction of the shower development from the light distribution, the gamma-ray direction can be estimated. The direction of a gamma ray can be used to identify if the gamma ray comes from a displaced position or from the target. Fig. 11.14 shows radial positions where high-energy ( $E_\gamma > 48$  MeV) gamma-rays are generated from the AIF of positrons in the MC simulation [2]. The  $\sim 60\%$  of the high-energy AIF gamma rays come from positions displaced from the target, such as the CDCH material. Therefore, the identification of AIF gamma rays from the displaced vertex has potential to improve the sensitivity by taking advantage of the granular readout with the MPPCs.

## Chapter 12

# Conclusion

The MEG II LXe gamma-ray detector that uses a granular readout with the VUV-MPPCs is fully commissioned to start searching for the  $\mu^+ \rightarrow e^+\gamma$  decay with the highest sensitivity.

The performance of the detector was measured with the 55 MeV gamma-ray from the  $\pi^0 \rightarrow \gamma\gamma$  decay and the 17.6 MeV gamma-ray from the CW-Li setup. The resolutions of the position, energy, and time are 2.5 cm ( $w_\gamma < 2$  cm), 2.0%/1.7% ( $w_\gamma < 2$  cm/ $w_\gamma > 2$  cm), and 65 ps, respectively. The position resolution for gamma-ray hits in the shallow region is improved by a factor of two from the MEG detector (5 mm). The energy resolution for gamma-ray hits in the shallow region is also improved from 2.4% to 2.0%. The detection efficiency for the 52.8 MeV signal gamma-ray is estimated to be  $67 \pm 2\%$  from the measured efficiency for the gamma ray from the  $\pi^0 \rightarrow \gamma\gamma$  decay. The total efficiency for the signal gamma-ray is  $63 \pm 2\%$ , considering the analysis efficiency of  $93.5 \pm 0.5\%$ .

The systematic uncertainties of the gamma-ray measurement are suppressed by several calibration measurements. The systematic uncertainty of the gamma-ray position is limited to 0.6 mm by combining two complementary measurements of the MPPC positions; one was the optical measurement with a laser scanner in the construction phase, and the other was the in-situ measurement with a well-aligned 120 keV gamma-ray beam. The systematic uncertainty of the gamma-ray energy is 0.4% based on the estimation of the stability, uniformity, and linearity of the energy reconstruction with several gamma-ray sources and cosmic rays.

The rate and distribution of the background events are studied by comparing the data with the MC simulation. The absolute rate of the background gamma rays and the fraction of the events that have an on-timing pulse in data are consistent with those in the MC simulation.

The MEG II experiment started a pilot physics data taking in 2021, followed by the first long-term data acquisition in 2022. The sensitivity with the measured performance of the detectors is evaluated by the likelihood analysis. The sensitivity with the dataset collected in the 2021 run is estimated to be  $(8.1 \pm 0.4) \times 10^{-13}$ . The sensitivity will improve to  $(2.1 \pm 0.1) \times 10^{-13}$  with the combined dataset already collected in 2021 and 2022. Furthermore, the sensitivity will improve to  $(8.1 \pm 0.4) \times 10^{-14}$  by adding datasets to be collected in another three years, assuming the data will be collected with the same detector performance as in the 2021 run. This sensitivity is six times better than the sensitivity of  $5.3 \times 10^{-13}$  in the MEG experiment.

## Appendix A

# Summary of commissioning runs

### A.1 Commissioning run 2017

The main purpose of the 2017 run was to take some gamma-ray data. After a signal check of photosensors, an MPPC alignment measurement with a  $^{60}\text{Co}$  gamma-ray source was performed in July as described in Sec. 4.7. Data acquisition with the muon beam started in late November at the beam intensity of  $3.2 \times 10^7 /s$ . Gamma-rays close to the signal energy were measured during the beam time. The PMT gain calibration and the PDE calibration were tested to measure the performance of the photosensors. While the PMT gain calibration was successful, the PDE calibration provided limited information about the sensor performance due to the severe noise condition of the readout electronics and the inappropriate arrangement of readout channels for PDE calibration.

### A.2 Commissioning run 2018

The purpose of the 2018 run was to measure the detector performance with several gamma-ray sources. The 17.6 MeV gamma-rays from the CW-Li setup were used to measure the position and energy resolution of the detector. The background gamma-rays were taken at beam intensities of  $7 \times 10^6 /s$  and  $7 \times 10^7 /s$  for a study on the background gamma-ray spectrum and the pileup elimination performance. The position resolution measurement described in Sec. 6 was performed in late December. On the other hand, the  $\pi^0$  run was canceled due to the delay in the installation of the drift chamber. While successful data acquisition was achieved, the 2018 run was not a stable beam time. The major reason was that the beam time was shared by several MEG II detectors. The beam intensity and DAQ configuration were often switched to reconcile requests from several detectors. Another reason was instability of the BTS magnet due to an instability of the liquid helium supply.

### A.3 Commissioning run 2019

The major goal of the 2019 run was as follows.

- Investigate the suspected radiation damage of the MPPCs of the LXe detector.
- Install and test a new drift chamber under a muon beam environment.

The observations that the measured PDE of MPPCs in the 2018 run was significantly lower than expected and that the deterioration of the PDE implied that PDE decreased during the beam time due to radiation damage. However, it was not conclusive because it was difficult to correlate the PDE and the beam usage only with a few times of PDE calibration measurements in the beam time. Since this degradation can be a crucial issue for the MEG II experiment, dedicated data acquisition time to confirm the degradation and measure its speed was assigned. Calibration measurements were performed frequently, twice per day, to measure the detailed time variation of the PDE. The radiation damage of the PMTs was also studied. Assuming the speed of radiation damage depends on the gain of PMT, the gain of PMT was halved from the nominal value of  $1.6 \times 10^6$  down to  $8 \times 10^5$ , and the decrease of gain was measured in a muon beam environment. Since the decrease was indeed mitigated, the nominal gain of the PMT is changed to  $8 \times 10^5$  from the 2020 run. Another purpose of the 2019 run was to measure the detector performance by the  $\pi^0$  run at the end of the beam time. However, it was again canceled by a failure of the BTS magnet. The BTS system could not recover from an unexpected power cutoff in the experimental area in November because of a breaking of the coil wire.

## A.4 Commissioning run 2020

The BTS was successfully repaired during the long shutdown period, and the beam time started in September. The major goal of 2020 run was as follows.

- Measure the performance of the LXe detector in  $\pi^0$  run.
- Measure the deterioration of MPPC PDE under muon beam.
- Achieve stable operation of the drift chamber under beam.

The readout electronics was not yet ready. To accomplish the goals,  $\pi^0$  run was scheduled in between two muon beam periods. The muon beam rate was adjusted to  $3 \times 10^7/s$  so that the PDE decrease under a moderate beam intensity can be measured. The conditioning and operation of the drift chamber was performed in parallel to find a working point under muon beam environment.

### A.4.1 2020 $\pi^0$ run

In the 2020  $\pi^0$  run, the LH2 target used in the MEG experiment was reused because a new LH2 target was not yet ready. Since this target was not compatible with the experimental setup of the MEG II experiment, it was shifted by about 7 cm to the downstream side to avoid conflict with the drift chamber. To collect back-to-back gamma-ray pairs, the MPPCs for the trigger were shifted by 6 cm downstream, and the BGO detector was shifted 7 cm downstream to match the target shift. Table. A.1 summarizes the beam rate and the duration of the data acquisition

in 2020  $\pi^0$  run. The pion beam rate was reduced from  $9.5 \times 10^4 /s$  to  $1.1 \times 10^4 /s$  by three steps to mitigate the radiation damage of the SiPMs of the pTC and reduce the pileup  $\gamma$ -rays.

Table A.1: Configuration of the 2020  $\pi^0$  run

Period	Beam rate [ $10^4/s$ ]	Duration [h]
20 Nov 22:00 - 21 Nov 22:00	9.5	14
21 Nov 22:00 - 23 Nov 13:00	6.8	30
23 Nov 13:00 - 26 Nov 16:00	2.9	27
26 Nov 16:00 - 27 Nov 8:00	1.1	27

## Appendix B

# Optimization of weights for uniform online $E_\gamma$ reconstruction

In the 2021 run, the reconstructed online energy had a large non-uniformity, especially in the  $v$  direction, as shown in Fig. 3.4, and the threshold value of EGamma trigger was lowered to secure a high trigger efficiency for gamma-rays in the analysis region ( $48 \text{ MeV} < E_\gamma < 55 \text{ MeV}$ ). The low online energy threshold led to a high trigger rate and data rate, which was a

obstacle to start the physics run with good efficiency at a higher beam rate, as described in Sec. 3.3. The primary reason for the non-uniform online energy reconstruction was the biased weights for the EGamma trigger. The weight of each readout channel was defined by a reciprocal of a product of the gain, ECF, and PDE (QE) of the photosensor as  $y_i = (G \times F_{\text{EC}} \times \epsilon_{\text{PD}})^{-1}$ . An algorithm to optimize the weights for the online energy reconstruction with the CW-Li dataset was developed to solve the issue. In this algorithm, the loss function is defined as

$$\text{Loss} = \sum_{\text{event}} (\Delta E)^2 / N_{\text{event}} \quad (\text{B.1})$$

$$\Delta E = \sum_{i \in \text{MPPC, PMT}} (CA_i w_i N_{\text{pho},i} - E_{\text{peak}}) / E_{\text{peak}}, \quad (\text{B.2})$$

where  $C$  is a factor to convert the number of photons to energy,  $w_i$  is the weight for each photosensor to be optimized,  $E_{\text{peak}}$  is the energy peak value of the CW-Li gamma ray (17.6 MeV), and  $N_{\text{event}}$  is the number of events in the 17.6 MeV peak. See Sec. 7.1 on the definition of  $A_i$ . The loss function is minimized iteratively by updating the weights as

$$w_{i,j+1} = w_{i,j} - \lambda \times \Delta E \quad (\text{B.3})$$

$$w_{i,0} = 1 \quad (\text{B.4})$$

where  $j$  stands for the step in the iteration and  $\lambda$  is the learning rate to update  $w_i$  (0.1). Fig. B.1 shows the spectrum of  $\sum_{i \in \text{MPPC, PMT}} (CA_i w_i N_{\text{pho},i})$  before and after the weight optimization. By using the updated weight  $w_i y_i$  instead of the original weight  $y_i$ , the uniformity of the online reconstructed energy improved significantly, as shown in Fig. 3.4.

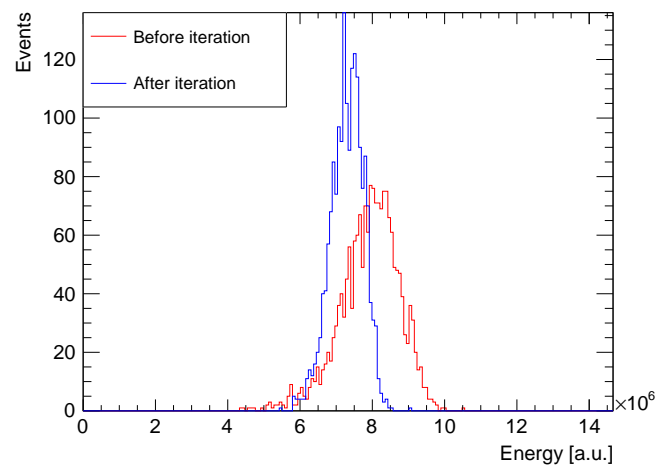


Figure B.1: The distribution of reconstructed energy with the weights before the optimization (red) and after the optimization (blue).

# Acknowledgements

I would like to express my appreciation to Prof. Toshinori Mori first. He gave me an opportunity to work on the MEG II experiment. Secondly, I am deeply grateful to Prof. Wataru Ootani for his insightful comments on my research. I would like to express my sincere gratitude to Dr. Toshiyuki Iwamoto for his support of my research activities. I appreciate Dr. Kei Ieki and Dr. Shinji Ogawa for enthusiastic discussion. I would like to thank the members of the MEG II LXe detector group, Dr. Sei Ban, Mr. Atsushi Oya, Ms. Ayaka Matsushita, Dr. Rina Onda, Mr. Kazuki Toyoda, Mr. Kohei Shimada, Mr. Kensuke Yamamoto, and Mr. Keisuke Yoshida. I give special gratitude to Dr. Yusuke Uchiyama for many insightful and constructive advice to improve the research. I also thank the MEG II Japanese colleagues, Dr. Miki Nishimura, Dr. Mitsutaka Nakao, Dr. Masashi Usami, Mr. Kosuke Yanai, Mr. Taku Yonemoto.

I would like to express many gratitudes to the members of the MEG II collaboration. In particular, I would like to thank the trigger and DAQ team, Dr. Stefan Ritt, Dr. Luca Galli, and Dr. Marco Francesconi, for their great effort to take data. I appreciate the beam team, Dr. Angela Papa, Dr. Patrick Schwendimann, Mr. Giovanni Dal Maso, Mr. Bastiano Vitali. I am happy that I could work on the development of the MPPC alignment method with the group from the University of California, Irvine: Prof. William Molzon, Dr. Terence Libeiro, Mr. William Kyle, and Mr. Dylan Palo.

I got financial support from Advanced Leading Graduate Course for Photon Science (ALPS) and Japan Society for the Promotion of Science (JSPS). I am deeply grateful to ICEPP secretaries and members. Especially, I appreciate Mori & Ootani laboratory members, Mr. Liu Linghui, Dr. Naoki Tsuji, Mr. Ryunosuke Masuda, Mr. Tatsuki Murata, Mr. Fumihito Ikeda, Mr. Yuki Ueda, Mr. Rintaro Yokota, and Mr. Weiyuan Li.

Last but not least, I would like to thank my family for their support.

December 2022,  
Tokyo,  
Satoru Kobayashi

# Bibliography

- [1] A. M. Baldini *et al.*, Search for the lepton flavour violating decay  $\mu^+ \rightarrow e^+\gamma$  with the full dataset of the MEG experiment, *Eur. Phys. J. C* 76 (8) (2016) 434.  
doi:[10.1140/epjc/s10052-016-4271-x](https://doi.org/10.1140/epjc/s10052-016-4271-x).  
URL <http://link.springer.com/10.1140/epjc/s10052-016-4271-x>
- [2] S. Ogawa, Liquid xenon detector with highly granular scintillation readout to search for  $\mu^+ \rightarrow e^+\gamma$  with sensitivity of  $5 \times 10^{-14}$  in MEG II experiment, Ph.D. thesis, The University of Tokyo (2020).  
URL [https://www.icepp.s.u-tokyo.ac.jp/download/doctor/phD2020\\_ogawa.pdf](https://www.icepp.s.u-tokyo.ac.jp/download/doctor/phD2020_ogawa.pdf)
- [3] R. Onda, Suppression of  $\gamma$ -ray backgrounds for the highest sensitivity of  $\mu^+ \rightarrow e^+\gamma$  search in MEG II experiment, Ph.D. thesis, The University of Tokyo (2021).  
URL [https://www.icepp.s.u-tokyo.ac.jp/download/doctor/phD2021\\_onda.pdf](https://www.icepp.s.u-tokyo.ac.jp/download/doctor/phD2021_onda.pdf)
- [4] K. G. Wilson, Renormalization Group and Strong Interactions, *Phys. Rev. D* 3 (8) (1971) 1818–1846. doi:[10.1103/PhysRevD.3.1818](https://doi.org/10.1103/PhysRevD.3.1818).  
URL <https://link.aps.org/doi/10.1103/PhysRevD.3.1818>
- [5] C. Patrignani *et al.*, Review of Particle Physics, *Chinese Physics C* 40 (10) (2016) 100001. doi:[10.1088/1674-1137/40/10/100001](https://doi.org/10.1088/1674-1137/40/10/100001).  
URL <https://iopscience.iop.org/article/10.1088/1674-1137/40/10/100001https://iopscience.iop.org/article/10.1088/1674-1137/40/10/100001/meta>
- [6] Y. Fukuda *et al.*, Evidence for Oscillation of Atmospheric Neutrinos, *Phys. Rev. Lett.* 81 (8) (1998) 1562–1567. doi:[10.1103/PhysRevLett.81.1562](https://doi.org/10.1103/PhysRevLett.81.1562).  
URL <https://link.aps.org/doi/10.1103/PhysRevLett.81.1562>
- [7] SNO Collaboration, Measurement of the rate of  $\nu_e + d \rightarrow p + p + e^-$  interactions produced by  $^8\text{B}$  solar neutrinos at the sudbury neutrino observatory, *Physical review letters* 87 (7) (2001) 071301. doi:[10.1103/PhysRevLett.87.071301](https://doi.org/10.1103/PhysRevLett.87.071301).  
URL <http://arxiv.org/abs/nucl-ex/0106015http://dx.doi.org/10.1103/PhysRevLett.87.071301>
- [8] G. Bertone, *Particle Dark Matter*, Cambridge University Press, 2010. doi:[10.1017/CB09780511770739](https://doi.org/10.1017/CB09780511770739).  
URL <https://www.cambridge.org/core/product/identifier/9780511770739/type/book>
- [9] T. P. Cheng, L.-F. Li,  $\mu \rightarrow e\gamma$  in Theories with Dirac and Majorana Neutrino-Mass Terms,

- Phys. Rev. Lett. 45 (24) (1980) 1908–1911. doi:10.1103/PhysRevLett.45.1908.  
URL <https://link.aps.org/doi/10.1103/PhysRevLett.45.1908>
- [10] K. Hirao, T. Moroi, *Leptonic CP and Flavor Violations in SUSY GUT with Right-handed Neutrinos*, Phys. Rev. D 104 (3) (2021) 035038. doi:10.1103/PhysRevD.104.035038.  
URL <http://arxiv.org/abs/2102.04070><http://dx.doi.org/10.1103/PhysRevD.104.035038>
- [11] J. Hisano *et al.*, *Lepton-flavor violation via right-handed neutrino Yukawa couplings in the supersymmetric standard model*, Phys. Rev. D 53 (5) (1996) 2442–2459.  
doi:10.1103/PhysRevD.53.2442.  
URL <https://link.aps.org/doi/10.1103/PhysRevD.53.2442>
- [12] J. Hisano, D. Nomura, *Solar and atmospheric neutrino oscillations and lepton flavor violation in supersymmetric models with right-handed neutrinos*, Phys. Rev. D 59 (11) (1999) 116005. doi:10.1103/PhysRevD.59.116005.  
URL <https://journals.aps.org/prd/abstract/10.1103/PhysRevD.59.116005>
- [13] R. Barbieri, L. Hall, *Signals for supersymmetric unification*, Phys. Lett. B 338 (2-3) (1994) 212–218. doi:10.1016/0370-2693(94)91368-4.  
URL <https://linkinghub.elsevier.com/retrieve/pii/0370269394913684>
- [14] J. Hisano *et al.*, *Exact event rates of lepton flavor violating processes in supersymmetric SU(5) model*, Phys. Lett. B 391 (3-4) (1997) 341–350.  
doi:10.1016/S0370-2693(96)01473-6.  
URL <https://linkinghub.elsevier.com/retrieve/pii/S0370269396014736>
- [15] K. Hirata *et al.*, *Experimental limits on nucleon lifetime for lepton+meson decay modes*, Phys. Lett. B 220 (1-2) (1989) 308–316. doi:10.1016/0370-2693(89)90058-0.  
URL <https://linkinghub.elsevier.com/retrieve/pii/0370269389900580>
- [16] T. Mori, W. Ootani, *Flavour violating muon decays*, Prog. Part. Nucl. Phys. 79 (2014) 57–94. doi:10.1016/j.pnpnp.2014.09.001.  
URL <https://linkinghub.elsevier.com/retrieve/pii/S014664101400057X>
- [17] M. Hildebrandt, *The drift chamber system of the MEG experiment*, Nucl. Instr. Meth. A 623 (1) (2010) 111–113. doi:10.1016/j.nima.2010.02.165.  
URL <https://linkinghub.elsevier.com/retrieve/pii/S0168900210004328>
- [18] P. Cattaneo *et al.*, *The Timing Counter of the MEG experiment: calibration and performance*, Nucl. Phys. B. 215 (1) (2011) 281–283.  
doi:10.1016/j.nuclphysbps.2011.04.031.  
URL <https://linkinghub.elsevier.com/retrieve/pii/S0920563211002702>
- [19] M. De Gerone *et al.*, *The MEG timing counter calibration and performance*, Nucl. Instr. Meth. A 638 (1) (2011) 41–46. doi:10.1016/J.NIMA.2011.02.044.
- [20] M. De Gerone *et al.*, *Development and commissioning of the timing counter for the MEG experiment*, IEEE Trans. Nucl. Sci. 59 (2) (2012) 379–388.  
doi:10.1109/TNS.2012.2187311.
- [21] W. Ootani *et al.*, *Development of a Thin-Wall Superconducting Magnet for the Positron*

- Spectrometer in the MEG Experiment, *IEEE Trans. Appl. Supercond.* 14 (2) (2004) 568–571. doi:10.1109/TASC.2004.829721.  
URL <http://ieeexplore.ieee.org/document/1324857/>
- [22] R. Sawada, Performance of liquid xenon gamma ray detector for MEG, *Nucl. Instr. Meth. A* 623 (1) (2010) 258–260. doi:10.1016/j.nima.2010.02.214.  
URL <https://linkinghub.elsevier.com/retrieve/pii/S0168900210004997>
- [23] A. Baldini *et al.*, A new cylindrical drift chamber for the MEG II experiment, *Nucl. Instr. Meth. A* 824 (2016) 589–591. doi:10.1016/j.nima.2015.10.103.  
URL <https://linkinghub.elsevier.com/retrieve/pii/S016890021501342X>
- [24] T. Kinoshita, A. Sirlin, Radiative Corrections to Fermi Interactions, *Phys. Rev.* 113 (6) (1959) 1652–1660. doi:10.1103/PhysRev.113.1652.  
URL <https://link.aps.org/doi/10.1103/PhysRev.113.1652>
- [25] Y. Kuno, Y. Okada, Muon Decay and Physics Beyond the Standard Model, *Rev. Mod. Phys.* (1999). doi:10.1103/RevModPhys.73.151.  
URL <http://arxiv.org/abs/hep-ph/9909265>  
<http://dx.doi.org/10.1103/RevModPhys.73.151>
- [26] Y. Uchiyama, Analysis of the First MEG Physics Data to Search for the Decay  $\mu^+ \rightarrow e^+\gamma$ , Ph.D. thesis, The University of Tokyo (2009).  
URL [https://www.icepp.s.u-tokyo.ac.jp/download/doctor/phD2009\\_uchiyaama.pdf](https://www.icepp.s.u-tokyo.ac.jp/download/doctor/phD2009_uchiyaama.pdf)
- [27] D. Kaneko, The final result of  $\mu^+ \rightarrow e^+\gamma$  search with the MEG experiment, Ph.D. thesis, The University of Tokyo (2016).  
URL [https://www.icepp.s.u-tokyo.ac.jp/download/doctor/phD2016\\_kaneko.pdf](https://www.icepp.s.u-tokyo.ac.jp/download/doctor/phD2016_kaneko.pdf)
- [28] A. M. Baldini *et al.*, MEG Upgrade Proposal (1 2013).  
URL <http://arxiv.org/abs/1301.7225>
- [29] A. M. Baldini *et al.*, The design of the MEG II experiment, *Eur. Phys. J. C* 78 (5) (2018) 380. doi:10.1140/epjc/s10052-018-5845-6.  
URL <http://link.springer.com/10.1140/epjc/s10052-018-5845-6>
- [30] D. Palo *et al.*, Precise photographic monitoring of MEG II thin-film muon stopping target position and shape, *Nucl. Instr. Meth. A* 944 (2019) 162511.  
doi:10.1016/j.nima.2019.162511.  
URL <https://linkinghub.elsevier.com/retrieve/pii/S0168900219310484>
- [31] G. Cavoto *et al.*, A photogrammetric method for target monitoring inside the MEG II detector, *Rev. Sci. Instrum.* 92 (4) (2021) 043707. doi:10.1063/5.0034842.  
URL <https://aip.scitation.org/doi/10.1063/5.0034842>
- [32] J. Adam *et al.*, The MEG detector for  $\mu^+ \rightarrow e^+\gamma$  decay search, *Eur. Phys. J. C* 73 (4) (2013) 2365. doi:10.1140/epjc/s10052-013-2365-2.  
URL <http://link.springer.com/10.1140/epjc/s10052-013-2365-2>
- [33] M. Nishimura *et al.*, Full system of positron timing counter in MEG II having time resolution below 40 ps with fast plastic scintillator readout by SiPMs, *Nucl. Instr. Meth. A* 958 (2020) 162785. doi:10.1016/j.nima.2019.162785.

- URL <https://linkinghub.elsevier.com/retrieve/pii/S0168900219312318>
- [34] A. Baldini *et al.*, The ultra light Drift Chamber of the MEG II experiment, Nucl. Instr. Meth. A 958 (2020) 162152. doi:10.1016/j.nima.2019.04.106.  
URL <https://linkinghub.elsevier.com/retrieve/pii/S0168900219306035>
- [35] M. Chiappini *et al.*, The new drift chamber of the MEG II experiment, Nucl. Instr. Meth. A 936 (2019) 501–502. doi:10.1016/j.nima.2018.10.182.  
URL <https://linkinghub.elsevier.com/retrieve/pii/S0168900218314967>
- [36] M. Tanabashi *et al.*, Review of Particle Physics, Phys. Rev. D 98 (3) (2018) 030001. doi:10.1103/PhysRevD.98.030001.  
URL <https://link.aps.org/doi/10.1103/PhysRevD.98.030001>
- [37] W. M. Haynes, CRC Handbook of Chemistry and Physics, CRC Press, 2014. doi:10.1201/b17118.  
URL <https://www.taylorfrancis.com/books/9781482208689>
- [38] C. W. Fabjan, F. Gianotti, Calorimetry for particle physics, Rev. Mod. Phys. 75 (4) (2003) 1243–1286. doi:10.1103/RevModPhys.75.1243.  
URL <https://link.aps.org/doi/10.1103/RevModPhys.75.1243>
- [39] T. Doke *et al.*, Absolute Scintillation Yields in Liquid Argon and Xenon for Various Particles, Jpn. J. Appl. Phys. 41 (Part 1, No. 3A) (2002) 1538–1545. doi:10.1143/JJAP.41.1538.  
URL <https://iopscience.iop.org/article/10.1143/JJAP.41.1538>
- [40] K. Fujii *et al.*, High-accuracy measurement of the emission spectrum of liquid xenon in the vacuum ultraviolet region, Nucl. Instr. Meth. A 795 (2015) 293–297. doi:10.1016/j.nima.2015.05.065.  
URL <https://linkinghub.elsevier.com/retrieve/pii/S016890021500724X>
- [41] A. Baldini *et al.*, Liquid xenon scintillation calorimetry and Xe optical properties, IEEE Trans. Dielectr. Electr. Insul. 13 (3) (2006) 547–555. doi:10.1109/TDEI.2006.1657967.  
URL <http://ieeexplore.ieee.org/document/1657967/>
- [42] E. Grace *et al.*, Index of refraction, Rayleigh scattering length, and Sellmeier coefficients in solid and liquid argon and xenon, Nucl. Instr. Meth. A 867 (2017) 204–208. doi:10.1016/j.nima.2017.06.031.  
URL <https://linkinghub.elsevier.com/retrieve/pii/S0168900217306848>
- [43] A. Hitachi *et al.*, Effect of ionization density on the time dependence of luminescence from liquid argon and xenon, Physical Review B 27 (9) (1983) 5279–5285. doi:10.1103/PhysRevB.27.5279.  
URL <https://link.aps.org/doi/10.1103/PhysRevB.27.5279>
- [44] NIST, XCOM: Photon Cross Sections Database.  
URL <https://www.nist.gov/pml/xcom-photon-cross-sections-database>
- [45] E. Aprile, T. Doke, Liquid xenon detectors for particle physics and astrophysics, Rev. Mod. Phys. 82 (3) (2010) 2053–2097. doi:10.1103/RevModPhys.82.2053.  
URL <https://link.aps.org/doi/10.1103/RevModPhys.82.2053>

- [46] R. Sawada, *A Liquid Xenon Scintillation Detector to Search for the Lepton Flavor Violating Muon Decay with a Sensitivity of  $10^{-13}$* , Ph.D. thesis, The University of Tokyo (2008).  
URL [https://www.icepp.s.u-tokyo.ac.jp/download/doctor/phD2008\\_sawada.pdf](https://www.icepp.s.u-tokyo.ac.jp/download/doctor/phD2008_sawada.pdf)
- [47] K. Ieki *et al.*, *Large-area MPPC with enhanced VUV sensitivity for liquid xenon scintillation detector*, Nucl. Instr. Meth. A 925 (2019) 148–155.  
doi:10.1016/j.nima.2019.02.010.  
URL <https://linkinghub.elsevier.com/retrieve/pii/S0168900219301858>
- [48] Hamamatsu Photonics K.K., *Technical note of MPPC*.  
URL [https://www.hamamatsu.com/content/dam/hamamatsu-photonics/sites/documents/99\\_SALES\\_LIBRARY/ssd/mpc\\_kapd9008j.pdf](https://www.hamamatsu.com/content/dam/hamamatsu-photonics/sites/documents/99_SALES_LIBRARY/ssd/mpc_kapd9008j.pdf)
- [49] Toyoda Gosei Co., Ltd., *Toyoda Gosei E1L49 – 3B1A – 02*.  
URL [https://www-jlc.kek.jp/~tauchi/index/LXeTPC/meetings/d070524-components/LED/E1L49\\_xxxxx\\_JEA.pdf](https://www-jlc.kek.jp/~tauchi/index/LXeTPC/meetings/d070524-components/LED/E1L49_xxxxx_JEA.pdf)
- [50] Kingbright Company, LLC., *Kingbright KA-3021QBS-D*.  
URL [https://www.kingbright.com/attachments/file/psearch/000/00/20160808bak/KA-3021QBS-D\(Ver.7B\).pdf](https://www.kingbright.com/attachments/file/psearch/000/00/20160808bak/KA-3021QBS-D(Ver.7B).pdf)
- [51] Keysight Technologies, *81150A Pulse Function Arbitrary Noise Generator*.  
URL <https://www.keysight.com/us/en/product/81150A/81150a-pulse-function-arbitrary-noise-generator.html>
- [52] OMRON Corporation, *Surface-mounting High-frequency Relay*.  
URL [https://omronfs.omron.com/en\\_US/ecb/products/pdf/en-g6k\\_2f\\_rf.pdf](https://omronfs.omron.com/en_US/ecb/products/pdf/en-g6k_2f_rf.pdf)
- [53] Paul Scherrer Institut, *Datasheet SCS3000*.  
URL [https://www.psi.ch/sites/default/files/import/ltp-electronics/WwwDocumentsEN/Datasheet\\_SCS3000.pdf](https://www.psi.ch/sites/default/files/import/ltp-electronics/WwwDocumentsEN/Datasheet_SCS3000.pdf)
- [54] A. Baldini *et al.*, *A radioactive point-source lattice for calibrating and monitoring the liquid xenon calorimeter of the MEG experiment*, Nucl. Instr. Meth. A 565 (2) (2006) 589–598. doi:10.1016/j.nima.2006.06.055.  
URL <https://linkinghub.elsevier.com/retrieve/pii/S0168900206011685>
- [55] S. Mihara *et al.*, *Development of a method for liquid xenon purification using a cryogenic centrifugal pump*, Cryogenics 46 (9) (2006) 688–693.  
doi:10.1016/j.cryogenics.2006.04.003.  
URL <https://linkinghub.elsevier.com/retrieve/pii/S0011227506000828>
- [56] R. Onda, *Research and Development on Time Calibration and Background Reduction for  $\gamma$ -ray Detection in MEG II Experiment (in Japanese)* (2019).  
URL [https://www.icepp.s.u-tokyo.ac.jp/download/master/m2018\\_onda.pdf](https://www.icepp.s.u-tokyo.ac.jp/download/master/m2018_onda.pdf)
- [57] N. P. Samios, *Panofsky Ratio*, Phys. Rev. Lett. 4 (9) (1960) 470–472.  
doi:10.1103/PhysRevLett.4.470.  
URL <https://link.aps.org/doi/10.1103/PhysRevLett.4.470>
- [58] J. Spuller *et al.*, *A remeasurement of the Panofsky ratio*, Phys. Lett. B 67 (4) (1977)

- 479–482. doi:10.1016/0370-2693(77)90449-X.  
URL <https://linkinghub.elsevier.com/retrieve/pii/037026937790449X>
- [59] S. Ritt, *The DRS chip: cheap waveform digitizing in the GHz range*, Nucl. Instr. Meth. A 518 (1-2) (2004) 470–471. doi:10.1016/j.nima.2003.11.059.  
URL <https://linkinghub.elsevier.com/retrieve/pii/S016890020302922X>
- [60] S. Ritt, R. Dinapoli, U. Hartmann, *Application of the DRS chip for fast waveform digitizing*, Nucl. Instr. Meth. A 623 (1) (2010) 486–488.  
doi:10.1016/j.nima.2010.03.045.  
URL <https://linkinghub.elsevier.com/retrieve/pii/S0168900210006091>
- [61] MIDAS, *Maximum Integrated Data Acquisition System*.  
URL [https://daq00.triumf.ca/MidasWiki/index.php/Main\\_Page](https://daq00.triumf.ca/MidasWiki/index.php/Main_Page)
- [62] S. Agostinelli *et al.*, *Geant4—a simulation toolkit*, Nucl. Instr. Meth. A 506 (3) (2003) 250–303. doi:10.1016/S0168-9002(03)01368-8.  
URL <https://linkinghub.elsevier.com/retrieve/pii/S0168900203013688>
- [63] ROME, *Root based Object oriented Midas Extension*.  
URL <https://elog.psi.ch/rome/>
- [64] A. Baldini *et al.*, *Absorption of scintillation light in a 100 l liquid xenon  $\gamma$ -ray detector and expected detector performance*, Nucl. Instr. Meth. A 545 (3) (2005) 753–764.  
doi:10.1016/j.nima.2005.02.029.  
URL <https://linkinghub.elsevier.com/retrieve/pii/S0168900205008259>
- [65] FARO, *FARO® Quantum ScanArm with Laser Line Probe*.  
URL <https://www.faro.com/en/Products/Hardware/ScanArms>
- [66] S. Kobayashi *et al.*, *Precise measurement of 3D-position of SiPMs in the liquid xenon gamma-ray detector for the MEGII experiment*, Nucl. Instr. Meth. A 936 (2019) 189–191.  
doi:10.1016/j.nima.2018.10.170.  
URL <https://linkinghub.elsevier.com/retrieve/pii/S0168900218314840>
- [67] Hexagon AB, *Leica Absolute Tracker AT960*.  
URL <https://www.hexagonmi.com/products/laser-tracker-systems/leica-absolute-tracker-at960>
- [68] E. Garutti, Y. Musienko, *Radiation damage of SiPMs*, Nucl. Instr. Meth. A 926 (2019) 69–84. doi:10.1016/j.nima.2018.10.191.  
URL <https://linkinghub.elsevier.com/retrieve/pii/S0168900218315055>
- [69] G. Lindström, *Radiation damage in silicon detectors*, Nucl. Instr. Meth. A 512 (1-2) (2003) 30–43. doi:10.1016/S0168-9002(03)01874-6.  
URL <https://linkinghub.elsevier.com/retrieve/pii/S0168900203018746>
- [70] I. Nakamura, *Radiation damage of pixelated photon detector by neutron irradiation*, Nucl. Instr. Meth. A 610 (1) (2009) 110–113. doi:10.1016/j.nima.2009.05.086.  
URL <https://linkinghub.elsevier.com/retrieve/pii/S0168900209010407>
- [71] Y. Qiang *et al.*, *Radiation hardness tests of SiPMs for the JLab Hall D Barrel calorimeter*, Nucl. Instr. Meth. A 698 (2013) 234–241. doi:10.1016/j.nima.2012.10.015.

- URL <https://linkinghub.elsevier.com/retrieve/pii/S0168900212011473>
- [72] M. Centis Vignali *et al.*, Neutron irradiation effect on SiPMs up to  $\Phi_{neq} = 5 \times 10^{14} \text{ cm}^{-2}$ , Nucl. Instr. Meth. A 912 (2018) 137–139. doi:10.1016/j.nima.2017.11.003.  
URL <https://linkinghub.elsevier.com/retrieve/pii/S0168900217311890>
- [73] T. Matsubara, Radiation damage of MPPC by gamma-ray irradiation with Co 60, in: Proceedings of International Workshop on new Photon-Detectors — PoS(PD07), Vol. 51, Sissa Medialab, Trieste, Italy, 2008, p. 032. doi:10.22323/1.051.0032.  
URL <https://pos.sissa.it/051/032>
- [74] Flora M. Li, Arokia Nathan, CCD Image Sensors in Deep-Ultraviolet, Microtechnology and Mems, Springer-Verlag, Berlin/Heidelberg, 2005. doi:10.1007/b139047.  
URL <http://link.springer.com/10.1007/b139047>
- [75] K. Shimada, Research on photon detection efficiency of VUV-MPPC in MEG II liquid xenon detector (in Japanese) (2021).  
URL [https://www.icepp.s.u-tokyo.ac.jp/download/master/m2020\\_shimada.pdf](https://www.icepp.s.u-tokyo.ac.jp/download/master/m2020_shimada.pdf)
- [76] K. Yoshida, Research on decrease of photon detection efficiency of VUV-MPPC in MEG II liquid xenon detector and on stable operation of the detector (in Japanese) (2022).  
URL [https://www.icepp.s.u-tokyo.ac.jp/download/master/m2021\\_yoshida.pdf](https://www.icepp.s.u-tokyo.ac.jp/download/master/m2021_yoshida.pdf)
- [77] Teledyne FLIR, Support for FLIR E50.  
URL <https://www.flir.com/support/products/e50/?vertical=condition+monitoring&segment=solutions#Overview>
- [78] G. Cowan *et al.*, Asymptotic formulae for likelihood-based tests of new physics, Eur. Phys. J. C 71 (2) (2011) 1554. doi:10.1140/epjc/s10052-011-1554-0.  
URL <http://link.springer.com/10.1140/epjc/s10052-011-1554-0>
- [79] S. S. Wilks, The Large-Sample Distribution of the Likelihood Ratio for Testing Composite Hypotheses, Ann. Math. Stat. 9 (1) (1938) 60–62. doi:10.1214/aoms/1177732360.  
URL <http://projecteuclid.org/euclid.aoms/1177732360>